




Publicly Accessible Penn Dissertations

2021

Low-Dimensional Material Devices For Atomic Defect Engineering, Ionic And Molecular Transport

Jothi Priyanka Thiruraman
University of Pennsylvania

Follow this and additional works at: <https://repository.upenn.edu/edissertations>

 Part of the [Condensed Matter Physics Commons](#), [Mechanics of Materials Commons](#), and the [Nanoscience and Nanotechnology Commons](#)

Recommended Citation

Thiruraman, Jothi Priyanka, "Low-Dimensional Material Devices For Atomic Defect Engineering, Ionic And Molecular Transport" (2021). *Publicly Accessible Penn Dissertations*. 3954.
<https://repository.upenn.edu/edissertations/3954>

This paper is posted at ScholarlyCommons. <https://repository.upenn.edu/edissertations/3954>
For more information, please contact repository@pobox.upenn.edu.

Low-Dimensional Material Devices For Atomic Defect Engineering, Ionic And Molecular Transport

Abstract

With the advancement of nanofabrication techniques and the growth and synthesis of novel low-dimensional materials, such as graphene and transition metal dichalcogenides, it is possible to probe the fundamental principles of ion and molecule transport down to the single-atom scale. Understanding these ionic and atomic interactions during molecular transport at an atomic level play a pivotal role in developing solid-state aquaporins or bio-mimicking artificial membrane proteins channels. Apart from biological processes in living cells, ionic transport plays a vital role in membrane-based technologies such as water purification, desalination, separation techniques and energy harvesting. This thesis focuses on developing low-dimensional devices and creating sub-nanometer pores or point defects for exploring molecular and ionic transport phenomena at an atomic scale. Additionally, defect engineering of such point defects also has potential quantum applications, including quantum sensing and computation. First, I discuss the fabrication process of these low-dimensional devices, including 2D materials growth, transfer with the help of nanofabrication techniques and various characterization modes. Further, in this regime of angstrom-scale confinements, I investigate ionic transport phenomenon in monolayer 2D materials with single sub-nanometer pore and an ensemble of sub-nanometer pores and report experimental results showing strong deviation from continuum physics. Macroscopic quantities such as bulk ion concentration for these angstrom-size systems become insufficient to explain features of the measured ion conductance and its scaling with experimental parameters such as ion concentration and surface charge of the pore (edge atoms).

Degree Type

Dissertation

Degree Name

Doctor of Philosophy (PhD)

Graduate Group

Electrical & Systems Engineering

First Advisor

Marija Drndic

Keywords

2D Materials, Angstrom-size Pore, Defect Engineering, Low-Dimensional Materials, Nanofluidics

Subject Categories

Condensed Matter Physics | Mechanics of Materials | Nanoscience and Nanotechnology

LOW-DIMENSIONAL MATERIAL DEVICES FOR ATOMIC DEFECT
ENGINEERING, IONIC AND MOLECULAR TRANSPORT

Jothi Priyanka Thiruraman

A DISSERTATION

Electrical and Systems Engineering

Presented to the Faculties of the University of Pennsylvania

in

Partial Fulfillment of the Requirements for the

Degree of Doctor of Philosophy

2021

Supervisor of Dissertation

Dr. Marija Drndić, Professor of Physics & Astronomy

Graduate Group Chairperson

Dr. Victor M. Preciado, Associate Professor, Electrical and Systems Engineering

Dissertation Committee

A. T. Charlie Johnson, Professor of Physics and Astronomy, University of Pennsylvania

Mark G. Allen, Professor of Electrical and Systems Engineering, University of Pennsylvania

Haim Bau, Professor of Mechanical and Applied Mechanics, University of Pennsylvania

LOW-DIMENSIONAL MATERIAL DEVICES FOR ATOMIC DEFECT
ENGINEERING, IONIC AND MOLECULAR TRANSPORT

COPYRIGHT

2021

Jothi Priyanka Thiruraman

This work is licensed under the
Creative Commons Attribution-
NonCommercial-ShareAlike 4.0
License

To view a copy of this license, visit

<https://creativecommons.org/licenses/by-nc-sa/4.0/us/>

*அகர முதல எழுத்தெல்லாம் ஆதி
பகவன் முதற்றே உலகு.*

ACKNOWLEDGMENT

I'm in gratitude for the innumerable people I encountered during my research years for their conversations, suggestions and any advice.

First, I would like to express my sincere gratitude to my advisor Dr. Marija Drndić for giving me this opportunity to do research as a Masters' student and then continuing for a PhD. I'm grateful for her advice and lessons professionally and in life otherwise. I would also like to thank Dr. Mark Allen, Dr. Haim Bau and Dr. A.T. Charlie Johnson for serving on my committee and for their knowledgeable remarks that helped shape this thesis.

On the academic front, I would like to extend my thanks to all Professors whose lectures I've attended as part of the curriculum and otherwise, especially those who granted me permission to audit or sit in on their classes. I thoroughly enjoyed learning, they gave me a wider perspective on science and were a pleasant refreshment from my experimental work.

I am extremely privileged and grateful to the Vagelos Institute for Energy, Science and Technology (VIEST), Dr. Nadine Gruhn and Dr. Karen Goldberg for selecting my work for a PhD Fellowship.

This work would not had made the same impact without our exceptionally talented collaborators who took interest in our work and joined forces. Thank you for contribution and guidance: Dr. Mauricio Terrones, Dr. Kazunori Fujisawa, Dr. Vincent Meunier, Dr. Radha Boya, Dr. Ashok Keerthi, Dr. Eric Stach, Dr. Deep Jariwala, Dr. A.T Charlie Johnson, Dr. Adrien Nicolai, Dr. Patrick Senet, Dr. Aleksandra Radenovic.

Furthermore, I am fortunate to have had a friendly, healthy and encouraging work environment around me— my research group members and other research colleagues: Dr. Gopinath Danda, Dr. William Parkin, Dr. Matthew Puster, Dr. David Niedzwiecki, Dr. Francis Chen-Chi, Dr. Adrian Balan, Dr. Paul Masih Das, Killian Chou, Rachael Keneipp, Dr. Alice Castan, Dr. Carl Naylor, Tiyani Zhang, Dr. Daniela Perez, Dr. Sanjin Marion.

I would like to also mention the staff members of the Singh Center for Nanotechnology whose support and cooperation helped tremendously in achieving research goals: Dr. Eric Johnston, Charles Veith, Dr. Jamie Ford, Dr. Matt Brukman, Dr. Doug Yates. Dr. Gerald Lopez and Noah Clay.

I would also like to thank Dr. Robert Kyser from Lehigh University where we carried out much for our AC-TEM work. More recently the usage of Ga-source FIB at Drexel University, thanks to Dr. Craig Johnson for their cooperation with external users. A lot of my project direction and timely results would have collapsed if not for the existence of these equipment around Penn.

I would like to mention Penn Physics Admin staff: Millicent Minnick, Helen Jackson, Doug Feldman and Penn ESE Admin staff: Lilian Wu, Christina Burton, Liz Kopeczky, Sovannary Heang and for their help and support during the PhD program.

Lastly, I would like to share my gratitude to my Amma, Appa, Chithi, my late Chinnu Thatha for their conditional love and time spent with me and other friends and family for their love and support for all these years of my life.

ABSTRACT

LOW-DIMENSIONAL MATERIAL DEVICES FOR ATOMIC DEFECT ENGINEERING, IONIC AND MOLECULAR TRANSPORT

Jothi Priyanka Thiruraman

Marija Drndić

With the advancement of nanofabrication techniques and the growth and synthesis of novel low-dimensional materials, such as graphene and transition metal dichalcogenides, it is possible to probe the fundamental principles of ion and molecule transport down to the single-atom scale. Understanding these ionic and atomic interactions during molecular transport at an atomic level play a pivotal role in developing solid-state aquaporins or bio-mimicking artificial membrane proteins channels. Apart from biological processes in living cells, ionic transport plays a vital role in membrane-based technologies such as water purification, desalination, separation techniques and energy harvesting. This thesis focuses on developing low-dimensional devices and creating sub-nanometer pores or point defects for exploring molecular and ionic transport phenomena at an atomic scale. Additionally, defect engineering of such point defects also has potential quantum applications, including quantum sensing and computation. First, I discuss the fabrication process of these low-dimensional devices, including 2D materials growth, transfer with the help of nanofabrication techniques and various characterization modes. Further, in this regime of angstrom-scale confinements, I investigate ionic transport phenomenon in monolayer 2D materials with single sub-nanometer pore and an ensemble of sub-nanometer pores and report experimental results showing strong deviation from continuum physics. Macroscopic quantities such as bulk ion concentration for these angstrom-size systems

become insufficient to explain features of the measured ion conductance and its scaling with experimental parameters such as ion concentration and surface charge of the pore (edge atoms).

TABLE OF CONTENTS

ACKNOWLEDGMENT	iv
ABSTRACT	vi
LIST OF TABLES	xi
LIST OF ILLUSTRATIONS	xii
1 Introduction	1
1.1 <i>Low-Dimensional Materials: A Brief Overview</i>	1
1.2 <i>Physics of Nanopore Structures and Molecular Interactions</i>	2
1.2.1 Solid-State Nanopores.....	4
1.2.2 Sizes of water molecules and ions and the comparably small apertures: $\sim 0.1 - 1$ nm	5
1.2.3 Ionic Selectivity of CNTs, Nanopores and Channels	7
1.3 <i>Outline and Intellectual Contribution of this Thesis</i>	18
2 Device Fabrication and Growth of Low-Dimensional Materials	22
2.1 <i>Device Fabrication</i>	22
2.1.1 Photolithography for Silicon Nitride Platform.....	22
2.2 <i>Graphene Growth</i>	27
2.2.1 Graphene Transfer	28
2.3 <i>Growth of Transition Metal Dichalcogenide (TMDs)</i>	29
2.3.1 Transfer of TMD and Device Fabrication	32
2.4 <i>Large-Scale fabrication of MoS₂ Film</i>	34
2.4.1 Introduction.....	34
2.4.2 Background.....	35
2.4.3 Growth and Characterization of MoS ₂ Thin Films.....	37
2.4.4 Controlled Large-Area Etching for Nanoporous MoS ₂ Films	41
2.4.5 Characterization and Fluid Transport of Nanoporous MoS ₂	43
2.4.6 Additional Experimental Methods	47
2.4.7 Summary	52
3 Defect Engineering and Nanopatterning in Transition Metal Dichalcogenide	55
3.1 <i>Introduction</i>	55
3.2 <i>Background</i>	56
3.3 <i>Fabrication of Angstrom-Size Pores Devices using Gallium Ion Beam</i>	59
3.3.1 Mechanism of Irradiation of TMDs using Focused Ion Beam.....	61
3.4 <i>Characterization of Atomic Defects in TMDs using Raman Spectroscopy and Aberration-Corrected Transmission Electron Microscopy (AC-TEM)</i>	65
3.4.1 Nanopatterning on Suspended and Supported TMDs Substrate	71
3.4.2 Statistical Image Analysis of Angstrom-Size Pores in TMDs	76
3.5 <i>Additional Experimental Methods</i>	81

3.6	<i>Summary</i>	84
4	Angstrom-Size Nanoporous Membrane Creation in MoS ₂ and Ionic Transport.....	85
4.1	<i>Introduction</i>	85
4.2	<i>Background</i>	86
4.3	<i>Fabrication of Angstrom-Size Nanoporous MoS₂ Membranes</i>	87
4.3.1	Raman and Photoluminescence Spectroscopy of Ga ⁺ irradiated monolayer MoS ₂ membrane 88	
4.4	<i>Electron Micrographs of Ga⁺ irradiated monolayer MoS₂ membrane</i>	91
4.4.1	Statistical Image Analysis of the Sub-nm size Pores using AC-STEM Images.....	92
4.5	<i>Experimental Ionic Transport Measurements of Sub-nm Size MoS₂ Pores</i>	93
4.6	<i>Theory of Sub-nm Pores: Non-Equilibrium Molecular Dynamics (NEMD)</i>	101
4.6.1	Calculation of Effective Diameters of Non-Circular Pores	104
4.7	<i>Additional Experimental Methods</i>	105
4.8	<i>Summary</i>	117
5	Single Zero-D Pore and Quantum Confinement in Ionic Transport	118
5.1	<i>Introduction</i>	118
5.2	<i>Background</i>	119
5.3	<i>Experimental Methods</i>	120
5.3.1	Fabrication of Zero D Pore.....	121
5.3.2	Geometric Pore Models and Atomic Structures of Fabricated Pores.....	124
5.4	<i>Experimental Ionic Transport Measurement of a Single Zero-D Pore Device</i>	127
5.4.1	Experimental Ionic Properties of Single OD Pores	130
5.5	<i>Discussion on Sub-nm MoS₂ Pore Studies</i> ^{57,190,43,42,188}	136
5.5.1	Reversible Wetting–Rewetting Behavior.....	137
5.5.2	Hydrophobic Characteristics of Single Atomic Pores	138
5.5.3	Noise Characteristics of Single Atomic Pore Chips	141
5.6	<i>Confinement Effects in Zero D with various Ionic Molarities</i>	142
5.7	<i>Calculation of pore conductivities based on measured conductance and pore sizes</i>	145
5.8	<i>Saturation of Conductance vs Molarity</i>	148
5.9	<i>Additional Experimental Methods</i>	150
5.10	<i>Conclusion and Future Directions</i>	161
6	Gas flow through atomic-scale apertures	164
6.1	<i>Introduction</i>	164
6.2	<i>Background</i>	165
6.3	<i>Fabrication of Devices with Atomic Apertures</i>	166
6.4	<i>Experimental Gas Measurements in Atomic Apertures Devices</i>	168
6.4.1	Understanding Apertures “Sizes”	170

6.5	<i>Additional Experimental Methods</i>	177
6.6	<i>Discussion on Gas Permeance in literature and Conclusion</i>	193
BIBLIOGRAPHY.....		196

LIST OF TABLES

Table 1.1. Comparison of Ionic Transport Properties in Selected Pore, Channel, and Tube Architectures.	9
Table 2.1 Controlled parameters for monolayer WS ₂ flake growth.....	30
Table 2.2. Controlled parameters for monolayer MoS ₂ flake growth.....	31
Table 3.1. Total imaged area of atomic resolution HAADF AC-STEM micrographs.	77
Table 3.2. FIB irradiation dose calculations and defect densities from Equation (1) and Equation (2).	78
Table 5.1. Illustration of geometrically possible configurations of MoS ₂ atomic (0D) pores with areas ≤ 1 nm ²	125
Table 6.1. Effective areas of atomic-scale apertures in WS ₂ monolayer membrane for transport of He	191

LIST OF ILLUSTRATIONS

Figure 1.1. Overview of the relevant order-of-magnitude sizes of fluidic transport channels and selected examples of recently measured structures. Diameters, d , as small as the sizes of single-atom-vacancies, on the order of 0.1 nm, can be achieved.	4
Figure 1.2. Current-voltage measurements for asymmetric ion concentrations on the two sides of the membrane, used to measure the “reverse potential” or “zero-current potential” across the pore.....	14
Figure 2.1. Lithographic patterning and etching of Si/SiO ₂ /SiN _x chips.	24
Figure 2.2. Schematics of experimental CVD graphene growth setup. Adapted from Danda et al.	27
Figure 2.3. Schematics of experimental bubble transfer of graphene on copper foil. Adapted from Danda et al.	28
Figure 2.4. Schematics of experimental CVD growth setup for WS ₂ flakes. Adapted from Danda et al.	29
Figure 2.5. TMD Characterization techniques.....	31
Figure 2.6. Position-controlled transfer of TMDs from as-grown substrate to a desired device.....	32
Figure 2.7. Characterization of pristine (as-grown) and transferred MoS ₂ films.	37
Figure 2.8. Monolayer regions in a few-layer MoS ₂ matrix.	39
Figure 2.9. Schematic of nanoporous MoS ₂ membrane fabrication using PAN etchant.	42
Figure 2.10. TEM-based quantification of nanoporous MoS ₂ membranes.....	43
Figure 2.11. Nucleation and expansion of nanopores in monolayer MoS ₂ regions due to PAN etchant exposure.....	46
Figure 2.12. Characterization of the Mo foil growth substrate.....	50
Figure 2.13. Current power spectral densities for nanoporous MoS ₂ membranes.....	51
Figure 3.1. Irradiation mechanism and HAADF images of monolayer TMD flake.....	59
Figure 3.2. Mechanism of Irradiation of TMDs using Focused Ion Beam.....	62
Figure 3.3. Characterization of atomic defects in TMDs using Raman Spectroscopy and Aberration-Corrected Transmission Electron Microscopy (AC-TEM).....	65
Figure 3.4 Raman peak shifts for suspended monolayer WS ₂ exposed to FIB irradiation with doses between 0 and 10 ¹⁷ ions/cm ²	66

Figure 3.5. HAADF AC-STEM images of pristine monolayer MoS ₂ and WS ₂	67
Figure 3.6. Nanopatterning on Suspended and Supported Substrate.....	71
Figure 3.7 AC-STEM images of substitutional dopants.....	72
Figure 3.8. AC-STEM micrographs of FIB-irradiated (6.4×10^{14} ions/ cm ²) monolayer WS ₂ under constant imaging conditions (<i>i.e.</i> , STEM raster scanning).....	73
Figure 3.9. High magnification AC-STEM images of individual defects along with their observed atomic configuration.....	74
Figure 3.10. Statistical Image Analysis of Angstrom-Size Pores in TMDs	76
Figure 3.11. Statistical Image Analysis of irradiated MoS ₂ on different substrates.....	79
Figure 3.12. Statistical Image Analysis of irradiated WS ₂ at various doses on different substrates.....	80
Figure 4.1. Irradiation of monolayer MoS ₂ flake under controlled 30kV Ga ⁺ ion beam.	87
Figure 4.2. Raman and Photoluminescence Spectroscopy of Ga ⁺ irradiated monolayer MoS ₂ membrane.....	88
Figure 4.3. Aberration corrected scanning transmission electron microscopy (AC-STEM) characterization of single-layer MoS ₂ showing an evolution of angstrom-size defects with Ga ⁺ ion beam irradiation.	91
Figure 4.4. (a) The experimental setup to measure the conductance of nanoporous MoS ₂ membranes and (b) Current-voltage plot of a MoS ₂ device irradiated with a dose of 1.60×10^{13} ions/cm ² showing a non-linear trend in the voltage range $V_B = \pm 0.8$ V.	94
Figure 4.5. (c) Current versus time traces at an applied voltage of $V_B = 0.1$ V and (d) the corresponding power spectral density for two devices (device P and Q, dose = 1.60×10^{13} ions/cm ²). (e) Current versus time trace for device Q at an applied voltage of $V_B = 1$ V	95
Figure 4.6 Ionic current vs. voltage (I-V) curves and conductances measured for pristine and irradiated MoS ₂ membranes with Dose 1 = 6.25×10^{12} , Dose 2 = 1.11×10^{13} , Dose 3 = 2.5×10^{13} ions/cm ²	97
Figure 4.7 Molecular Dynamics of individual sub-nm MoS ₂ pores with current-voltage characteristics and individual sub-nm pore conductance.....	101
Figure 4.8. Distributions of diameters computed from MoS ₂ pores atomic structures. The center of mass of the pore is shown using a grey sphere in the structure images in inset.	105
Figure 4.9. (a) Optical and (b) fluorescence (673 nm-centered bandpass filtered) microscopic image of transferred single-layer MoS ₂ flake onto SiN _x window with FIB hole at the center.	107

Figure 4.10. The setup of the deterministic transfer stage for micro-positioning MoS ₂ flakes onto SiN _x windows.	107
Figure 4.11. Optical images (top) and fluorescence images (bottom, 673 nm-centered bandpass filtered) of the pristine and the Ga ⁺ ion irradiated single-layer MoS ₂ on Quantifoil TEM grid.	108
Figure 4.12. Raw STEM image of a V ₃ Mo+5S type vacancy-defect in MoS ₂ lattice (left).	109
Figure 4.13. Step-by-step images of the binary creation process from the raw STEM images.	110
Figure 4.14. Low magnification STEM-HAADF image of the pristine and Ga ⁺ ion irradiated MoS ₂	111
Figure 4.15. Statistical analysis of sub-nm diameter pores identified by AC-STEM observation.	114
Figure 4.16. Statistical analysis of missing Mo atom using high magnification the STEM-HAADF images.	115
Figure 5.1. Selected area AC-STEM drilling for individual sub-nm MoS ₂ pores.	122
Figure 5.2. TEM images of MoS ₂ (sub-nm-size) atomic pores and pore geometric models. Zigzag-armchair 0D pores in MoS ₂	128
Figure 5.3. Schematic of single pore STEM drilling, solution treatment, and measurement setup.	130
Figure 5.4. Ion current–voltage and noise curves in single pore devices.	132
Figure 5.5. Ion current–voltage curves and pore conductivities calculated from a bulk model.	142
Figure 5.6. Image processing for TEM pore area and diameter determination.	155
Figure 5.7. Conductance of zero-D pores	156
Figure 5.8. Samples containing multiple sub-nm MoS ₂ pores drilled with AC-TEM... ..	157
Figure 5.9. Current-voltage and noise characteristics of sub-nm MoS ₂ pores on a low-capacitance glass chip	158
Figure 5.10. Power Spectral Density of a glass chip	159
Figure 5.11. Molecular dynamics simulation equation for sub-5 nm-diameter MoS ₂ pore conductance in 1 M KCl	160
Figure 6.1. Atomic apertures fabricated using an FIB scanning technique.	167

Figure 6.2. Gas flow through atomic apertures.....	170
Figure 6.3. Atomic apertures and electron density isosurfaces.	175
Figure 6.4. Schematic of fabrication process for WS ₂ single atom aperture devices	188
Figure 6.5. Characterization of CVD-grown pristine WS ₂ flakes.....	189
Figure 6.6. Characterization of FIB-irradiated WS ₂ flakes.....	189
Figure 6.7. Atomic apertures.	190
Figure 6.8. Helium flow measurement	191
Figure 6.9. Tears in SEM analysis	192
Figure 6.10. Current-voltage (I-V) analysis.....	192

1 Introduction

Some sections of this chapter have been adapted from the invited Perspective publication, titled “Ions and Water Dancing through Atom-Scale Holes: A Perspective toward “Size Zero”” by J. P. Thiruraman, P. Masih Das, M. Drndić. Cite This: ACS Nano 2020, 14, 4, 3736–3746

1.1 Low-Dimensional Materials: A Brief Overview

With the advancement of the rapidly emerging technology and silicon being the frontrunner, there is a constant strive to explore new materials, what could perhaps augment this industrially perfected 50-year-old material, silicon? To this end, low-dimensional materials have shown tremendous potential and exciting properties that can revolutionize the semiconductor research and industry with applications in electronics and optoelectronic devices including field-effect transistors, heterostructure junctions, photodetectors, photovoltaics, and sensors. This is mainly due the existence of bandgap, semi-metallic, superconducting nature of 2D materials.⁷⁴

Beyond electronics, low-dimensional materials have an irreplaceable position as the thinnest material on this planet! The atomic thickness of the low-dimensional materials make is extremely attractive candidate for many research fields working in the similar atomic size regime. In this thesis, I presented contributed results to the nascent field of nanofluidics which explores the transport of ionic species and fluidics.¹⁹ The advent of nanomaterials and low-dimensional materials such as graphene, graphene oxide, h-BN, Mo

and W based transition metal dichalcogenides and other TMDs have been instrumental in investigating this ionic and molecular properties at a nanoscale.

While pristine low-dimensional devices show impermeability to gas molecules as small as helium indicative of the thinnest physical barrier, atomic defects in such 2D materials transcend them to contain smallest possible nanopores.¹⁵² In the past few years, nanoporous atomically thin membranes (NATMs) in 2D materials have shown immense potential to transform and redefine mass transport at a nanoscale.²⁰⁹

It has been a special and an interesting journey to especially see how the field has evolved over the course of my PhD. From just a few papers on graphene showing the ability to host nanopores to the enormous experimental and theoretical research articles and dedicated conferences held today, is testimony to the potential and promise of these next-generation materials.

Ionic transport is a critical process prevalent in living cells to water filtration systems. Apart from membrane-based technologies, bio-mimicking solid-state structure can have a tremendous impact on understanding of biological systems. Artificial solid-state structure that bio-mimicking protein pores such as membrane protein including K^+ and Na^+ channels which play a critical role for physiological function in living cells, ionic pumps in neurons and nephrons, aquaporins which demonstrate superior water permeability and selectivity are other possible applications of these angstrom-scale confinements structure.

1.2 Physics of Nanopore Structures and Molecular Interactions

With the advancement of nanofabrication techniques and the growth and synthesis of new low-dimensional materials, such as nanotubes and graphene, it is possible to probe the

fundamental principles of ion and molecule transport down to the single-atom scale. Many different artificial structures have been realized and tested such as low-dimensional nanopores and “nanoporous” membranes (See for recent review, Danda *et al.*³³). This is an interesting size regime (about 1 nm and below) where single ions and molecules are only a few times smaller or even comparable to the characteristic size of the apertures through which they translocate and their interactions with the atoms of the structures can be significant and govern the types of phenomena observed. The geometrically restricted flow of ions and water can give rise to new phenomena where atomistic details become important, and that can differ from the leading phenomena at larger scales. The single and sub-nanometer scale is also typically a regime where, for many materials, simple calculations such as Ohm’s law for ion current *vs.* pore size, otherwise typically applicable for larger pores, fail. Macroscopic quantities such as bulk ion mobilities or bulk ion concentration become inadequate and have to be modified within the pores to explain features of the measured ion conductance and its scaling with experimental parameters such as ion concentration, net charges of the pore “walls” (edge atoms) that depends on the pH value. Figure 1.1 illustrates several different types of solid-state fluidic transport structures, including examples of 2D material pores^{34,41,44,46,114,116,139,133,167,235}, silicon-^{28,158,171,206,213} and hafnium-based¹⁰⁴ pores, carbon nanotubes^{7,169,202}, and nanopatterned channels³⁹. A concise and useful table comparing main characteristics of notable 2D pores has been published by Mojtavavi *et al.*¹³³ in their paper on MXene pores. Other discussions can be found in a review by Danda *et al.*³³ Diameters, d , as small as the sizes of single-atom-vacancies, on the order of 0.1 nm, can be achieved. Channel length, L , from ~ 0.1 nm to 10 μm , corresponds to “pores” *vs.* “tubes” and “channels”, in order of increasing L .

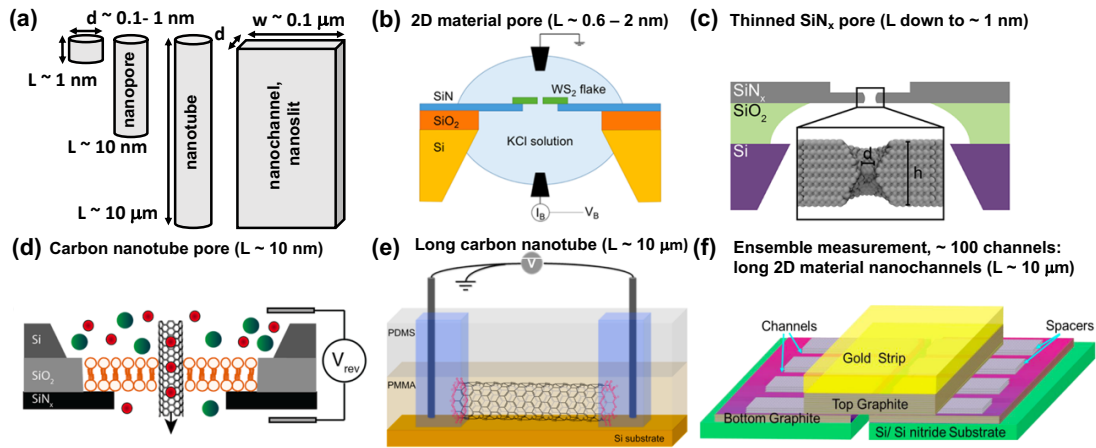


Figure 1.1. Overview of the relevant order-of-magnitude sizes of fluidic transport channels and selected examples of recently measured structures. Diameters, d , as small as the sizes of single-atom-vacancies, on the order of 0.1 nm, can be achieved.

(a) Channel length, L , can be tuned from ~ 0.1 nm to $10 \mu\text{m}$, corresponding to “pores” vs. “tubes” and “channels”, as the dominant terminologies used in recent literature to describe such structures. Note that calculated sizes of water molecules are ~ 0.3 nm and of hydrated ions about 0.7 to 1 nm^{39,149}. (b) to (f) Examples of recent experiments and device configurations, shown in the order of increasing channel length, from $L \sim 1$ nm for “nanopores” as in 2D pores made of graphene^{46,130,167}, MoS₂¹¹⁴, WS₂³⁴, BN^{116,235}, MXenes¹³³, sub-10-nm-thick silicon nitride membranes^{28,158,171,206,213}, and sub-7-nm-thick HfO₂,¹⁰⁴ to $L \sim 10$ nm, for “ultra-short” carbon nanotubes reported by Yao *et al.*²²¹ in this issue of *ACS Nano*, to long nanotubes, $L \sim 10 \mu\text{m}$ ^{7,169}, and similarly long, but 100- to 1000-times-wider nanoslits made by stacking and patterning 2D materials³⁹. Copyrights 2013, 2017, 2019 of American Chemical Society. Copyright 2017 of American Association for the Advancement of Science.

1.2.1 Solid-State Nanopores

The ionic conductance of the pore (greater than few nanometers) is inversely proportional to the thickness of the membrane as given by:

$$G_0 = \sigma_{\text{bulk}} \left[\frac{4t}{\pi d^2} + \frac{1}{d} \right]^{-1} \quad \text{Eq.1}$$

where G is the conductance of the nanopore, ' σ ' is the electrolyte bulk conductivity, ' t ' is the membrane thickness and ' d ' is the diameter of the pore. This would mean a thinner membrane will give rise to a stronger signal. Atomically thin 2D nanopores can as a result provide the maximum available signal owing to the minimum thickness of monolayer of atoms. In fact, the equation becomes simpler for 2D materials, as the first term becomes negligibly small, and the signal becomes dependent only on the nanopore diameter and the electrolyte concentration:

$$G = \sigma_{\text{bulk}} d$$

For the purpose of DNA sequencing, single base resolution is also predicted to be possible by using 2D materials, as the thickness of such nanopores approach that of a single base thickness (thickness of graphene ~ 0.3 nm).

1.2.2 Sizes of water molecules and ions and the comparably small apertures: $\sim 0.1 - 1$ nm

In addition to the physical size of water molecules and common ions in solution, estimated to about ~ 0.3 nm to ~ 1 nm^{39, 43, 149, 198}, another relevant size scale to consider and compare to the characteristic size of the nanostructures is the *Debye screening length*, λ_D , which is a good estimate of how far the electrostatic effects of unscreened charges will persist (that is, the distance at which the electrostatic potential drops by a factor of $1/e$). This characteristic length scale, obtained from Poisson's equation, governs the exponential decay of the electric potential away from the charges, and describes the screening of a charge's electrostatic potential due to the net effect of the interactions it undergoes with the

other mobile charges (electrons and ions) in the system. For concentrated ion solutions, such as 1 M KCl, this length is calculated to be $\lambda_B \approx 0.3$ nm, the size of one water molecule. It increases to $\lambda_B \approx 1$ nm for 0.1 M KCl, equivalent to about four water diameters, and to $\lambda_B \approx 10$ nm for 1 M KCl¹⁻⁴. Therefore, as the size of the channels and nanostructures becomes smaller, it is more difficult for charges to be screened within that space even for relatively high ion concentrations and Coulomb interactions become important. An “ionic Coulomb Blockade” was first suggested analytically and by means of molecular dynamics simulations⁹⁷ and recently reported for sub-1-nm-diameter 2D monolayer molybdenum disulfide (MoS₂) nanopores⁴³.

Another conceptually simple, classical length scale directly related to the Debye length, arising in phenomena in electrolytes, polyelectrolytes and colloidal dispersions, is the *Bjerrum length*, λ_B , the separation at which the electrostatic interaction energy between two elementary charges is comparable in magnitude to the thermal energy,¹⁶²

$$\lambda_B = \frac{e^2}{4\pi\epsilon_0\epsilon_r k_B T}, \text{ Eq. 1,}$$

where $k_B \approx 1.38 \times 10^{-23}$ m² kg s⁻² K⁻¹ is the Boltzmann constant, $e = 1.6 \times 10^{-19}$ C is the elementary charge, ϵ_r is the relative dielectric constant, ϵ_0 is the vacuum permittivity, and T is temperature. For water at room temperature $\epsilon_r = 80$, so that $\lambda_B \approx 0.7$ nm. Roughly, we may assume that at separations smaller than λ_B , the Coulomb interaction between unit charges in water dominates compared to the thermal energy. The Debye length in electrolyte solution, $\lambda_D \sim 1/\sqrt{\lambda_B I}$, where I is the ionic strength, frequently expressed in molar (M).

Given the values of these characteristic length scales, $\sim 0.1-1$ nm, it is not a big shocker that some interpretations using equations underlined by assumptions valid only for large-scale ion flow channels may start to dielectrically breakdown for atom-scale apertures. Applying old terminology, concepts and theoretical tools for these new atomic-transport problems, may not be applicable here. “All-atom” viewpoints, such as put forth by molecular dynamics simulations, analyzing the more realistic movement of atoms and molecules and relying on appropriate potential functions, can then be expected to have more predictive power than the older, mean-field and many-body approaches. Experimental outcomes now frequently depend on the minute details and differences in the atomic structures. The corresponding models and theories should be able to reflect this.

At the same time, experimental approaches at the atomic scale can also suffer from significant errors and deficiencies, such as from contamination of samples, and a generally small numbers of samples from which conclusions are drawn, due to challenges with working at this scale. Additionally, it is reasonable to assume that there may be some preferential selection of devices and/or data that fit preconceived expectations and older theories. As we proceed in measuring, rationalizing and theorizing atom-scale devices it is important to determine related errors and outline assumptions and limitations. It is with these upfront, cautionary notes, that we proceed to discussing recent “atom-scale hole measurements”.

1.2.3 Ionic Selectivity of CNTs, Nanopores and Channels

Many recent experiments were focused on the concept of “ion selectivity”, a calculated quantity discussed below, viewed as a particularly important aspect of these systems. Increasingly in the recent literature, solid-state nanopores, nanotubes and nanochannels

have been reported to be “K⁺ ion selective” (or “cation selective”) meaning that they only or preferentially allow the K⁺ ions to pass through, while impeding others. For example, recent experiments on a garden variety of pores, tubes and channels made out of a wide range of low-dimensional solid-state materials (see Table 1) have been carried out in a conventional KCl solution. Carbon nanotubes are excellent candidates for such experiments since the surface can be functionalized using appropriate pH for ion selective transport. Yao *et al.*²²¹, demonstrate successful CNT devices which can be tuned to selectively pass K⁺ ions. They hypothesized that due to the presence of carboxyl groups (COO⁻) at the pore edge, neutral or higher pH helps keep the pore charged, and the pore attracts more K⁺ ions. In contrast, in acidic pH, the negative charge on the pore’s rim created by COO⁻ groups is neutralized by COO⁻ becoming COOH). Additionally, the authors also analyze noise properties and power-law dependence of the noise on frequency and find a 1/f dependence similar to other solid-state pore such as silicon nitride¹⁷⁵ and graphene pores¹³⁰. They report that noise decreases with increasing ion concentrations for pH 7.5, for which the pore is charged, suggesting that more screening of the pore charge means lower noise.

This concept of “ion selectivity” is analogous and borrowed from the field of ion channels and ion pumps found in nature^{45,161}, that already existed at these small scales before the solid-state structures were possible. These are, for example, the protein molecules that span across the cell membrane. Ion channels can allow the passage of certain ions through them while blocking others, thus playing important roles in controlling neuronal excitability, and therefore, they can be selective for particular ions. Specifically, some biological

channels allow the flow of K^+ ions effectively, but do not allow Na^+ ions to cross the membrane. Ion passage through the “ K^+ channel selectivity filter” is believed to proceed as 2-3 K^+ ions interspersed by water molecules move in a single file, while permeation through the wider and less selective Na^+ channels proceeds similarly, although the ions may not be dehydrated¹⁶¹. Simple structural concepts like these and schematics of how ions pass through these channels are often invoked in biology to rationalize the mechanism of ion selectivity.

Selected Ion Transport Experiments with Pores, Tubes, Channels (by Year of Publication)	Material	Pore Diameter (d) Dimensions	Pore Fabrication Technique	Maximum Applied Voltage	Maximum Conductance/IV Linearity (in 1 M KCl)	Conductance (G) vs. Concentration (C) Dependence/Range Measured (in KCl)	Calculated Pore Surface Charge	Maximum Calculated K^+/Cl^- Selectivity Ratio	Type of Measurements	pH	Comments
Siria <i>et al.</i> , 2013 ⁴⁴	Boron nitride nanotubes (BNNTs)	Single tube; d = 30-80 nm, L = 1 μ m	Nanomanipulation	100 mV	23 nS, linear	G saturates as C decreases below 0.1 M; 10^{-4} to 3 M	0.1 to 1 C/m ²	N/A	Pressure-assisted ionic conductance	3.0 to 11	Osmotic energy conversion
O'Hern <i>et al.</i> , 2014 ⁴⁵	Monolayer graphene	Multiple pores; d = 0.2-0.6 nm, L = 0.6 nm	Ga ion irradiation and acid etching	N/A	N/A	N/A	N/A	1.3, Eq. (3)	Membrane potential	N/A	Cation-selective ionic transport
Rolling <i>et al.</i> , 2016 ⁴⁸	Monolayer graphene	Single pore; d = 2-20 nm, L = 0.6 nm	Breakdown, 5-7 V applied to make pore	150 mV	1 μ S, linear	Power law dependence between G and C; 10^2 to 3 M	-0.6 to 0 C/m ²	>100, Eq. (3)	Ionic conductance	2.0 to 8.0	Selectivity in pores up to d = 20 nm
Feng <i>et al.</i> , 2016 ⁴⁶	Monolayer MoS ₂	Single pore; d = 2-25 nm, L = 0.7 nm	Transmission electron microscopy (TEM) drilling or breakdown, 0.8 V applied to make pore	400 mV	500 nS, linear	G saturates as C decreases below 10^{-3} M; 10^{-6} to 1 M	-90 to -20 mC/m ²	N/A	Ionic conductance	2.0 to 11	Nanopower generation
Tunuguntla <i>et al.</i> , 2017 ¹⁹	Narrow carbon nanotube porins (nCNTPs)	Single and multiple tubes; d = 0.8 nm, L = 10 nm	Self-insertion into lipid bilayers	200 mV	180 pS, linear	Power law dependence ($-C^{19}$, $-C^1$) between G and C; 4×10^{-3} to 3 M	N/A	184, Eq. (2)	Ionic conductance	3.0, 7.5, 7.8	nCNTPs are strongly cation selective
Esfandiari <i>et al.</i> , 2017 ⁷	Graphene, MoS ₂ , and hBN	Single and multiple channels; d = 0.6 nm, w = 0.13 μ m, L = 3-7 μ m	Electron beam lithography and dry etching	200 mV	30 nS, nonlinear (0.5 M)	G saturates as C decreases below 10^{-4} M; 10^{-6} to 1 M	20 to 300 μ C/m ²	~3, mobility ratio	Ionic conductance	2.0 to 10	Channels are selective to small cations (i.e., K ⁺ , Li ⁺ , Na ⁺)
Amiri <i>et al.</i> , 2017 ¹²	Single-wall carbon nanotubes (SWCNTs)	Single tube; d = 1.5 nm, L = 20 μ m	Electron beam lithography and dry etching	400 mV	100 nS, N/A	Power law dependence ($-C^{13}$) between G and C; 10^{-3} to 1 M	N/A	121, permeability ratio	Ionic conductance through PMMA resist	2.0 to 8.0	Negative surface charges localized at nanotube entrance
Thiruraman <i>et al.</i> , 2018 ⁴⁸	Monolayer MoS ₂	Multiple pores; d = 0.2-0.8 nm, L = 0.7 nm	Ga ion irradiation	800 mV	40 nS, nonlinear	N/A	N/A	N/A	Ionic conductance	8.7	Tunable sub-nm defect production in monolayer MoS ₂
Chien <i>et al.</i> , 2019 ¹⁸	SiN _x /Si	Single pore; d = 0.9-2.4 nm, L = 3-8 nm	TEM thinning and drilling	900 mV	15 nS, N/A	N/A	~20 mC/m ²	N/A	Ionic conductance	8.0	DNA translocations at 10 MHz bandwidth
Yao <i>et al.</i> , 2019 ⁹	Wider carbon nanotube porins (wCNTPs)	Single tube; d = 1.5 nm, L = 10 nm	Self-insertion into lipid bilayers	100 mV	800 pS, linear	Power law dependence ($-C^{23}$) between G and C; 4×10^{-3} to 3 M	-75 to -20 mC/m ²	~10, Eq. (2)	Ionic conductance	3.0, 7.5	Ionic transport dominated by strong electroosmotic coupling

Table 1.1. Comparison of Ionic Transport Properties in Selected Pore, Channel, and Tube Architectures.

List of selected reports from the literature on low-dimensional porous systems. The dimensions, composition, and method of fabrication for various pores are given in addition to ionic transport characteristics such as ionic conductance, G, scaling with ion concentration, C, surface charge, and ion selectivity ratio. Unless noted, we report values for 1 M KCl solution.

Table 1.1 summarizes the details of recent measurements of small diameter systems including their pore sizes, applied voltage, measured conductance and other measured and calculated parameters such as the ion selectivity. For convenience, results are listed in the order of the year published.

In these systems, the typical first measurement involves immersing the sample in solution and if the relatively delicate structure does not break during handling, determining the dependence of the ion current, I , on the externally applied voltage, V . Voltage is limited to ~ 100 mV and maximum ≈ 1 V, for slightly larger structures; for larger voltages the sample dielectrically or otherwise breaks down as the electric field reaches $\sim 0.1 - 1$ V/nm across the membrane, sufficient to ionize atoms of the membrane material. The nonzero magnitude of the current, in the pA to nA range, and the lack of hysteresis is a good indication that transport of ions is occurring. When the I - V relationship is linear one can define the slope, which is the ion conductance, G , and one can also consider its dependence on the ion concentration. In the case of non-linear I - V curves, G is not well defined and the slope of the current at zero-voltage can be used to estimate a conductance value. Another directly measured quantity is the bulk concentration, C , or the ion concentration used in the experiment; the ion concentrations and mobilities within the constricted regions are different than bulk conductivities for these restricted ion flows. Pore conductivity and ion mobilities are sometimes calculated from the measured conductance and some assumed transport model, G vs. size, either analytically or from numerical simulations (see example of 2D channels³⁹), to show that they are smaller than bulk values.

In many solid-state nanopores and channels, the conductance is limited by the surface charge of the pore and saturates at low concentrations^{96,205}, and reported surface charge density varied several orders of magnitude, both positive and negative and dependent on pH, from $\sim \mu\text{C}/\text{m}^2$ in 2D stacked channels³⁹, $\sim \text{mC}/\text{m}^2$ in silicon nitride²⁰⁵, MoS₂ pores⁴¹ and short CNTs²²¹, to C/m^2 in boron nitride nanotube¹⁷³ and graphene nanopores¹⁵⁹ (see Table 1.1). This is by no means a careful overview of all the values and experimental details reported for such systems, but it is already sufficient to notice the large variation of charge densities across six orders of magnitude. We should also note that in many cases the surface charge density is inferred from a fit of G vs. C and there are significant errors associated with these fits.

To evaluate ion selectivity quantitatively, a salt concentration gradient is set up, at zero applied voltage, and both K⁺ and Cl⁻ ions diffuse from high to low concentration. When the rate of diffusion of ion (K⁺) is higher than the counter-ion (in this case Cl⁻), a net current (also known as *short-circuit current* because the external voltage is zero) is produced across the pore. *Diffusion potential* or *reverse potential* (also called *open-circuit voltage*) is referred to as the value of external voltage that can be applied to set the net current to zero. This selectivity (*i.e.*, larger diffusion rate of the ion compared to its counter-ion) is governed by the pore surface chemistry and size of the pore. The pH of the solution plays an influential role together with the intrinsic surface charge of the material. Depending on the salt concentration, a cloud of counter-ions is created in response to total surface charge of the pore material, known as Electric Double Layer (EDL). The spatial extent of this layer is defined by the Debye length λ_D . In case of pore dimensions approaching this Debye

length, the EDL can overlap causing an excess concentration of counter-ions in the channel. Further, these excess counter-ions can then dominate ionic transport through the channel.^{20,}

87,149

To quantify ionic selectivity, the diffusion potential (equal to the external voltage applied to set the measured current to zero) is given as:

$$V_{rev} = (2t_+ - 1) \frac{RT}{F} \ln \frac{c_{top}}{c_{bottom}}, \quad \text{Eq. 2.}^{221}$$

in the form that Yao *et al.*²²¹ suggest, where R is the universal gas constant (8.314 J mol K⁻¹), T is temperature, F is Faraday's constant (96,485 C mol⁻¹) and c_{top} and c_{bottom} are the electrolyte concentration on either side of the chamber. In the work by Yao *et al.*²²¹, c_{bottom} was fixed at 10 mM and c_{top} was increased from 10 mM to 600 mM (**Fig. 2.2a**). The authors define “ t_+ ” as the “transference number” for the cation, that is the fraction of electrical current carried by the cation under the influence of applied voltage. The transference number can serve as an index of the ion selectivity, $t_+=1$ or 0 for complete cation or anion selectivity respectively. Hence, $t_+=0.5$ corresponds to a non-ion selective channel ($V_{rev} = 0$ for $t_+=0.5$ in *Eq. 1*).

The form of *Eq. 2.* can be contrasted to another form for the reverse potential that was used by Rollings *et al.*¹⁵⁹ for graphene nanopores:

$$V_{rev} = \frac{k_B T}{e} \mathbf{n} \left(\frac{S_{GHK} c_{high} + c_{low}}{S_{GHK} c_{low} + c_{high}} \right), \quad \text{Eq. 3.}^{159}$$

where $k_B \approx 1.38 \times 10^{-23}$ m² kg s⁻² K⁻¹ is the Boltzmann constant, $e = 1.6 \times 10^{-19}$ C is the electron charge, S_{GHK} is the “selectivity ratio” (GHK stands for the Goldman–Hodgkin–

Katz model) and c_{high} and c_{low} are the high and low concentrations, respectively, on the two sides of the membrane.

Slightly different terminology and different forms of these equations are used, for example see studies of 2D graphite/MoS₂ nanochannels (Fig. 1.2b) and 2D MoS₂ nanopores (Fig. 1,2c)⁴³. Values of reported “selectivity ratios”, S , for related systems are listed in Table 1.1. Although the way selectivity is measured and calculated, and the structures and their fabrication methods changed across various studies, the one observation that appears consistent across various studies is that ionic selectivity occurs for neutral pH or higher (see Table 1.1).

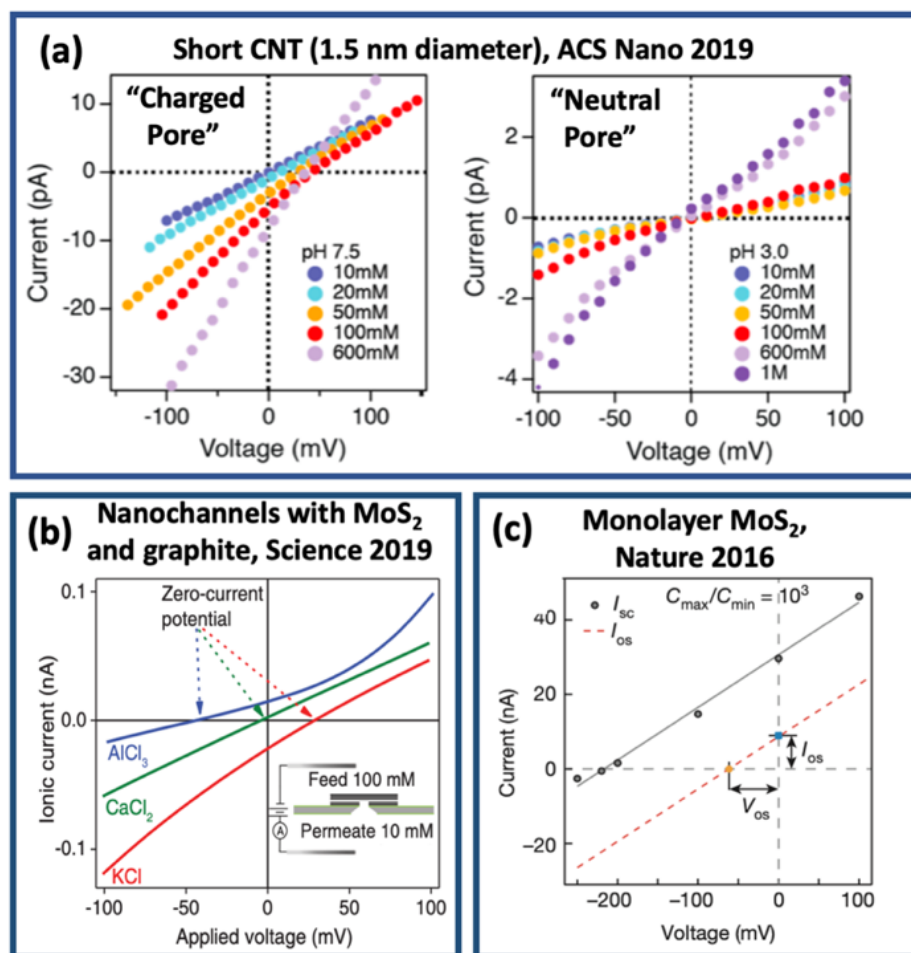


Figure 1.2. Current-voltage measurements for asymmetric ion concentrations on the two sides of the membrane, used to measure the “reverse potential” or “zero-current potential” across the pore.

These measurements are performed to determine the extent to which current is carried by the positive and negative ions. (a) a single, 1.5-nm-diameter, ≈ 13 -nm-long carbon nanotube (CNT)²²¹ in 10 mM to 600 mM KCl on one side, and 10 mM on the other side of the membrane, for pH 7.5 (pore is charged) and pH 3 (pore is neutral), respectively, (b) \approx two hundred, 0.6-thick (~ 0.13 μm wide and 3-7 μm -long) parallel graphite/MoS₂ nanochannels³⁹ in 100 mM / 10 mM KCl, CaCl₂ and AlCl₃ (this is an ensemble measurement rather than a single channel measurement), and, (c) a single 15-nm-diameter 2D MoS₂ nanopore⁴¹ in 1M / 1mM KCl. In (b), in the case of CaCl₂ and AlCl₃ solutions, the current at zero applied voltage is approximately zero and positive, respectively; positive current means that anions (Cl⁻) have a higher mobility than cations. Copyrights 2019 American Chemical Society. Copyrights 2017 American Association for the Advancement of Science. Copyrights 2016 Springer Nature.

Short Carbon Nanotubes (CNTs):

In the case of CNTs, Yao et al.²²¹ observe a weak K⁺ selectivity at pH of 7.5 (Fig. 2a). It is interesting to note that this concentration range corresponds to an electric double layer (EDL) of 3 nm to 0.4 nm, similar to the pore CNT diameter, 1.5 nm. The region of K⁺ is built up in response to the negatively charged CNT nanopore rim. In their work, the authors define “Permselectivity”, $P = \frac{t_+ - t_{+bulk}}{1 - t_{+bulk}}$; where t_+ and t_- are the transference numbers (the ratio of current derived from the K⁺ ions to the total current produced) for positively and negatively charged ions and $t_{+bulk} = 0.49$ for KCl solution. This investigation is similar and consistent with their previous CNT study²⁰², where they observe similar K⁺ selectivity which they attributed to the negatively charged (COO⁻) rim of the pores at pH 7.5 or higher. They observed weak Cl⁻ selectivity with CNTs at pH 3 for 0.8-nm-diameter tubes²⁰², but the wider, 1.5-nm-diameter tubes in this issue were not ion selective at the same pH 3.²²¹ It is interesting to appreciate what a small difference in diameter by 0.7 nm can do in this size range.

2D Nanopores:

Similar cation (K⁺) selectivity has been investigated for a range of nanopores (a few-nm-diameter to 20-nm-diameter pores) in materials such as graphene¹⁵⁹ and MoS₂⁴¹. In the case of few-nm-diameter ($d = 2$ nm to 25 nm) 2D MoS₂ pores, Feng et al.⁴¹ calculate a decrease in ionic selectivity, from 0.62 to 0.23 as the pore size increased from 2 nm to 25 nm. Rollings et al.¹⁵⁹ investigated graphene nanopores made using dielectric breakdown with diameters up to 20 nm and concluded that ionic selectivity $S_{GHK} > 100$ (Eq.2) was independent of pore diameter. More recently, Caglar et al.²³ studied ion selectivity in randomly defective graphene and hBN membranes, deposited on glass capillaries, and

claim that ~500 anions per each cation get transported across the membrane in case of a multivalent hafnium tetrachloride (HfCl_4) salt solution. These authors also used a variation of the Goldman–Hodgkin–Katz (GHK) equation and model to extract their quoted selectivity ratios. Their samples seem to contain random, irregularly shaped pores with a large size distribution of diameters up to ~ 30 nm. In our opinion, one good aspect of these samples is that they rely on random defects in material rather than some sophisticated pore fabrication method that may be timely and costly. However, in this case it is then challenging to study systematically the fundamental aspects of selectivity as a function of pore properties if they are random.

Thiruraman et al.¹⁹⁰ previously fabricated well-characterized ensembles of much smaller (sub-nm) pores in monolayer MoS_2 using Ga ion irradiation and observed non-linear current-voltage relationship through these pores for a range of irradiation doses corresponding to different pore size distributions. They observed suppressed low-bias conductance compared to larger-diameter pores and extracted a simple scaling of conductance with effective pore diameter as $G \approx 9 \text{ S/m} \times (d - 0.7 \text{ nm})$ in 1 M KCl, where d is the diameter in nm, and 0.7 is the minimum pore diameter for ionic flow. Moreover, for such atom-scale pores the concept of characteristic pore “diameter” or pore “size” could be further discussed and possibly re-defined given that pore cross-sections are not circular, but rather have a well-defined atomic structure and edge terminations. There is a there is garden variety of 2D pore-shapes and structural options to consider¹⁹⁰. Liu et al.¹¹⁵ compared and contrasted the properties of few-nanometer-size triangular h-BN nanopores vs. circular MoS_2 nanopores in DNA translocation experiments. The pore resistance for the

triangular pore had to be modified compared to circular pores. Similarly, from the atomic structure of angstrom-size MoS₂ pores, one can plot the distribution of “diameters” measured from the center of mass (COM) of the pore.¹⁹⁰

For MoS₂ pores with diameters below ~ 2.0 nm, the behaviors of the concentration and mobility of ions strongly deviate from bulk properties. Ion concentration, mobilities, and hydration are different than their bulk counterparts, as was already shown previously for graphene nanopores using MD simulations by Suk et al.²²⁶. Wilson et al.²¹⁶ used molecular dynamics to model 3.5-nm-diameter graphene pores and observed that at ~ 500 mV to 1V applied across the membrane, water molecules will polarize, and the electric field will compress the polarized molecules inside of the pore, thus creating outwards pressure. Atomic structures of single-layer MoS₂ nanopores were also modeled, by an equilibrium “all-atom” molecular dynamics (MD) model (see also Fig. 3b) in 1M KCl to estimate the ratio between pore and KCl bulk conductivity, σ , showing a drop from $\sigma_{\text{pore}}/\sigma_{\text{bulk}} \sim 80\%$ to 10% with the decrease in the effective pore diameter from ~ 2.5 nm to ~ 0.7 nm¹⁴⁸. Non-equilibrium MD simulations assuming an external voltage applied were then used to develop an analytical expression for conductance, which is convenient for direct comparisons with experiments¹⁹¹.

In other work on graphene, O’Hern et al.¹⁴⁰ showed a selectivity of 1.3 in graphene sub-nm-diameter pores that were fabricated using ion beam irradiation of graphene to make holes, and further processed in an acidic etchant to enlarge them.^{72, 159} The diameters of pores created in this process were shown to be < 1 nm. There are also other, more robust,

laminated and much thicker (few-micron-thick) membranes, such as graphene oxide (GO) membranes⁶³ and laminated MoS₂⁶⁰, some of them shown to be ion selective and apparently some of them are being commercialized for applications in the near future.

2D Nanochannels:

Silica nanochannels have been studied for decades with regard to ionic transport and power generation in the presence of concentration gradient. Specifically, Kim et al.⁸⁷ have shown power generation of $\sim 8 \text{ W/m}^2$ with an efficiency of $\sim 30\%$. While arrays of nanopores in 2D materials (MoS₂) have been envisioned to possibly produce power densities in range of mega Watts per m², based on a simple scaling of results from single pores, this is yet to be realized.⁴¹ Recently, Esfandiar et al.³⁹ have realized a variety of 2D channels fabricated using hBN, MoS₂, and graphite. In this work, they also measured the zero-current potential (here as “E_m”) and observed that K⁺ and Al³⁺ diffuse through nanochannels faster and slower than Cl⁻, respectively (Fig. 2b). Further, the Henderson equation was used to calculate the ratio of ion mobilities. The authors concluded that in case of such 2D nanochannels, they detect a decrease in Cl⁻ mobility ($\sim 2 \times 10^{-8} \text{ m}^2 \text{V}^{-1} \text{s}^{-1}$) from K⁺ ($\sim 7 \times 10^{-8} \text{ m}^2 \text{V}^{-1} \text{s}^{-1}$) in the channel and speculate this to arise from polarization of water molecules around the ions. In analogy to ion transport, we note that there is a growing work in gas transport through similar structures, but this is beyond the scope of our perspective.

1.3 Outline and Intellectual Contribution of this Thesis

In this thesis, we advanced the fundamental understanding of low-dimensional devices for the purpose of ionic and gas transport mechanism at single atomic level. In

chapter 2, I developed new nanofabrication techniques, methods to produce standard SiN_x platform which are then processed to create novel low-dimensional membranes and devices. Next, we advanced the growth synthesis of low-dimensional materials to yield high quality crystals contributing to this growing field. Improving the growth of 2D materials was a key ingredient in my work and the quality of the synthesis was observed to affect results are also included. In addition, one of the contributions of this thesis includes a new growth technique to synthesize MoS_2 films with an industrial-standard Mo foil as a starting growth precursor, to create 2D membranes on centimeter scale. These resulting large area, few-layer membranes contain regions of monolayer MoS_2 . This allowed us to investigate the fundamental laws governing atomic-scale ionic transport and indicate a path towards industrial-scale application. Nanopores are creation by simple chemical etching, and preliminary ionic transport studies through these few-layer matrix nanofilms of MoS_2 were performed. We observe how the ionic conductance scales with the nanoporous area of the membrane, which can be controlled by adjusting the etching time reported.

In chapter 3 and initial sections of chapter 4, I developed the novel irradiation mechanisms using ion beam to produce “point defects”, “vacancy defects”, “single atomic” pores or “sub-nanopores” pore or “angstrom-size” pores (various names for related works of nanoscience), essentially pores that are few atoms in diameter. Here, we pioneered the use Focused Ion Beam (FIB) irradiation. While FIB was frequently used for other materials, its use for 2D materials has not been developed prior to my thesis work. Now, ion irradiation effects on 2D materials have grown into a mature subfield. are a growing topic. We have explored how the ion irradiation parameters such as dose result in the

creation of defects with different sizes and properties. Defect type is examined and confirmed using various characterization techniques such as Raman spectroscopy, aberration- corrected scanning transmission electron microscopy. In chapter 3, I also present results of ion beam irradiation of 2D materials placed on various substrates, as well as suspended atomically thin membranes (MoS_2 and WS_2). For the first time, we created nanoporous MoS_2 membranes in pores in the sub-nanometer range. In this study, detailed statistical image analysis of the defect type or missing atoms and the evolution of defect size/area as a result of irradiation are included. Towards the end of chapter 4, I report on investigations and results from ionic transport studies through these sub-nanometer pores, share specific insights on experimentally observed of ionic current suppression at low voltage range (few hundred mV).

In chapter 5¹⁹⁴, I elaborate on a different technique to produce a ‘single’ sub-nanometer pore in an aim to create the ultimate angstrom-size confinement. This is created using the state of the art, aberration-corrected transmission electron microscopy to have the ultimate atomic control on membrane lattice. Additionally, we compute a table of atomic model with possible pore/ defect types of diameter ranging from a 1 transition metal atom to 5 transition metal atoms. Interestingly, a few pores from these theoretically illustrated models are experimentally fabricated and demonstrated. Further, I investigate the ionic transport in these single angstrom-size confinement and report elusive findings on suppressed ionic current that are independent of molarities of salt solution that is yet to be understood. Importantly, we observed that the ionic conductance through such small pores was not proportional to the bulk conductivity of the surrounding solution. We explain this

by the fact that the concentration of ions in small pores is dominated by surface charge effects.

Lastly, in chapter 6¹⁹⁵, I present our experimental work on helium transport studies in TMD membrane devices with single atomic apertures. Prior to our work, there were only a handful of studies, primarily in graphene membranes, investigating how gas flows through small apertures. While pristine WS₂ membrane acts as the thinnest physical barrier, atomic apertures created on these monolayer membranes (using my irradiation technique from chapter 3) showcase helium transport. At an atomic scale, we observe that these angstrom-scale apertures are invisible to helium gas and helium atoms experience no energy barrier, thereby abiding by the predicted Knudsen flow rates.

2 Device Fabrication and Growth of Low-Dimensional Materials

2.1 Device Fabrication

All devices presented in this thesis work involve a silicon-based substrate or supporting platform onto which the 2D material is supported. Although intriguing architectures are being developed using low-dimensional materials, there is an inevitable need for these materials to be integrated with micro-device or platform to further study its properties. For example, we investigate ionic properties in a solution-based environment which calls for compatibility with micron sized electrodes of an amplifier. Another critical use of SiN membrane is its ubiquitous use in TEM microscopy. Since a majority of studies discussed in the following chapters use TEM techniques to characterize pores and defects, the use of such platform aid in experimental procedures.

The 2D materials are grown using CVD techniques as explained in later sections of this chapter. In this section, the details of the photolithography to create “SiN chips” (referred to 5x5mm devices in the nanofabrication community) using the semiconductor equipment and other cleanroom tools are discussed.

2.1.1 Photolithography for Silicon Nitride Platform

Silicon-based support chips are developed with the help of nanofabrication techniques delineated in the figure 2.1 (adapted from Danda thesis) The process starts typically with a 4-inch Si/SiO₂ wafers of respective thickness 525 μm/5 μm wafer (<100> lattice oriented, phosphorus-doped, 1-10 Ω- cm resistivity) with 50nm or 100 nm of low stress silicon

nitride (SiN_x) deposited on both sides of the wafer. The thickness of SiN deposition is crucial since this starting thickness is the same as the supporting SiN membrane thickness useful for 2D materials (as seen in Figure 2.1 (i)). SiO_2 is desired for its capacitive properties which further enhance the signal to noise ratio in ionic measurement of such devices. In fact, this dielectric property led to the invention of “glued-glass” chips (which I was briefly experimenting with as a master’s student) and more popularly “Glass- chips” (also sold at Goepfert LLC) which use fused-silica glass wafers instead of the silicon/silicon dioxide wafer as seen in this work. For reference, dielectric constant at 300K in increasing order for SiO_2 , Si_3N_4 , Si is 3.9, 7.5, 11.7 respectively.

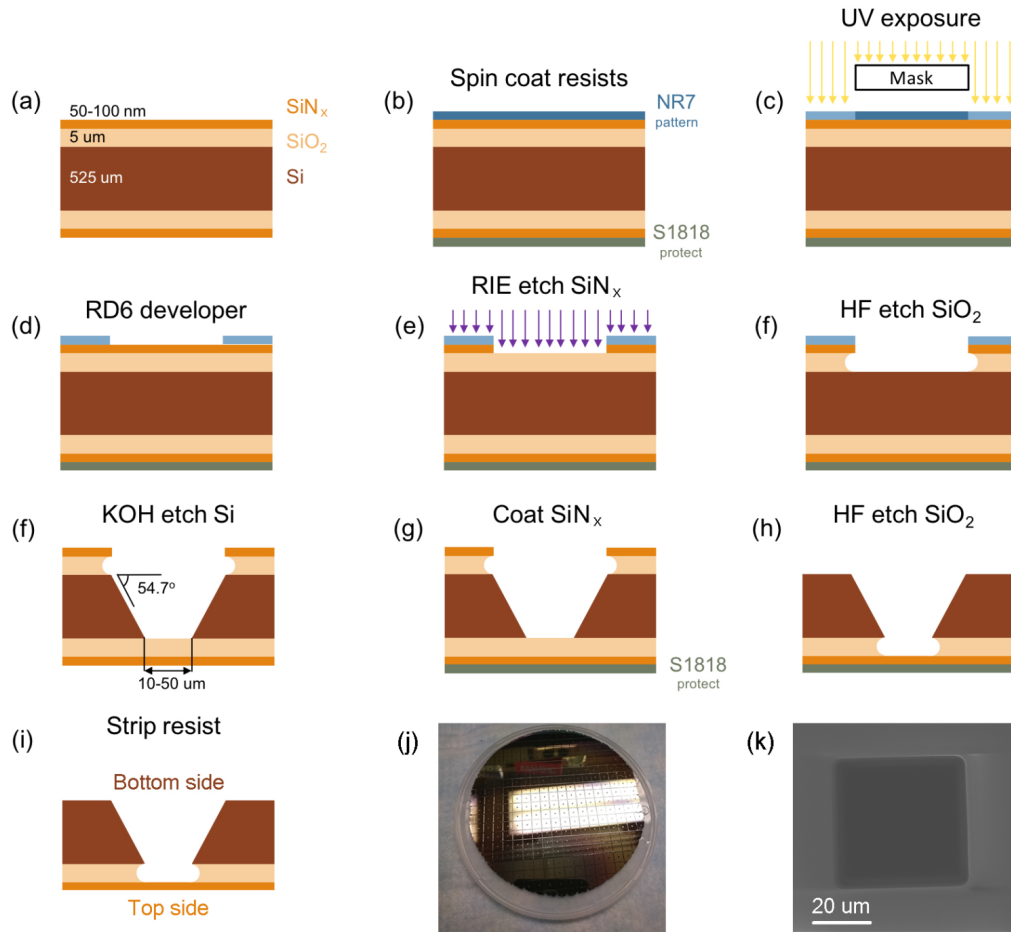


Figure 2.1. Lithographic patterning and etching of Si/SiO₂/SiN_x chips.

(a-i) Photolithography, RIE/HF etching, and KOH etching steps to fabricate free-standing SiN_x windows. (j) Optical image of the trench side of a wafer with ~ 100 chips. (k) SEM image of a 50 μm × 50 μm square free-standing SiN_x window on a Si/SiO₂ substrate. This figure has been adapted from Danda et al.

In order to fabrication the supporting SiN membranes, we follow the steps elaborated in figure 2.1. The wafer is spin-coated (4000 rpm, 45seconds) with a negative photoresist (NR7) on one side while the other side is carefully coated with S1818 positive photoresist (this resist serves as a protective layer to the SiN underneath) using a pipette. Ensuring that this layer completely covers the SiN is crucial to obtain defect-free SiN chips. Next, the

wafer is pre-baked at 115°C for 3 minutes on a hotplate between each resist coating steps described previously. Following this step, the NR7 side of the wafer is placed onto the mask aligner (Karl SUSS MicroTec MA-6).

The chrome mask is patterned using the Heidelberg DWL 66+ and designed with the software, layout editor or CAD. The design contains a square pattern which is transformed to the square SiN window or suspended membrane. The design also contains outlines for each chip which help in cleaving the chips free once the etching steps are complete.

For the UV exposure, a dose of 5 mW/ cm² or 170 mJ/ cm² for 3-4 seconds (3.4 seconds) at 365nm is carried out. Further, the wafer is then post-baked at 115°C for 3 minutes.

For resist development, the wafer is gently dunked in RD6 developer for 7 seconds to reveal the developed pattern. Next, the wafer is thoroughly rinsed in DI water followed by drying with a N₂ gun.

For the Nitride etch, Oxford PlasmaLab 80+ reactive ion etcher is used with SF₆ with a plasma power of 50 W and pressure of < 30 mT for 10 minutes. The exposed SiN_x is dry etched using Oxford Plasma Lab 80+ reactive ion etcher with SF₆ with a plasma power of 50 W and pressure of < 30 mT. Timed at 2 mins for 50 nm and 4 mins for 100nm.

BOE etch (5:1 volume ratio of 40% NH₄F in water to 49% HF in water) is conducted to create the trenches as seen in Figure 2.1 (f) and (h). Ensure to knock-off any air bubbles present on the surface which will lead to surface defect and poor quality of chips. The wafer

in etched in BOE for 70 minutes (with additional 10 to 20 minutes as seen in some cases) and is inspected with a profilometer (Filmetrics F40, reflectometer) to ensure complete SiO₂ etching. Finally, acetone and IPA wash removes any residual resist.

To etch the Si, a 40% by weight KOH solution (1000ml of water with 666.67g of KOH pellets) is prepared with thermostat (external probe connected the hot plate) to monitor the stable temperature at 62 C of the solution. Note: Solution is highly exothermic, and solution must be prepared with caution by adding the salts pellets gradually into the water. A magnetic stir bar (set to 120 rpm) is also added to maintain a more consistent solution concentration. The trench is formed in about ~22 hours and again, optically observed and monitored after the first 20 hours, to ensure the desired SiO₂ layer is achieved. Finally, this is washed with DI water and acetone/ IPA as explained previously.

To etch our final layer of SiO₂, the wafer is coated with S1818 using a pipette (again the protective layer to prevent any damage to the SiN_x windows) and dried overnight in the dark (to prevent any photoreaction). This SiO₂ BOE etch step is again done for about 100 mins followed by the washing off the protective resist with acetone and IPA.

2.2 Graphene Growth

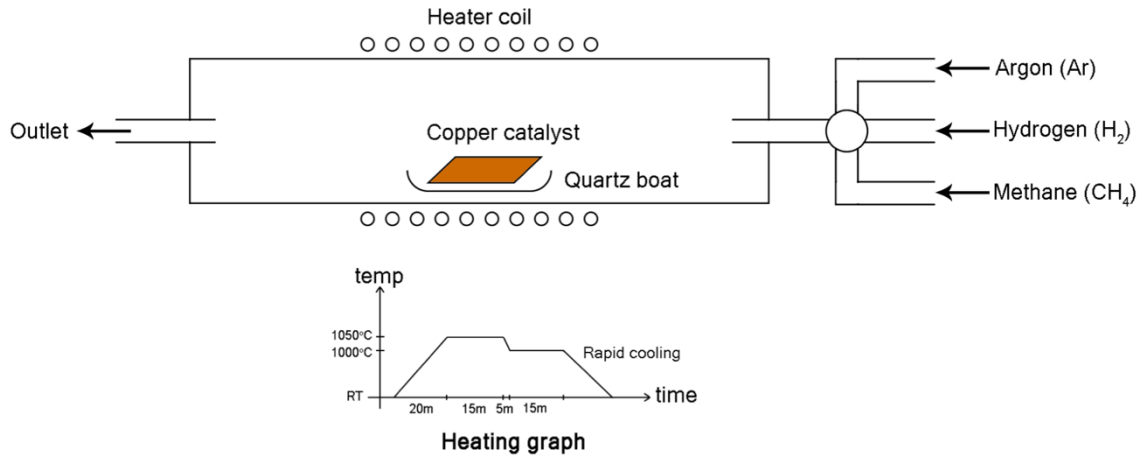


Figure 2.2. Schematics of experimental CVD graphene growth setup. Adapted from Danda et al.

All graphene growth was synthesized with the CVD technique with copper foil (Alfa Aesar 99.999% pure copper foil) as the catalyst along with methane as precursor. Thin foils of copper are cut typically about 1cm× 3cm (could larger, if there is a need for it) and rinsed and cleaned in 30% HCl solution. The pre-cleaned foil is placed in a quartz tube and placed in the center of the tube furnace as shown in the figure. This is heated to 1050°C in argon (Ar) and hydrogen (H₂) at flow rates 350 sccm and 20 sccm, respectively, at a ramp rate of ~ 50°C/min. Further, the foil is annealed with an increased Ar flow of 500 sccm while the H₂ flow remained at 20 sccm at 1050°C for 15 minutes. Finally, the temperature of the furnace is reduced to 1000°C at a ramp rate of -10°C/min, for the optimal growth along with introducing methane CH₄ at 10 sccm (Ar at 500 sccm Ar, H₂ 20 sccm) for another 15 mins. At last, the furnace is rapidly cooled down and sample is carefully removed.

2.2.1 Graphene Transfer

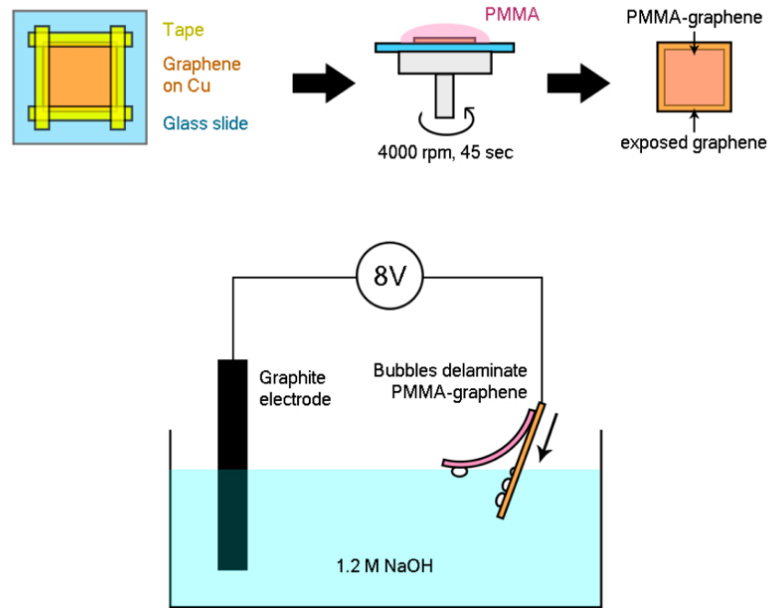


Figure 2.3. Schematics of experimental bubble transfer of graphene on copper foil. Adapted from Danda et al.

Bubble transfer was been a clean method to obtain a large area of monolayer of graphene. The sodium hydroxide (NaOH) salt solution is prepared with $\sim 1\text{M}$ (sometimes a much lower molarity was also used, 2 grams of NaOH in 1 liter of DI water). This mixture is first filtered through a $0.22\ \mu\text{m}$ membrane filter. The as grown graphene-copper foil is spin coated with PMMA and bake for 100°C for 2 mins. Using Carbon electrode as Anode and cathode with Cu/graphene/PMMA stack, a simple setup like the electrolysis of water is carried out. A voltage range of 5-10V is used (6V is optimal for 0.01M solution). Graphene + PMMA stack peel-off clean from Cu substrate. The Graphene/ PMMA stack is further rinsed in nanopure DI water several times (use 3-4 different beakers and let it sit for 2-3 mins each beaker) to remove any salt residue. The graphene/ PMMA stack is ready for its

final transfer onto a desired substrate, further the PMMA can be washed off after transfer and drying with acetone/ IPA.

Alternatively, the copper film can also be etched away by floating Cu/graphene/PMMA stack on a solution of 0.3M iron chloride (12g/ 250 ml water)

2.3 Growth of Transition Metal Dichalcogenide (TMDs)

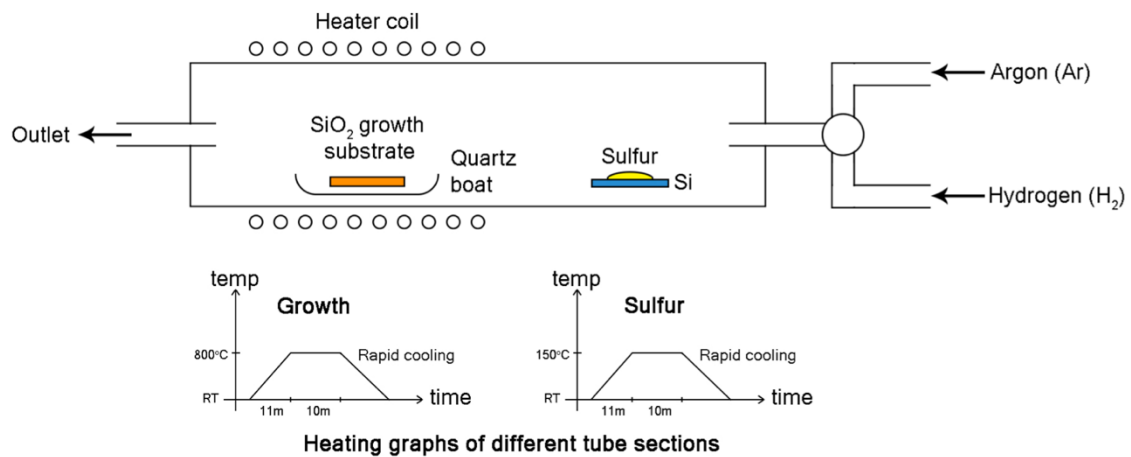


Figure 2.4. Schematics of experimental CVD growth setup for WS₂ flakes. Adapted from Danda et al.

For TMD growth, a SiO₂ wafer (thickness 150 nm thick) is cut into small pieces, roughly to 1cm × 1 cm. For these substrates are cleaned in the piranha acid for about 40 minutes. In parallel, the growth precursors are prepared in separate vials in the following concentration, in the case of WS₂ (1) sodium cholate (4% = 0.04 g/1 ml DI water) and (2) For WS₂- ammonium metatungstate (15 mM = 45 mg/1 mL DI water). In the case of MoS₂, 1% sodium cholate (10 mg/1 mL) and 1% ammonium heptamolybdate (11 mg/1 mL) solution is used. These prepared solutions are then sonicated for 1 hour in a water bath. Once the precursor solutions are ready and SiO₂ substrates are clean from piranha acid etching

(sometimes followed with Ozone plasma clean), these substrates are then spin coated (4000 rpm for 15 sec) with 1 drop of ammonium metatungstate solution for WS₂ (and ammonium heptamolybdate solution for MoS₂), once dried (dried in the fume hood for a few minutes) the substrates are again spun with sodium cholate solution with the respective concentration for the desired TMD flake.

Finally, the growth substrates are carefully positioned on a quartz boat and placed in the center of the 1-inch diameter tube furnace (Thermo Fisher Scientific Lindberg/Blue M). In addition, 70 grams of sulfur crystal for WS₂ and (150 mg for MoS₂) are placed on a SiO₂ piece (on the unpolished Si side of a 1cm× 1 cm piece of Si/SiO₂ wafer piece) and positioned about 2.5cm away from the end of the furnace (and ~ 22 cm from the substrates), in the upstream direction at a temperature of 150 °C. A heating belt is utilized to monitor a temperature of 150 C at the sulfur location. The sulfur is placed outside the furnace, away from the center portion of tube in an upstream direction. The furnace is ramped up to 800 C in 11 mins (as shown in the table below) at 65°C min⁻¹. The gas flow is controlled as shown in the table below. For WS₂, hydrogen is flown during the growth phase only for about 10 mins at 15 sccm.

Temperature (C)	Time (min)	Argon Flow Rate (sccm)	H ₂ Flow Rate (sccm)
Room	20	1000	0
Room-800	11	100	0
800	5	100	0
800	10	100	15
800-Room	120	100	0

Table 2.1 Controlled parameters for monolayer WS₂ flake growth

Temperature (°C)	Time (min)	N ₂ Flow Rate (sccm)
Room	10	1000
Room-750	12	400
750	15	400
750-Room	90	400

Table 2.2. Controlled parameters for monolayer MoS₂ flake growth

Note- in the case of WS₂, that the growth temperature is at 800C and the 5 mins with carrier gas Argon is followed to stabilize the furnace temperature at 800C. The first 20 minutes of Ar is flown to ensure the furnace tube is purged of other gases. The temperature of the furnace and tube is well calibrated at various steps and this is critical just as any other step in the growth procedure. After 10 mins of growth time, the H₂ was turned off and the furnace was rapidly cooled to room temperature by opening the furnace hood while Argon is allowed to flow. For MoS₂ flake, during step 2, the heating belt must be plugged in (with a set point of 180°C) at the time when the temperature of the furnace reaches 700°C. When the furnace reaches 750°C, the sulfur should be either glistening (i.e., partly melted) or fully melted. After the third step, for rapid cooling - heating belt and furnace are turned off with the furnace open. Additionally, two fans are also positioned at the furnace to create a rapid cooling environment. After about 2-3 hours, the substrates are carefully removed.

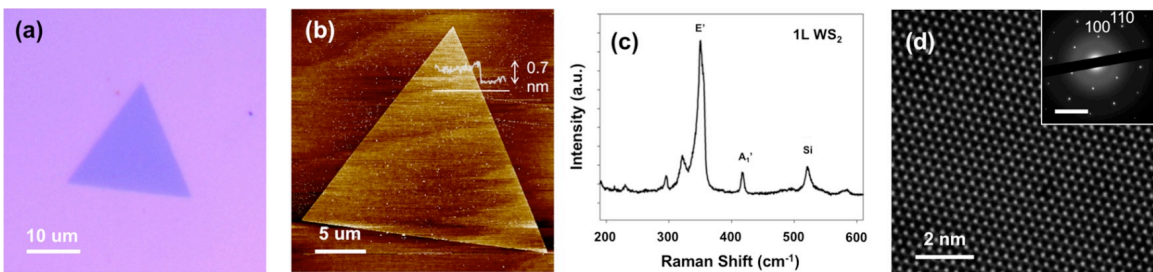


Figure 2.5. TMD Characterization techniques.

(a) AFM scan of a monolayer WS₂ flake. The line profile in white indicates a thickness of 0.7 nm, which corresponds to a monolayer. (b) Raman spectra ($\lambda = 532$ nm) of a monolayer WS₂ flake with indicated primary modes. (c) Photoluminescence (PL) spectra of a pristine suspended monolayer WS₂ membrane showing three spectral components: neutral exciton (X0), trion (XT), and defect (XD). (d) Gaussian blur- filtered AC-HRSTEM lattice image taken at 80 kV. The inset is a SAED pattern with expected (100) and (110) diffraction spots. Adapted from references³⁴.

2.3.1 Transfer of TMD and Device Fabrication

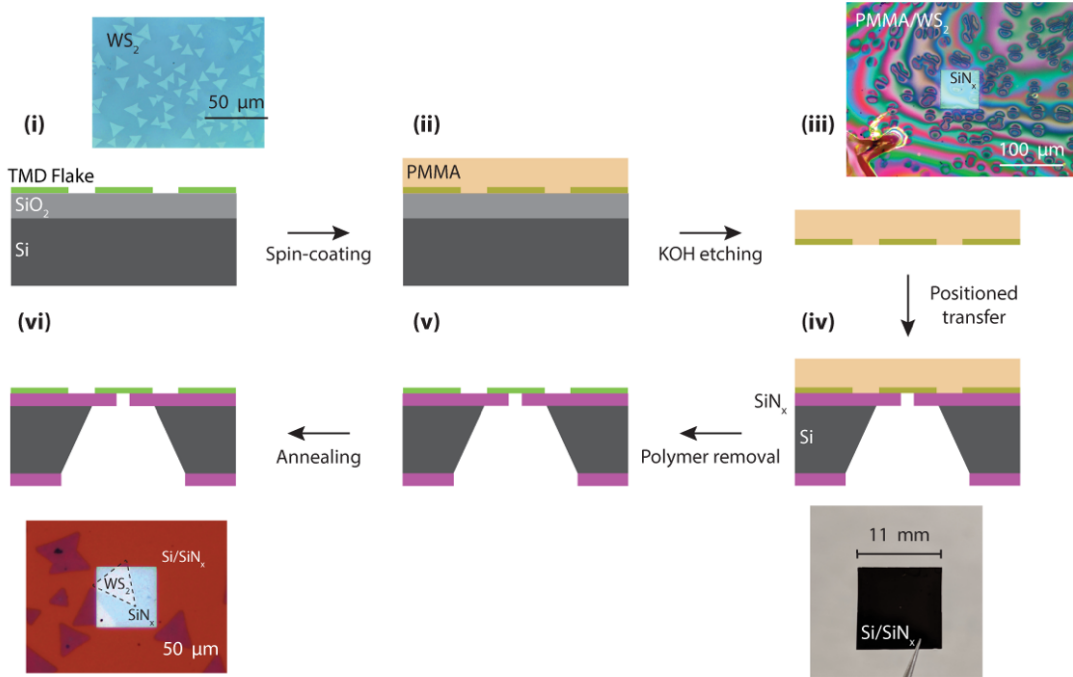


Figure 2.6. Position-controlled transfer of TMDs from as-grown substrate to a desired device.

Figure 2.6. shows the transfer process for TMD flakes that is ubiquitously used in this work. Pictured before step (iv) is the Si/SiN device used in Chapter 6. With WS₂ flakes grown on Si/SiO₂ wafer pieces, we cut smaller pieces with areas about 3×3 mm² that contain good WS₂ flakes. Using a wet transfer technique, the TMD flake side of the SiO₂ pieces is coated with polymethyl methacrylate (PMMA, MicroChem C4, 4000 rpm for 60 seconds). The PMMA coated substrates are left to dry at ambient temperature for a few

minutes before being floated onto the KOH etchant (prepared with 8g of KOH pellets dissolved in 100 ml of water). Depending on the thickness of the SiO₂ wafer, the time for etching away the SiO₂ layer varies, lasting between 30-90 mins. This etching results in the PMMA+TMD flake peeling off the substrate and floats on the KOH etchant. These PMMA+TMD flakes are then collected with a glass slide, rinsed about 2 or 3 times in clean DI water baths before being transferred onto a SiN_x/Si chip with a hole (diameter range, 100 to 200 nm) drilled by Focused Ion Beam. Manual position transfer is practiced when the flake size and their number density are high, so as to maximize the possibility of covering a SiN_x FIB hole with one single PMMA+TMD flake. This step of placing the PMMA+TMD flake over the SiN_x FIB hole is somewhat challenging as the coverage of the FIB hole depends on the flake density since this process is carried out by trial and error. However, majority of effort was directed towards improves flake density and flake size and therefore the transfer is completed within a few trials. Average time to transfer a flake in this fashion did not exceed more than 20 mins per SiN device. In addition to this manual transfer, I have also experimented with custom-built manipulators, with needles and tweezers to move the flake on the substrate to increase device yield. These manipulations come at a cost, since there is now a higher risk of device failure caused by the usage of additional tools, which can sometimes break the SiN_x membrane. In this work, all devices were fabricated by manually “fishing” the PMMA+TMD flake onto the SiN_x FIB hole (unless stated otherwise). After we transfer the flake and optically verify the coverage, the sample is then dried in ambient temperature for 30 min. Furthermore, the sample is placed into hot acetone (90°C) to remove the supporting PMMA and finally washed with IPA and annealed in RTA usually at 300 C in Argon gas for 90 mins to remove any contaminants.

2.4 Large-Scale fabrication of MoS₂ Film

This work has been adapted from the journal publication, titled “Centimeter-Scale Nanoporous 2D Membranes and Ion Transport: Porous MoS₂ Monolayers in a Few-Layer Matrix” by Paul Masih Das, Jothi Priyanka Thiruraman, Yung-Chien Chou, Gopinath Danda and Marija Drndic. Cite This: Nano Lett. 2019, 19, 392–399

2.4.1 Introduction

Two-dimensional nanoporous membranes have received attention as catalysts for energy generation and membranes for liquid and gas purification but controlling their porosity and facilitating large-scale production is challenging. We show the growth and fabrication of centimeter-scale molybdenum disulfide (MoS₂) membranes with tunable porous areas up to ~ 10% of the membrane and average nanopore diameters as large as ~ 30 nm, controlled by the etch time. We also measure ionic conductance between 0.1 and 16 μS per μm^2 through variably etched nanoporous membranes. Ensuring the mechanical robustness and large-area of the membrane, bilayer and few-layer regions form a strong supporting matrix around monolayer regions, observed by aberration-corrected scanning transmission electron microscopy. During etching, nanopores form in thin, primarily monolayer areas whereas thicker multilayer regions remain essentially intact. Atomic-resolution imaging reveals that after exposure to the etchant, the number of V_{1mo} vacancies increases and nanopores form along grain boundaries in monolayers, suggesting that etching starts at intrinsic defect sites. This work provides an avenue for the scalable production of nanoporous atomically thin membranes.

2.4.2 Background

Two-dimensional (2D) transitional metal dichalcogenides (TMDs) have demonstrated new physical phenomena in electronics, nanofluidics, and biosensing, and have shown myriad applications in each of these fields.^{33,86,211} While electronics strive for defect-free materials, other fields such as DNA sequencing,^{34, 129} battery/electrochemical storage,¹⁰⁰ and membrane separation technologies like water desalination^{57, 190} and gas separation^{29,229} have a different set of requirements – including mechanically robust and large-area membranes – to achieve transport of molecules through atomic vacancies and nanopores in suspended membranes.

In addition to ionic/molecular transport applications, nanoporous TMD membranes have been tested as electrodes and catalysts for a range of photo- and electrochemical processes.^{77,236} For example, it has been shown that edge sites in molybdenum disulfide (MoS₂) display particularly high electrocatalytic activity during hydrogen evolution reactions.^{73,201,220} However, current chemical syntheses for porous TMDs based on hydrothermal chemical processes offer limited sample purity and porosity control.^{107,230,236} Alternative mechanical fabrication techniques based on focused ion beam (FIB) and transmission electron microscope (TEM) irradiation, though accurate, have scalability limitations.^{27, 190}

Nanoporous membrane characteristics such as fluid flux and permeance exhibit enhancement in the regime of atomically thin membranes.^{137,141,209} However, existing techniques for fabricating nanoporous atomically thin membranes (NATMs) from mechanical exfoliation, liquid-phase exfoliation, and chemical vapor deposition (CVD) of monolayer TMDs are usually limited in size to the μm - or mm -scale.^{34,139,190,211} More

importantly, cm-scale suspended monolayer membranes are too fragile for most applications requiring high flux fluid or gas flow, and often require extensive pre-processing such as defect sealing.^{141, 209} To meet both requirements, here we propose a way to increase the robustness of large-area suspended membranes, while also preserving atomically thin regions required for high volume ionic/molecular transport, by fabricating cm-scale nanoporous membranes consisting of monolayer regions embedded in a few-layer matrix. Specifically, we demonstrate the acid-assisted etching of MoS₂ films as a new means of fabricating 2D nanoporous membranes. These structures are produced through a simple and scalable process that results in mechanically stable, high quality membranes. The structural characteristics of cm-scale MoS₂ films grown by sulfurizing Mo foil are first analyzed using a combination of atomic force microscopy (AFM), Raman spectroscopy, and aberration-corrected scanning TEM (AC-STEM). We then develop a multi-step wet-etch procedure to produce suspended membranes and utilize an industry-standard etchant to induce nanopore formation. AC-STEM is used to quantify the size and density of nanopores as well as to provide insights into the pore formation mechanism at the atomic scale.

2.4.3 Growth and Characterization of MoS₂ Thin Films

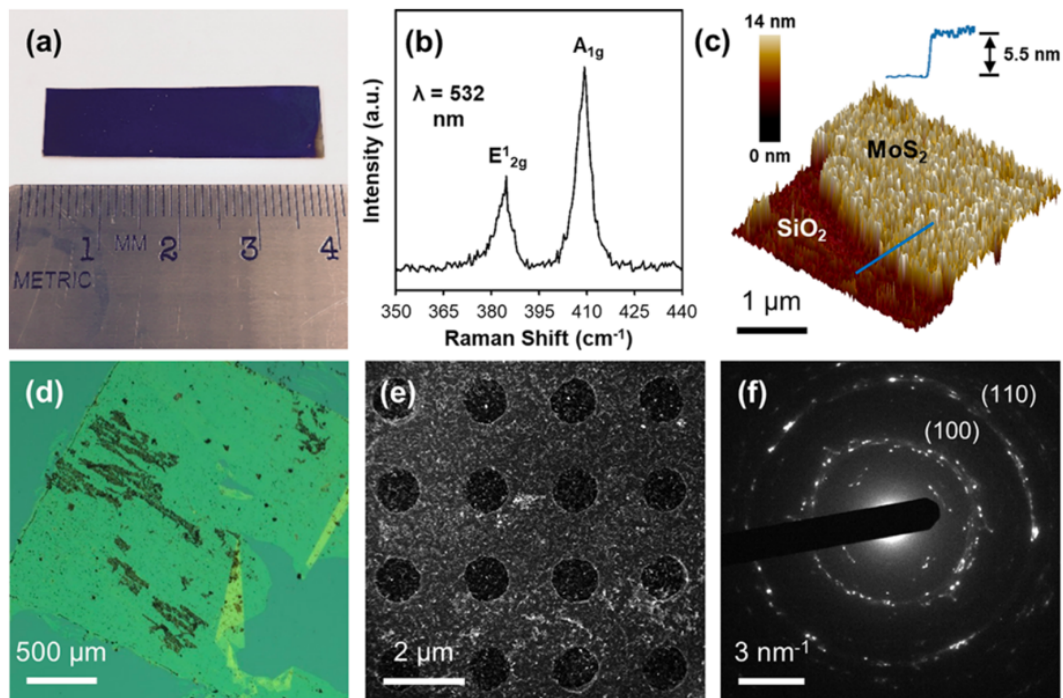


Figure 2.7. Characterization of pristine (as-grown) and transferred MoS₂ films.

(a) Optical image of a centimeter-scale MoS₂ film grown through Mo foil sulfurization. (b) Raman spectrum (excitation wavelength = 532 nm), (c) AFM scan, and (d) optical image of a continuous 0.2 cm × 0.2 cm MoS₂ film transferred onto a Si/SiO₂ substrate. The difference between the in-plane (E^1) and out-of-plane 2g (A) phonon modes ($E^1 - A = 24.5 \text{ cm}^{-1}$) in (b) and the line 1g 2g 1g profile in (c) are both consistent with an average thickness of 5.5 nm ($N \sim 6-7$ layers). (e) Low-magnification AC-STEM image of a 4 × 4 array of 1 μm diameter MoS₂ membranes (i.e., suspended MoS₂ films) on a holey carbon film. (f) SAED pattern of a MoS₂ membrane showing (100) and (110) ring patterns, suggesting a polycrystalline structure.

We grow cm-scale MoS₂ films through the sulfurization of unannealed, commercially available Mo foil (see Methods and Supplementary Figure S1).^{8,10,187} Figure 2.7a shows a 1 cm x 4 cm piece of Mo foil after the sulfurization process. The growth of MoS₂ on top gives the gray Mo foil a purple hue under ambient light. A Raman spectrum reveals two

characteristic vibrational modes: an in-plane E_{2g}^1 mode at 384.7 cm^{-1} and an out-of-plane A_{1g} mode at 409.2 cm^{-1} (Figure 2.7b). The separation of 24.5 cm^{-1} between the two modes suggests that the average thickness of the MoS₂ is approximately ($N \sim$) 6-7 layers.¹⁰⁹ This is consistent with AFM scans, which reveal an average height of 5.5 nm (Figure 2.7c). Because of their multi-layer structure, these MoS₂ films are more robust than their monolayer counterparts and can therefore be more readily processed and transferred from substrate to substrate on large scales.^{88,91,209} These observations are consistent with previously published experimental and theoretical works showing that suspended few-layer thick MoS₂ exhibits higher in-plane elastic moduli and effective spring constants (*i.e.*, rigidity) in comparison to monolayer MoS₂.^{16,26,135} Figure 2.7d shows an optical image of a 0.2 cm x 0.2 cm piece of MoS₂ film that has been transferred (see section 2.4.5) onto a Si/SiO₂ substrate with mostly no tears or discontinuities. Similarly, transferring a film to a substrate such as holey carbon results in a relatively large array of MoS₂ membranes, such as the one shown in Figure 1e. It should be noted that the term membrane is used here to refer to any freestanding region of a 2D (*i.e.* MoS₂) film that is suspended over a hole. Subsequent selected area electron diffraction (SAED) patterns reveal two concentric rings corresponding to the (100) and (110) lattice spacings of the MoS₂ basal plane (Figure 2.7f). The presence of rings as opposed to distinct diffraction spots indicates that the MoS₂ membranes have an overall polycrystalline structure.¹⁷⁴

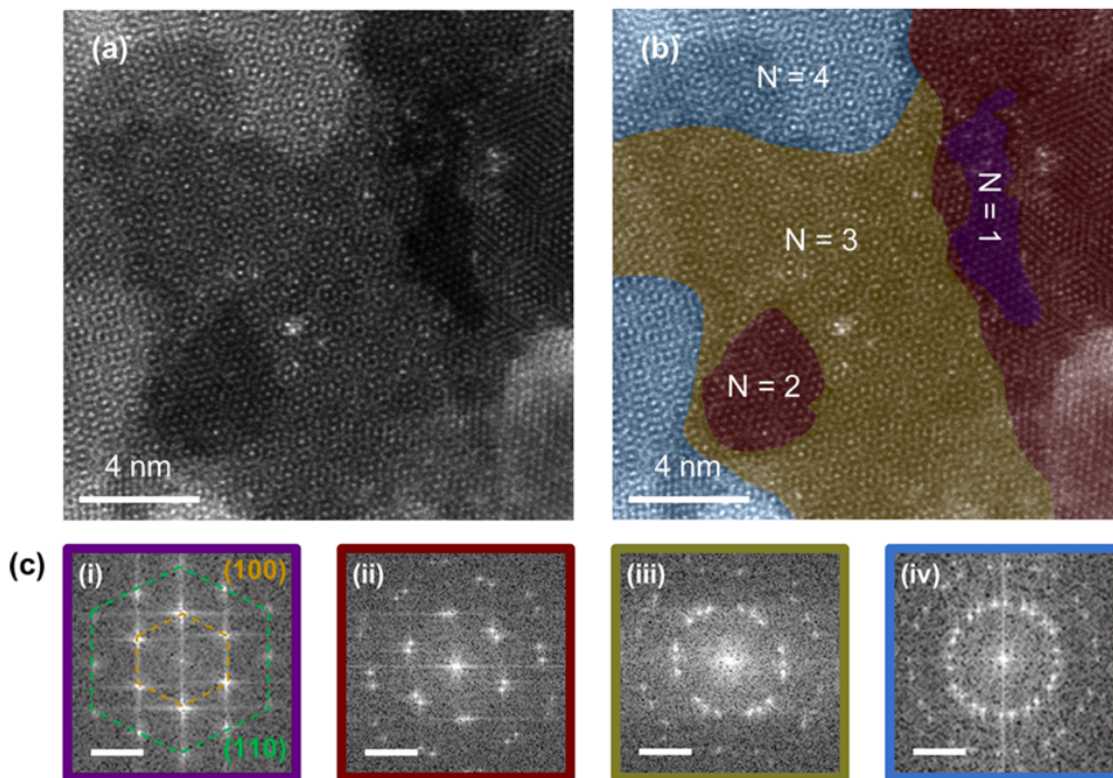


Figure 2.8. Monolayer regions in a few-layer MoS₂ matrix.

(a) High- magnification HAADF AC-STEM image of a few-layer matrix in a pristine MoS₂ membrane. Excluding areas with polymer contamination (bottom right), thicker regions generally have a higher intensity due to HAADF Z-contrast behavior. (b) False-colored version of (a) with highlighted regions of the membrane for $N = 1$ (purple), 2 (red), 3 (yellow), and 4 (blue) layers. (c) (i–iv) Corresponding FFT patterns for selected areas within the few-layer matrix shown in (b) with (100) and (110) diffraction spots highlighted in yellow and green, respectively. The number of layers (N) in a particular region of the matrix is equivalent to the number of sets of 6-fold symmetric diffraction spots in the corresponding FFT. For $N = 2–4$, the twist angle between layers is $\sim 9–11^\circ$. The scale bars in (c) correspond to 4 nm^{-1} .

In addition to being polycrystalline (Figure 1f), these MoS₂ membranes also have a relatively high surface roughness ($\sigma \sim 1.9 \text{ nm}$) in comparison to exfoliated monolayer MoS₂ ($\sigma \sim 0.1 \text{ nm}$) (Figure 2.7c).¹⁵³ This suggests that despite having an average thickness of $N \sim 6-7$ layers, the resulting membranes contain a varying number of layers. We

therefore utilize high-angle annular dark field (HAADF) AC-STEM imaging, which provides insight into both crystal structure and thickness at the atomic scale.^{101,190} Figure 2.8a shows a representative few-layer region (*i.e.* matrix) of a MoS₂ membrane measuring roughly 280 nm² (AC-STEM field of view). The trigonal prismatic (2H) MoS₂ lattice in a monolayer region transitions to a Moiré superlattice in thicker multi-layer regions due to interlayer twisting.^{67,227} The false-colored image in Figure 2.8b highlights distinct grains within the matrix based on their thickness: $N = 1$ (purple), 2 (red), 3 (yellow), and 4 (blue) layers. About 4% of the matrix area shown is monolayer ($N = 1$) whereas the bi- ($N = 2$), tri- ($N = 3$), and quad-layer ($N = 4$) areas occupy 29%, 41%, and 26%, respectively. A fast Fourier transform (FFT) of the monolayer region encased in this few-layer matrix reveals one set of six-fold symmetric (100) (orange) and (110) (green) diffraction spots as expected for a 2H phase TMD (Figure 2.8 c(i)).⁷⁶ FFT patterns of thicker regions containing N layers each exhibit a corresponding N sets of six-fold symmetric diffraction spots with twist angles of ~ 9 - 11° between layers (Figures 2.8 c(ii)-(iv)). We note that while the annealed Mo foil growth substrates have been shown to yield monolayer MoS₂ films,¹⁸⁷ the unannealed Mo foils are integral in producing the few-layer matrix-like structures shown here, due to their comparatively high surface roughness of $\sigma \sim 13$ nm (see Figure 2.2). In other words, the initial roughness of the underlying substrate is exploited in this work as it facilitates the simultaneous growth of monolayers and multilayers within the same sample. Further characterization on annealed Mo foils, such as Raman and X-ray photoelectron spectroscopy (XPS), can be found in the works of Tai *et al.*¹⁸⁷ and Bai *et al.*¹⁰

2.4.4 Controlled Large-Area Etching for Nanoporous MoS₂ Films

Nanoporous membranes from uniformly monolayer 2D materials are often limited by crystal size, poor transfer techniques, and/or non-scalable pore formation methods.^{86,90,141,209,228} By utilizing the matrix-like structure of these MoS₂ films, we fabricate atomically thin membranes that can be grown, transferred, and etched over relatively large (cm-scale) areas, limited by our sulfurization chamber size. While thicker sections of the MoS₂ membrane are preserved in order to provide robustness to the overall membrane, interspersed thin regions are etched away to form nanopores. Figure 2.9 is a step-by-step schematic of the process through which we use PAN etchant to form nanoporous MoS₂ membranes with tunable porosity. We found that pores nucleate at defect sites within monolayer regions of the pristine material and expand under further etchant exposure (see Figure 2.11). Etch time can be used to control sample porosity, from impermeable membranes to nanoporous membranes containing holey areas occupying up to 7.1% of the total suspended area (see Figure 2.10).

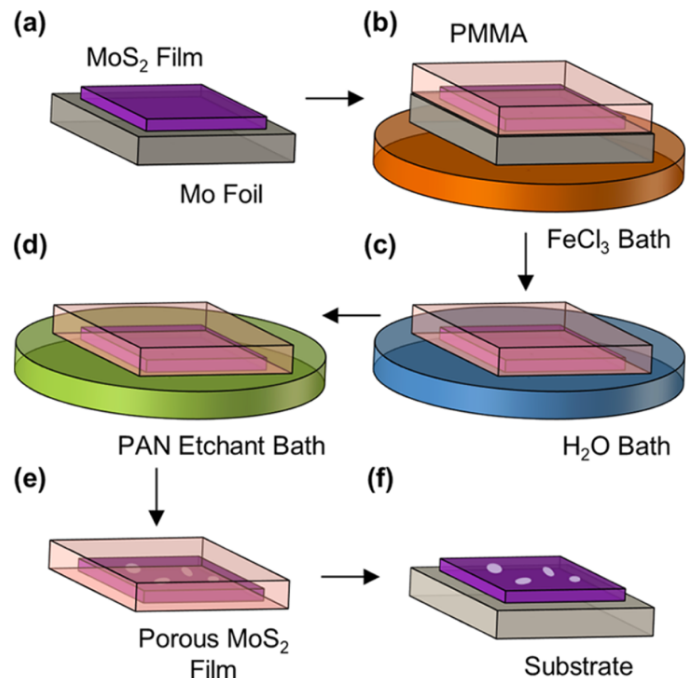


Figure 2.9. Schematic of nanoporous MoS₂ membrane fabrication using PAN etchant.

(a) MoS₂ films are isolated by (b) depositing a protective polymer (PMMA) layer and etching away the underlying Mo foil. (c) After being cleaned in DI H₂O, the film is (d) placed in the PAN etchant, which results in the (e) formation of pores (Figure 2.11). After being cleaned in DI H₂O, the MoS₂ is (f) placed on a supporting substrate such as a holey carbon film (Figure 2.7e), dried, and rinsed with acetone, which dissolves the PMMA and leaves behind a nanoporous MoS₂ membrane.

The procedure to achieve robust, large-area porous MoS₂ membranes is illustrated in Figure 2.9: the MoS₂ film supported on Mo foil is first cut into cm-scale pieces, coated with a protective polymer (PMMA) layer, and placed in iron chloride (FeCl₃) solution (Figures 2.9a-b). In the presence of FeCl₃, which acts as a Lewis acid, the Mo foil is etched away via an oxidation reaction.⁶ Residual FeCl₃ is then removed by transferring the floating polymer coated MoS₂ film to a water bath (Figure 2.9c). Next, the MoS₂ is placed in a bath containing PAN etchant (54:21:13:12 (v/v) mixture of H₂O, phosphoric, nitric, and acetic acids), which is ubiquitously used in the semiconductor industry as an etchant for Mo and Al thin films.^{117,134} This results in the formation of pores over the entirety of the film

(Figures 2.9d-e), the mechanism of which is discussed later (see Figure 2.11). We use etch times of 0 (pristine), 30, 60, and 90 minutes in this study. The process is completed by an additional water rinse, transfer to a substrate such as holey carbon or silicon nitride (SiN_x), and finally placement in acetone. The latter causes removal of the sacrificial polymer layer and results in a nanoporous MoS_2 membrane (Figure 2.9f).

2.4.5 Characterization and Fluid Transport of Nanoporous MoS_2

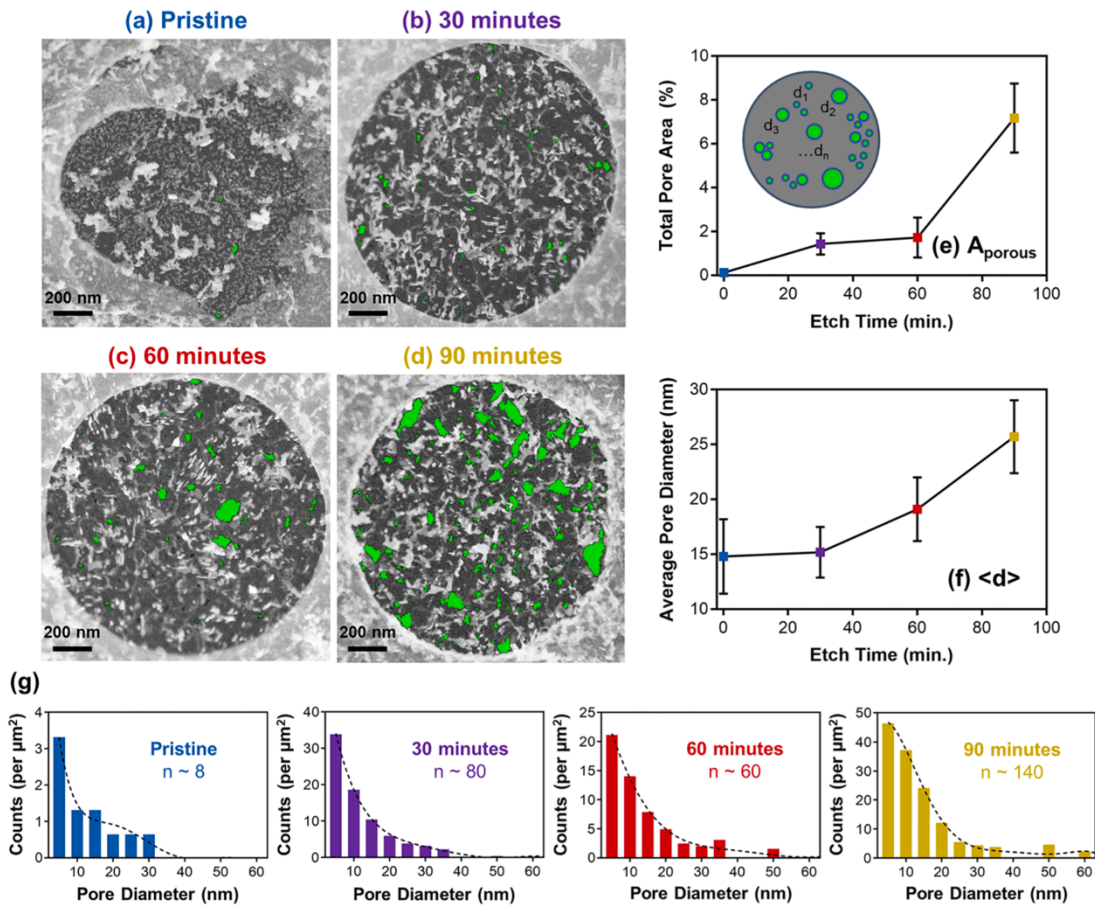


Figure 2.10. TEM-based quantification of nanoporous MoS_2 membranes.

(a) Low-magnification AC-STEM image of a pristine 1.3 μm diameter MoS_2 membrane. Images of different membranes after treatment in PAN etchant for (b) 30, (c) 60, and (d) 90 min with nanoporous/ etched regions highlighted in green. Plots of (e) total pore area A_{porous} and (f) average pore diameter $\langle d \rangle$ as a function of exposure time to the PAN etchant. Error bars correspond to the standard deviation over multiple (~ 20) membranes. The schematic shown in the inset of (e) indicates the labeling of n pores (green) in a

membrane (gray), each with diameter d_i corresponding to a circular pore with the same area (see eqs 1 and 2). (g) Averaged distributions (per μm^2) of pore diameters and corresponding n values for pristine (blue), 30 (purple), 60 (red), and 90 (yellow) minute etched MoS_2 membranes. Best fit lines (dashed) are drawn as a guide to the eye.

Figure 2.10a shows a low-magnification AC-STEM image of a pristine MoS_2 membrane covering a $1.3 \mu\text{m}$ diameter hole after the transfer process and before etching. Statistical analysis of pore membranes was performed using global thresholding of AC-STEM images for different etch times in ImageJ (see section 2.4.6). For n pores in a membrane, each with diameter d_i corresponding to a circular pore with the same area, we first define average pore diameter $\langle d \rangle$ as

$$\langle d \rangle = \frac{\sum_{i=1}^n d_i}{n} \quad (1)$$

This is illustrated in the inset of Figure 2.10 e. Here, we only consider nanopores with $d_i > 3 \text{ nm}$ due to imaging resolution limitations at this magnification. We also define the total porous area percentage A_{porous} as

$$A_{\text{porous}}(\%) = \frac{\sum_{i=1}^n \pi \left(\frac{d_i}{2}\right)^2}{A_{\text{hole}}} \times 100\% \quad (2)$$

where A_{hole} is the area of the underlying FIB hole ($\sim 1.3 \mu\text{m}^2$). As shown in the summarized results in Figure 2.10 e,f, both A_{porous} and $\langle d \rangle$ are obtained by averaging over multiple (~ 20 , total area $\sim 27 \mu\text{m}^2$) images of suspended regions. n values normalized to an area of $1 \mu\text{m}^2$ are given in Figure 2.10g. The few pores found in pristine membranes

(Figure 2.10 g, $n \sim 8$) yield $A_{\text{porous}} \sim 0.1\%$ and $\langle d \rangle \sim 14$ nm. As reported by others, this is most likely the result of imperfect transfer or irregular growth due to the high surface roughness of the unannealed Mo foil (see Figure 2.12).¹⁸⁷ After treatment in the PAN etchant for 30 min, A and $\langle d \rangle$ increase to roughly 1.4% porous and 15 nm, respectively (Figure 2.10 b). We also note that the etchant assists in removing residual polymer (PMMA) from the MoS₂ surface, which appears as a white haze in the pristine film (Figure 2.10 a) but disappears after PAN treatment (Figure 2.10b). Additional exposure to the etchant for 60 and 90 min increases A_{porous} to 1.7% and 7.1%, respectively (Figure 2.10 c,d). The average pore diameter also increases from 19 to 26 nm while n more than doubles from 60 to 140 pores. Figure 2.10 e,f demonstrates that increasing etch time leads to monotonic rises in both A_{porous} and $\langle d \rangle$, respectively. Similarly, the average pore diameter distributions (per μm^2) shown in Figure 2.10 g indicate that longer etch times result in an increase in the percentage of pores in the membrane with larger (>5 nm) diameters. This demonstrates that etch time can be used to controllably fabricate nanoporous MoS₂ membranes with tunable pore ensemble characteristics.

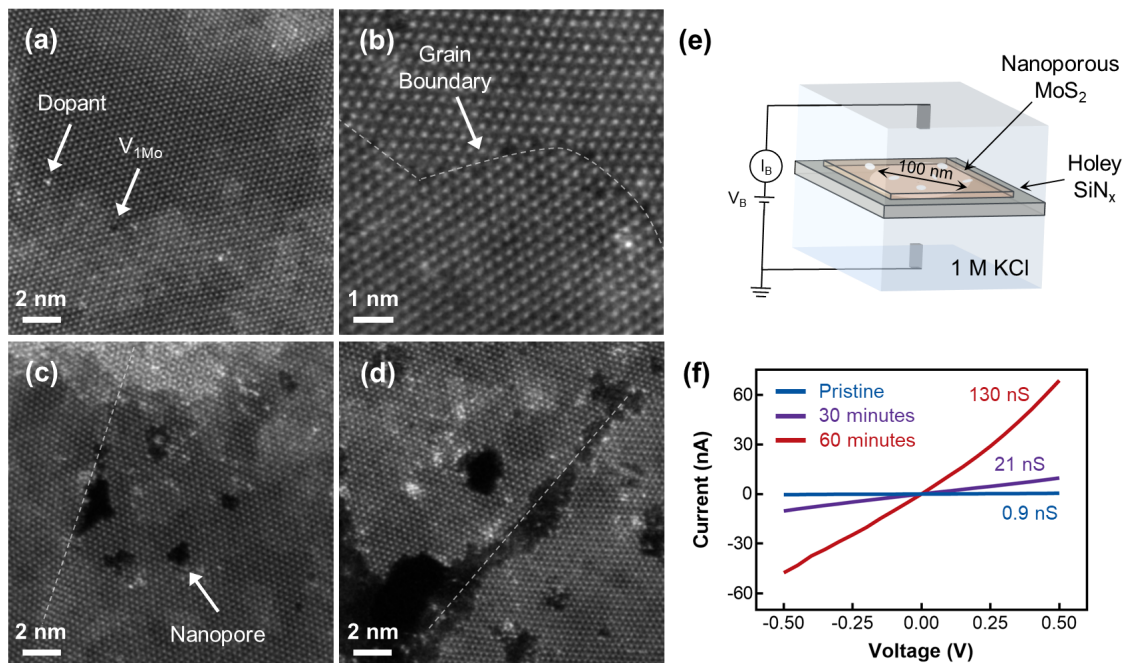


Figure 2.11. Nucleation and expansion of nanopores in monolayer MoS₂ regions due to PAN etchant exposure.

(a) High-magnification AC-STEM lattice image of a monolayer region in a MoS₂ membrane showing the presence of a low concentration of foreign dopants and intrinsic transition metal vacancies (V_{1Mo}). (b) High-angle ($\theta = 31^\circ$) grain boundary (outlined in white) between two monolayers showing the preferential formation of vacancies along grain boundaries due to PAN etchant exposure. Further exposure results in the (c) expansion of vacancies into larger nanopores and eventually the (d) complete etching of grain boundaries. (e) Schematic of the ionic transport setup used to measure the conductance of nanoporous MoS₂ membranes (see Methods). (f) Current-voltage (I_B - V_B) curves (± 500 mV) for pristine (blue) and etched (purple – 30 minutes, red – 60 minutes) MoS₂ membranes with corresponding ionic conductance values.

We also use AC-STEM imaging to investigate the mechanism for pore fabrication at the atomic level. Figure 2.11a shows a high-magnification AC-STEM image of the monolayer region of a pristine MoS₂ membrane. We focus here on monolayer areas, which are observed to etch before thicker multilayer regions (see Figure 2.11c). Transition metal vacancies (V_{1Mo}) and heavy-atom dopants are visible within the MoS₂ lattice as missing

and high-intensity atoms, respectively (Figure 2.11a). After exposure to the PAN etchant, more V_{1Mo} vacancies in the membrane become visible. In particular, vacancies tend to appear along or near grain boundaries in the polycrystalline membrane (Figure 2.8c). Figure 2.11b shows a high-angle ($\theta = 31^\circ$) grain boundary (outlined in white) between two monolayer regions in which a large concentration of V_{1Mo} vacancies is spatially localized to the interface. Such vacancies are not present at other grain boundaries in the pristine material (Figures 2.8a-b) and are therefore attributed to the etching process. Further etching of the membranes results in the expansion and joining of vacancies into larger nanopores that form preferentially along grain boundaries (Figure 2.11c). In some cases, grain boundaries over 20 nm in length were found to be completely etched to form linear voids (Figure 2.11d). Previous reports have shown that grain boundaries in TMDs contain a high density of defects such as chalcogen vacancies (V_{1S} and V_{2S}) and distorted 4/8-fold rings.^{38,234} The highly confined formation of pores and vacancies along grain boundaries observed with AC-STEM (Figures 2.11b–d) therefore suggests that intrinsic defects primarily located at grain boundaries within the polycrystalline MoS_2 membrane act as nucleation sites for the PAN etchant-based reaction.

2.4.6 Additional Experimental Methods

MoS₂ Film Growth: MoS_2 films were grown via the sulfurization of Mo foil. A centimeter-scale piece of Mo foil (Alfa Aesar, 0.025 mm thick) was first sonicated in 30% acetic acid for 15 min. The foil was then washed with deionized (DI) H_2O , blow dried with N_2 gas, and positioned in the middle of a 1 in. diameter tube furnace (Barnstead Thermolyne 21100). The foil was placed directly on quartz plates in a quartz boat in order to limit MoS_2

growth to one side. After being flushed with N₂ gas (1000 sccm), the furnace was heated to 800 °C with a ramp rate of 70 °C/min and a N₂ flow rate of 100 sccm. The furnace was then held at 800 °C for 5 min under a N₂ flow rate of 700 sccm while 25 mg of sulfur, placed 23 cm away from the foil, was kept at 180 °C. Afterward, the system was rapidly cooled by shutting off the furnace, sliding the foil out of the furnace, and turning on cooling fans.

Device Fabrication: MoS₂ films were isolated and transferred by first spin-coating one side of a mm/centimeter-scale piece of the growth product with C4 PMMA. We note that the backside of the foil is polished with sandpaper prior to spin-coating to remove any extraneous MoS₂. The underlying Mo foil was then etched by floating the film in 2 M FeCl₃ solution for 24 h. The floating film was transferred with a glass slide to DI H₂O for an additional 24 h to remove residual FeCl₃. Nanoporous membranes were then fabricated by treating the PMMA-coated MoS₂ film in an acid-based etchant known as PAN (54:21:13:12 (v/v) mixture of H₂O, phosphoric, nitric, and acetic acids) for between 30 and 90 min (see Figure 2.9). The film was then washed with DI H₂O, transferred to a supporting substrate such as holey carbon, dried overnight, and immersed in HPLC-grade acetone for 24 h to remove the polymer coating. The final membrane consists of a nanoporous MoS₂ film suspended over one or multiple (up to centimeter-scale arrays) micron-sized holes.

Bulk Characterization: Raman spectroscopy was performed using an NT-MDT NTEGRA Spectra with a 532 nm Nd:YAG laser excitation and 1800 lines/mm spectrometer grating

(0.5 cm^{-1} resolution). AFM scans were completed with a Bruker Dimension Icon operating in tapping mode.

TEM Imaging and Analysis: AC-STEM images were obtained using a HAADF detector with a collection angle of 54–220 mrad on a Cs-corrected JEOL ARM-200CF operating at 80 keV and SAED patterns were acquired using a JEOL 2010F operating at 200 keV. AC-STEM image analysis and nanopore quantification were performed using custom-scripted ImageJ and DigitalMicrograph software: Images were first Gaussian blurred to reduce background noise, porous regions were then isolated via intensity thresholding and counted using ImageJ's "Analyze Particles" functionality. All measurements were performed at room temperature.

Ionic Transport Measurements: Nanoporous MoS₂ membranes were fabricated on 100 nm diameter FIB holes in SiN membranes using the process described above. Prior to experiments, samples were annealed at 300 °C for 90 min under a continuous 95:5 (v/v) Ar/H₂ gas flow. Afterward, samples were glued into a custom PDMS mold and immersed in 50:50 (v/v) water/ethanol solution for 30 min. Membranes were then flushed with 1 M KCl (with 10 mM EDTA and 1 mM Tris) solution. Ionic measurements were obtained using Ag/AgCl electrodes connected to a EPC-10 HEKA amplifier operating at 10 kHz.

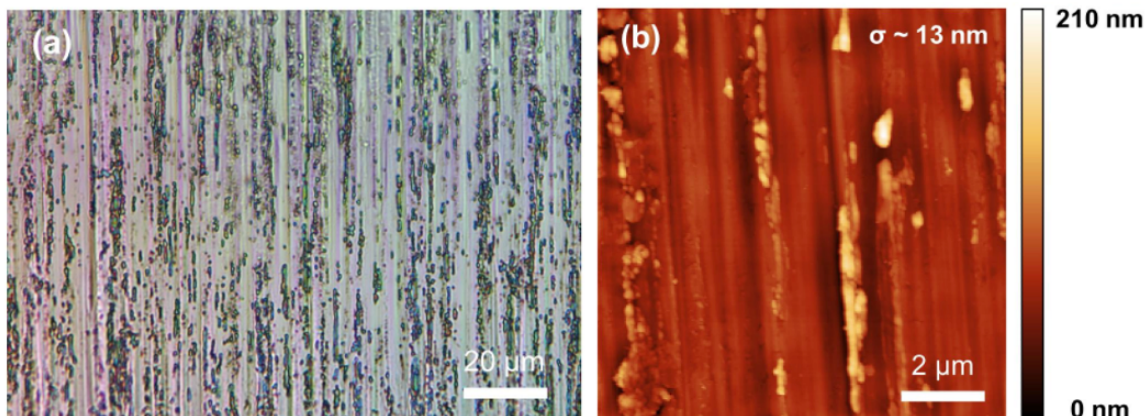


Figure 2.12. Characterization of the Mo foil growth substrate

(a) Optical microscope image and (b) AFM scan of the surface of the unannealed Mo foil (see Methods in the main text) prior to the sulfurization process. The unannealed foils display a relatively high surface roughness ($\sigma \sim 13$ nm) and result in the matrix-like structure of the MoS₂ films with both mono- and few-layer regions (see Figures 1-2).

Conversely, the sulfurization of Mo foil annealed at 1400°C yields uniformly monolayer MoS₂.^{21,22}

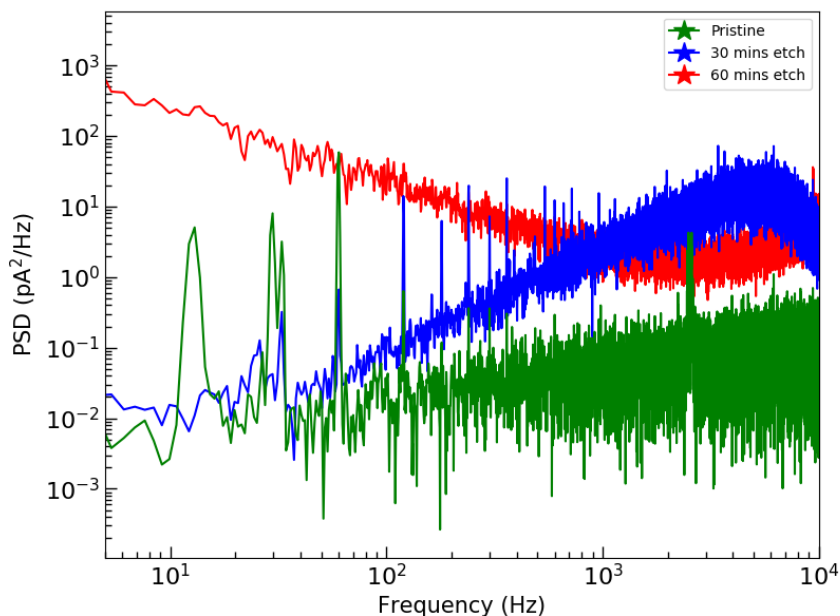


Figure 2.13. Current power spectral densities for nanoporous MoS₂ membranes

Power spectral densities (PSD) for pristine (green) and etched (blue – 30 minutes, red – 60 minutes) membranes. Pristine and 30 minute-etched membranes exhibit power spectra that contain noise contributions from only the amplifier (see Methods). This is also similar to the power spectra seen in thicker materials such silicon nitride.^{36,37} On the other hand, samples exposed to PAN etchant for 60 minutes yield power spectra that agree with the behavior of pores in 2D materials such as graphene³⁶ and MoS₂,⁸ where $1/f$ noise is dominant at low frequencies. This finding is intuitive as the 60 minutes etch results in a highly nanoporous membrane that allows for significant ion flow through thin, monolayer regions of the membrane. The PSD plotted above are extracted from current traces at 0 V

for each device and fitted to the equation $PSD = \frac{AI^2}{f^\alpha}$ where the noise coefficient, $A = 1.60 \times 10^{-1}$, and the low frequency exponent, $\alpha = 1.03$.

2.4.7 Summary

Fluid filtration, energy generation, and biomolecule detection have recently been demonstrated using porous TMD membranes due to the ability of pores and vacancies to form ionic channels in solution.^{34,60,220} Here, we demonstrate variable ionic conductance through nanoporous MoS₂ membranes fabricated via PAN etching. The experimental setup (see section 2.4.6) consisting of a 100 nm diameter, SiN- supported nanoporous membrane (orange) separating two chambers of 1 M KCl solution (blue) is shown in Figure 2.11e. The obtained current–voltage (I_B – V_B) curve for a pristine MoS₂ membrane yields an ionic conductance (i.e., slope) of roughly 1 nS (Figure 2.11f, blue). A membrane that has been exposed to 30 min of PAN etching exhibits an increase in conductance to 21 nS due to the formation of additional pores in the MoS₂ (Figure 2.11f, purple). The red curve in Figure 2.11f shows the comparatively high conductance (130 nS) obtained from a membrane etched for 60 min. This monotonic increase of conductance with etch time is expected due to higher values of $\langle d \rangle$ and A_{porous} (Figure 2.10e–f), resulting in increased ionic current across the membrane. The corresponding current noise power spectral densities for pristine and variably etched MoS₂ membranes are presented in section 2.4.6, Figure 2.13. Pristine and 30 min-etched membranes exhibit current noise power spectra that are similar to spectra from thick materials such as silicon nitride (SiN_x).^{130,175} Samples etched for 60 min yield spectra that agree with previously published data on nano- porous monolayer MoS₂ membranes, in which 1/f noise (f = amplifier frequency) is dominant at low frequencies.¹⁹⁰

The fact that the measured noise in our samples is similar to the reported noise for pores in monolayer membranes is also consistent with the overall picture that ionic transport primarily occurs through pores in thin, monolayer regions of the MoS₂ membrane, despite having an average thickness of a few layers (see Figures 2.7 and 2.8).

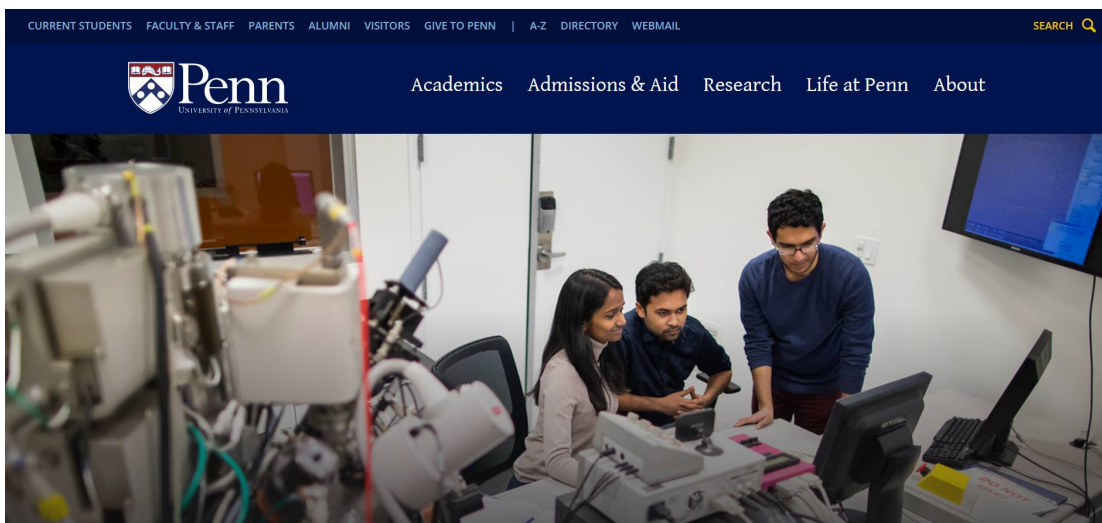
In conclusion, we have demonstrated a new method for the production of suspended centimeter-scale nanoporous MoS₂ membranes offering tunable pore sizes and densities. These membranes satisfy several practical requirements: the presence of monolayers for obtaining high ion/gas flux, combined with the structural robustness of multilayers and large membrane areas. AFM and Raman spectroscopy were used to show that large-scale MoS₂ films grown with Mo foil sulfurization had an average thickness N of $\sim 6-7$ layers. Mass-contrast HAADF AC-STEM imaging was utilized to further show that suspended films are comprised of a polycrystalline, multilayer matrix structure with embedded regions as thin as a single layer. MoS₂-based NATMs were fabricated by implementing a novel wet-etch process based on the industry-standard PAN etchant. Using AC-STEM imaging, it was shown that etchant treatment time can be used to control the porosity of the membrane with total porous areas A_{porous} of between 0.1 and 7% and average pore diameters $\langle d \rangle$ of up to 26 nm. Although the mechanical robustness of the overall membrane was preserved by intact multilayer regions during PAN etching, nanopores formed in thin, monolayer regions and subsequently expanded under further etchant exposure. Atomic-resolution images demonstrated that the mechanism by which pores are formed relies on intrinsic defects and is frequently localized to grain boundaries within the polycrystalline structure. Variable ionic conductance as a function of etch time was also established

through nanoporous membranes. The methods and characterization techniques presented here can be extended to the growing family of TMDs. This work also provides a unique approach to increasing the robustness of such membranes by characterizing and employing the often underutilized multilayer form of 2D materials, while at the same time not relying on thicker, laminate membranes. Coupled with recent advances in 2D materials growth and substrate engineering, the few-layer matrix structure of these MoS₂ films can likely be further tuned to control nanopore characteristics. Likewise, the direct spatial correlation between atomic defects and larger pores yields opportunities to tune the size, density, and location of pores within the membrane.

3 Defect Engineering and Nanopatterning in Transition Metal Dichalcogenide

3.1 Introduction

Manipulation and structural modifications of 2D materials for nanoelectronic and nanofluidic applications remain obstacles to their industrial-scale implementation. Here, it is demonstrated that a 30 kV focused ion beam can be utilized to engineer defects and tailor the atomic, optoelectronic, and structural properties of monolayer transition metal dichalcogenides (TMDs). Aberration-corrected scanning transmission electron microscopy is used to reveal the presence of defects with sizes from the single atom to 50 nm in molybdenum (MoS_2) and tungsten disulfide (WS_2) caused by irradiation doses from 10^{13} to 10^{16} ions cm^{-2} . Irradiated regions across millimeter-length scales of multiple devices are sampled and analyzed at the atomic scale in order to obtain a quantitative picture of defect sizes and densities. Precise dose value calculations are also presented, which accurately capture the spatial distribution of defects in irradiated 2D materials. Changes in phononic and optoelectronic material properties are probed via Raman and photoluminescence spectroscopy. The dependence of defect properties on sample parameters such as underlying substrate and TMD material is also investigated. The results shown here lend the way to the fabrication and processing of TMD nanodevices.



Photograph featured on web via University of Pennsylvania's landing page on March 15th, 2018. This work was subsequently published in *ACS Nano* and highlighted in Penn Today's magazine (link: <https://penntoday.upenn.edu/spotlights/creating-atomic-water-filters>). The equipment photographed in the background is the Focused Ion Beam (FEI FIB Strata DB235) at Singh Center, Penn. This industrial standard, Gallium sourced FIB tool served "instrumental" in new 2D materials endeavors during my PhD.

The results presented here were published in 2019, in the article "Irradiation of Transition Metal Dichalcogenides Using a Focused Ion Beam: Controlled Single-Atom Defect Creation" by Thiruraman J.P., Masih Das, P., Drndić, M., *Advanced Functional Materials*, 29, 1904668

3.2 Background

Among the expanding catalogue of two-dimensional (2D) materials, transition metal dichalcogenides (TMDs) have generated significant interest due to their exceptional electronic, optical, and structural properties.^{86,121,211} In particular, TMDs have been noted

for transmembrane applications such as DNA sequencing,^{34,140} energy harvesting,²⁰⁹ water desalination,^{57,190} and gas separation^{223,232} because of their extreme thinness and ability to host sub-nm scale pores. Other studies have shown that defects in single-atom thick materials can be used to manipulate electronic, magnetic, and catalytic properties.^{72,222} For example, defects in wide-bandgap h-BN exhibit spin effects and potential quantum functionality.^{40,172} The widespread realization of these applications is contingent upon the development of scalable processes for the fabrication of atomic-level defects with precisely-controlled sizes, spatial densities, and locations within the lattice.

Focused ion beams (FIBs) are widely utilized for doping, device fabrication, and micromachining in semiconductors such as SiC, GaAs, and Ge.^{129,155} More recently, FIB irradiation has been extended as a means of structural modification and nanopatterning in 2D materials such as graphene.¹⁴³ Theoretical studies^{2,48,99,166} on the role of ion incidence angle and substrate effects in the defect creation process in 2D materials like TMDs and graphene, and similar experimental studies,^{119,139,190} are starting to emerge. A wide range of techniques for defect creation have been reported in literature including plasma etching,¹⁸³ thermal decomposition,¹¹⁸ acid etching,^{126,140} electron irradiation,¹⁴⁵ and ion irradiation.^{119,190} The latter two irradiation methods directly allow for accurate and spatially selective defect sites. While electron irradiation is exercised for defect creation, it predominately leads to mono-sulfur and disulphur vacancies in TMDs.^{95,145,225} In this study, exploiting the higher mass of energetic ions, we are able to generate single atom vacancies in monolayer TMDs using ion irradiation. Previously, we have also demonstrated ion irradiation as a method of fabricating sub-nm pores in MoS₂ for ionic transport through nanoporous membranes.¹⁹⁰

As of now, there is a relatively poor correspondence between ion irradiation experiments and theory in 2D materials.^{48,99,190,199,223} One likely reason for these discrepancies is the inadequate understanding of experimental parameters. For example, material contamination has been ubiquitously reported after ion irradiation and while it plays a significant role in analytical and structural characterization, such “substrates” are rarely accounted for in theoretical simulations.^{14,143,184,190,199,200} Similarly, Surwade *et al.* demonstrated that water transport properties in nanoporous graphene with defects produced from electron and ion irradiation result in negligible water flux while defects from oxygen plasma etching exhibit rapid water transport, despite identical Raman spectra from the two defect creation techniques.¹⁸³ We speculate that this difference in filtration performance may result from the lack of thorough information of FIB operation on 2D materials. FIBs were developed with a primary focus for material fabrication and ablation to produce micro-structures, and therefore their usage on 2D materials is still unconventional and underdeveloped. For example, traditional Stopping Range/Transport of Ions in Matter (SRIM/TRIM) software²³⁷ is widely used to replicate FIB-based micro-manufacturing/doping in bulk materials, but its approach of binary-collision approximation treats 2D materials as an amorphous material with no regard to atomic crystallinity and thus produces inaccurate results.^{99,105, 119,139}

In this report, we investigate the effects of FIB irradiation on the structural, optoelectronic, and phononic properties of monolayer TMDs. Aberration-corrected scanning transmission electron microscopy (AC-STEM) along with scanning electron microscopy (SEM) provide information into a tenable irradiation mechanism and feature properties of fabricated defects with sizes over three orders of magnitude from ~ 0.1 nm (atomic vacancies) to 50-

nm-large holes. Irradiated TMD materials appear less contaminated than graphene systems due to less reactive defect sites, which allows for consistent defect creation and analysis over comparatively large, mm-length scales across different samples. Characteristics of the irradiated membranes such as defect density percentage and average defect size are also quantified and reported as a function of TMD material, supporting substrate, and irradiation dose. Raman and photoluminescence (PL) spectroscopy results demonstrate macro-scale changes in material properties due to FIB irradiation.

3.3 Fabrication of Angstrom-Size Pores Devices using Gallium Ion Beam

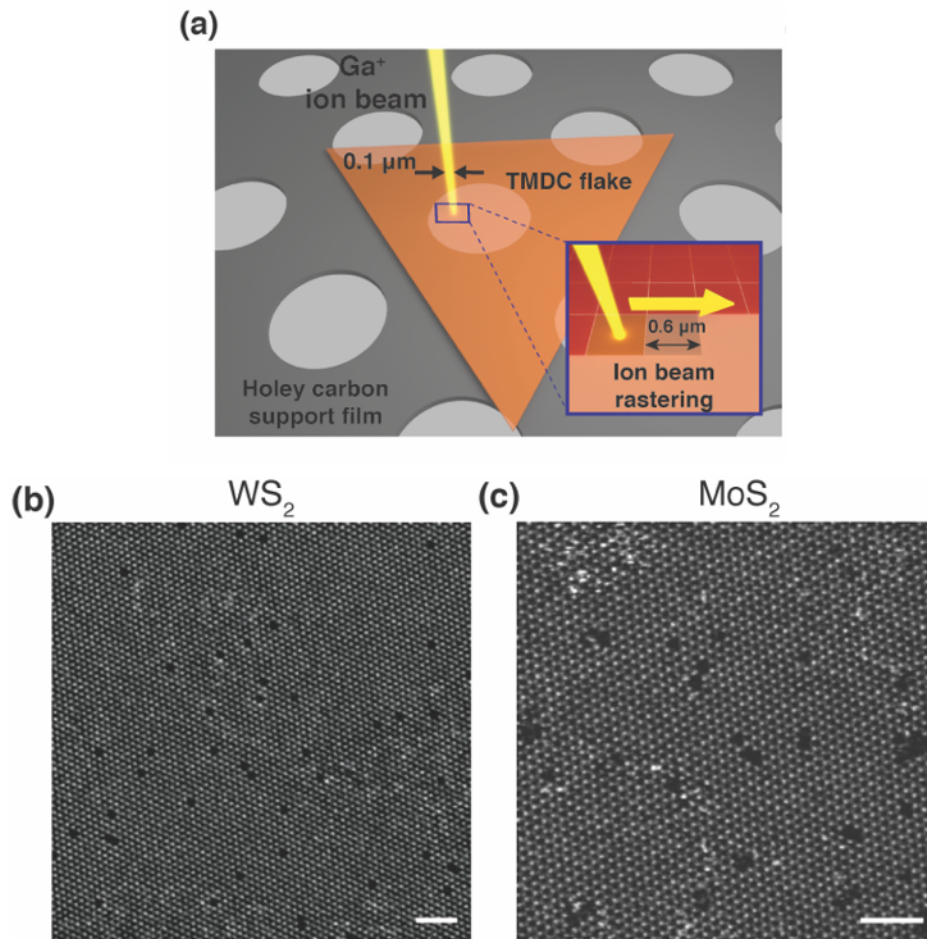


Figure 3.1. Irradiation mechanism and HAADF images of monolayer TMD flake

Graphic of pixel-by-pixel irradiation mechanism on a monolayer TMD flake (orange) suspended over 1-micron diameter holes using a focused Ga⁺ ion beam (yellow). The inset illustrates the raster pattern of the FIB. HAADF AC-STEM images of suspended monolayer (b) WS₂ and (c) MoS₂ flakes after FIB irradiation with doses of 1.5×10^{14} and 5.1×10^{13} ions/cm², respectively. Defects are recognized by the absence of contrast at lattice sites. Due to the Z-contrast behavior of HAADF imaging, the image intensity of S atoms is weaker compared to heavier Mo/W atoms. Scalebars in (b) and (c) denote 2 nm.

Figure 3.1 shows a schematic of the process used to irradiate monolayer TMDs. A TMD flake grown by chemical vapor deposition (CVD) is transferred through a chemical wet etch process (see the Experimental Section), suspended on a holey carbon substrate, and exposed to a 30 kV Ga⁺ focused ion beam that is incident normal to the sample. In our study, we use a combination of Raman spectroscopy (see Figure 3.3 and Figure 3.4 in the Section 3.4), PL spectroscopy (see Figure 3.4), and atomic resolution AC-STEM imaging (see Figures 3.1,3.3, and Figure 3.6 in the Section 3.4) to confirm the monolayer nature of our materials. These data are consistent with previous reports of monolayer TMDs.^{4,12,26, 32}

Exposure parameters and dose calculations are discussed later. Irradiated samples are first characterized through high-angle annular dark-field (HAADF) imaging, an AC-STEM technique by which mass contrast information of individual atomic positions is obtained, particularly well-suited to atomically thin 2D materials^{15,24, 190} Figure 3.1 b,c shows HAADF lattice image of WS₂ and MoS₂, respectively, that have been exposed to FIB irradiation with doses of 1.5×10^{14} and 5.1×10^{13} ions cm⁻², respectively. Within the hexagonal lattice structure, single-atom defects (i.e., vacancies) are identified by the absence of contrast at regularly spaced lattice positions. We focus here on transition metal sites due to the weak HAADF contrast of S atoms compared to heavier Mo/W atoms²³³ and

observe that defects with tunable densities and sizes down to a single atom can be engineered over millimeter-scale areas in TMDs (limited by the FIB exposure area). STEM imaging was performed at an acceleration voltage of 80 kV while focusing time and probe current were minimized (see the Experimental Section) such that transition metal defect fabrication from electron beam knock-on damage is expected to be negligible.^{95, 145}

3.3.1 Mechanism of Irradiation of TMDs using Focused Ion Beam

We first demonstrate the underlying mechanisms involved in the irradiation process and highlight certain features that are unique in the context of 2D materials. Ion beam exposure dose D for bulk materials is typically given as

$$D = \frac{It}{qA} \quad (1)$$

where I is the ion beam current, t is the total exposure time, q is the ion charge, and A is the exposure area.⁶⁹ In bulk materials, dose—i.e., the number of ions hitting the sample surface per cm^2 —is used as a measure of doping or implanting ions into a substrate.^{1, 65} However, this concept has been loosely borrowed for 2D materials where ions are used for defect creation^{55, 119, 190} and as shown later, fails to accurately account for the irradiated area since beam raster can cause nonuniform irradiation on materials at the nanoscale.

We suggest the following empirical formula that more accurately describes the direct-ion impact which can cause the spatial distribution of defects formed in 2D materials. This is given as

$$D = \frac{I_{beam}(t_a N_s)}{q} \quad (2)$$

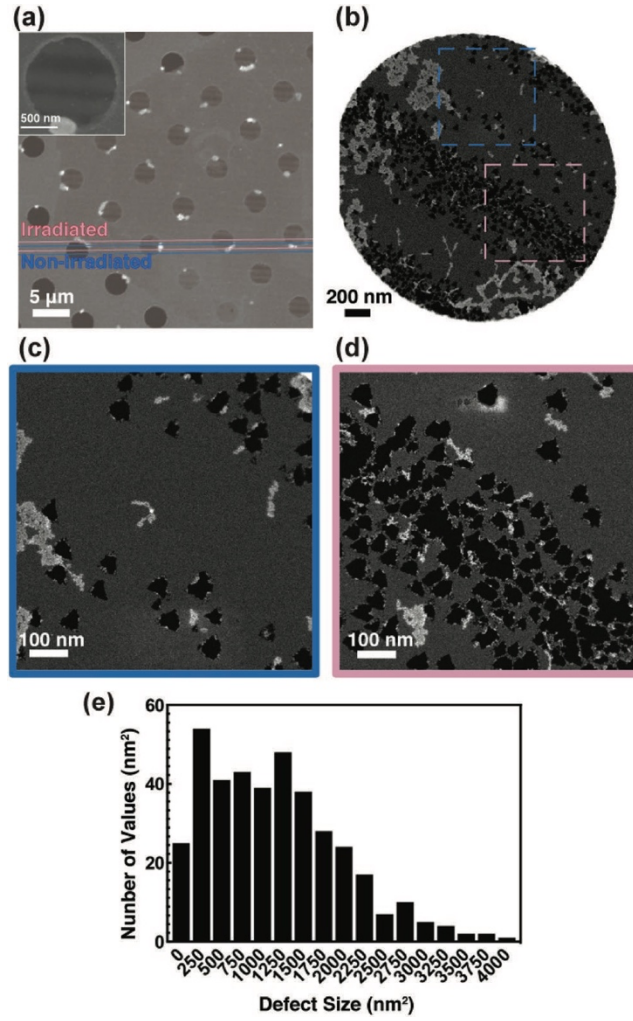


Figure 3.2. Mechanism of Irradiation of TMDs using Focused Ion Beam

a) SEM micrograph displaying the raster pattern caused by an ion beam at 4.3×10^{13} ions cm^{-2} ($t_d = 32 \mu\text{s}$ per pixel) with (inset) high resolution image of raster bands/strips on suspended monolayer WS_2 . b) TEM micrograph of suspended monolayer WS_2 irradiated with a dose of 5.3×10^{15} ions cm^{-2} showing varying defect density across a suspended WS_2 membrane of $2.5 \mu\text{m}$ diameter. c,d) Zoomed-in images of the two regions indicated in (b), clearly showing triangular tears caused by Ga^+ ion irradiation. e) Histogram of defects for suspended WS_2 samples exposed to 5.3×10^{15} ions cm^{-2} exhibiting average and median defect sizes of ≈ 1420 and 1140 nm^2 .

where t_d is the dwell time per pixel, N_s is the number of scans, and A_{beam} is the area of the ion beam spot. Compared to the bulk formula, total exposure time here is determined

by the number of repetitive scans, N_S , on each pixel. As in this study, N_S is applicable in techniques where imaging/rastering mode (or “grab frame”) capture is involved. We utilize an ion probe current of 10 pA and spot-size of 100 nm diameter (Figure 3.1a). Previous dose calculations^{1, 65} typically use Equation (1) where area A corresponds to the total area of all pixels in the imaging area. However, only a small region of each pixel is exposed to the ion beam. Therefore, our dose calculation (Equation (2)) only accounts for the area of the ion beam spot size (A_{beam}) that is irradiated within each pixel (see Figures 3.1a and 3.2b). To calculate the dose, we multiply the irradiated area by the number of times the beam scans over the surface of the sample. Using the total scan area (Equation (1)) gives a less accurate dose estimate because defects caused by ion irradiation in 2D materials are only created in irradiated regions and not across the whole sample surface that is scanned under the ion beam. Differences in dose calculations between Equations (1) and (2) can be found in Table 3.2 in the Section. In this study, scans are controlled with a resolution (n_p) of 416×416 pixels, pixel width of 600×600 nm, and dwell time (t_d) of ≈ 16 μs per pixel to irradiate a selected region of the suspended flake, unless otherwise specified.

Observation of these values and the corresponding dose calculation reveal the resolution at which the irradiation was conducted and the possible nonuniform spacing between defects. Figure 3.2a shows one such scenario where the raster pattern on a monolayer WS_2 flake is noticed as dark, irradiated (pink line) and bright, unirradiated (blue line) bands in a scanning electron micrograph. This is intuitive as the ion beam spot can be described as a Gaussian function whose maximum is incident at the center of each pixel.^{103, 129} With a set resolution, the FIB software divides the imaging area into a number of pixels over which

the beam will scan in a raster pattern. The pixel width, spot size, and overlap % of the ion beam play a significant role in decoding and mapping the pattern and spacing of defects on an irradiated sample. This is clearly demonstrated in the low-magnification HAADF image of FIB-irradiated monolayer WS₂ suspended over a 2.5 μm diameter hole in Figure 3.2b. Here, we observe linear bands of defective areas spaced ≈500 nm apart. This nonhomogeneous pattern corresponds to the raster mechanism of the FIB where the spacing between bands or stripes is controlled by the specified resolution (i.e., pixel width).

High-magnification images reveal that the individual holes or tears in the material are shaped as equilateral triangles with side lengths of ≈50 nm (area ≈1200 nm²) (Figure 3.2c). Single triangles coalesce into larger defects near band centers, where the middle of the Gaussian ion beam hits the sample (Figure 3.2d). Quantitative analysis of the defects (see the Experimental Section) yields average and median defect areas of ≈1420 and 1140 nm², respectively (Figure 3.2e).

3.4 Characterization of Atomic Defects in TMDs using Raman Spectroscopy and Aberration-Corrected Transmission Electron Microscopy (AC-TEM)

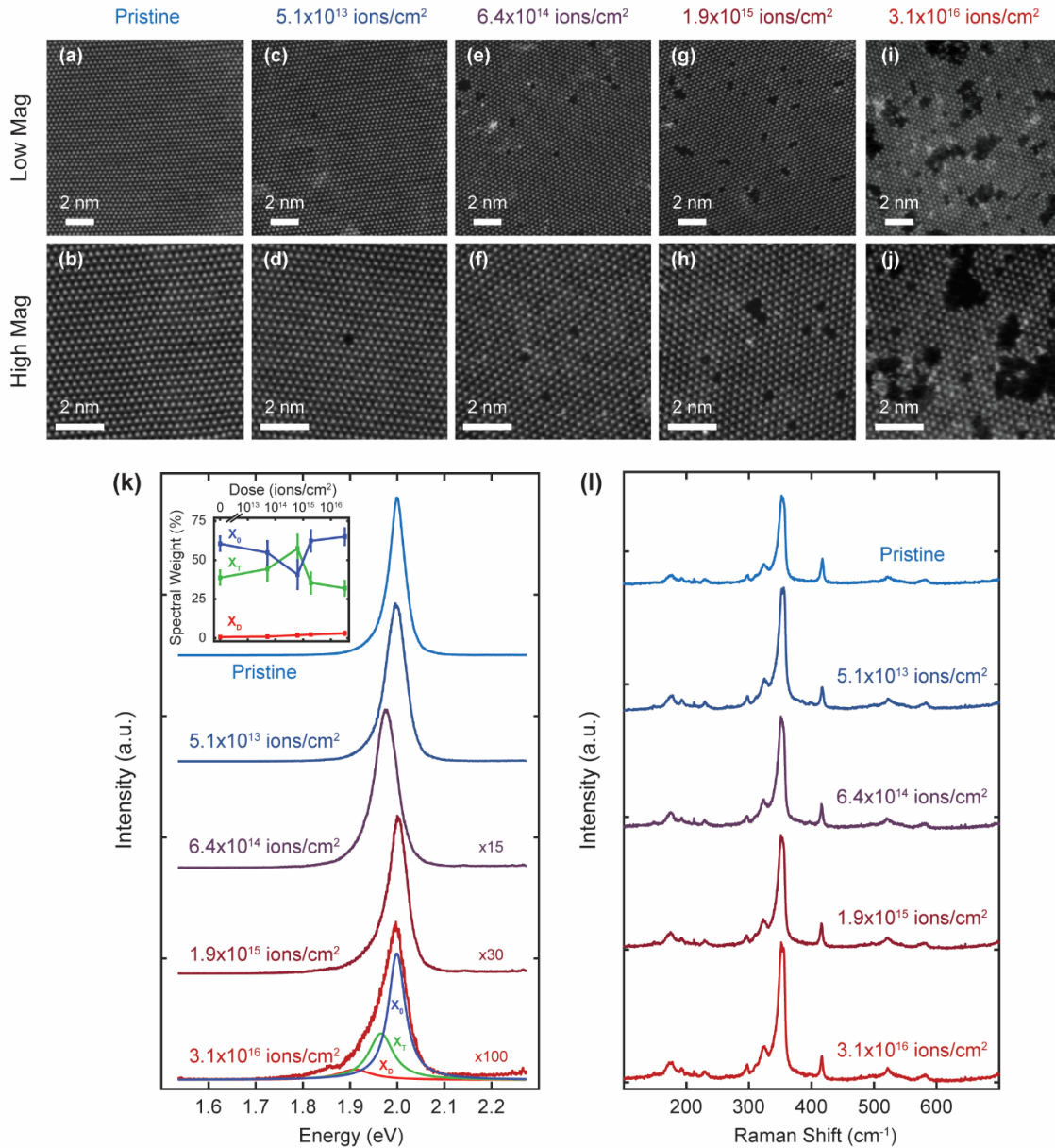


Figure 3.3. Characterization of atomic defects in TMDs using Raman Spectroscopy and Aberration-Corrected Transmission Electron Microscopy (AC-TEM)

(Top row) Low- and (bottom row) high-magnification HAADF AC-STEM images of suspended monolayer WS₂ exposed to Ga⁺ FIB irradiation with doses of (a-b) 0, (c-d) 5.1 × 10¹³, (e-f) 6.4 × 10¹⁴, (g-h) 1.9 × 10¹⁵, and (i-j) 3.1 × 10¹⁶ ions/cm². Quantitative analysis for all doses is provided in Figures 3.6 and 3.10. (k) PL spectra of FIB-irradiated WS₂ with

(inset) spectral weight percentage plot for the exciton (X_0 , blue), trion (X_T , green), and defect (X_D , red) peaks. (l) Raman spectra of FIB-irradiated WS_2 showing no change over the irradiation dose range (see also Figure 3.4).

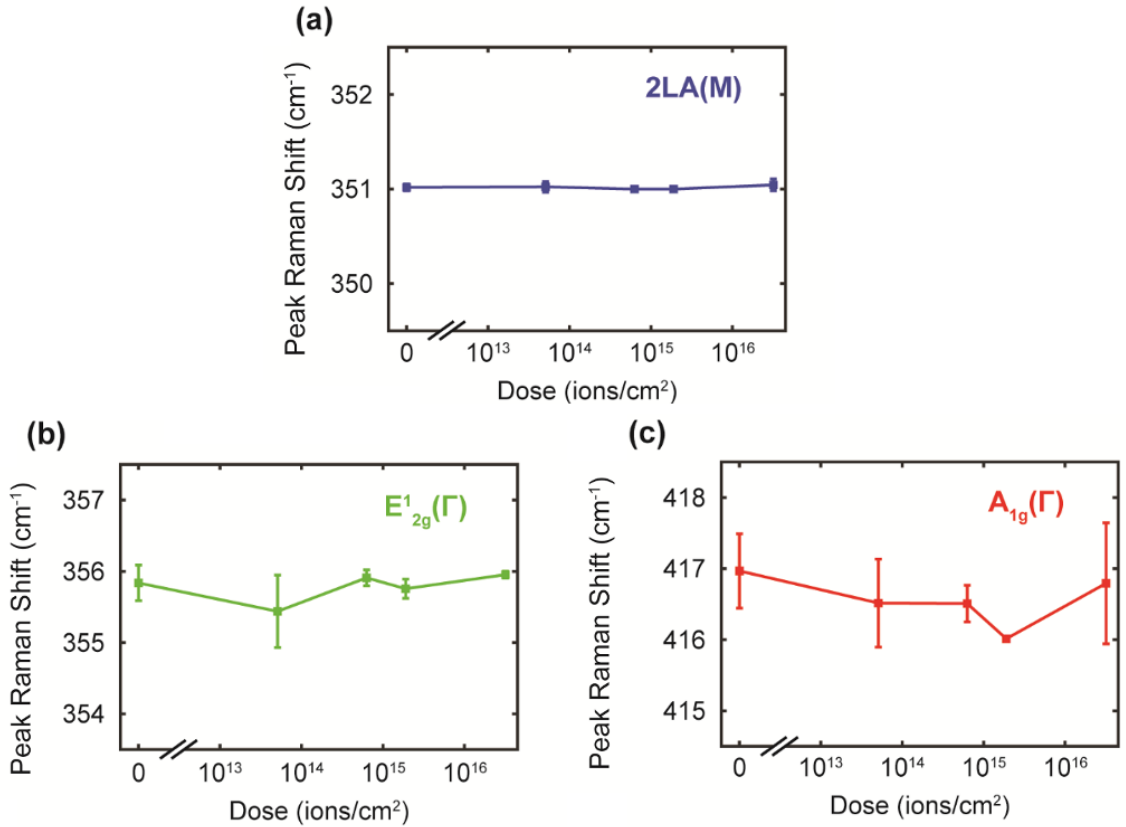


Figure 3.4 Raman peak shifts for suspended monolayer WS_2 exposed to FIB irradiation with doses between 0 and 10^{17} $ions/cm^2$

Raman spectra (shown in Figure 3.2) were fit to three phonon modes: (a) second-order longitudinal acoustic $2LA(M)$, (b) in-plane $E_{2g}^1(\Gamma)$, and (c) out-of-plane $A_{1g}(\Gamma)$ (see Experimental Section). No discernible peak shifts above the spectrometer resolution (0.5 cm^{-1}) were observed over the dose range studied here.

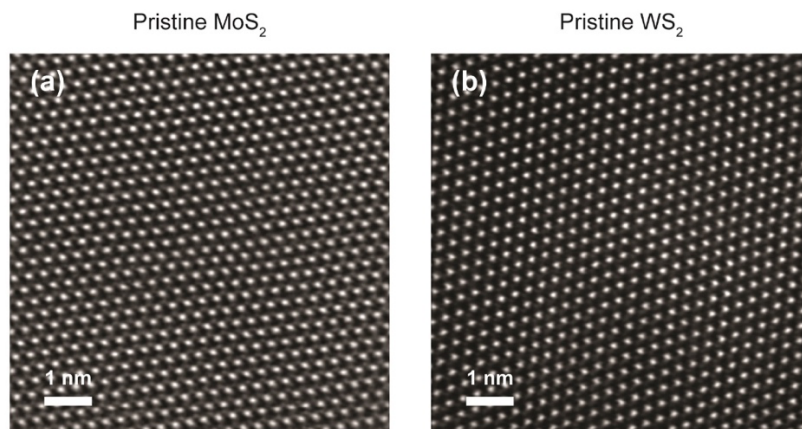


Figure 3.5. HAADF AC-STEM images of pristine monolayer MoS₂ and WS₂

HAADF AC-STEM images of pristine CVD-grown monolayer (a) MoS₂ and (b) WS₂ taken at 80 kV. Bright spots correspond to transition metal (Mo, W) atoms in a trigonal prismatic (2H) coordination with chalcogen (S) atoms.

We also probe the effects of varying irradiation dose D , achieved by retaining a constant dwell time per pixel, t_d , and changing the total number of FIB raster scans, N_s . In addition to pristine material (Figure 3.5), irradiation doses ranging over three orders of magnitude from 5.1×10^{13} to 3.1×10^{16} ions cm^{-2} are studied. Figure 3.3 shows a series of low-magnification (top row) and high-magnification (bottom row) HAADF AC-STEM images of variably irradiated suspended monolayer WS₂ membranes. A low degree (5.1×10^{13} ions cm^{-2}) of irradiation results in the appearance of single transition metal atom defects (Figure 3.3 c,d). Larger levels of FIB irradiation (6.4×10^{14} – 1.9×10^{15} ions cm^{-2}) show a denser distribution of single atom to sub-nanometer defects (Figure 3.3e–h). The atomic configuration of these defects is described later in Figure 3.9. We note observable defect areas of ≈ 0.10 , ≈ 0.14 , and ≈ 0.27 nm^2 for V(1W+6S), V(2W+2S), and V(3W+12S), respectively.

Quantitative analysis for all doses is provided in Figure 3.6 and Figure 3.10 in section 3.4. Under an order of magnitude higher dose 3.1×10^{16} ions cm^{-2} , the membrane begins to display larger, nanometer-scale defects (Figure 3.3 i,j). We note that unlike irradiated graphene, which becomes heavily contaminated due to the pinning of atmospheric impurities at defect sites,^{184,199} the exposed TMDs did not exhibit a noticeable increase in contamination until doses above 10^{16} ions cm^{-2} due to the presence of ablated material on the membrane. This suggests that defects in TMDs are less chemically reactive than defects in graphene, which can facilitate consistent structural characterization across samples and over large length scales. Above 3.1×10^{16} ions cm^{-2} , irradiated membranes were observed to be mechanically unstable and prone to collapse.³⁵

Moving from atomic- to bulk-scale properties, we utilize PL and Raman spectroscopy to characterize the effects of FIB irradiation on the optoelectronic and phononic structure of TMDs, respectively. Figure 3.3k shows the PL spectra (excitation wavelength = 532 nm) obtained from suspended monolayer WS_2 membranes exposed to FIB irradiation from 0 (pristine) to 3.2×10^{16} ions cm^{-2} . Spectra were fit to three characteristic WS_2 excitations: defect (X_D , 1.88 eV), trion (X_T , 1.96 eV), and exciton (X_0 , 2.02 eV).³⁵ The spectral weight percentage for each excitation as a function of irradiation dose is shown in the inset of Figure 3k. In particular, X_D exhibits a direct dependence on dose and monotonically increases from 0.7% in the pristine case to 3% for 3.2×10^{16} ions cm^{-2} . This is similar to the case of plasma-irradiated WS_2 , in which X_D increases up to 40% as a function of plasma exposure.³⁰ However, unlike plasma-etched WS_2 , where X_T steadily decreases with exposure time, FIB-irradiated WS_2 experiences a peak (57%) in X_T at 6.4×10^{14} ions cm^{-2} .

², which results in redshift of the PL signal. Similarly, X_0 is lowest (41%) at this dose. This suggests that X_T and X_0 are not sensitive to atomic defects (i.e., sub-nanometer defects do not induce doping). We attribute this peak in X_T at 6.4×10^{14} ions cm^{-2} to the presence of substitutional dopants in suspended WS_2 at this dose (see Figure 3.7 in the Section 3.4.2). The origin and effect of these substitutional dopants that appear in AC-STEM images in place of W atoms are being studied extensively as a part of a separate work. We are currently not able to confidently attribute their origin to a specific step during sample growth or subsequent handling.

We also note that with increasing FIB irradiation, PL peak intensity decreases monotonically by roughly two orders of magnitude for both monolayer WS_2 and MoS_2 .¹⁹⁰ Although further analytical TEM studies are needed, the PL intensity decrease observed here suggests that FIB irradiation likely produces mainly transition metal defects rather than chalcogen vacancies, because chalcogen vacancies were previously found to cause an increase in PL intensity, opposite from what we measure.^{24,197}

In addition to PL, Raman spectroscopy is widely implemented to characterize vibrational modes within 2D materials and has previously been used to analyze He⁺, Ne⁺, Mn⁺, and Ga⁺-irradiated MoS_2 . Figure 3.3 exhibits the Raman spectra for FIB-irradiated WS_2 for the corresponding doses in Figure 3k. Spectra were normalized and fit to characteristic WS_2 vibrational modes, in particular the second-order longitudinal acoustic 2LA(M), in-plane $E^{12}_g(\Gamma)$, and out-of-plane $A_{1g}(\Gamma)$ modes (Figure 3.4).^{15, 132} Over the irradiation dose range measured here, we do not observe any changes or significant shifts in the Raman

spectra. This has also been reported in plasma-irradiated WS₂ under the same excitation (532 nm) by Chow et al. and implies that the primary phonon modes in WS₂ are not sensitive to defects at this wavelength.

While several low-frequency peaks do appear, we similarly did not see changes in the E_{12g}(Γ) and A_{1g}(Γ) modes of FIB-irradiated MoS₂.¹⁹⁰ This is consistent with previous reports, which only observe peak shifts in highly defective MoS₂,^{119,131} and suggests that sub-nm defects with low densities (< 1%) do not affect the Raman spectra of monolayer MoS₂.

Due to the versatility of FIB instrumentation, irradiation can be performed on a wide range of substrates and materials under a variety of conditions. Here, we investigate the role of the underlying substrate on the resulting structural and defect characteristics of different monolayer TMD materials. Figure 3.3 a,b shows schematically the substrate-supported irradiation and characterization process. CVD-grown TMD flakes were exposed to 5.1×10^{13} ions cm⁻² FIB irradiation while sitting on a Si/SiO₂ substrate, transferred to a holey carbon film using a wet etch process, and imaged using HAADF AC-STEM (see the Experimental Section for more details). Figure 3.3 c,d exhibits the obtained AC-STEM images for MoS₂ (blue) and WS₂ (red) flakes, respectively. Figure 3.3 e,f shows corresponding images for flakes that were exposed to the same irradiation dose (5.1×10^{13} ions cm⁻²) while suspended on a holey carbon film (Figure 1a).

3.4.1 Nanopatterning on Suspended and Supported TMDs Substrate

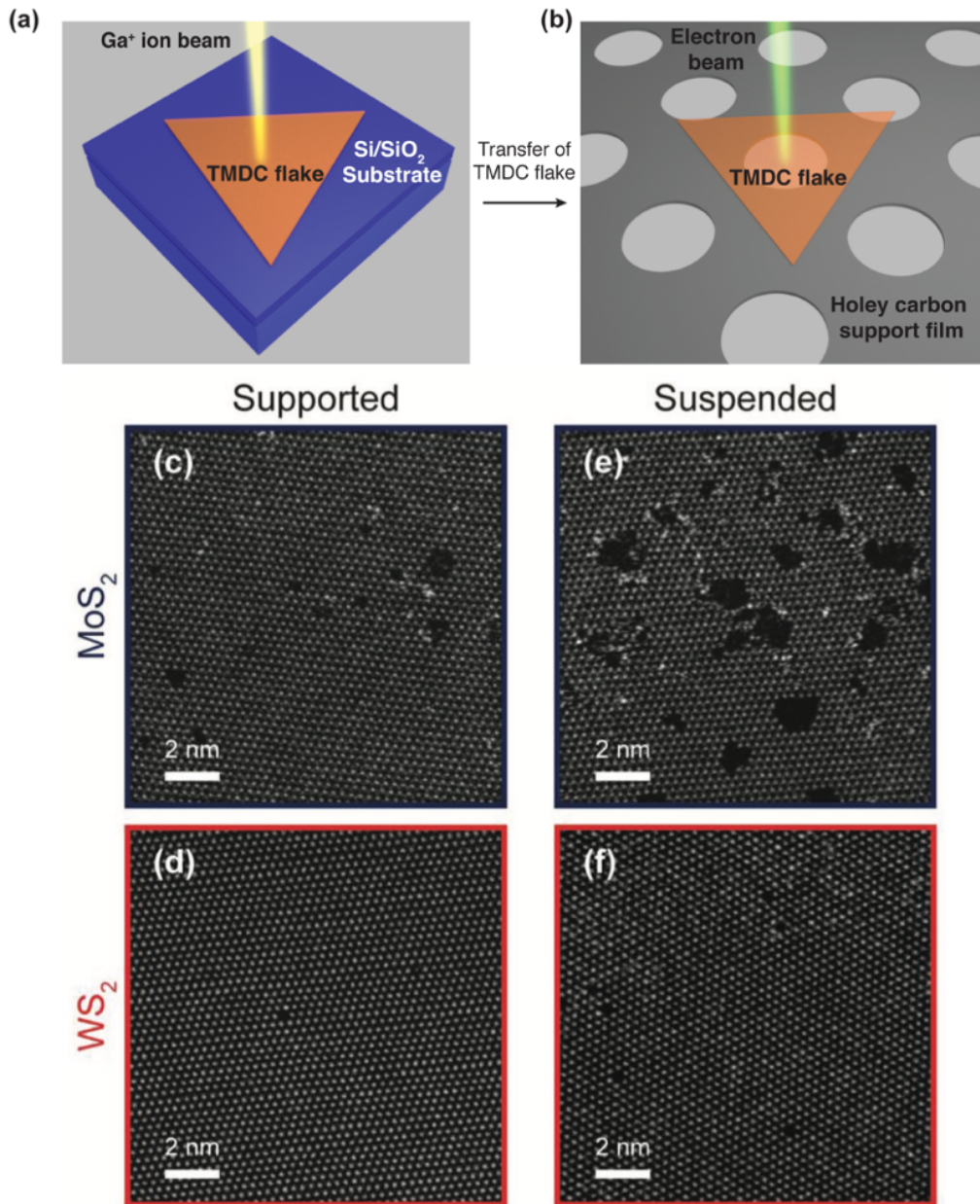


Figure 3.6. Nanopatterning on Suspended and Supported Substrate

a) Schematic of the irradiation mechanism for monolayer TMDs supported on a Si/SiO₂ substrate using a focused Ga⁺ ion beam (yellow). b) After irradiation, samples are transferred onto holey carbon films and imaged using AC-STEM (electron beam, green). HAADF AC-STEM images of c) substrate-supported MoS₂, d) substrate-supported WS₂,

e) suspended MoS₂, and d) suspended WS₂ after exposure to FIB irradiation with a dose of 5.1×10^{13} ions cm⁻².

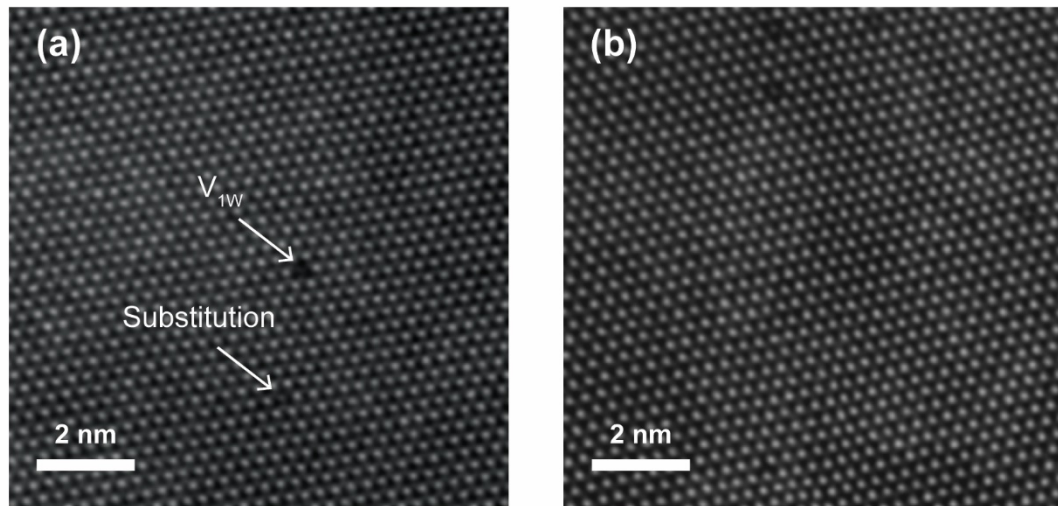


Figure 3.7 AC-STEM images of substitutional dopants.

AC-STEM images of substitutional dopants from (a) suspended WS₂ exposed to 6.4×10^{14} ions/cm² and (b) substrate-supported WS₂ exposed to 5.1×10^{13} ions/cm². Substitutions are primarily observed in samples at low irradiation doses (10^{13} - 10^{14} ions/cm²) and are not seen in pristine MoS₂ and WS_{2s} (Figure 3.5).

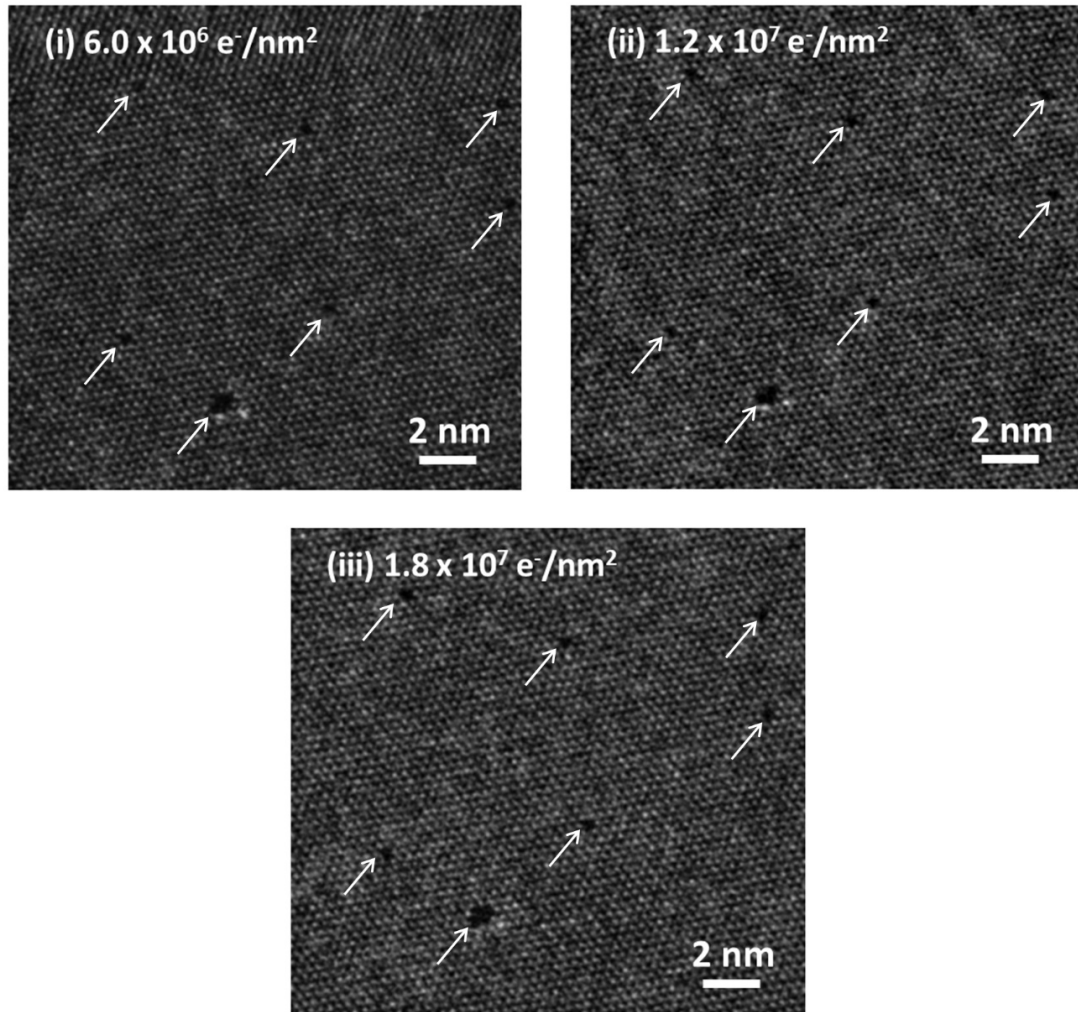


Figure 3.8. AC-STEM micrographs of FIB-irradiated ($6.4 \times 10^{14} \text{ ions/cm}^2$) monolayer WS₂ under constant imaging conditions (*i.e.*, STEM raster scanning).

Under electron doses of (i) 6.0×10^6 (1 scan), (ii) 1.2×10^7 (2 scans), and (iii) $1.8 \times 10^7 \text{ e}^-/\text{nm}^2$ (3 scans), existing defects (white arrows) did not expand or migrate, suggesting negligible electron beam-induced radiation damage during imaging. This study utilizes an acceleration voltage of 80 kV, STEM probe current of 22 pA, and imaging doses of $\sim 10^6 \text{ e}^-/\text{nm}^2$ (see Methods), which does not cause knock-on damage in monolayer TMDs.^{62, 145}

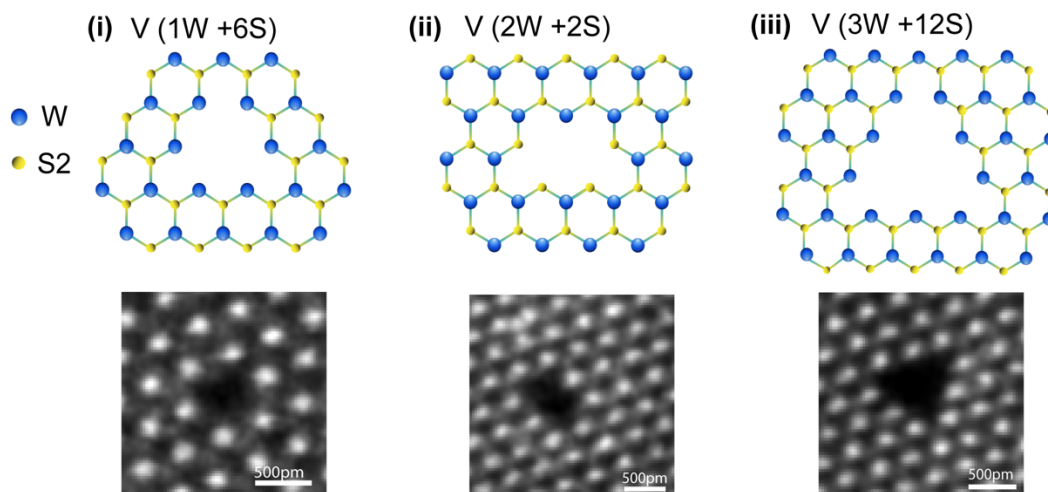


Figure 3.9. High magnification AC-STEM images of individual defects along with their observed atomic configuration.

The average areas of V(1W+6S), V(2W+2S), and V(3W+12S) are $\sim 0.1 \text{ nm}^2$, $\sim 0.14 \text{ nm}^2$, and $\sim 0.27 \text{ nm}^2$, respectively.

By sampling over multiple atomic resolution images (see the Experimental Section), we obtain values for average defect area and defect density, defined as the percentage of transition metal sites containing vacancies. The total image area analyzed for each sample configuration (total $\approx 10^5 \text{ nm}^2$) is listed in Table 3.1 in the Section 3.4.2 while histograms of defect sizes for MoS₂ and WS₂ are given in Figures 3.11 and 3.12 in the Section 3.4.2, respectively.

The application of different TMD materials and substrates offers additional methods of tuning defect properties. For example, under an irradiation dose of $5.1 \times 10^{13} \text{ ions cm}^{-2}$, suspended monolayer MoS₂ (blue circles, Figure 3.8) has a defect density and average area of 1.2% and 0.28 nm^2 , respectively. These are significantly larger than the corresponding values of 0.08% and 0.12 nm^2 obtained for suspended WS₂. Similar trends are observed in supported materials and suggest that defects are more readily produced in MoS₂ compared

to WS₂ possibly due to its lower displacement threshold energy. The relationship between average defect area and defect density (%) is presented for substrate-supported and suspended monolayer TMDs exposed to FIB irradiation in Figure 3.9a. We measure that the average defect area increases to $\approx 1 \text{ nm}^2$, as the defect density increases to $\approx 10\%$.

Figure 3.8 also demonstrates that the presence of a substrate causes lower defect densities and average defect areas. For instance, suspended MoS₂ displays an average defect area of 0.28 nm^2 while supported MoS₂ (blue diamonds, Figure 3.6 g,h) has a lower value of 0.14 nm^2 under $5.1 \times 10^{13} \text{ ions cm}^{-2}$ irradiation. Likewise, the defect density of 0.007% for supported WS₂ (red diamonds, Figure 4g,h) at this dose is an order of magnitude smaller than 0.08% for suspended WS₂. We note that while supported WS₂ demonstrates a low defect density due to the occurrence of FIB-induced substitutional dopants (see Figure 3.7), it displays an average defect area (0.08 nm^2) that is consistent with the size of a single transition metal vacancy (0.07 nm^2). In other words, for the same irradiation dose of $5.1 \times 10^{13} \text{ ions cm}^{-2}$, we obtain single-atom defects in case of WS₂ and larger defects ranging from 0.05 to 0.4 nm^2 in the case of MoS₂ (see Figures 3.11 and 3.12 in the Section 3.4.2). This effect of larger defects in MoS₂ compared to WS₂, for a given dose is consistent for both suspended and supported material.

Recent simulations with kV-range Ne⁺ and Ar⁺ ion irradiation of MoS₂ suggest that in addition to direct sputtering, further defects in supported MoS₂ are created due to backscattered ions and atoms sputtered from the substrate.^{99, 119} However, this is not expected for heavier ions such as Ga⁺. This is consistent with the fact that we do not see larger/denser defects in supported materials and also shows that direct ion sputtering is more dominant than substrate-induced defects in Ga⁺-irradiated TMDs. While FIB

irradiation enables defect engineering with tunable densities and sizes down to a single atom, further experimental and theoretical studies are needed in order to clarify the different mechanisms that result in defects as a function of ion composition, TMD material, and different sample architectures.

3.4.2 Statistical Image Analysis of Angstrom-Size Pores in TMDs

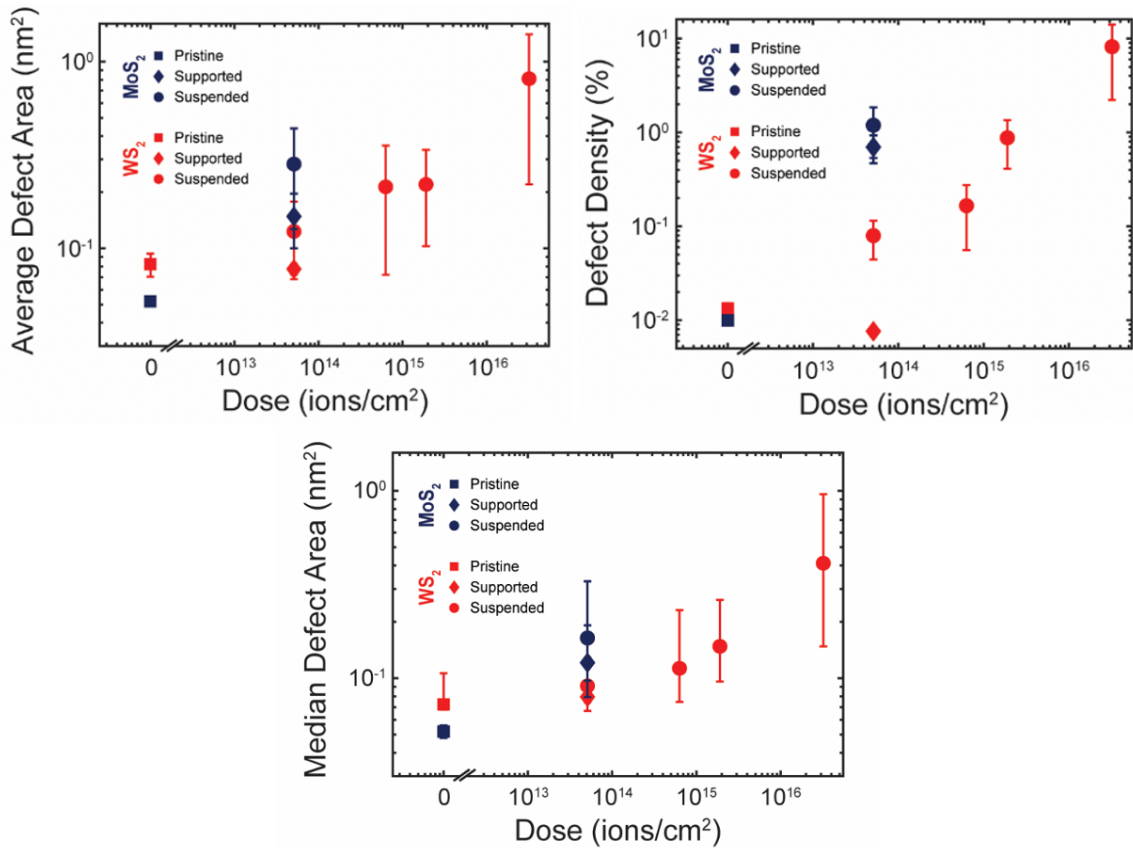


Figure 3.10. Statistical Image Analysis of Angstrom-Size Pores in TMDs

Summarized average defect area, defect density and median defect area values of (square) pristine, (diamond) substrate-supported, and (circle) suspended monolayer TMDs for irradiation dose values of 0, 5.1×10^{13} , 6.4×10^{14} , 1.9×10^{15} , and 3.1×10^{16} ions cm⁻². Results for MoS₂ and WS₂ are shown in blue and red, respectively. Pristine, substrate-supported, and suspended systems are represented by squares, diamonds, and circles, respectively.

Further statistics and histograms of individual defects are provided in figures below.

Error bars represent two quartiles above and below the median. Similar to defect density and average defect area, median defect areas are larger (i) at higher irradiation doses, (ii) in suspended systems, and (iii) in MoS₂ (compared to WS₂). The results for different FIB exposure conditions including irradiation dose (see Figure 3.7), underlying substrate, and TMD material are summarized in Figure 3.8. A direct dependence of defect density (Figure 3.8 right), average defect area (Figure 3.8 left), and median defect area (Figure 3.8, bottom) on irradiation dose is observed. For example, suspended WS₂ (red circles, Figure 3.8) has defect densities of $\approx 0.01\%$, 0.08% , 0.2% , 0.9% , and 8% for increasing irradiation doses of 0 , 5.1×10^{13} , 6.4×10^{14} , 1.9×10^{15} , and 3.1×10^{16} ions cm⁻², respectively. Such increases in defect area and density are expected due to the creation of new defects as well as the enlargement of existing defects as the number of raster scans (N_S) across the sample increases.

Sample Type	FIB Exposure Dose (ions/cm²)	AC-STEM Imaged Area (nm²)
Pristine MoS ₂	0	1.56×10^3
Substrate-Supported MoS ₂	5.1×10^{13}	3.56×10^3
Suspended MoS ₂	5.1×10^{13}	1.66×10^4
Pristine WS ₂	0	2.47×10^3
Substrate-Supported WS ₂	5.1×10^{13}	4.07×10^3
Suspended WS ₂	5.1×10^{13}	1.69×10^4
Suspended WS ₂	6.4×10^{14}	2.29×10^4
Suspended WS ₂	1.9×10^{15}	4.28×10^4
Suspended WS ₂	3.1×10^{16}	2.94×10^4

Table 3.1. Total imaged area of atomic resolution HAADF AC-STEM micrographs.

Total imaged area of atomic resolution HAADF AC-STEM micrographs used to calculate defect density, average defect area, and median defect size for various suspended and

substrate-supported TMDs. A description of the analysis procedure can be found in the **Experimental Section**. Defect histograms for each listed sample are shown in Figures 3.11-3.12 while summarized results are given in Figures 3.6 and 3.10.

Sample Type	Equation (1): $D = \frac{It}{qA}$ (ions/cm ²)	Equation (2): $D = \frac{I t_d N_s}{q A_{beam}}$ (ions/cm ²)	Defect Density (sites/cm ²)
Pristine MoS ₂	0	0	1.1×10 ¹¹
Substrate-Supported MoS ₂	1.1×10 ¹²	5.1×10 ¹³	7.9×10 ¹²
Suspended MoS ₂	1.1×10 ¹²	5.1×10 ¹³	1.4×10 ¹³
Pristine WS ₂	0	0	1.5×10 ¹¹
Substrate-Supported WS ₂	1.1×10 ¹²	5.1×10 ¹³	8.6×10 ¹⁰
Suspended WS ₂	1.1×10 ¹²	5.1×10 ¹³	9.0×10 ¹¹
Suspended WS ₂	1.4×10 ¹³	6.4×10 ¹⁴	1.9×10 ¹²
Suspended WS ₂	4.2×10 ¹³	1.9×10 ¹⁵	9.9×10 ¹²
Suspended WS ₂	7.0×10 ¹⁴	3.1×10 ¹⁶	9.3×10 ¹³

Table 3.2. FIB irradiation dose calculations and defect densities from Equation (1) and Equation (2).

FIB irradiation dose calculations (columns 2-3) and defect densities (column 4) for pristine, suspended, and substrate-supported TMDs. As discussed in the main text, calculations using equation (1) are inaccurate for 2D materials and result in ion dose values an order of magnitude lower than defect densities (for example, see Suspended MoS₂). Equation (2) provides a more accurate dose estimate.

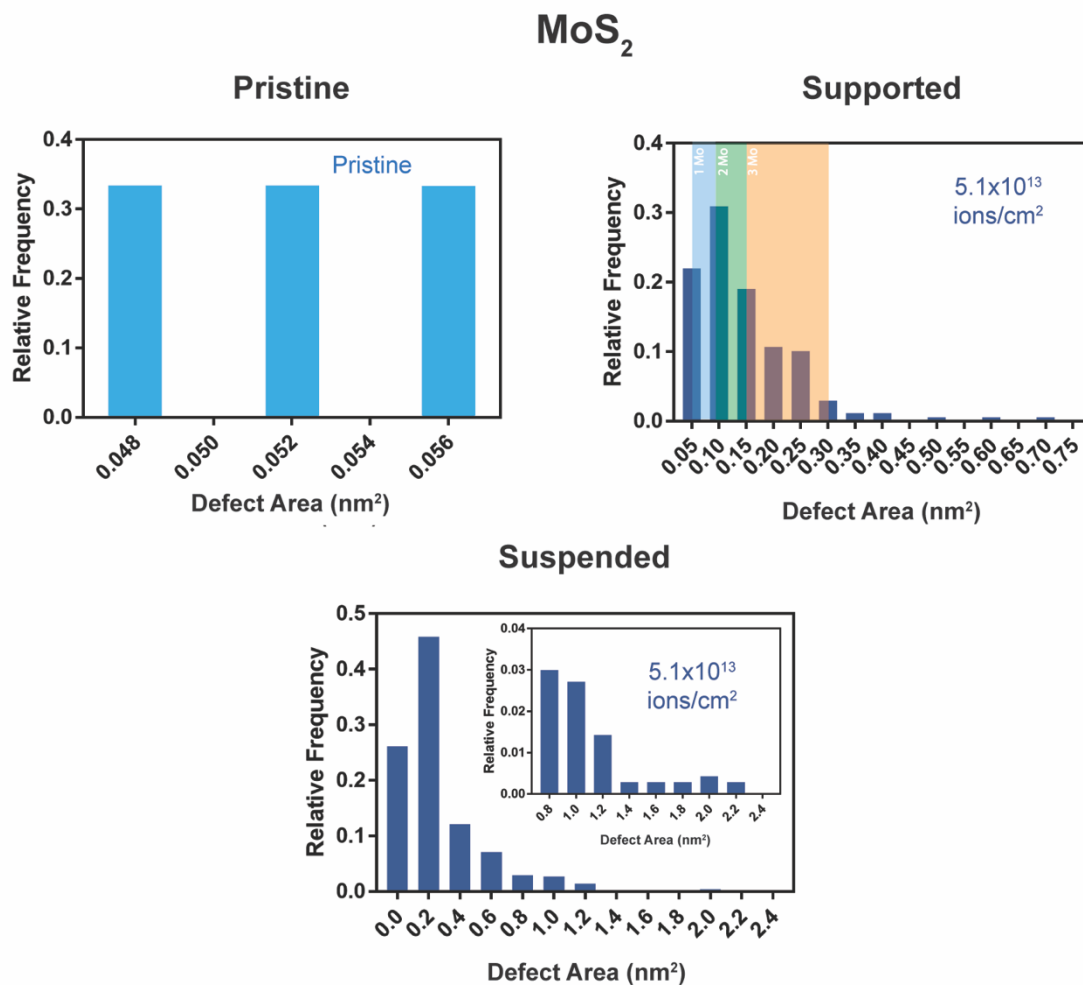


Figure 3.11. Statistical Image Analysis of irradiated MoS₂ on different substrates

Histograms of individual defects for MoS₂ under several irradiation conditions (see Figure 3.6) showing relative frequency of defect occurrence (sum normalized to one) as a function of defect area. Only defects above the size of a single transition metal atom (area > 0.05 nm²) are included due to AC-STEM resolution and contrast limits. Light blue, green and orange shading indicate the 1Mo, 2Mo and 3Mo defect types respectively. The inset in the bottom row is a zoom in of the larger defect area regime, showing a small proportion of somewhat larger defects (up to ~2.2 nm²).

WS₂

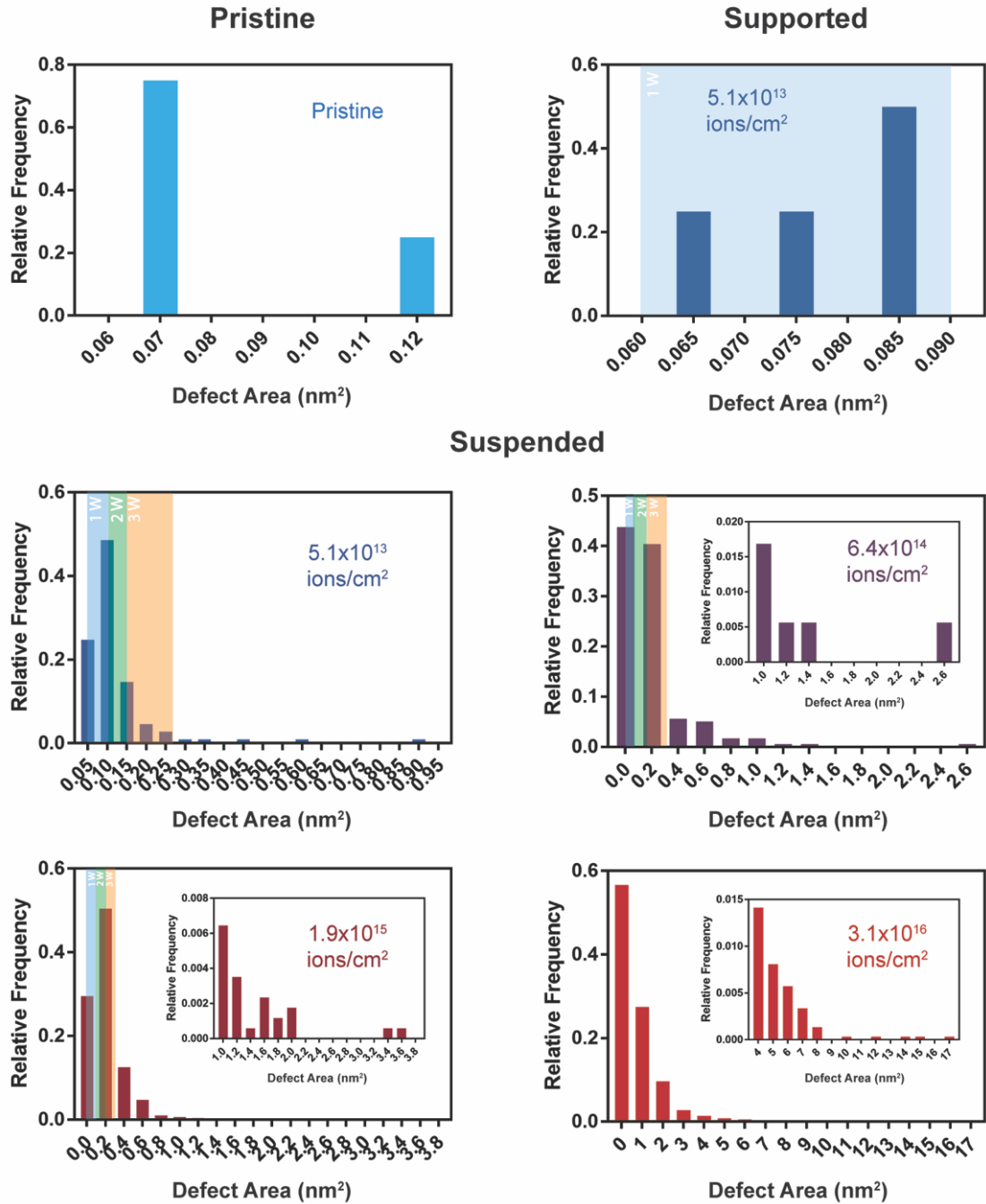


Figure 3.12. Statistical Image Analysis of irradiated WS₂ at various doses on different substrates

Histograms of individual defects for WS₂ under several irradiation doses (see Figure 3) and substrate conditions (see Figure 3.6) showing relative frequency of defect occurrence (sum normalized to one) as a function of defect area. Only defects above the size of a single

transition metal atom (area > 0.05 nm²) are included due to AC-STEM resolution and contrast limits. Light blue, green and orange shading indicate the 1W, 2W and 3W defect types respectively (as shown in Figure 3.9). The insets in the middle and bottom rows are zoom ins for the larger defect area regime, showing a small contribution of larger defects up to ~ 17 nm².

3.5 Additional Experimental Methods

CVD Growth:

Monolayer MoS₂ and WS₂ flakes were grown using CVD processes similar to previously reported methods.^{34,136} Solutions of 0.2 (2) % sodium cholate growth promoter and 18 (15) mM ammonium heptamolybdate (metatungstate) were spun onto piranha-cleaned Si substrates coated with 300 (150) nm of SiO₂, which were then loaded into the center of a 1-inch tube furnace (Thermo Scientific Lindberg/Blue M). For the MoS₂ growth, samples were heated under N₂ gas flow (700 sccm) at a rate of 70°C/min and held at 750°C for 15 minutes. For WS₂, samples were heated in Ar (100 sccm) at a rate of 65°C/min and held at 800°C for 10 minutes, during which time 15 sccm of H₂ was also added. Approximately 100 mg of sulfur precursor placed 22 cm from the substrates was kept at 180°C during the growth procedures. Both samples were rapidly cooled to room temperature by cracking open the furnace.

Device Fabrication:

WS₂ and MoS₂ crystals were transferred from Si/SiO₂ substrates to holey carbon TEM grids using a wet etch technique. Crystals were first coated with C4 PMMA while aqueous 1 M KOH solution was used to etch away the underlying substrate. After being washed in deionized (DI) H₂O, crystals were scooped onto TEM grids and dried for 30 minutes. Polymer liftoff and sample cleaning were performed using acetone and rapid thermal annealing in Ar:H₂ gas, respectively.

Gallium Ion Irradiation:

Monolayer TMDCs flakes were irradiated with a Ga⁺ sourced ion beam FEI Strata-Dual Beam instrument. The acceleration voltage of the ion beam was set to 30 kV and incident normal to the surface. The beam spot size was observed to be 100 nm for a flash second at 10 pA current. In order to produce atomic defects, an area of 250 × 250 μm was irradiated with the dwell time (16 μs), current (10 pA) and pixel resolution (1024 × 884) kept constant. The exposure is carried out in an imaging mode which follows a raster pattern where the beam sequentially exposes each pixel in a row. *FEI FIB Strata DB 235* has an option to ‘grab frame’ which takes a single scan at a set resolution, this option was employed for all our scans. The dose is varied by changing the number of scans. Suspended and substrate-supported samples were exposed to FIB irradiation while sitting on holey carbon TEM grids and Si/SiO₂ substrates, respectively.

AC-STEM Imaging:

MoS₂ and WS₂ samples were imaged using a Cs-corrected JEOL ARM 200CF STEM operating at 80 kV. Images were obtained using a HAADF detector with a collection angle of 54-220 mrad and 10 cm camera length. Probe current (22 pA), focusing time (< 2 s), and electron dose (~ 6.0 × 10⁶ e⁻/nm²) were kept low to minimize beam-induced knock-on damage (see Table 3.1).^{62,145}

AC-STEM Image Analysis:

All images from various doses were analyzed using Fiji or ImageJ software.¹⁶⁵ Custom macros were built for studying large number of files. Since images for doses of 1.9 × 10¹⁵ and 3.1 × 10¹⁶ ions/cm² consisted of large/nanoporous defects, a repeatable macro was used to calculate the number of defects (see Supplementary Information of Ref. 8 for

more details). In order to reduce noise and increase visibility of the atoms ImageJ was used, a Gaussian blur filter with 0.03 nm of blurring radius was applied. Prior to defect counting from AC-STEM images, further noise reduction was applied using the “Remove Outliers” process. At this point AC-STEM signal from sulfur atoms were spread. Cleaned images were then subjected to the “Local Threshold” process with the Sauvola method to obtain binary images which consist of black-colored defect regions and white-colored TMD regions. Statistical analysis of the defect area and the number of defects were carried out using these binary images.

Images for doses of 0, 5.1×10^{13} , and 6.4×10^{14} ions/cm² primarily consisted of smaller/single-atom defects such that filters, and noise reduction tools were utilized as required by each image. The core procedure for image analysis remained the same as above. Overall, a Gaussian blur filter (radius = 0.03 to 2 nm) was applied to increase the signal of the transition metal atom. The sulfur site vacancy and sulfur defects were ignored due to lack of contrast caused by polymer contamination. Additional noise reduction tools such as “background subtraction” were employed if the resultant image yielded better contrast. The goal was to count the individual defect sizes (~ 0.06 nm², single W defect) from each image using “Analyze Particle” in ImageJ.

Raman & PL Spectroscopy:

Raman and PL spectra from multiple pristine and FIB-irradiated samples were obtained in an NTEGRA Spectra system with 532 nm excitation and CCD detector. Raman measurements were acquired with an 1800 lines/mm grating while PL spectra were attained under a 150 lines/mm grating. Raman data (intensity vs. Raman shift) for monolayer WS₂ were fit to three vibrational Lorentzian modes: 2LA(M) at 350 cm⁻¹, E¹_{2g}(Γ) at 356 cm⁻¹,

and $A_{1g}(\Gamma)$ at 418 cm^{-1} .^{15,132} PL data (intensity vs. energy) was fit to three excitations: defect (X_D) at 1.88 eV, trion (X_T) at 1.96 eV, and exciton (X_0) at 2.02 eV.³⁰

3.6 Summary

In conclusion, we studied the effects of ion beam irradiation on the atomic structure and properties of monolayer TMDs and demonstrated how an industry-prevalent tool can be used to fabricate single atom defects over mm-scale areas. In addition to ion beam current and exposure time, we have highlighted the importance of other overlooked parameters such as magnification/resolution, dwell time, and exposure technique under which the FIB irradiation is performed since this directly dictates the spatial distribution of defects, especially in 2D materials. It is important for future studies to recite the specifications of their ion irradiation parameters as presented in this study for any potential reproducibility and comparison. Using a precise set of parameters, we created defects with tunable sizes and densities over several orders of magnitude in MoS_2 and WS_2 for different sample configurations (*i.e.*, suspended vs. substrate-supported) across irradiation doses from 10^{13} - 10^{16} ions/cm². SEM and AC-STEM revealed that average defect areas and densities were larger in suspended materials and in MoS_2 compared to WS_2 . Raman spectroscopy under a 532 nm excitation revealed little to no variations in the phononic structure of FIB-irradiated TMDs while PL showed changes in the optoelectronic structure arising from increased defect states. The observations presented here promote future studies on utilizing defects for a thriving variety of potential applications in TMDs ranging from nanoporous membranes for gas and fluid transport to newly emerging ideas of quantum information processing.

4 Angstrom-Size Nanoporous Membrane Creation in MoS₂ and Ionic Transport

4.1 Introduction

Atomic defect engineering in thin membranes provides opportunities for ionic and molecular filtration and analysis. While molecular dynamics (MD) calculations have been used to model conductance through atomic vacancies, corresponding experiments are lacking. We create sub-nm vacancies in suspended single-layer molybdenum disulfide (MoS₂) via Ga⁺ ion irradiation producing membranes containing ~ 300 to 1200 pores with average and maximum diameters of ~ 0.5 nm and ~ 1 nm, respectively. Vacancies exhibit missing Mo and S atoms, as shown by aberration corrected scanning transmission electron microscopy (AC-STEM). The longitudinal acoustic band and defect-related photoluminescence were observed in Raman and PL spectroscopy, respectively. As the irradiation dose is increased, the median vacancy area remains roughly constant, while the number of vacancies (pores) increases. Ionic current versus voltage is nonlinear and conductance is comparable to that of ~ 1-nm-diameter single MoS₂ pores, proving that the smaller pores in the distribution display negligible conductance. Consistently, MD simulations show that pores with diameters < 0.6 nm are almost impermeable to ionic flow. Atomic pore structure and geometry, studied by AC-STEM, are critical in the sub-nanometer regime where the pores are non-circular and the diameter is not well-defined. This study lays the foundation for future experiments to probe transport in large distributions of angstrom-size pores.

The results presented here were published in the article "Angstrom-Size Defect Creation and Ionic Transport through Pores in Single-Layer MoS₂" by Thiruraman J.P. *, Fujisawa K. *, Danda G., Masih Das P., Zhang T., Bolotsky A., Perea-Lopez N., Nicoli A., Senet P., Terrones M., Drndić M., Nano Letters, 18 (3), 1651–1659

4.2 Background

Ionic and molecular transport through individual solid-state nanopores have been studied thanks to the ability to fabricate nanometer scale holes in thin membranes.²¹ In contrast, ionic transport through smaller, sub-nanometer (sub-nm) pores and nanoporous two-dimensional (2D) membranes has not yet been explored in detail, although these systems present fascinating opportunities to study phenomena at the atomic scale. Most studies infer the conductance and sub-nm pore diameters indirectly from modeling.^{159, 72} With the recent availability of 2D materials¹¹² that can be suspended as membranes,¹³² and the ability to image atomic-scale defects,¹⁴⁵ it is now possible to study the fundamental principles behind ion flow through sub-nm pores⁷². A few recent papers have reported transport measurements in individual molybdenum disulfide (MoS₂) sub-nm pores.^{41, 43}

Thin nanoporous membranes containing large numbers of pores provide opportunities for fluid filtration, molecular analysis and energy generation. In water desalination applications, there is a demand for high-throughput, where atomic-scale pores (atomic vacancies in the material) provide unique benefits. This is because (i) water transport scales inversely with membrane thickness allowing for high water fluxes and (ii) membranes with sub-nm pores are highly selective.^{183, 209, 31, 32} Previous experiments explored ionic transport

in nanoporous graphene membranes.^{209,141,142} Heiranian et al. indicated the benefits of MoS₂ pores compared to graphene⁶⁵. To the best of our knowledge, there have been no studies of transport in nanoporous MoS₂ membranes.

4.3 Fabrication of Angstrom-Size Nanoporous MoS₂ Membranes

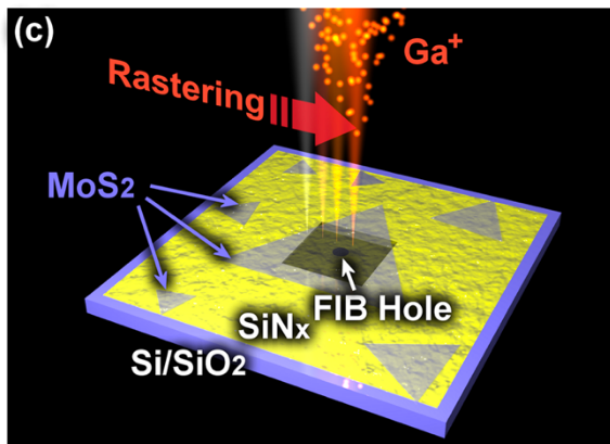


Figure 4.1. Irradiation of monolayer MoS₂ flake under controlled 30kV Ga⁺ ion beam.

Low-dimensional devices are fabricated for hosting a population of angstrom-sized pores and for further conducting ionic transport investigations. In this work, Single-layer MoS₂ triangular-flakes were synthesized via a halide-assisted powder vaporization method (Figure 4.1(a)).¹⁰⁸, transfer the 2D flake onto a substrate (carbon grid or SiN_x chip depending on the experimental procedure) (Figure 4.9, 4.10) and create angstrom-sized pores with the help of Focused Ion Beam. In addition, we also investigate the vacancy defects and the resulting properties of the suspended MoS₂ lattices using AC-STEM, Raman spectroscopy, and photoluminescence (PL) spectroscopy.

The presence of single-layer material was confirmed by fluorescence microscopy (Figure 1(b), 673 nm bandpass filtered). While single-layer MoS₂ shows strong

photoluminescence, the signal is quenched in multilayered MoS₂.¹⁷⁷ Similar to graphene,⁶⁶ polycrystalline MoS₂ fractures at grain boundaries under strain.³⁶ In order to maintain the rigidity of the material, we focused on single crystal MoS₂. Single-layer MoS₂ flakes were transferred onto carbon grids¹¹¹ or SiN_x¹³² using a PMMA-assisted transfer (Figure S1 and S2). Atomic vacancy-defects were introduced by rastering the Ga⁺ ion probe over a certain area (Figure 1(c)) using a focused ion beam (FIB).^{131,25} The degree of defectiveness was controlled by varying the Ga⁺ ion dose from 6.25×10^{12} ions/cm² (see S3) until the photoluminescence (PL) signal of the irradiated MoS₂ fell into noise level (2.50×10^{13} ions/cm²). After prolonged irradiation, the fluorescence signal was suppressed regardless of dose.

4.3.1 Raman and Photoluminescence Spectroscopy of Ga⁺ irradiated monolayer MoS₂ membrane

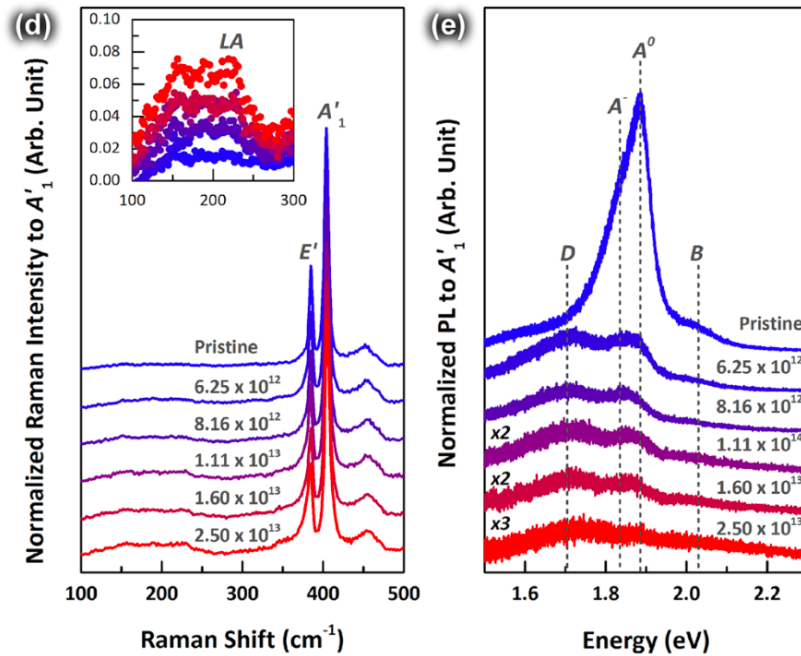


Figure 4.2. Raman and Photoluminescence Spectroscopy of Ga⁺ irradiated monolayer MoS₂ membrane

In the context of Raman and photoluminescence spectroscopy, we observe the longitudinal acoustic (LA) band and defect-related PL and determine the vacancy-defect size distribution as a function of Ga^+ ion irradiation dose, showing the median defect diameter in the range of 0.3–0.4 nm.

Single-layer MoS_2 triangular-flakes were synthesized via a halide-assisted powder vaporization method (Figure 4.1(a)).¹⁰⁸ The presence of single-layer material was confirmed by fluorescence microscopy (Figure 4.1(b), 673 nm bandpass filtered). While single-layer MoS_2 shows strong photoluminescence, the signal is quenched in multilayered MoS_2 .¹⁷⁷ Similar to graphene,⁶⁶ polycrystalline MoS_2 fractures at grain boundaries under strain.³⁶ In order to maintain the rigidity of the material, we focused on single crystal MoS_2 . Single-layer MoS_2 flakes were transferred onto carbon grids¹¹¹ or SiN_x ¹³² using a PMMA-assisted transfer (Figure 4.9 and 4.10). Atomic vacancy-defects were introduced by rastering the Ga^+ ion probe over a certain area (Figure 4.1(c)) using a focused ion beam (FIB).^{131,25} The degree of defectiveness was controlled by varying the Ga^+ ion dose from 6.25×10^{12} ions/cm² (see 4.11) until the photoluminescence (PL) signal of the irradiated MoS_2 fell into noise level (2.50×10^{13} ions/cm²). After prolonged irradiation, the fluorescence signal was suppressed regardless of dose.

The effect of Ga^+ ion irradiation on MoS_2 flakes was investigated by Raman spectroscopy and photoluminescence (PL) microscopy (panels d and e of Figure 4.2, respectively). After Ga^+ ion irradiation of the MoS_2 , several Raman peaks located around 200 cm⁻¹, in the vicinity of the longitudinal acoustic (LA) band emerged, whereas the first-order in-plane (E') and out-of-plane (A'_1) modes remained unaffected.¹³¹ The LA band consists of several

peaks including LA (\sim M), LA (\sim K) and a van Hove singularity at the saddle point between K and M point in the Brillouin zone.²⁵ Since these LA (\sim M) and LA (\sim K) modes far from Γ -point are only activated when defects are introduced into the MoS₂ lattice, their relative intensity with respect to the A'₁ mode ($I(\text{LA})/I(\text{A}'_1)$) can be used as an indicator of the degree of crystallinity.^{131,25} The relative intensity, $I(\text{LA})/I(\text{A}'_1)$ increased with higher Ga⁺ ion doses (see inset of Figure 4.2(d)), as expected.

The PL of the MoS₂ flakes was found to be sensitive to ion irradiation.¹⁹⁷ For pristine MoS₂, there were two peaks at 1.88 and 2.03 eV in the PL spectra, corresponding to the A and B exciton peaks. The A exciton peak was composed of two sub-peaks with energy at 1.88 eV (neutral exciton: A⁰) and 1.82 eV (trion: A⁻).¹²⁰ After Ga⁺ ion irradiation, the neutral exciton A⁰ was suppressed and a new peak: a bound exciton (D) located at \sim 1.72 eV emerged. This newly emerged photoemission peak can be correlated to defect-mediated radiative recombination processes.^{197, 30,24} The bound exciton peak is also observed when the MoS₂ is irradiated by α particles¹⁹⁷ and energetic plasma.³⁰ The spectral weight of the bound exciton peak becomes higher with increasing Ga⁺ ion dose similar to the relative intensity of the LA band, and at a dose of 2.5×10^{13} ions/cm², the PL intensity becomes close to the noise level. The enhancement of the LA band and the suppression of the neutral exciton reflect a qualitative increase of defectiveness (e.g., number and size of vacancies), within MoS₂ monocrystals after the Ga⁺ ion irradiation. However, upon the collision between an ion and an atom, several different types of defects including topological defects, atomic vacancies, holes and amorphous regions can form¹¹² depending on the ion species and their kinetic energy.⁴⁸ A quantitative study of vacancy-defects; such as type, density and edge termination of defects, is required but cannot be completed using

only the techniques above. In this context, Surwade et al. mentioned that even when similar optical signatures were observed in differently prepared defective graphene membrane, water transport properties of the membranes varied.¹⁸³

4.4 Electron Micrographs of Ga⁺ irradiated monolayer MoS₂ membrane

In 2D systems, the type of vacancy-defects introduced by ion irradiation changes depending on the ion characteristics and kinetic energy.^{119,224} For electron irradiation of MoS₂ using a parallel beam, mono-sulfur vacancies (V_S) and di-sulfur vacancies (V_{2S}) are predominant.^{145,25} With increased electron irradiation time, sulfur vacancies migrate and aggregate into line defects.⁹⁴ In contrast to electrons, the mass of an ion is larger and varies, resulting in ion-species dependent effects. Molecular dynamics (MD) simulations suggest that higher mass causes more displacement and sputtering of atoms.^{119,224} Direct observation of vacancy-defects created by Ga⁺ ion irradiation is needed in order to fully understand their characteristics.

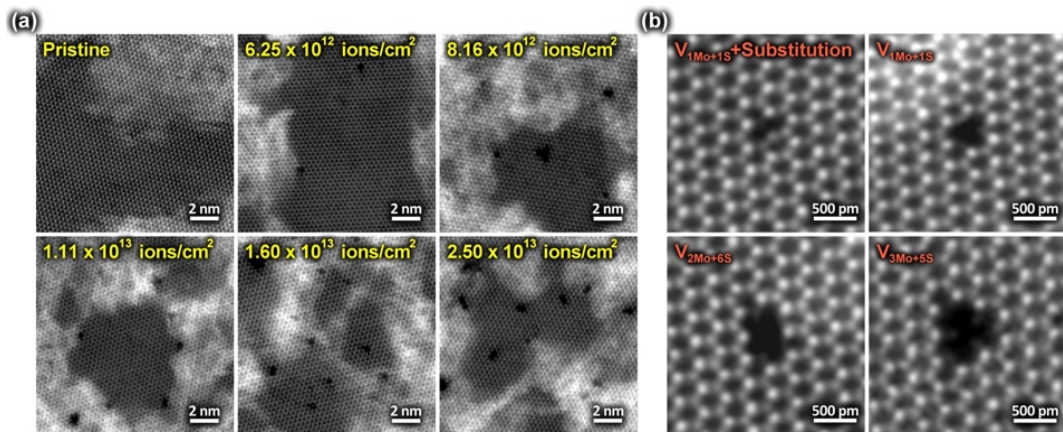


Figure 4.3. Aberration corrected scanning transmission electron microscopy (AC-STEM) characterization of single-layer MoS₂ showing an evolution of angstrom-size defects with Ga⁺ ion beam irradiation.

Ion irradiated MoS₂ membranes were investigated by aberration corrected scanning transmission electron microscopy (AC-STEM). Figure 4.3(a) shows high angle annular dark-field (HAADF) images of MoS₂ before and after Ga⁺ ion irradiation for different doses: 0 (pristine), 6.25×10¹², 8.16×10¹², 1.11×10¹³, 1.60×10¹³ and 2.50×10¹³ ions/cm². HAADF intensity changes depending on $\sim Z^2$ (Z: atomic number), allowing us to roughly distinguish elements (Mo or S) and therefore the atomic configuration of vacancy-defects. Figure 4.3(b) shows magnified STEM-HAADF images of several atomic vacancies. Metal atomic vacancies with several sulfur vacancies (V_{xMo+yS}) are formed rather than sulfur vacancies (V_S), topological defects (bond changing), or amorphous regions. This is consistent with expected sputtering behavior due to the relatively higher mass of Ga⁺ in comparison to electrons and leads to di-sulfur or mono-sulfur termination-rich edge structures.

4.4.1 Statistical Image Analysis of the Sub-nm size Pores using AC-STEM Images

In order to investigate the effect of the Ga⁺ ion dose on pore (i.e. vacancy-defect) area and density, statistical analysis was performed on AC-STEM images (see Figure 4.15). Within the irradiation dose ranges we used, the pore density increases with larger doses whereas the pore area remains roughly constant. For the lowest dose (6.25×10¹² ions/cm²), the majority of the atomic pores were single-molybdenum-based vacancies (V_{1Mo+yS}), while the number of missing sulfur varied. With increasing Ga⁺ ion dose, the number of double-molybdenum-based vacancy (V_{2Mo+yS}) increased and some triple-molybdenum-based vacancies were also found (V_{3Mo+yS}) (Figure 2(b)), exhibiting low intensity STEM-

HAADF signals inside the defect. Since these defects were observed far from carbon contamination caused by the transfer process (Figure S4) and the STEM-HAADF intensity was close to V_S , we assigned the structure inside the defect to sulfur. When the Ga^+ ion dose reached 2.50×10^{13} ion/cm², the density of pores with size > 0.8 nm in diameter increased (See Figure 4.15).

To investigate the effect of the Ga^+ ion dose on pore (i.e., vacancy-defect) area and density, statistical analysis was performed on AC-STEM images (see Figure 4.15). Within the irradiation dose ranges we used, the pore density increases with larger doses, whereas the pore area remains roughly constant. For the lowest dose (6.25×10^{12} ions/cm²), the majority of the atomic pores were single-molybdenum-based vacancies (V_{1Mo+yS}), while the number of missing sulfur atoms varied. With increasing Ga^+ ion dose, the number of double- molybdenum-based vacancies (V_{2Mo+yS}) increased, and some triple-molybdenum-based vacancies were also found (V_{3Mo+yS} ; Figure 4.3), exhibiting low-intensity STEM-HAADF signals inside the defect. Because these defects were observed far from carbon contamination caused by the transfer process (Figure 4.12) and the STEM-HAADF intensity was close to V_S , we assigned the structure inside the defect to sulfur. When the Ga^+ ion dose reached 2.50×10^{13} ion/cm², the density of pores with size >0.8 nm in diameter increased (see Figure 4.4).

4.5 Experimental Ionic Transport Measurements of Sub-nm Size MoS₂ Pores

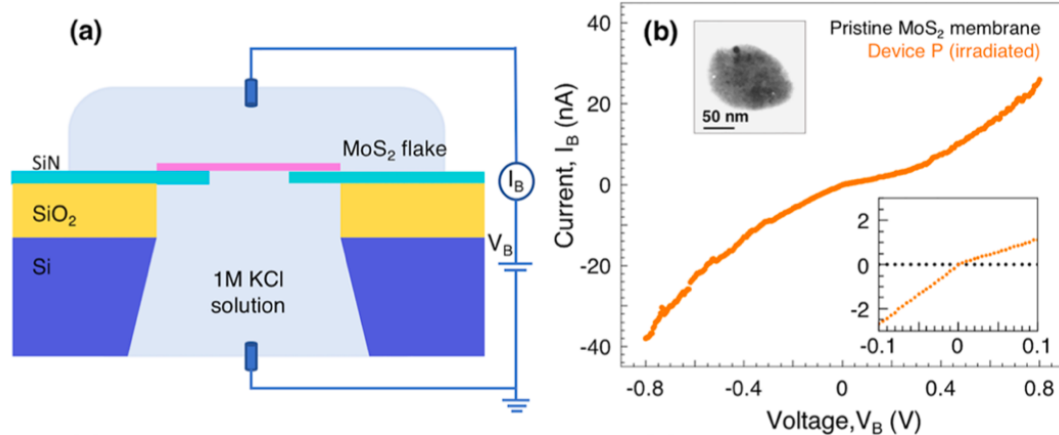


Figure 4.4. (a) The experimental setup to measure the conductance of nanoporous MoS₂ membranes and (b) Current-voltage plot of a MoS₂ device irradiated with a dose of 1.60×10^{13} ions/cm² showing a non-linear trend in the voltage range $V_B = \pm 0.8$ V.

In order to observe the ionic transport characteristics of the angstrom-size defects in the MoS₂ membranes, we implement the device setup shown in Figure 4.4 (a). A MoS₂ flake was selected under an optical microscope and then transferred over a SiN_x window with a ~ 200 nm diameter FIB hole (Appendix A).^{34,130} The membrane was then irradiated with doses ranging from 6.25×10^{12} to 2.50×10^{13} ions/cm² to create atomic vacancies with average single defect diameters between 0.4 and 0.5 nm. The top inset of Figure 4.4 (a) shows a STEM image of a suspended MoS₂ membrane over a FIB hole exposed with a dose of 2.50×10^{13} ions/cm². A resultant non-linear current-voltage (IV) curve is shown in Figure 4.4 (b) for an irradiated MoS₂ membrane (device P, dose = 1.60×10^{13} ions/cm²). For comparison, a similar trace is shown in the bottom inset for a pristine sample demonstrating a baseline ionic conductance ($G = dI/dV$) of ~ 10 pS.

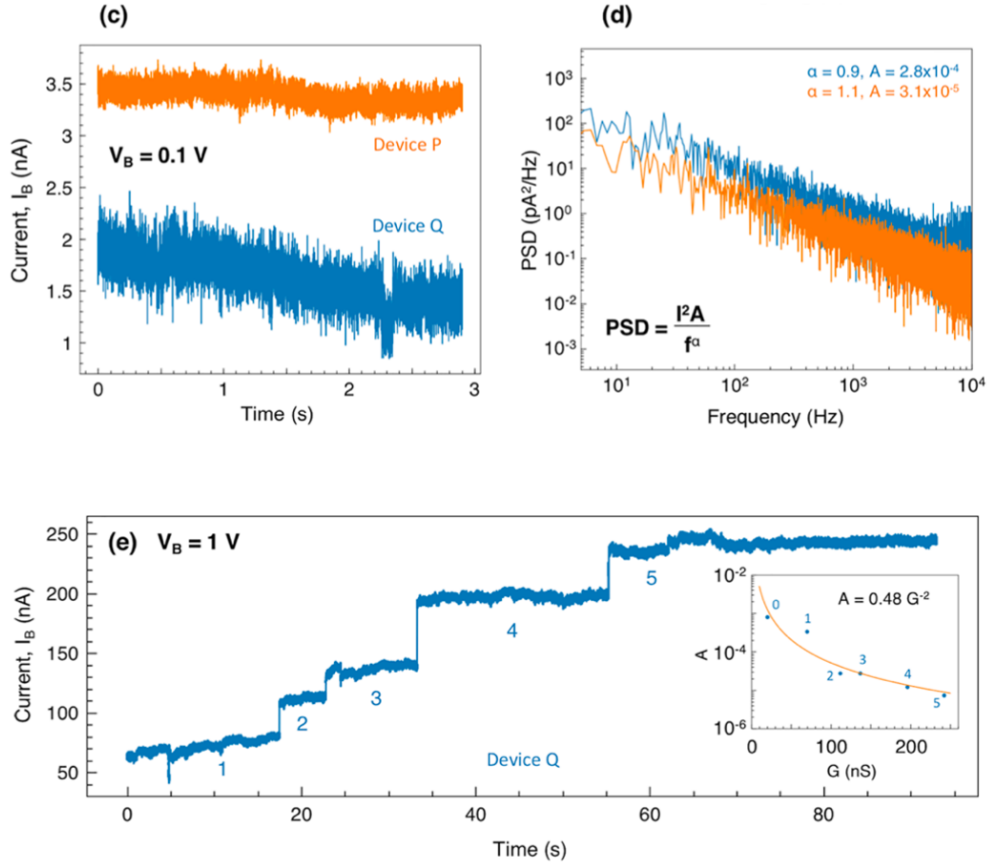


Figure 4.5. (c) Current versus time traces at an applied voltage of $V_B = 0.1$ V and (d) the corresponding power spectral density for two devices (device P and Q, dose = 1.60×10^{13} ions/cm²). (e) Current versus time trace for device Q at an applied voltage of $V_B = 1$ V

Figure 4.5(c-d) show ionic current traces at $V_B = 0.1$ V and the corresponding current noise for two devices (dose = 1.60×10^{13} ions/cm²). It should be noted that only those devices are shown here which have an ionic conductance $G > 5$ nS in the range ± 0.1 V. For devices exhibiting $G < 5$ nS, the defects are too small to allow significant ionic flow below a certain threshold voltage (discussed below), thus making ionic noise extraction difficult. The power spectral density was extracted from the current traces and fit to the equation:

$$\text{PSD} = \frac{I^2 A}{f^\alpha} \text{ (Eq. 1)}$$

where PSD is the power spectral density, I is the corresponding ionic current, f is the frequency, A is the noise coefficient and α is the low-frequency noise exponent. All the devices showed a noise exponent value, $\alpha \sim 1$ and noise coefficient, $A \sim 10^{-4}$ - 10^{-5} , suggesting dominant low-frequency noise as has been demonstrated previously in 2D nanopore devices.^{141,130,235}

To further investigate the stability of our devices, we applied a constant $V_B = 1$ V and monitored the change in ionic current for another device with the same dose (device Q, dose = 1.60×10^{13} ions/cm²) as shown in Figure 4.5(e). The current increased in jumps from 20 nA (from Figure 4.5(c)) to 250 nA, suggesting incremental damage of the membrane as opposed to gradual increase of defect sizes.⁴² The noise coefficients extracted from each section and plotted in the inset (0-th point is from Figure 4.5(c)) reveal that the low-frequency noise decreases when increasing the conductance, in accordance to a power law:

$$A = 0.48 G^{-2} \text{ (Eq. 2)}$$

A similar trend of increasing conductance was also observed in other devices when V_B exceeded ± 0.8 V. To ensure that we did not damage our devices during ionic experiments, V_B was kept between ± 0.5 V for most of our devices.

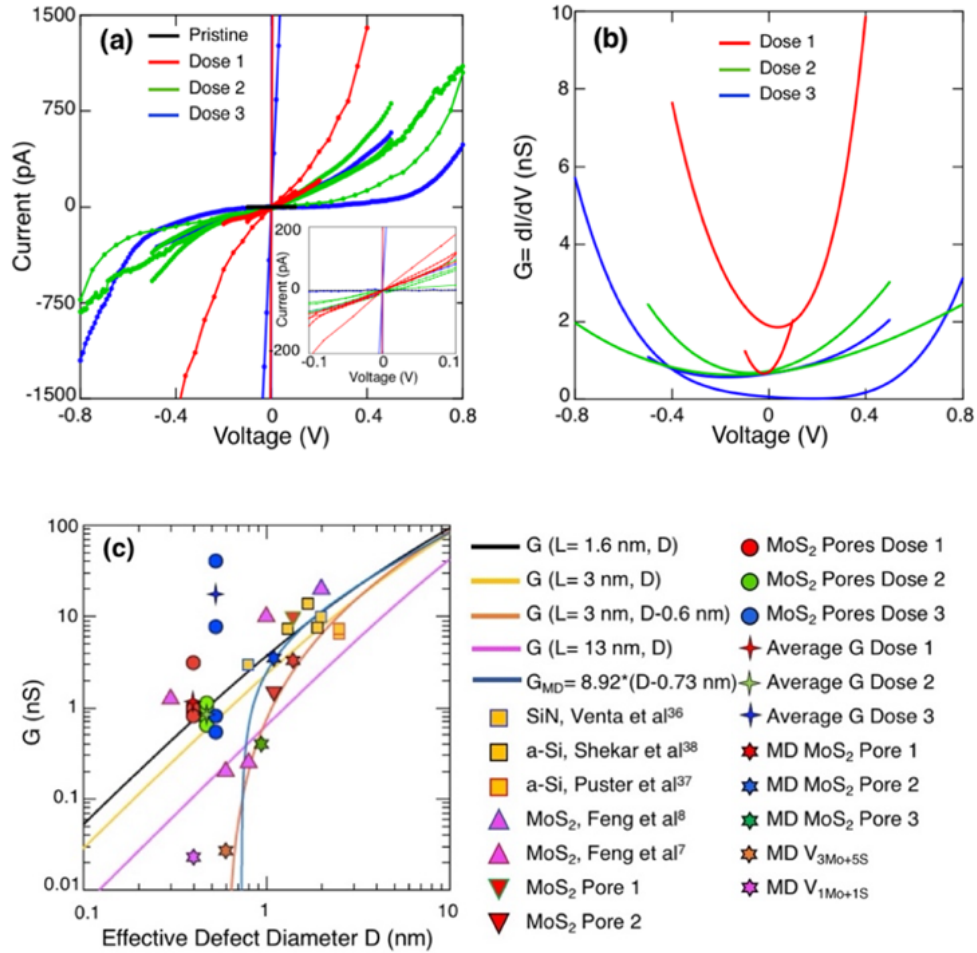


Figure 4.6 Ionic current vs. voltage (I-V) curves and conductances measured for pristine and irradiated MoS₂ membranes with Dose 1 = 6.25×10^{12} , Dose 2 = 1.11×10^{13} , Dose 3 = 2.5×10^{13} ions/cm².

(a) Ionic current vs. voltage (I-V) curves measured for pristine and irradiated MoS₂ membranes with Dose 1 = 6.25×10^{12} , Dose 2 = 1.11×10^{13} , Dose 3 = 2.5×10^{13} ions/cm². The applied sweep rate was between 5-20 mV per second. (b) Corresponding dI/dV with respect to voltage for non-linear I-V curves in (a). (c) Conductance, G is shown as a function of the pore diameter for both the continuum (black, yellow, orange, and pink) and molecular dynamics (MD) simulated (blue) models. Plotted are also G values from the MD model discussed in the text for five pores shown in Figure 5, the experimentally obtained G values for MoS₂ nanoporous membranes and single nanopores, as well as reported values from previous works on SiN,²⁰⁶ a-Si,^{158,171} and MoS₂ nanopores.^{41,43}

Figure 4.6 (a) presents the I-V curves for a pristine membrane and 15 devices irradiated at three different doses (Dose 1 = 6.25×10^{12} , Dose 2 = 1.11×10^{13} , Dose 3 = 2.50×10^{13} ions/cm²). We note that while a total of 25 devices were irradiated and tested, 10 of these

devices yielded negligible ionic conductance ($G \sim 10$ pS) comparable to non-irradiated, i.e. pristine samples, close to our detection limit, and are not shown here. In Figure 4.6 (a), several of the 15 I-V curves plotted overlap (6 red- Dose 1, 4 green- Dose 2, 5 blue- Dose 3, 1 black- pristine). Six representative differential conductances (dI/dV) for Doses 1-3 are shown in Figure 4.6(b). Collective current passing through multiple angstrom-size pores in a MoS₂ membrane resulting in non-linear I-V curves at voltages, $V_B \geq 0.1$ V, are displayed by $\sim 80\%$ of the devices. At lower voltages ($V_B < 0.1$ V), the I-V curves are linear (Figure 4(a) inset). Such non-linear trends have been observed previously for sub-nm 2D pores and were attributed to stripping of the ionic solvation shell at higher driving voltages.^{72,43} About 20% of devices showed higher conductance ($G > 5$ nS) and a linear trend even up to 1 V. This may be due to the merging of individual angstrom-size pores or their enlargement over time, resulting in higher conductance values and linear I-V curve behavior that is typically observed in nanometer-size pores that are well-described by the continuum model.⁴³

Using the previously stated AC-STEM analysis (Figure 4.15), we estimate the number of pores, N , and their diameters, D , within the nanoporous membranes for the various doses. The mean and maximum diameters of pores are 0.4 nm and 0.8 nm for Dose 1, 0.5 nm and 0.9 nm for Dose 2, and 0.5 nm and 1.3 nm for Dose 3, respectively. The number of pores ranges from $N \sim 300$ for Dose 1, $N \sim 700$ for Dose 2 and $N \sim 1200$ for Dose 3. This is estimated using the results from Figure 4.15(a) and calculating how many pores of average diameter are contained in the suspended area $\sim 3 \times 10^4$ nm². From the defect size distributions, we also estimate the number of pores with diameters larger than the hydrated K⁺ ion diameter (the smaller ion compared to Cl⁻),¹⁵⁰ $D > 0.6$ nm: ~ 30 , ~ 120 and ~ 240

for Doses 1 to 3, respectively. Similarly, the estimated number of pores with $D \geq 1$ nm are zero for Doses 1 and 2 and ~ 34 for Dose 3. Doses 1-3 were chosen because they produce well-separated, angstrom-size defects. For higher doses, defects start to merge resulting in larger, irregularly shaped pores.

Despite a large number of defects, most of them are very small, below ~ 5 Å. Based on molecular dynamics simulations,⁶⁵ such pores are expected to be too small for ions to flow through but should allow water molecules to pass. We therefore expect the measured conductance in the range of $V_B = \pm 0.1$ V of the irradiated MoS₂ membranes to be low, and indeed, it was found to be ~ 1 nS in 80% of the devices shown in Figure 4.6 (a). The average conductances of the irradiated devices were ~ 1 nS for Doses 1 and 2, increasing to ~ 10 nS for Dose 3. We compare and contrast the irradiated membranes to single nanopore devices in Figure 4.7(c), which plots the conductances of the nanoporous membranes as a function of the effective defect diameter (including the mean G for each dose), as well as the conductances of two single MoS₂ nanopore devices that were drilled using AC-STEM with effective $D \sim 1.4$ nm and ~ 1.1 nm (shown in Figure 4.6 (a) i-ii). Effective D is defined as D of a circle with the same area as the pore (calculated using ImageJ software). We also compare our results with previously published literature on single sub-2 nm diameter pores in MoS₂,^{41, 43} thinned silicon nitride²⁰⁶ and amorphous silicon membranes with $D \sim 0.3$ to 2 nm.^{158,171}

The average conductance measured for Dose 1 is ~ 1.4 nS, slightly higher than that of Dose 2 (1.11×10^{13} ions/cm²), where the measured average conductance is 0.9 nS. While the larger Dose 2 is expected to give larger mean conductance than Dose 1, the averaged experimental results can be explained by the following two factors: (i) the mean vacancy

sizes obtained from these two doses are very close to each other, *i.e.*, 0.4 nm and 0.5 nm for Dose 1 and Dose 2, respectively, as shown in Figure 4.15, and (ii) the spread in the conductance values for different samples, irradiated at each dose, is larger than the difference between the averages of the two doses. Dose 3 (2.5×10^{13} ions/cm²), which is the highest dose used, yielded the largest mean conductance (~ 10 nS), consistent with expectations that samples irradiated with larger dose yield higher ionic conductance.

We observe a two orders of magnitude variation in the experimental conductance values corresponding to single pores and nanoporous membranes, from $G \sim 0.1$ to 10 nS for single pores with $D \sim 0.3$ to 2 nm, and $G \sim 1$ to 100 nS for nanoporous devices with average $D \sim 0.5$ nm. This enhancement in conductance is expected due to the presence of multiple nanopores. However, the scatter among devices could come from several reasons, including the variations in atomic structure and edge terminations that can result in different properties of the pores when they are introduced in the salt solutions. This has not yet been explored experimentally. It is also challenging to determine the diameter accurately. The effective D used on the x-axis is measured from AC-TEM images with pores in vacuum before ionic measurements and it can change later, for example due to expansion or contamination in solution.³⁴

4.6 Theory of Sub-nm Pores: Non-Equilibrium Molecular Dynamics (NEMD)

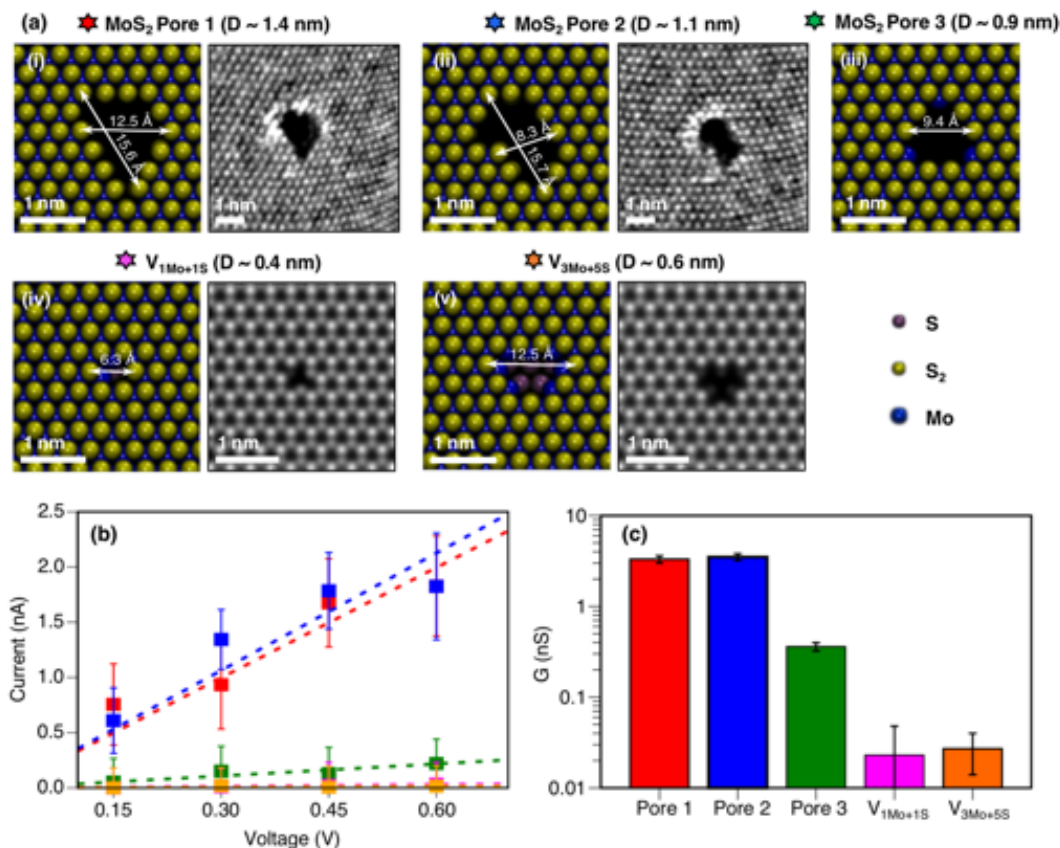


Figure 4.7 Molecular Dynamics of individual sub-nm MoS₂ pores with current-voltage characteristics and individual sub-nm pore conductance.

(a) AC-STEM images of individual MoS₂ pores (i) pore 1 and (ii) pore 2 with effective diameter ~ 1.4 and 1.1 nm, respectively. Corresponding all-atom structures used in NEMD (Non-Equilibrium Molecular Dynamics, see SI Section 10) simulations are presented aside. Mo, S₂, and S atoms are shown in blue, yellow, and purple spheres, respectively. (iii) Atomic structure of an equivalent circular pore of diameter ~ 0.9 nm. QSTEM simulations⁹² for vacancy-defects caused by (iv) 1Mo and 1S missing (V_{1Mo+1S}) and (v) 3Mo and 5S atoms (V_{3Mo+5S}). (b) I-V characteristics and (c) conductance G panel computed from NEMD simulations for the five pores shown in panel (a). Error bars represent the standard deviation from the ionic current computed from NEMD runs.

In order to estimate the conductance of the pores with precise and stable diameters, we perform molecular dynamics simulations¹⁴⁷ (see section 4.6). Figure 4.6(a) (i) – (v) shows

the five configurations that were tested, where pores 1 and 2 (same as in Figure 4.6 (c)) correspond to AC-STEM drilled MoS₂ pores with effective diameters of ~ 1.4 nm and 1.1 nm, respectively (see Figure 4.7), pore 3 corresponds to a perfectly circular pore of effective diameter 0.9 nm, and finally V_{1Mo+1S} and V_{3Mo+5S}, which represent the defect-vacancies with one of the smallest and largest diameters, respectively (Section 4.6, Figure 4.15). The conductances of these five pores are plotted in Figure 4.6(c). As shown in Figure 4.6 (b), I-V curves were computed for each system via MD simulations and conductances G were obtained by linear fitting of I-V curves with 0.15 V < V_B < 0.6 V. Figure 4.6 (c) presents the conductance obtained for all the simulated pores, showing a variation of three orders of magnitude depending on the pore size. Pores 1 and 2 are characterized by conductance values of 3.3 and 3.5 nS, respectively, which agree within a factor of 2-3 with the experimental values (~10 nS and 1.5 nS in Figure 4.6c), while pore 3 shows a conductance of 0.4 nS. The conductance G drops drastically for pore 3 because of its smaller diameter when compared with pore 1 and 2 and because its diameter is close to the limiting diameter value for zero conductance. Finally, pores made of defects V_{1Mo+1S} (D ~ 0.4 nm) and V_{3Mo+5S} (D ~ 0.6 nm) exhibited a negligible conductance G of ~ 0.02-0.03 nS, confirming the fact that pores made of defects smaller than ~ 0.6 nm do not conduct ions in our experiments.

In this size range (< 1 nm), small changes in D by ~ 0.1 nm result in conductance changes by one order of magnitude or more (notice the sharp drop of the blue line in Figure 4.6(c)). Using the MD simulations, we obtain an empirical linear model of open conductance for sub-3 nm MoS₂ pores, plotted as the blue line in Figure 4.6(c):

$$G_{MD} = C(D - D_{min}) \text{ (Eq. 3)}$$

where G_{MD} is the pore conductance derived from MD, $C = 8.92$ S/m is the conductivity of KCl ions through sub-3 nm single-layer MoS₂ nanopores and $D_{min} = 0.73$ nm is the minimum pore diameter for ionic flow. Furthermore, in Figure 4.6(c), this model derived from MD simulations¹⁴⁷ is featured as a blue line along with the black, yellow, pink and orange fit lines $G(L, D)$ which represent the continuum model for the conductance for different values of pore thickness, L .

Ionic measurements have validated the continuum model for pores with nanometer-scale diameters and shown that an effective pore thickness, $L \sim 1.6$ nm is a good approximation for MoS₂.²¹⁴ This corresponds to the black line in Figure 4.6(c). Here, the pore is modeled as a system of three resistors in series. The interior of the nanopore is modeled as a cylindrical resistor, $R_p = \frac{1}{\sigma} \frac{4L}{\pi D^2}$, where σ is the conductivity of the electrolyte, L is the thickness of the nanopore and D is its diameter. Additionally, there is an access resistance in series on each side where current paths converge from the bulk electrolyte into the pore,⁵⁸ $R_a = \frac{1}{\sigma} \frac{1}{2D}$. The total resistance of the single nanopore, R_1 , is given by the sum of the three resistances – the interior of nanopore and two access resistances:

$$\mathbf{R_1 = R_p + 2R_a = \frac{1}{\sigma} \left(\frac{4L}{\pi D^2} + \frac{1}{D} \right)} \quad \mathbf{(Eq. 4)}$$

This gives us an equation for conductance through a single nanopore of diameter D and thickness L :

$$\mathbf{G_1 = \frac{\sigma \pi D^2}{(4L + \pi D)}} \quad \mathbf{(Eq. 5)}$$

We stress that $G(L = 1.6$ nm, $D)$ does not fit the conductance measured in single MoS₂ sub-nm pores plotted in Figure 4.6(c), in contrast to the agreement found in pores with larger diameters ($D > 1$ nm). In fact, the data clearly shows that small pores conduct less

than expected from this model and a better fit can be obtained by assuming a larger pore thickness (pink line in Figure 4.6(c) where $L = 13$ nm) or by assuming an effectively smaller diameter. The orange line, $G(L = 1.6$ nm, $D - 0.6$ nm) corresponds to a continuum model assuming that the pore diameter is smaller than the actual diameter by 0.6 nm, meaning that a pore with $D = 0.6$ nm would give zero current. This best fit is also consistent with the assumption that for a KCl ionic solution, K^+ is the smallest hydrated ion with a diameter of 0.6 nm, such that a pore diameter, $D = 0.6$ nm will effectively resist the transport of ions.^{72,150} This model closely resembles the linear model of conductance obtained from MD simulations for sub-2nm pores. For large D , $G(L = 1.6$ nm, $D - 0.6$ nm) $\approx G(L = 1.6$ nm, D) and the two models converge (orange and black lines). To our knowledge, besides these data points, the only comparable pores that have been measured in the sub-2 nm diameter range are Si/SiO₂ pores²⁰⁶ and ultra-thin Si₃N₄.³⁰ The corresponding fit $G(L = 3$ nm, D) is shown in yellow for comparison with $G \sim 3$ to 10 nS for $D \sim 0.8$ to 2 nm.

4.6.1 Calculation of Effective Diameters of Non-Circular Pores

In order to define an effective diameter, we measured the total sub-nm diameter pore area using a threshold function from a commercial, ImageJ software, and then calculated the diameter that corresponds to a circle with an equivalent area. For TEM images (MoS₂ pore 1 and pore 2), the scale bar used was derived from the averaged distances between two adjacent Molybdenum atoms (0.32 nm) in the vicinity of the pore.

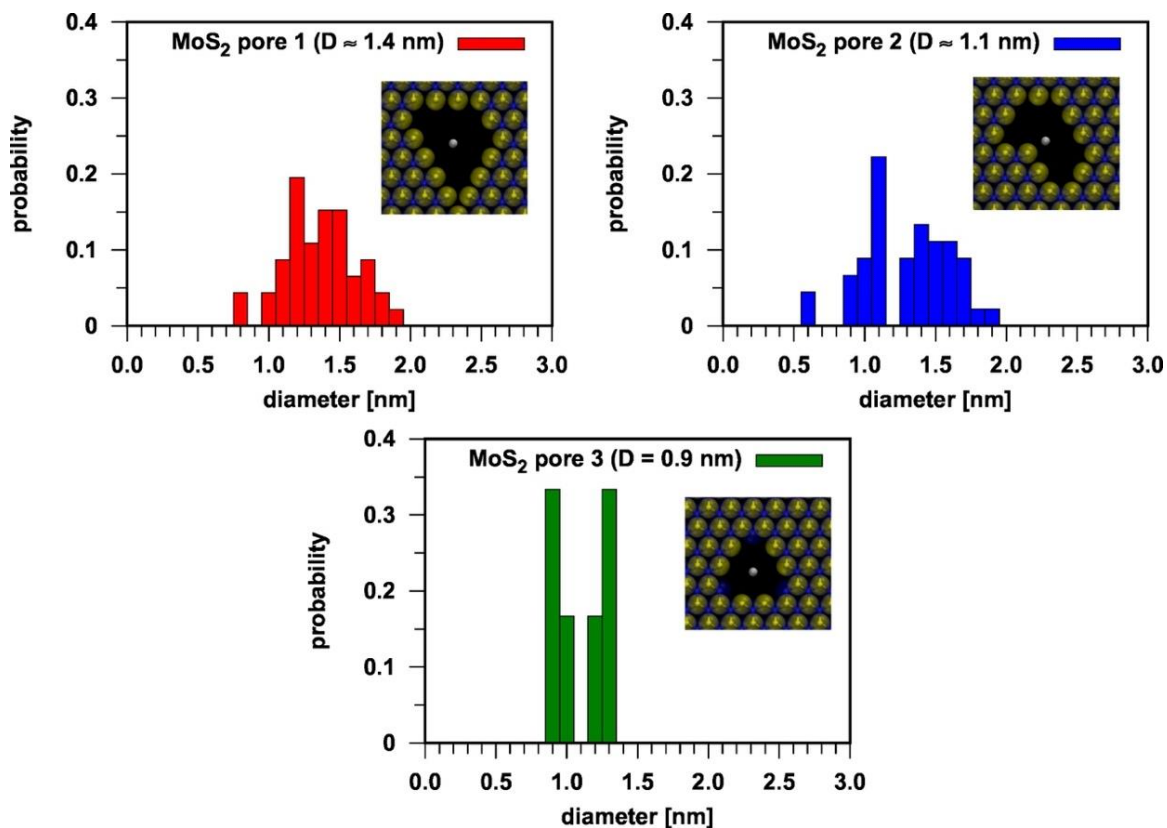


Figure 4.8. Distributions of diameters computed from MoS₂ pores atomic structures. The center of mass of the pore is shown using a grey sphere in the structure images in inset.

4.7 Additional Experimental Methods

Fabrication of MoS₂ Devices:

A 50-nm thick suspended window of silicon nitride of dimensions 50 μm × 50 μm was fabricated on a 5 μm/525 μm SiO₂/Si wafer using optical lithography and KOH and HF wet etching techniques^{1,2}. A 200-nm-diameter hole was drilled in the center of the window using a 30 kV, 10 pA Ga⁺ FIB source and a single-layer MoS₂ flake was transferred onto it using a custom-built manipulator (Figure 4.10) to form a suspended MoS₂ membrane.

Transfer of Single-Layer MoS₂ onto Carbon Grids:

To transfer single-layer MoS₂ onto gold Quantifoil TEM grid (from SPI), a layer of poly methyl methacrylate (PMMA) (495K, A4) was first spin-coated onto as-grown MoS₂ flakes. After PMMA cured, it was immersed in 2M NaOH etchant solution to lift off the PMMA-coated MoS₂ flakes. Subsequently, the detached film was rinsed in deionized water and fished onto the grid. Finally, PMMA layer was cleaned in acetone and IPA, leaving the transferred single-layer MoS₂ on the grid.

Transfer of Single-Layer MoS₂ onto SiN_x Membrane:

Procedure for monolayer MoS₂ flake transfer onto the SiN_x chips were carried out with a dry-transfer process with the help of a PDMS stamp technique. The SiN_x chips have a focused ion beam (FIB) drilled holes of diameter ~100-200 nm onto which the 2D flake is transferred and stays suspended, the stamping process hence needs immense skill, patience and technique. Here, the technique developed involved a micron sized PDMS stamp glued with a double-sided tape to a narrow bar (as shown in Figure 4.9). This PDMS stamp was used to lift-off the 2D flake from the as-grown substrate and carefully “stamped” onto the center of the desired SiN chip. The FIB drilling was cautiously performed in the center of the SiN chip so the further stamping process yields successful suspended-2D flake devices. A micromanipulator consisting of a piezoelectric stage (NanoMax-TS flexure stage, Thorlabs) and a custom-built cantilever was applied to align the MoS₂ flake sample with SiN_x chip. An optical microscope (Olympus BH2 Microscope) was used to monitor the deterministic transfer process.

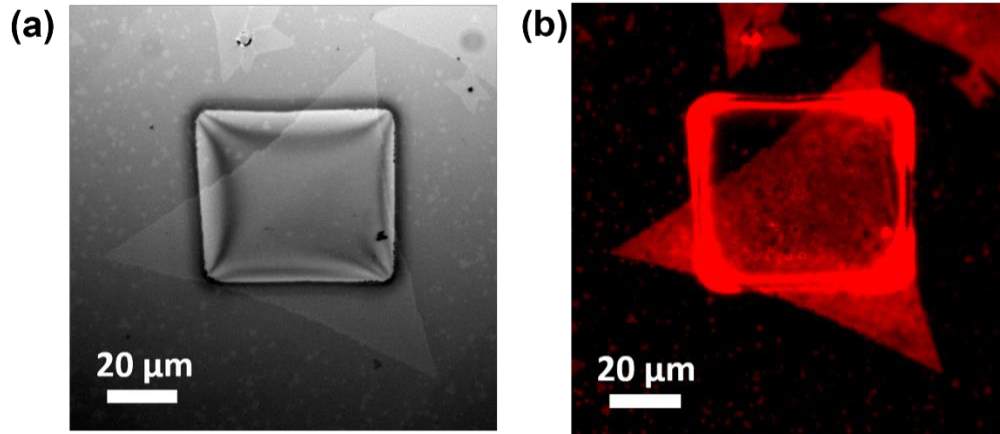


Figure 4.9. (a) Optical and (b) fluorescence (673 nm-centered bandpass filtered) microscopic image of transferred single-layer MoS₂ flake onto SiN_x window with FIB hole at the center.

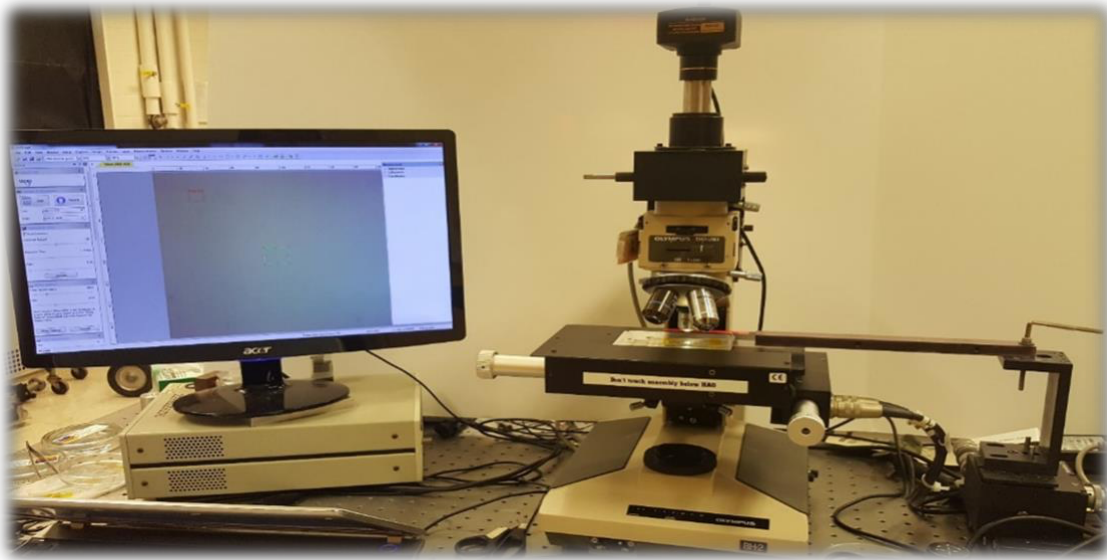


Figure 4.10. The setup of the deterministic transfer stage for micro-positioning MoS₂ flakes onto SiN_x windows.

Control of Defects by varying Ga⁺ Ion Dose:

Suspended MoS₂ flakes were irradiated with Ga⁺ ions using the ion gun of a FEI Helios dual beam instrument. To perform the Ga⁺ ion irradiation, we set the acceleration voltage at 30 kV and the current intensity at 230 pA. The beam incidence was normal to the surface

and followed a raster path over a rectangular area, 410 μm long and 274 μm wide. The beam impinges the sample in imaging mode, in this condition the beam dwelled 50 ns in each step; the spacing between steps was approximately 260 nm. Finally, the different doses on the single-layer MoS₂ were achieved by manually varying the irradiation time.

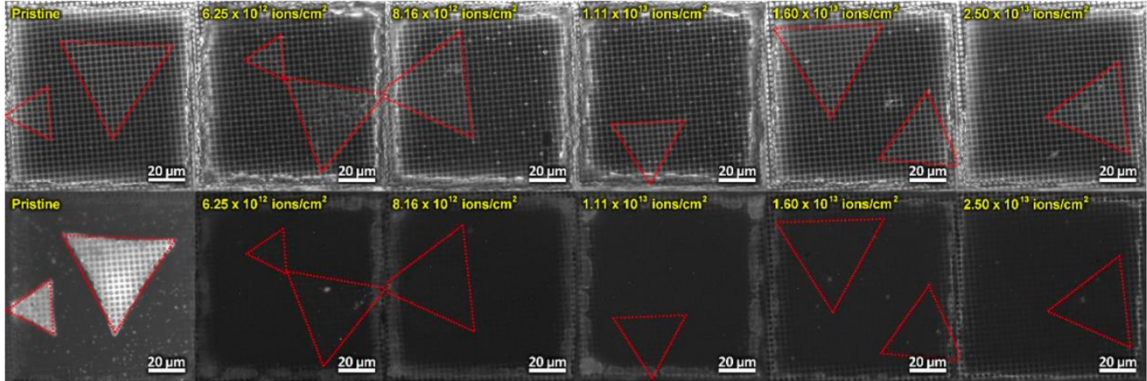


Figure 4.11. Optical images (top) and fluorescence images (bottom, 673 nm-centered bandpass filtered) of the pristine and the Ga⁺ ion irradiated single-layer MoS₂ on Quantifoil TEM grid.

Raman/Photoluminescence Spectroscopy of Irradiated Membranes:

All Raman spectra and photoluminescence spectra were collected from suspended MoS₂ flakes over Quantifoil TEM grid. To avoid both heating effect and laser induced damage to the suspended MoS₂, 10-50 μW of laser power under $\times 100$ (N.A. 0.95) objective lens was used. The Raman and Photoluminescence spectra were acquired using the ‘inVia Raman Microscope’ (Renishaw) equipped with a 488 nm laser.

AC-STEM Observation and Counting Defects:

Aberration corrected scanning transmission electron microscopy (AC-STEM) study was carried out by FEI Titan³ G2 S/TEM operated at 80 kV to investigate the atomic structure

of MoS₂ triangles. A high-angle annular dark field (HAADF) detector was used for Z contrast imaging. In order to reduce noise and increase visibility of atoms, Gaussian Blur filter with 0.03 nm of blurring width was applied by ImageJ program. Prior to vacancy-defect counting from STEM-HAADF images, further noise reduction was applied using the “Remove Outliers” process. At this point STEM-HAADF signal from sulfur atoms were spread. Cleaned STEM-HAADF images were then subjected to the “Local Threshold” process with the Sauvola method to obtain binary STEM- HAADF images which consist of black-colored defect regions and white-colored MoS₂ regions. Statistical analysis of the defect area and the number of defects were carried out using these binary STEM-HAADF images.

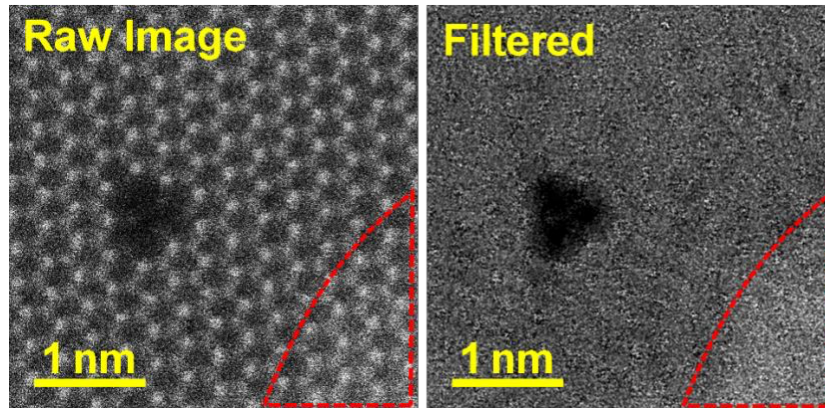


Figure 4.12. Raw STEM image of a V₃Mo+5S type vacancy-defect in MoS₂ lattice (left). The periodic feature of MoS₂ lattice was removed by applying several circular band pass filters to FFT (right). The highlighted area in red corresponds to the carbon deposited area.

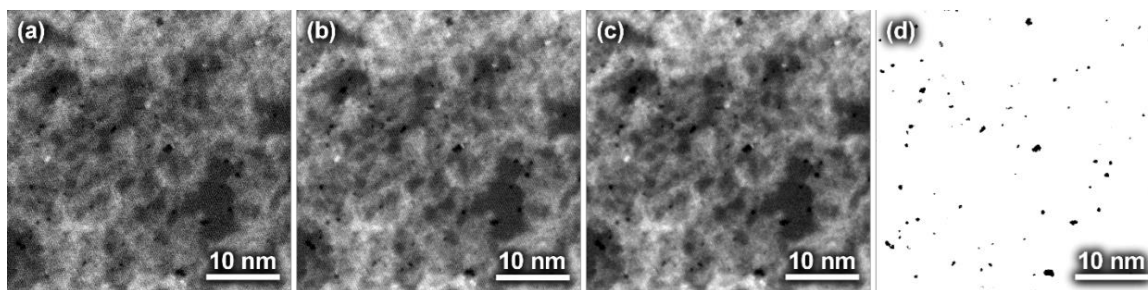


Figure 4.13. Step-by-step images of the binary creation process from the raw STEM images.

The ImageJ software was used for all processing. A raw STEM image ((a), $38.4 \text{ nm} \times 38.4 \text{ nm}$, $2048 \text{ pixel} \times 2048 \text{ pixel}$) is processed using the *Gaussian Blur* filter (filtering radius: 0.03 nm) to reduce noise (b). Further, noise reduction is applied by using the *Remove Outliers* process (10 pixel of radius and threshold 50 was used) (c). After this step, the ADF signal from Mo and S are dispersed, then the crystal and defect parts are separated. Finally, to efficiently ignore the carbon contamination layer present on the surface of MoS_2 , *Local Threshold* process (*Sauvola* method, radius: 40 pixel , k -value: 0.20 , r -value: 200) is applied, and then the binary image is obtained (d).

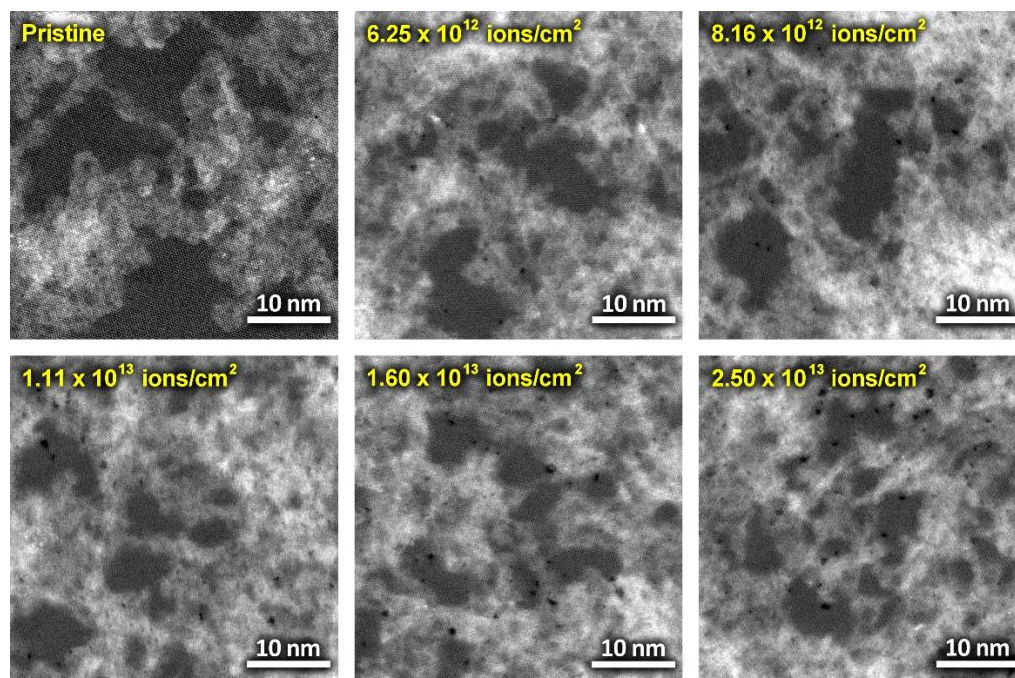


Figure 4.14. Low magnification STEM-HAADF image of the pristine and Ga^+ ion irradiated MoS_2 .

Simulation of HAADF Images of Defects:

The STEM-ADF image simulation was conducted by the QSTEM package⁹². Simulation parameters such as acceleration voltage, spherical aberration (C_3 and C_5), convergence angle and inner and outer angles for HAADF detector were set according to experimental conditions. All other aberrations except spherical aberration and defocus were kept as 0.

Statistical Analysis of the Sub-nm size pores using AC-STEM Images:

In order to investigate the effect of the Ga^+ ion dose on nanopore area and density, statistical analysis was applied to AC-STEM images. Binary images were first prepared from AC-STEM images by post-image processing (see Figure 4.13). Nanopore density, average area and total pore area percentage (see Figure 4.15 (a)-(c)) increase linearly with irradiation dose. By extrapolating the linear regression (Figure 4.15 (c)), an atom sputtering

rate was calculated as 1.07 atom/ion. The area of the pore slightly increases when the Ga^+ ion dose is increased, but since the pore area is limited by the atomic configuration, a Gaussian distribution is not expected. By comparing the average and the median of the nanopore area (Figure 4.15 (b)), only the average increased when the Ga^+ ion dose increased to 2.50×10^{13} ions/cm², indicating that some pores expanded or merged laterally. Therefore, the nanopore diameter distribution was obtained (Figure 4.15 (d)). Instead of the average nanopore area, S (nm²), the effective nanopore diameter, D (nm), was calculated from the area using $S = \pi(D/2)^2$. The pore diameter distribution showed that diameters of most defective samples were several angstroms in size.

Further, to understand the distribution of nanopore diameters, the same nanopore counting procedure was applied to simulated STEM-HAADF images. The simulated STEM-HAADF images (Figure 4.15(e)) were acquired using parameters from the actual imaging conditions. The effect of six different nanopore structures—three types of single-Mo-based nanopores (V1Mo (0.38 nm), V1Mo+3S (0.56 nm), V1Mo+6S (0.56 nm)) and three types of double-Mo-based nanopores (V2Mo+2S (0.54 nm), V2Mo+6S (0.68 nm), V2Mo+10S (0.70 nm))—were considered, and the diameter for each nanopore was obtained using the simulated STEM-HAADF images. These were also plotted in the nanopore diameter distribution (see bars in Figure 4.4 (d), the color of the bar corresponds to the nanopore structure in inset of Figure 4.4 (d)). Since the nanopore counting procedure was carried out at low magnification (Figure 4.14), the effect of mono-sulfur vacancies exhibiting low STEM-HAADF intensities at the edges of nanopores, was mostly ignored. This leads to the conclusion that the diameter of V1Mo+3S is almost the same as the diameter of

V1Mo+6S. When we compare experimental diameter distributions with simulated diameters for V1Mo nanopores, a large number of nanopores exhibit diameters smaller than the V1Mo pores. In order to understand this difference, we counted the number of missing Mo atoms from high magnification STEM-HAADF images (Figure 4.16).

For the lowest irradiation dose (6.25×10^{12} ions/cm²), 80% of the defects consist of single-Mo-based nanopore, indicating that the overall nanopore diameter distribution shifted to smaller diameters, possibly due to broadening of atoms by higher order aberrations in the STEM-HAADF image. Assuming that a random number of surrounding sulfur atoms are sputtered along with a molybdenum atom by Ga⁺ ion irradiation, and that the sputtering probability for sulfur atoms is low, V1Mo and V2Mo+2S can be a major contribution to the nanopore distribution.

For 6.25×10^{12} ion/cm² irradiations, the main peak in the pore diameter distribution is close to the V1Mo, whereas the density of nanopores with diameter corresponding to 0.54 nm (diameter for simulated V2Mo+2S), is low. As the Ga⁺ ion dose increased, the nanopore density centered at nanopore diameters of 0.54 nm increased, indicating that the density of double-Mo-based pores increased. Moreover, when the Ga⁺ ion dose reached 2.50×10^{13} ion/cm², densities of pores with size > 0.8 nm in diameter increased.

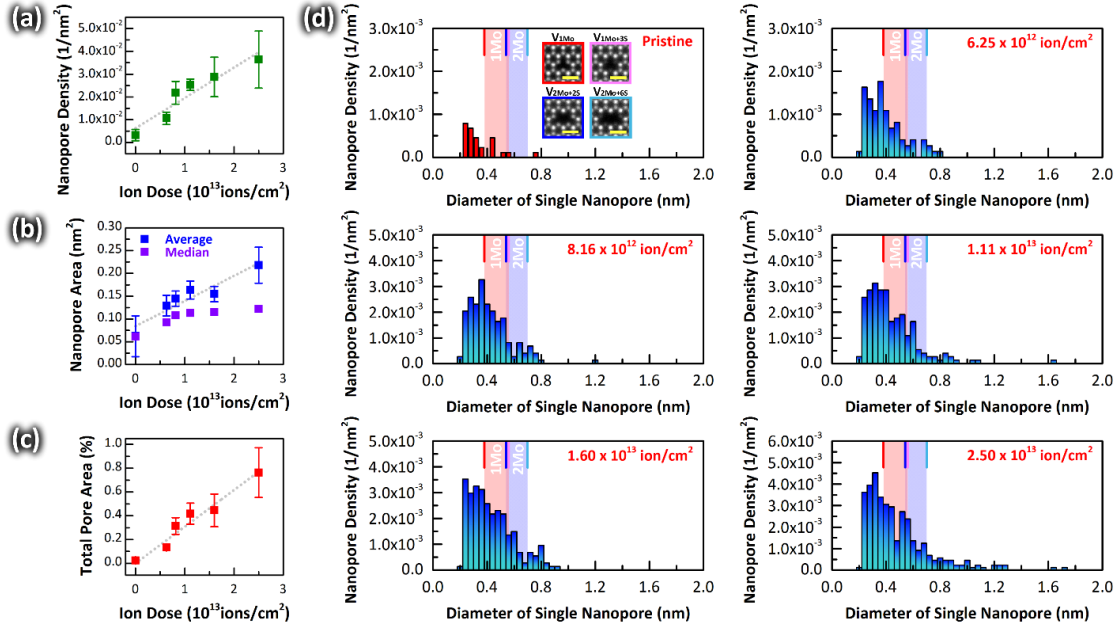


Figure 4.15. Statistical analysis of sub-nm diameter pores identified by AC-STEM observation.

Statistical analysis of sub-nm diameter pores identified by AC-STEM observation. (a) pore density, (b) pore area and (c) total pore area percentage were calculated from binary images created from AC-STEM image. (d) Distribution of the pore diameters for defects produced by Ga^+ ion irradiation, for different Ga^+ ion doses. The red (blue)-colored box corresponds to diameter ranges for $\text{V}_{1\text{Mo}+y\text{S}}$ ($\text{V}_{2\text{Mo}+y\text{S}}$) pores which is calculated from simulated STEM-HAADF images by a commercial software, QSTEM (inset, scale bar is 500 pm).

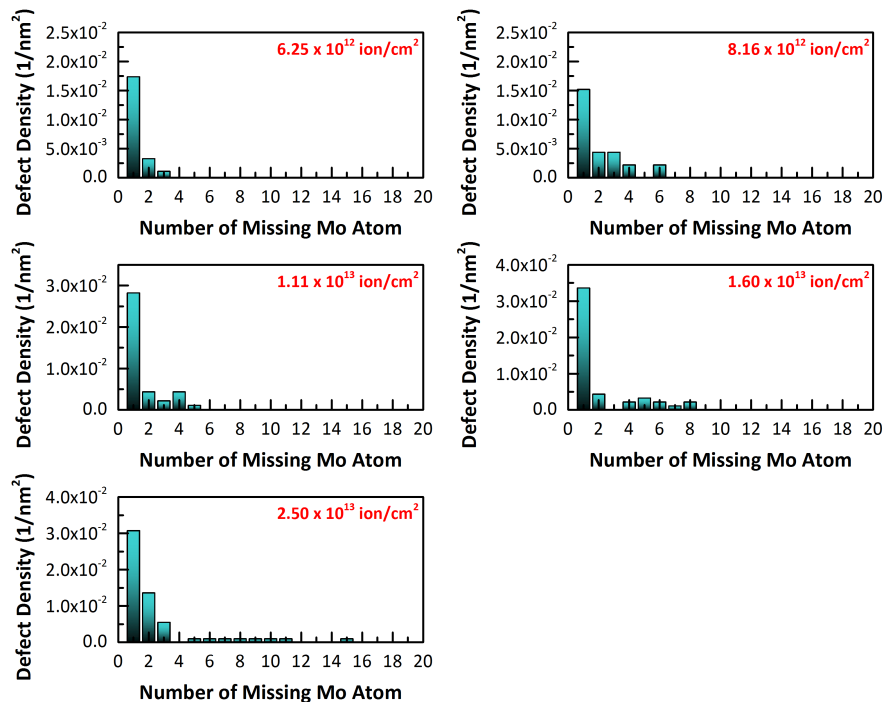


Figure 4.16. Statistical analysis of missing Mo atom using high magnification the STEM-HAADF images.

Ionic Current Measurements:

EPC-10 HEKA amplifier with Ag/AgCl electrodes was used to perform ionic measurements on our devices. 1 M KCl (with 10 mM EDTA and 1 mM Tris; measured solution conductivity = 11.18 S/m, pH 8.7) solution was prepared using DI water, and the conductivity and pH were measured with Accumet XL-20 pH conductivity meter. Ionic measurements were conducted on pristine samples (non-irradiated, MoS₂ suspended samples) and irradiated samples. Prior to ionic measurements, the device was annealed at 300° C in an Ar-H₂ environment for 90 minutes. This was a crucial step as it was found to prevent delamination of the flakes when the device interacts in a liquid environment. The device was then immersed in a 50% water-ethanol solution for at least 30 minutes to help in wetting and formation of ionic channels through the defects^{1,2}. 1 M KCl solution was then introduced on both sides of the device and a voltage bias (V_B) was applied while

simultaneously measuring the ionic current (I_B). To ensure no damage to our devices during ionic experiments, V_B was kept between ± 0.5 V for most of our devices.

Non-Equilibrium Molecular Dynamics (NEMD):

Simulations were performed using the LAMMPS software package.¹⁵⁰ The simulation box of dimension $7.5 \times 7.5 \times 15$ nm³ is comprised of a MoS₂ nanoporous membrane plus a 1M KCL ionic solution. A Stillinger-Weber potential is used to characterize Mo-S bonded interactions⁷⁹ and non-bonded interactions between MoS₂, water and ions were described using a Lennard-Jones (LJ) plus Coulomb potential. The water model used in the present work is the TIP3P model.⁸¹ LJ parameters for K⁺ and Cl⁻ ions were taken from references,¹⁷⁹ where specific parameters were developed for the water model employed. LJ parameters and bulk partial charge for Mo and S atoms were taken from references respectively,^{110,204} as already used in other works.⁶⁵ Before running NEMD, an equilibrium of the system in the NPT ensemble (T= 300K and P= 1 bar) without any electric field was performed during 100 ps to relax the system at the target temperature and pressure. Relaxation was followed by MD runs of 10 ns carried out in the NVT ensemble using the velocity-Verlet algorithm¹⁸⁵ with a time step of 1 fs. A Nosé-Hoover thermostat^{138,64} was used to maintain the temperature at 300 K with a time constant of 0.1 ps. Particle-particle particle-mesh method was used to describe long-range electrostatic interactions. A cutoff of 1.0 nm was applied to LJ and Coulomb potential for non-bonded interactions. A SHAKE algorithm¹⁶³ was used to constrain the bond lengths and angle of TIP3P water molecules. Finally, Non-Equilibrium MD simulations (NEMD) using periodic boundary conditions were carried out by applying an external uniform electric field, directed normal to the

nanoporous membrane (z-direction), acting on all charged particles throughout the simulated system. This gives rise to a force $q_i \cdot E$ that applied to all the atoms in the simulation box, *i.e.*, Mo, S, O_w, H_w, K⁺ and Cl⁻. The resulting applied voltage is $V = -EL_z$, where L_z is the length of the simulation box in the z-direction, with $V = 0.15, 0.3, 0.45$ and 0.6 V. The ionic current and conductance calculations were performed using the same method as described in previous work.¹⁴⁷

4.8 Summary

In conclusion, we created nanoporous MoS₂ membranes containing ~ 100 - 1000 , angstrom-size pores with a mean diameter of ~ 0.5 nm, and the devices were characterized by atomic-resolution imaging, Raman and PL spectroscopy. The measured conductance in 80% of the devices was of the order of 1 nS. We have also fabricated two single ~ 1 -nm-diameter MoS₂ pores with corresponding AC-STEM images and G was found to be ~ 1 and 10 nS. Our experiments and comparison with single pore data demonstrate that conductance must occur only through the few larger pores within the distribution and that majority of the defects do not allow ions to pass through. These results have a direct application for water desalination. Our MD simulations reveal that the defects with diameters less than ~ 0.6 nm are too small for ions to go through and result in negligible conductance < 20 pS. This conductance is comparable to the conductance obtained in a controlled experiment using a pristine membrane. Future studies may use atomic-resolution imaging to correlate the ionic transport measurements with the detailed information of the atomic structure of the individual conducting defects. Furthermore, there is a need for modeling of nanoporous membranes containing a large distribution of angstrom size pores, that is now possible using the AC-STEM insights provided by this work.

5 Single Zero-D Pore and Quantum Confinement in Ionic Transport

This section has been represented from the publication titled, “Stochastic Ionic Transport in Single Atomic Zero-Dimensional Pores” by Jothi Priyanka Thiruraman, Paul Masih Das, and Marija Drndić. *ACS Nano* **2020** *14* (9), 11831-11845

5.1 Introduction

In the recent years, biological proteins such as Na⁺ channels, K⁺ channels and aquaporins are being revered as touchstones for their water molecule and ionic transport properties. Studies have shown unique non-linear current-voltage (I-V) characteristics in sub-nm solid-state pores fabricated and tuned under a variety of operating conditions.^{43,57,72,164,190} These observations constitute a breakthrough in understanding water purification and ionic selectivity with low-dimensional materials. Among reports on fabrication using novel solid-state materials, there have been a few innovative device architectures that mimic biological protein ion channels such as K⁺ channels. For example, carbon nanotubes (CNTs) with 0.8-1.5 nm diameters,^{202,221} nanocapillaries with 0.6 nm heights,^{39,50} and nanopores in graphene, MoS₂, and WS₂ with ~ 0.2 nm to few-nm diameters,^{174,202,190} have shown cation selectivity. Arrays of pores with diameters comparable to the hydrated ion sizes have been demonstrated in two-dimensional (2D) materials, opening a regime of transport studies at the atomic scale.^{72,190,192} A few notable experimental studies were conducted on single sub-1-nm-diameter 2D pores.^{43,192} Here they used theoretical fits of conductance vs. pore diameter to quote the “experimental” 2D pore diameter in the sub-nm regime from measured currents^{72,43} rather than measure it directly, assuming that models are correct in the sub-nm regime. These pore diameter values were then used as

important ingredients to obtain, what could be considered, a “by-design” match with theories⁷² such as claiming evidence for “Coulomb blockade”⁴³ and “atom-by-atom” pore formation phenomena.⁴² However, the fabrication and ionic transport properties of *individual* atomically engineered pores in 2D membranes is yet to be experimentally established.^{43, 192} Effects arising from ion confinement such as quantized ionic conductance *vs.* pore diameter, Coulomb blockade and steric hindrance where the drop in conductance as successive hydration shells are prevented from passing through the small pores have been anticipated.^{190,43,97,157,238,239} Other competing effects may include hydrophobicity of pores.^{151, 176} Understanding ionic conduction phenomena in these confined geometries will expand their applications in drug delivery, biomedical, water filtration, nanopower generation and energy harvesting.^{2,190,140,82,183,41}

5.2 Background

In this study, we create single atomic (sub-nm) pores in a monolayer 2D material, obtain their single-atom-resolution structural images, and probe the correlated current-voltage behavior in salt solutions. We fabricate devices with individual atomically precise MoS₂ pores using aberration-corrected scanning transmission electron microscopy (AC-STEM). The resulting pores contain 1 to 5 missing Mo atoms with effective diameters (d_{TEM} , see *Methods* for definition and discussion) ranging from ~ 0.53 to 0.92 nm. Using atomic resolution images, we also present a library of predicted MoS₂ pores with discretized sub-nm diameters and zigzag-armchair edge configurations. These pores constitute quasi-zero-dimensional (zero-D) channels^{43, 97, 192} with feature sizes comparable to the dimensions of

water molecules (~ 0.3 nm), hydrated ions (~ 0.7 nm to 1 nm) and Debye screening lengths (~ 0.1 nm to 3 nm in 3 M to 10 mM KCl, respectively).^{43,121,198}

Using ionic transport measurements, the wetting properties, ion current noise, and conductivity properties of individual zero-D MoS₂ pores are characterized. We present a methodology for inducing a conducting ion channel in a sub-nm 2D pore using ethanol solutions and probe different ionic states (un-wet, partially wet, and fully wet) through current-voltage and noise power spectral density measurements. Due to their similar effective sizes, the measured conductance (G) range for zero-D pores (0.6 nS - 1 nS) in monolayer MoS₂ is similar to the conductance in biological ion channels. In the low-bias regime (± 100 mV), we also observe that the ionic conductivity of zero-D MoS₂ pores is largely independent of the bulk conductivity of different salt solutions and concentrations, making the pore almost equally conducting in 0.01 M KCl as in 3 M KCl. This is in contrast to larger-diameter pores in the same material where pore and bulk conductivity are approximately the same.^{52,114} These experimental findings are overall consistent with molecular dynamics simulations of sub-5 nm MoS₂ nanopores for 1 M KCl¹⁸⁸ and provide opportunities for further studies on low-dimensional ionic transport in solid state materials.

5.3 Experimental Methods

Pore fabrication³³ in 2D materials has been realized using several methods including electron^{130,167} and ion irradiation,¹⁹³ electroporation,^{42,102} polymer patterning,^{207,189} annealing/healing⁸³ *in-situ* transmission electron microscopy (TEM),¹¹⁸ and plasma etching.^{33,140,209} Electron beam drilling with sub-nm size probes enables the formation of individual pores while offering control over pore size and geometry. With the growing use

of aberration-corrected electron optics, transmission electron beams can be focus to diameters < 0.1 nm and have enabled studies of 2D materials down to an unprecedented resolution of ~ 39 pm.⁸⁰ Recent advancements in electron microscopy also open possibilities for precise nanopore device engineering in 2D materials: to controllably make single and few-atom-sized pores and to atomically control the pore edges. Defect and pore creation in 2D materials has been studied in vacuum inside the TEM^{95,124,125,127,145,212}, where 2D flakes typically hang off the supporting substrate or TEM grid and the chip is not designed for *ex situ* nanofluidics. Correlating advanced microscopy (AC-TEM) insights with transport properties from the same 2D devices measured *ex situ* has been challenging due to device requirements, such as having a single nanopore within an otherwise continuous membrane that does not leak, and a nanopore that is sufficiently stable in liquid or gas environments.

5.3.1 Fabrication of Zero D Pore

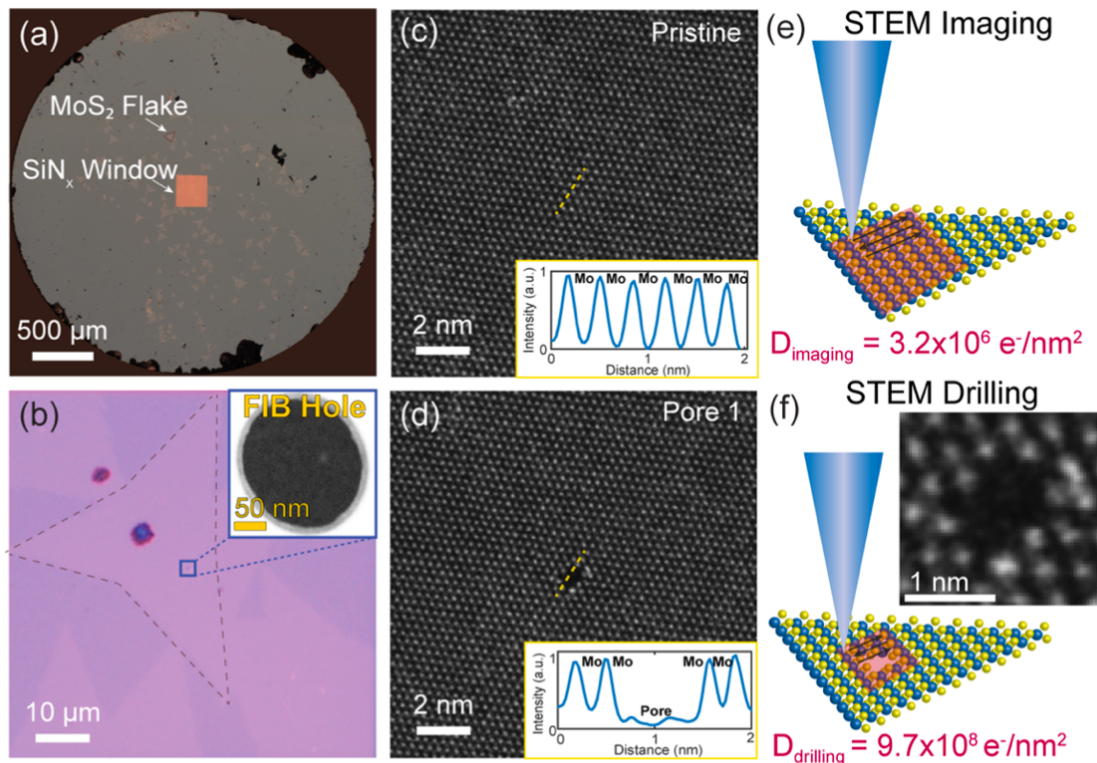


Figure 5.1. Selected area AC-STEM drilling for individual sub-nm MoS₂ pores.

(a) Optical image of a 3 mm-diameter SiN_x/Si circular chip platform (gray) for the TEM-beam fabrication of sub-nm pores with transferred MoS₂ flakes. (b) A monolayer MoS₂ flake (outlined by the purple dashed lines) transferred over a ~150–200 nm diameter FIB hole on a SiN_x/Si chip (inside the blue square) and annealed to form a seal with the supporting chip. Inset: Enlarged TEM image of the FIB hole with suspended MoS₂ flake. (c) Atomic resolution image of pristine (as-grown and transferred) monolayer MoS₂ suspended on a SiN_x/Si chip and (d) the lattice with a pore of effective diameter (d_{TEM} , see Methods for definition) ~1.1 nm. Z contrast is indicative of Mo and S atoms. (e) Schematic showing imaging of suspended monolayer MoS₂ under an AC-STEM beam (light blue) with a dose of $3.2 \times 10^6 \text{ e}^-/\text{nm}^2$. Mo and S atoms are shown in dark blue and yellow, respectively, while the electron exposure area is shown in orange. (f) Illustration of the sub-nm pore drilling using STEM selected area exposure technique with a dose of $9.7 \times 10^8 \text{ e}^-/\text{nm}^2$ and (inset) a completely drilled 0D pore.

Figure 5.1 shows the sub-nm diameter MoS₂ pore fabrication process using AC-STEM selected-area exposure of the 2D membrane. A monolayer MoS₂ flake is transferred onto a

$50 \times 50 \mu\text{m}^2$ window in the center of the 3 mm diameter TEM grid with a 30 nm-thick SiN_x film on top of a 290 μm -thick Si support substrate (Figure 5.1a). As indicated in the inset of Figure 5.1b, the electron transparent SiN_x window contains a ~ 150 nm diameter hole drilled with a focused Ga^+ ion beam (FIB). The MoS_2 flake $\sim 50\text{--}80 \mu\text{m}$ in size is positioned such that it is suspended over the FIB hole (Figure 5.1b) and annealed at 300 $^\circ\text{C}$ with Ar:H_2 . The pore drilling process starts by zooming into the suspended MoS_2 region covering the FIB hole to acquire a high-angle annular dark-field (HAADF) image (dose = $3.2 \times 10^6 \text{ e}^-/\text{nm}^2$, time = 8 s) of the pristine (as-grown and transferred) lattice (Figure 5.1c).

For a 2D material exposed to an electron beam, defect production is mediated by momentum transfer from energetic electrons to lattice atoms (knock-on damage) and in-plane electronic excitations (radiolysis).⁵ Here, we employ a STEM acceleration voltage of 80 kV, in which the maximum knock-on electron energy transfer is lower than the displacement thresholds for Mo (20 eV) and S (6.5 eV) atoms in monolayer MoS_2 .^{95,225} Previous reports have also demonstrated that an exposure dose of $\sim 10^6 \text{ e}^-/\text{nm}^2$ causes negligible radiolysis damage in monolayer MoS_2 . To drill a sub-nm diameter pore, the STEM instrument is switched from full scan ($13 \text{ nm} \times 13 \text{ nm}$ area) to selected area ($1 \text{ nm} \times 1 \text{ nm}$ area) exposure, in which the raster area of the electron beam is reduced, thereby increasing the dose to $9.7 \times 10^8 \text{ e}^-/\text{nm}^2$ (total exposure time = 10 s). At this exposure dose, radiolysis causes atoms to be sputtered off the lattice within the selected area,^{5,226} thus creating a sub-nm pore (pore 1, Figure 5.1d). The process is demonstrated schematically

in Figure 5.1 e,f. Atomic pores are formed by removing a fixed, small number of Mo and S atoms, with edges that mainly follow the lattice shape.

Compared to other electron exposure techniques such as high-resolution TEM (HRTEM) drilling and electron beam lithography, the use of a highly focused (probe beam with full width at half-maximum (fwhm) ~ 0.1 nm) STEM beam allows for simultaneous imaging and atom removal while creating pores with atomically precise geometries. The resulting electron micrographs of the 0D pore are crucial in accurately characterizing pore size and atomic structure for subsequent ionic transport measurements.

5.3.2 Geometric Pore Models and Atomic Structures of Fabricated Pores.

Selected area STEM drilling enables fabrication and investigation of a finite number of pores fabricated with an area below 1 nm^2 . MD modeling has shown how the pore edge configuration in a 2D material drastically affects its molecular transport.⁵⁷ For example, Heiranian et al. theoretically predicted that a nanopore with only Mo- terminated edges allows for higher water fluxes compared to pores that are mixed (i.e., edges with Mo and S atoms), S- terminated pores, and C-terminated (i.e., graphene) pores.⁵⁷ We first present a library of 27 geometrically possible combinations of missing atoms to create 0D MoS₂ pores, $\leq 1 \text{ nm}^2$ in area. These pore model configurations are shown in Table 5.1 and correspond to 1–5 Mo atoms missing and up to 12 S atoms missing. Pore areas range from (i) $A_{\text{model}} \sim 0.26 \text{ nm}^2$ for missing 1 Mo atom to (xxvii) $A_{\text{model}} \sim 1.0 \text{ nm}^2$ for missing 5 Mo and 12 S atoms.

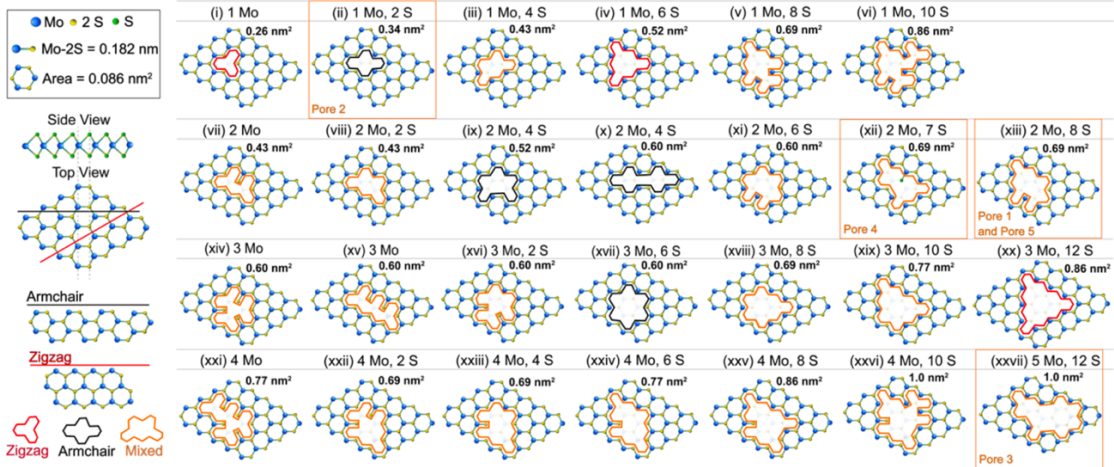


Table 5.1. Illustration of geometrically possible configurations of MoS₂ atomic (0D) pores with areas ≤ 1 nm².

Red and black pore edges correspond to zigzag and armchair edge configurations, respectively, and in orange are the mixed pore edges that are a combination of zigzag and armchair. The pore areas are approximately equal to the multiples of the area of a unit ring, 0.086 nm², comprised of 3 Mo and 6 S atoms, illustrated on the top left. These geometrical pore models assume perfect pore edges following the shape of the lattice, and their thermodynamic stability in vacuum and ionic solutions is not a priori guaranteed.

The geometric models provided in Table 5.1 are labeled as (n Mo, m S) and defined by (n, m), where n and m are the numbers of missing Mo and S atoms, respectively. These models show ideal pores without lattice distortions around the pore edges that we can occasionally observe in experiments. For example, in the image of pore 1 in Figure 5.f, we observe about 3–4 Mo atoms that have been displaced at the upper right side of the pore's edge. The specific pore models (i), (vii), (xiv), and (xxi) have only Mo atoms missing and are simply labeled as (1 Mo) to (4 Mo). To compute pore sizes, the area of one hexagonal ring, $A_{\text{ring, model}} = 0.086$ nm² (Table 5.1, top view of the lattice) is estimated from the normal distance from the Mo atom to the line connecting the two out-of-plane S atoms, a distance of 0.182 nm.^{190,188} For each model, the pore area is estimated from the number of missing hexagonal

rings. For example, for pore (i) (1 Mo), $A(1\text{Mo})_{\text{model}} = n_r \times A_{\text{ring, model}} = 0.26 \text{ nm}^2$, where the number of missing rings is $n_r = 3$.

Since STEM drilling preserves the localized atomic structure of the MoS_2 , pore edges are combinations of zigzag and/or armchair paths, which are defined in Table 5.1. A few examples of purely zigzag pores are (i) (1 Mo) and (xx) (3 Mo, 12 S), while purely armchair pores include (x) (2 Mo, 4 S) and (xviii) (3 Mo, 6 S). Conventional descriptions of pore diameter applicable for nm-scale pores break down since these pores can no longer be assumed circular (Table 5.1). A better way to capture the pore size and anisotropy is using the histogram of pore sizes in different planar directions passing through the pore's center of mass (see the Supporting Information of ref 4).¹⁹⁰ Here we use the number of missing Mo and S atoms along with a schematic of the most probable pore edge configuration and suggest to generalize this notation for similar 2D nanopore studies in the future.

While Table 5.1 shows the majority of the geometrically possible combinations of 0D pores in a monolayer MoS_2 lattice with an area below 1 nm^2 , it explicitly displays a few pore geometries that are likely feasible and can be fabricated through STEM drilling (such as in Figure 5.1). For example, armchair pores (ix) (2 Mo, 4 S) and (x) (2 Mo, 4 S) contain the same missing atoms of 2 Mo atoms and 4 S atoms, however, they are neither identical in their pore shape nor in area ((ix) 0.52 nm^2 and (x) 0.60 nm^2). Similarly, (xiv) 3 Mo and (xv) 3 Mo illustrate pores that are a combination of zigzag and armchair pore edges (i.e., mixed) with the same theoretical area of 0.60 nm^2 but differ in their shape as seen in Table 5.1.

In this case, we find that the pore in (xv) is difficult to experimentally fabricate, and we attribute this to its highly elongated shape: Under electron irradiation, pores prefer circular expansion due to the reduced displacement energy for atoms on the pore edge.¹²⁴ More convoluted and intricate pore edges such as those depicted in (xxi) and (xxii) pose a challenging fabrication and detection task even for tools with high controllability such as STEM due to the low displacement threshold and Z-contrast of chalcogen sites.^{95,193} Even more importantly, the structural stability of such artistically rendered, intricate pores is far from guaranteed, is likely lattice dependent, and yet to be explored and understood in different environments.

5.4 Experimental Ionic Transport Measurement of a Single Zero-D Pore Device

Atomic structure, formation, and stability of 2D MoS₂ pores (as in pore configurations in Table 5.1) made by the electron beam irradiation in vacuum have been investigated using density functional theory (DFT), for example, by Wang et al.²⁶⁶ who claimed that it is favorable for the ejected Mo atoms to attach to the 2D sheet as well as by other authors who also modeled the ion conductance through 2D MoS₂ pores.^{57,188,190} Ironically, many structural DFT stability simulations consider the material in vacuum. While these simulations seem suitable for TEM-only studies, their relevance is lower for nanofluidic devices where additional atoms and ions are present around the pore and can interact with the 2D material to form chemical bonds and even etch the material.^{33,42,34} Stability of pores in salt solution is therefore a different and more complex problem than stability of pores in vacuum, as evidenced by various electrochemical phenomena observed between salt

solutions and 2D materials such as oxidation.^{33, 42,34,35} There are exceptions of MoS₂ nanopore modeling in fluids,^{57,188, 190, 41} but further work is required. DFT combined with MD simulations may provide further insight, especially if they are in concordance with experimental findings. Our experiments outline several pores that were stable enough to be measured in ionic solutions.

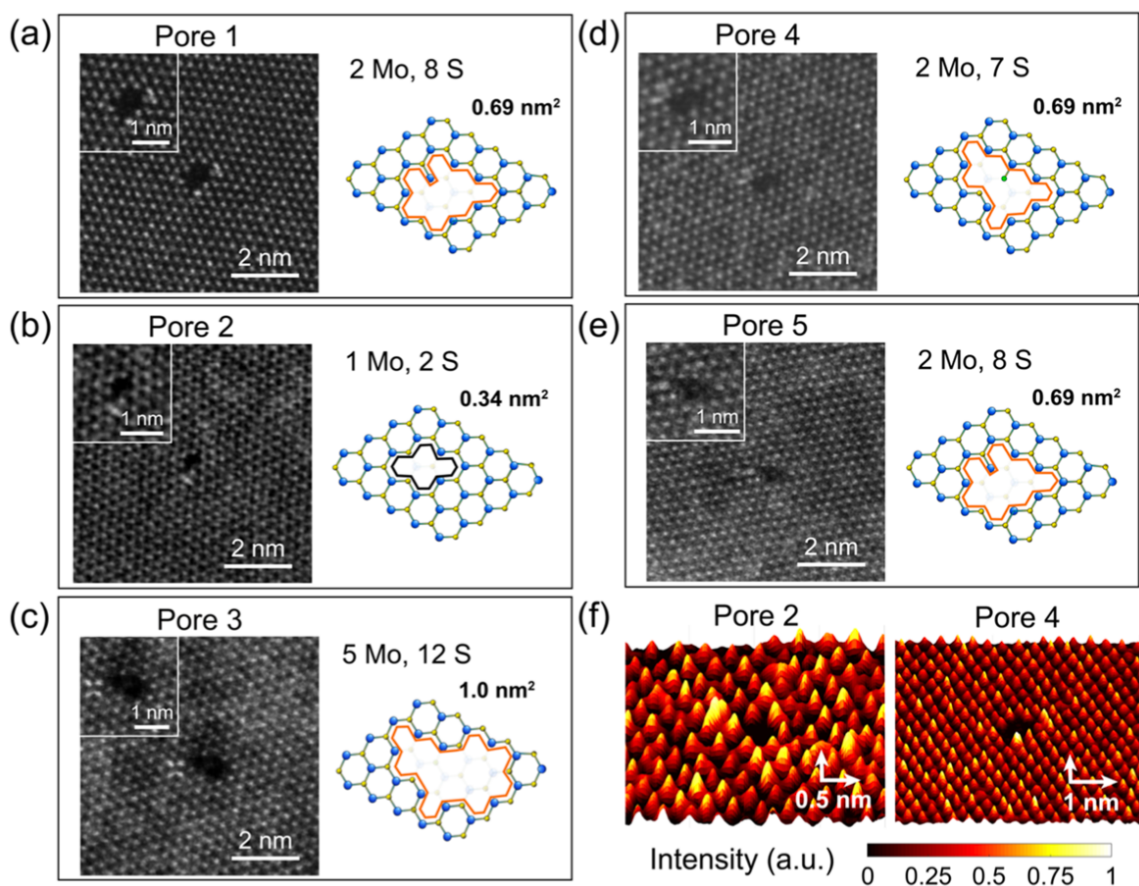


Figure 5.2. TEM images of MoS₂ (sub-nm-size) atomic pores and pore geometric models. Zigzag-armchair 0D pores in MoS₂.

AC-STEM image (left) and schematic (right) of 0D pores with (a) (2 Mo, 8 S), (b) (1 Mo, 2 S), (c) (5 Mo, 12 S), (d) (2 Mo, 7 S), and (e) (2 Mo, 8 S) atoms missing. (f) The 3D renderings of the intensity from the HAADF images of the pores shown in (b) and (d) are also provided.

Figure 5.2 demonstrates five example devices with AC-STEM HAADF images of zigzag and armchair structures successfully drilled and examined using the selected area technique shown in Figure 5.1c–f. The five pores include: (a) (2 Mo, 8 S), (b) (1 Mo, 2S),(c) (5Mo,12S),(d) (2Mo,7S),and (e) (2Mo,8S). Overall, the pores in this study range from 1–5 Mo vacancies with a pore area from 0.34 nm² to 1.0 nm². Figure 5.2f shows three-dimensional (3D) renderings of the intensity from the HAADF images of pores 2 and 4. The STEM beam can be controlled down to a ~ 0.1 nm probe size, nevertheless, the precision of this technique is limited due to sample drift and the relatively low displacement threshold (~ 7 eV) for S vacancies.^{31,95} As a result of this, AC-STEM is mainly employed to create defects at Mo sites ($Z = 42$), while further efforts are needed to precisely control the composition of chalcogen (S) sites.

Pore Contamination: It is likely to have 2D membrane and pore contamination by a carbon/graphitic film partially or completely covering the MoS₂ that cannot be easily observed in our HAADF images, as specifically discussed for similar MoS₂ films by Wen *et al.*²¹⁵, who demonstrated the detection of often-missed, lighter atoms (C, O, N) by 4D-STEM imaging. This additional material could alter the pore's wetting and other properties, reduce its diameter or completely block the pore, and also yield smaller ionic current than predicted since the contaminated pore may be significantly thicker. For larger, nm-diameter MoS₂ pores, a good agreement was found between the ionic conductance models and expected 2D MoS₂ pore thickness in the range ~ 0.7 nm to 1.6 nm^{43, 114}, with the quoted device failure for 2 nm to 20-nm-diameter MoS₂ pores from membrane leakage ($G > 300$ nS) or pore clogging ($G < 10$ nS) of $< 30\%$.¹¹⁴ Future efforts of modeling 2D pores and

other ultrathin devices may wish to consider effects of carbon contamination, whose role is becoming increasingly more recognized and could be considered in interpreting behaviors of pores and devices at the atomic scale.

5.4.1 Experimental Ionic Properties of Single 0D Pores

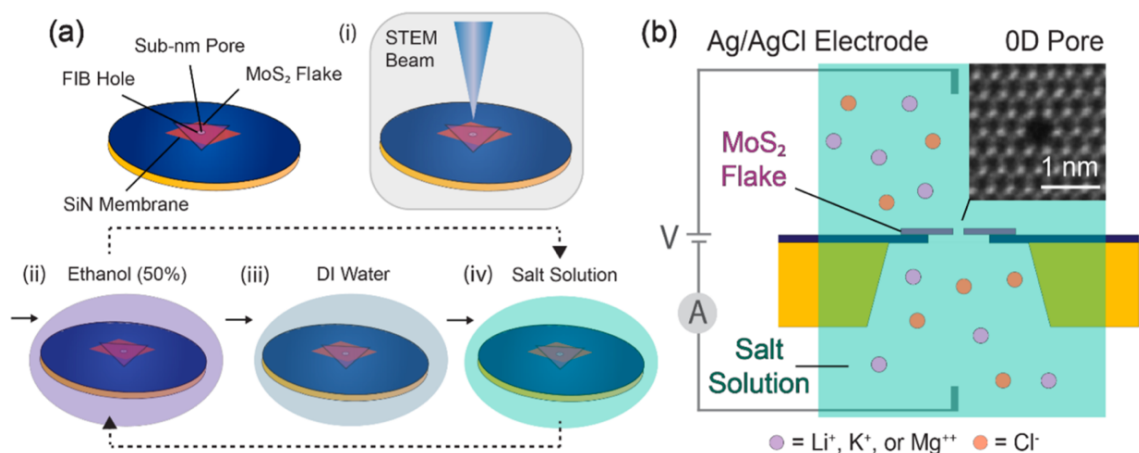


Figure 5.3. Schematic of single pore STEM drilling, solution treatment, and measurement setup.

(a) Fabrication and pore wetting workflow for a suspended monolayer MoS₂ 0D pore. (i) Drilling a sub-nm pore on the suspended MoS₂ flake. (ii) Wetting of pore with ethanol (50%) for 15– 30 min. (iii) Device rinsed in DI water before ionic measurement. (iv) Device flushed with salt solution for ionic measurement. (b) The design of nanopore ionic measurement consisting of a 2D MoS₂ nanopore separating two chambers of salt solution with Ag/AgCl electrodes (mounted on a microfluidic platform, not shown). (Inset) A sample HAADF image of a sub-nm MoS₂ pore.

After drilling in ultra-high vacuum ($p \sim 1.7 \times 10^{-5}$ Pa) in the aberration corrected STEM, the zero-D pore is immediately stored in a vacuum-sealed container prior to experimental measurements to minimize oxidation-induced pore changes and expansion.^{30,34,38} Figure 5.3(a) displays a schematic of the 3 mm-diameter SiN_x/Si device (also pictured in Figure 5.1(a)) with a monolayer MoS₂ flake. The single zero-D pore that is drilled and imaged is located in the center of this membrane as explained previously in Figure 1. A number of

studies have highlighted the importance of wetting nanochannels and pores prior to ionic measurements.^{39, 43} Here, we elaborate on the dedicated pre-treatment steps used to facilitate wetting of sub-nm MoS₂ pores while monitoring and examining intermediate responses before a measurable current state. We use a 1:1 mixture of ethanol and DI water to help wet our devices using the process shown schematically in Figure 5.3(a) (ii)-(iv). The process begins by immersing the device in the ethanol-water mixture for 15-30 minutes (Figure 5.3(a) (ii)). The following steps include rinsing with DI water and immersing the chip in salt solution (Figure 5.3(a) (iii)-(iv)). These last two steps take about one minute each with a total time of a few minutes. This cycle of processes is repeated sequentially a few times (about 3 to 6 times) until a detectable current (discussed later in Figure 5.4) is observed. Ionic transport measurements are performed with two-terminal Ag/AgCl electrodes (Figure 5.3(b)). The inset of Figure 5.3(b) shows an AC-STEM image of a pore which was not electrically measured. During measurements, we limit the applied voltage to ± 100 mV to minimize electric-field-induced damage to the device.^{43, 190}

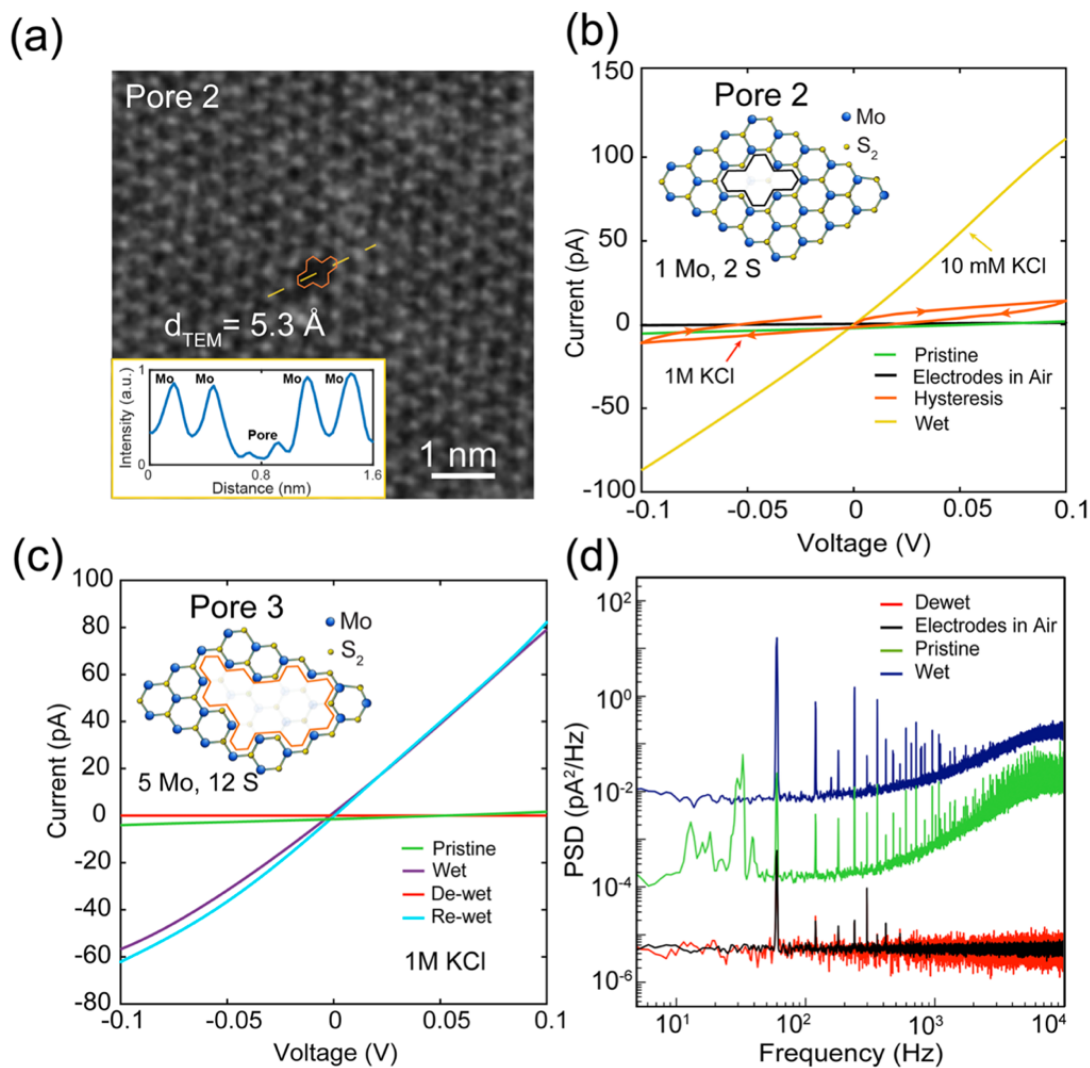


Figure 5.4. Ion current–voltage and noise curves in single pore devices.

(a) AC-STEM image of the as-fabricated sub-nm pore 2 (1 Mo, 2 S) in vacuum, prior to any I–V measurements with $d_{\text{TEM}} = 0.53 \text{ nm}$. (b) Control device and pore device I–V measurements: (black) bare Ag/AgCl electrodes in air, (orange) partially wet pore 2, and (yellow) likely a fully wet pore 2 after exposure to ethanol for 15 min. (c) I–V measurements of pore 3 (5 Mo, 12 S) with $d_{\text{TEM}} = 0.87 \text{ nm}$ in 1 M KCl, pH 8.7 (purple) after 15 min ethanol exposure, (red) de-wetting after an additional 30 min in 1 M KCl, and (blue) again after following the wetting procedure it was found to rewet. For comparison, I–V curves for a pristine MoS₂ membrane are shown in green in both (b) and (c). (d) Current noise PSD of samples in various conditions: (green) pristine membrane (no intentional holes), (black) bare Ag/AgCl electrodes in air, (red) a pore before ethanol wetting, and (blue) a pore after ethanol wetting.

Wetting Behavior of Zero-D Pores:

We observe that the wetting of 0D pore devices is a challenge for ionic measurements, indicating their hydrophobic nature. Figure 5.4 represents two different sequence of events involved in wetting 0D MoS₂ pores. The HAADF image of pore 2 shown in Figure 5.4a indicates a structure with area of $\sim 0.22 \text{ nm}^2$ ($d_{\text{TEM}} = \frac{\sqrt{4A_{\text{TEM}}}}{\pi} = 0.53 \text{ nm}$), consisting of 1 Mo and 2 S atoms missing (also shown in Table 5.1 as (ii)). The method to extract area from an HAADF images is shown in section 5.10, Figure 5.5. The intensity profile of the dashed yellow line is shown in the inset of Figure 5.4a and demonstrates the absence of a single Mo atom in the periodic lattice structure. In the linescan across this pore, we also observe residual peaks whose intensity appears consistent with the presence of single S atoms. To better characterize and understand differences in conductance levels observed in a single 0D pore sample (from vacuum to salt solution via ethanol immersion), we empirically categorize its observed transport behavior into three different states:

State 1: Negligible conductance $< 0.1 \text{ nS}$ ($\sim 10 \text{ pA}$ for $V < 0.1 \text{ V}$) with I–V curves similar to those measured in pristine membranes in solution. When pores were immersed in salt solution directly from vacuum, without any ethanol treatment, immeasurable ionic current was obtained ($< 10 \text{ pA}$ in some cases), similar as the noise of the open circuit setup. This means that either (i) the ionic solution did not reach the pores (unwet state) or that (ii) the ion current through these pores is below the detection limit. An example of this state is shown in red in Figure 4c.

State 2: Measurable ionic current with pronounced hysteresis in I–V curves. In this case, samples were immersed in ethanol prior to ionic measurements. The I– V curves were

characterized by pronounced hysteresis but measurable signals. This is possibly due to incomplete pore wetting and gas molecules dissolved in solution and present on the surface of the microfluidic chip that make their way to the pore region and affect the conductance.^{151, 176} Hysteresis in I–V curves were noticed to be temporary in some devices before obtaining a conducting state (state 3). The orange curve in Figure 5.4b shows an example of state 2.

(3) State 3: Measurable ionic current with no hysteresis in I–V curves. After immersing the samples for adequate (>15 min) time in ethanol, we observed I–V curves with no hysteresis corresponding to a measurable conductance up to ~ 0.8 nS. Such curves are shown in yellow in Figure 5.4b as well as purple and blue in Figure 5.4c. Additional examples of all three states can be found in section 5.9, Figure 5.8.

Current–voltage characteristics of samples in this work show different scenarios with various sequences of events. Three of such sequences involving states 1–3 are shown for pore 2 (Figure 5.4b), pore 3 (Figure 5.4c), and pore 4 (Figure 5.55), all successfully resulting in a measurable current and therefore ending in state 3. Figure 5.4b shows the first scenario where the ionic current–voltage curves obtained for pore 2 go through the following stages in the wetting process: (i) After soaking in an ethanol:water mixture for 15 min (see section 5.9), we measure an I–V curve (orange) in 1 M KCl with hysteresis behavior where the maximum current is ± 10 pA. This value of current is comparable to pristine MoS₂ membranes with ethanol wetting (green) but shows a looplike I–V curve characteristic of state 2. (ii) After placing the device into ethanol for 3 h, we measure in 10 mM KCl and observe an I–V curve (yellow) with $G \sim 0.98$ nS (i.e., state 3).

We also have fabricated several pores which led to hysteresis- like I–V behavior and ended in state 2 (pores 1 and 5 shown in Figure 5.1) or had other issues such as excessive PMMA contamination. Pore/membrane breakage was observed in three devices which exhibited excessive conductance (~ 375 nS or higher, see section 5.10 Figure 5.7a) caused likely due to (1) an unstable pore with significant PMMA contamination introduced during the transfer process and (2) device damage during measurements. Out of a total of ~ 30 fabricated devices, 41% accounted for devices with drilled pores where ionic measurement was attempted. This also includes devices which had multiple sub-nm pores, for example, pores 6–8 in section 5.10 Figure 5.7. In the case of pore 7 which was measured up to ± 0.5 V in 1 M KCl, we observe a nonlinear trend in I–V with a conductance $G \sim 2.2$ nS. In order to clearly distinguish between the background signal and signal dominated by pore conduction, the control I–V curves for bare Ag/AgCl electrodes (black) and pristine MoS₂ membranes (green) were also measured (Figure 5.4b). As expected, the bare electrodes in air show a negligible conductance $G \sim 10$ pS with a current of ~ 0.5 pA at -100 mV to 1 pA at $+100$ mV, also comparable to pristine membranes, $G \sim 10$ – 30 pS.

We do not detect any systematic dependence of conductance on pore size or geometry, but rather a stochastic set of values. For example, pore 2 showed a higher conductance than pore 3 despite a smaller pore size recorded during TEM drilling and measurement at a lower KCl concentration (Figure 5.4b vs Figure 5.4c). This may be a real, counterintuitive effect, or it may be an artifact from pores changing during the course of the experiments. Previous non-equilibrium molecular dynamics (NEMD) conductance simulations on selected MoS₂ pore geometries (including pores (ii) and (xix) from Table 5.1) showed that

conductance varies in magnitude (~ 0.01 nS to ~ 1 nS) in this pore size range (~ 0.4 to 0.9 nm).^{190,188}

5.5 Discussion on Sub-nm MoS₂ Pore Studies^{57,190,43,42,188}

It is useful to compare our findings with previous measurements. Single MoS₂ monolayer pores with somewhat larger diameters (1.1 nm and 1.4 nm, directly imaged by AC-TEM) yielded measured $G \sim 1.5$ nS and 10 nS in 1M KCl, respectively, and non-equilibrium molecular dynamic simulations for pores as in (ii) and (xix) in Table 5.1 computed $G \sim 0.02$ nS and $G \sim 0.03$ nS, respectively.¹⁹⁰ Feng *et al.*⁴³ reported conductance in pores made by electroporation to be ~ 1 nS (extracted at 100 mV) for quoted diameters of 0.3 nm, 0.6 nm, 0.8 nm and 1 nm,⁴³ but failed to explain how pore diameters were obtained given that the pore images were not presented. Salt (bulk) conductivities are not directly applicable for sub-nm pores,¹⁸⁸ and a simple cylindrical pore model for conductance when used to gauge the size of electroporated pores⁴² is not sufficient. Up to ± 5 V was applied (Section 5.10 Figure 5.10 in Ref.⁴³) in 1 M KCl across a pore of presumably 0.3 nm in diameter (a single sulfur vacancy),⁴³ while 0.8 V was previously found to be the critical voltage⁴² above which MoS₂ membrane can break. Single sulfur vacancies are common defects^{95,145} in “pristine” (*i.e.*, membranes without intentional holes) MoS₂ membranes, but give negligible ionic conductance of pristine membranes, < 0.01 nS¹⁹⁰ (see also Figure 5.4), rather than 1 nS. These experimental details require attention in order to experimentally test and reproduce the far-reaching conclusions⁴³ about a “voltage gap” for transport, the “signature” of “Coulomb Blockade”, that increases as the pore diameter decreases. The “voltage gap” proportional to multiples of $k_B T$ for which there is no transport, is not

observed in our measurements of pores with well-characterized structure by AC-TEM, where we report the low-bias conductance consistent with the picture of reduced pore conductivity compared to bulk. Furthermore, authors claimed⁴³ that soaking in ethanol, “30 min to 24 h to rule out hydrophobic effects”, “eliminates the possibility that nonlinearity originates from hydrophobic effects”.⁴³ However, we find that while ethanol helps obtain measurable currents, we did not find that ethanol treatment alone guarantees that pores will be fully wet or that it eliminates hydrophobic effects and possible resulting nonlinearities in I - V curves. Theoretical simulations appear to miss this connection to experimental details (including pore contamination),^{57,188,180,190} making the role of the alcohol-based wetting solvent unclear from an energy barrier standpoint which could elucidate its role in modification of the pore surfaces.

5.5.1 Reversible Wetting–Rewetting Behavior

It is important to note that these conducting states are reversible in a sense that a conducting pore (State 3) can switch to a non-conducting state (State 1) (more discussion on hydrophobicity in pores is below).^{151,176,9,75,123,160} This implies that the ionic current paths may easily close in zero-D pores. We find that if the same pore is treated in ethanol again, it can start to show measurable ionic current and conduct (State 3). Ethanol is therefore critical for ionic measurements in 2D materials and especially for smaller-diameter zero-D pores here. This is demonstrated in Pore 3 (5 Mo, 12 S), which shows the second scenario where the pore was initially measured in State 1 after both 30 seconds and 5 minutes of ethanol wetting where we obtained an immeasurable and unstable I - V response. However, after an interval of 15 minutes in ethanol, the pore was observed to conduct (*i.e.*, State 3)

with $G \sim 0.73$ nS in 1 M KCl (purple curve in Figure 5.4(c)). This conducting state (~ 0.7 nS) was verified periodically after 10 minutes but was found to de-wet and reverted to State 1 after about 30 minutes after measuring in salt solution. This is denoted by the red I-V curve in Figure 5.4(c) with a max current of 0.9 pA at -100 mV and 0.6 pA at +100 mV. By repeating the wetting procedure, the pore was measured after 60 minutes, and was found to return to the conducting state 3 (light blue) with a conductance of 0.72 nS in 1M KCl. Later, this pore was stored in an ethanol mixture overnight and observed to still conduct after 14 hours with similar conductance values of 0.73 nS in 1 M KCl and 0.72 nS in 1 M LiCl.

5.5.2 Hydrophobic Characteristics of Single Atomic Pores

We observe that pores can wet and de-wet repeatedly, manifested by the fluctuation in the pore's conductance “on” and “off” upon successive current-voltage measurements, on the timescales of minutes. This resembles, at least qualitatively, the behavior of biological (K⁺) ion channels where “hydrophobic gating” is observed, an “on/off” behavior where the channels opens and closes for ion flow due to changes in the degree of pore wetting and presence of nanobubbles.^{9,75, 160} In biological ion channels, the current depends on the degree to which the ion channels are wet with liquid which, in turn, was found to depend on pore diameter, on the hydrophobic nature of atoms lining the pore and the applied voltage.⁹ In our case, the 2D materials are largely hydrophobic, and wetting of the surface is a challenge. We explored an alcohol (ethanol) pre-wetting procedure in the context of sub-nm pores to maximize the amount of electrolyte that flows through the pore and to maximize the measured current.

The hydrophobic nature of 2D material solid-state nanopores has been previously observed and ethanol-prewetting of MoS₂⁴³ and WS₂³⁴ was found to help obtain measurable ion currents consistent with the pore size. Wetting can be probed further by applying external pressure to force the liquid transport through the pore.¹²³ The general concepts of wetting and de-wetting of pores used here are not new. Difficulty of pore wetting, the “dry”, “wet” and “partially-wet” states of hydrophobic solid-state (silicon nitride) and polymer pores with diameters of the order of ~ 10 nm and ~ 100 nm, and the corresponding hysteretic behavior observed in I - V curves, have been reported a while ago.^{151, 160, 176} A hydrophobic pore can transition between the dry (non-conducting) and the wet (conducting) state upon voltage application. As voltage is increased, the pore can transition to a conducting state at higher bias resulting in an apparent non-linear I - V curve. This phenomenon was referred to as “voltage-induced gating”¹⁷⁶ and “electric-field-induced wetting and dewetting”¹⁵¹ of a fabricated hydrophobic pore. Therefore, by applying voltage, a hydrophobic pore can be forced into a partially or fully-wet, conducting state. In this fully conducting state, the pore allows a maximum current possible based on its size, *i.e.*, the same current as in a hydrophilic pore of the same size. In addition, MD simulations have shown ionic “memcapacitive effects” and hysteresis loops (I - V measurement in a loop with no crossover) in nanopore systems, that depend on frequency and were proposed to arise from polarizability of ionic solutions.⁹⁸

Non-linearities in I - V curves can originate from hydrophobic effects and also from the ion confinement effects in small diameter pores, when their sizes are comparable to sizes of hydrated ions and Debye lengths. In biology, hydrophobicity is an essential property for ion channel behavior and gating, and it can be an inherent property of the pore. For

example, stable gas pockets (“bubbles”) can form inside hydrophobic regions of the pore; a sub-nm-wide pore region is required to make the bubbles stable long enough to observe relevant biological effects and when bubbles break, ions and water molecules flow through.¹⁶⁰ Analogous effects could be expected in solid-state pores and, because they are fabricated, these pores could serve as model systems to study such effects further and design artificial pores with specific functions. For example, according to modeling of MoS₂ pores, water flux can vary depending on whether Mo only, S only or mixed atoms, Mo and S, are at the edges.⁵⁷ Another approach to controlling the degree of hydrophobicity would be to coat the 2D pores, for example by atomic-layer-deposition of TiO₂, as demonstrated on graphene pores, to make them hydrophilic while only slightly increasing the pore thickness.¹³⁰ It is interesting to note that the non-linearity in I - V measurements is largely absent in molecular dynamics simulations¹⁹⁰ and this is yet to be understood.

Pores may be dynamic in shape and change their conformations and edge termination – like in ion channels, this is a possibility for solid-state pores as well, but it is hard to probe directly and more thermodynamic modeling would be beneficial to inform the experiment. It is likely that the pore structure could change over time. Atomic-scale fluctuations at the pore edge could have additional contributions to the degree of hydrophobicity inside of the atomic-scale pores. In biological pores, nanobubbles within the pore have been theoretically considered as possibly responsible for ion channel gating.¹⁶⁰ The extent to which the different parts of the pore itself are hydrophilic or hydrophobic depends on the ion channel diameter, the applied voltage and the local properties of pore edges and their interactions with ions and water molecules.⁹ Future

studies can attempt to directly probe effects of these parameters in atomic 2D pores and the degree to which these effects can be controlled at the atomic scale.

5.5.3 Noise Characteristics of Single Atomic Pore Chips

In addition to I–V characteristics, we find that the power spectral density (PSD) of these states yields insights into frequency- dependent properties and can be used to help determine the extent to which a 0D pore is wet. PSD in solid-state nanopores is given as

$$PSD = \frac{AI^2}{f^\alpha}$$

where I denotes the ionic current, A is the noise coefficient, α is the low-frequency noise component, and f is the frequency.¹⁸⁶ The PSD acquired at different stages of the wetting process for pore 4 is shown in Figure 5.4 d. For the bare electrodes (black), we obtain a noise coefficient of $A = 2 \times 10^{-7}$ and noise component of $\alpha = -0.3$, which is representative of instrumentation noise. Additionally, the spectrum for bare electrodes is identical to the PSD for a de-wet, incomplete wet pore (red), suggesting the absence of a conducting ion channel. For pore 4 (2 Mo, 7 S), a completely wet with ethanol (navy blue), we note $A = 5 \times 10^{-6}$ and $\alpha = -0.47$, which is similar to that of the pristine MoS₂ membrane wet with ethanol (green, $A = 7 \times 10^{-5}$, $\alpha = -0.14$). Crucially, the PSD for both cases exhibits a decrease in the sub- 10^2 Hz regime (Figure 5.4 c) compared to the rest of the frequency range and is characteristic of $1/f$ noise in conducting solid-state pores.^{34,221,190,231} This is in stark contrast to the flat PSD obtained for both bare electrodes and de-wet pore and suggests that ethanol is essential in creating a conducting ion channel through either intrinsic defects (in the pristine membrane) or STEM- fabricated 0D pores (in pore 4). A

combination of I–V and noise analysis can therefore be utilized to better understand these states (states 1–3) to determine whether a sub-nm pore is completely wet.

5.6 Confinement Effects in Zero D with various Ionic Molarities

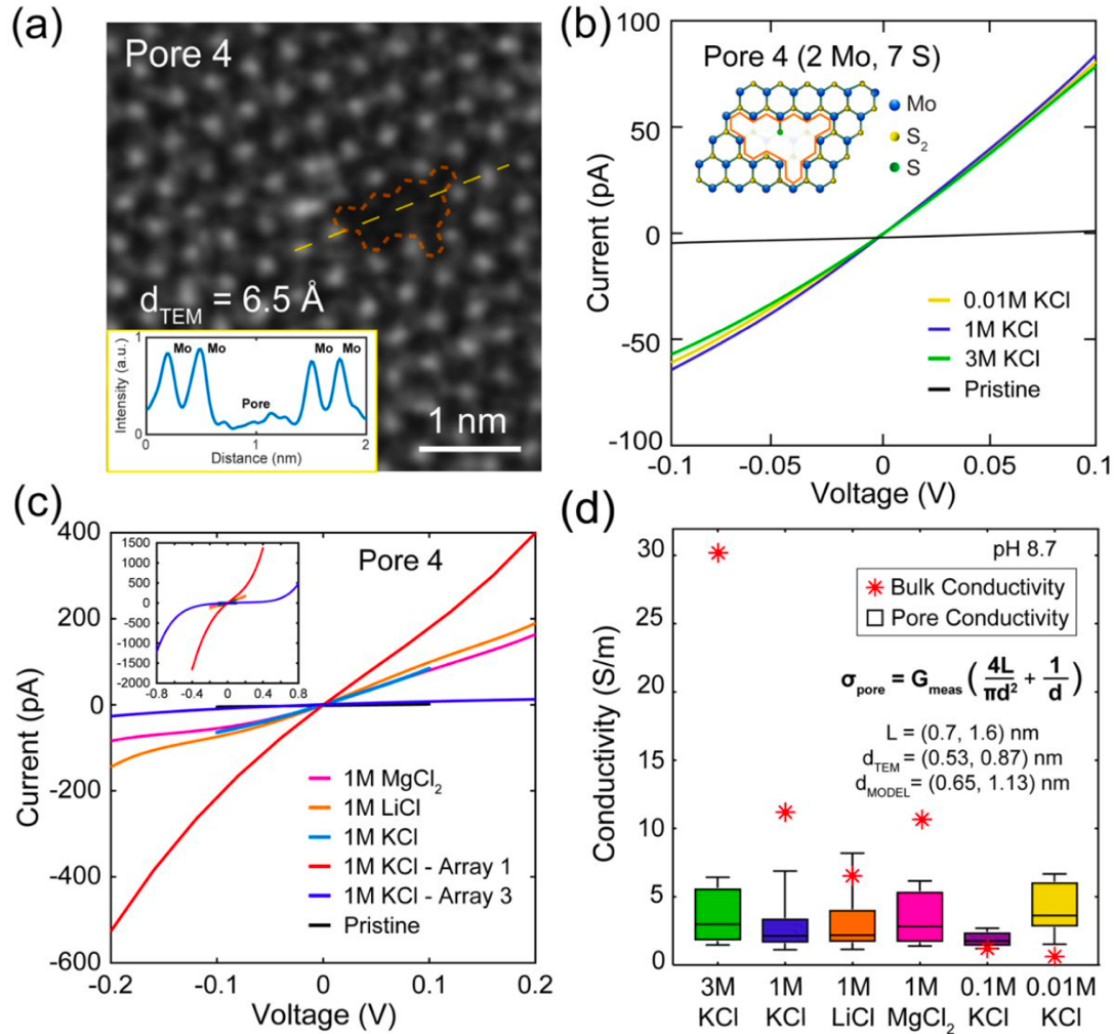


Figure 5.5. Ion current–voltage curves and pore conductivities calculated from a bulk model

(a) AC-STEM image and (inset) intensity profile of a sub-nm pore (pore5) with $d_{\text{TEM}} = 0.65 \text{ nm}$, where $d_{\text{TEM}} = 4A_{\text{TEM}}/\pi$ and A_{TEM} is the pore area. (b) I–V characteristics and (inset) schematic of pore 5 for various molarities of KCl–10 mM (yellow), 1 M (navy), and 3 M (green). (c) I–V curves for pore 5 obtained with different salt solutions, 1 M LiCl (orange), 1 M MgCl_2 (pink), 1 M KCl (light blue), and a pristine MoS_2 membrane (black). Also shown in (c) are the current–voltage curves for arrays of sub-nm pores (labeled as array 1 and array 3) produced with low (dose 1, red) and high (dose 3, blue) doses of FIB

irradiation reproduced here from previous work for comparison¹⁹⁰. (d) Pore conductivities of chloride-based salts (pH 8.7) including 1 M LiCl (orange), 1 M MgCl₂ (pink), and KCl at concentrations of 3 M KCl (green), 1 M KCl (navy), 0.1 M KCl (purple), and 0.01 M (yellow) from 3 different sub-nm MoS₂ pores (pores 2–4) are presented. Each bar includes pore conductivity derived from eq 2 (shown in inset) for upper and lower bounds of thickness ($L = 0.7$ nm and 1.6 nm) and diameter ($d_{\text{TEM}} = 0.53$ nm and 0.87 nm, and $d_{\text{Model}} = 0.65$ nm and 1.13 nm). Bulk conductivities of these salt solutions are plotted for comparison as asterixis (red).

Another example of such a zigzag–armchair pore (pore 4) is shown in Figure 5.5. A HAADF image of this pore is shown in Figure 5.5a, alongside its atomic edge configuration shown in the inset of Figure 5.5b. Pore 4 has 2 Mo atoms and 7 pairs of S atoms missing, shown as (xii) in Chart 1, corresponding to a geometric area of 0.69 nm². This is, again, confirmed by the Z contrast produced across the pore (yellow line) in the inset of Figure 5.5a. In the case of pore 5 (which is our third I–V scenario), abiding by the procedure outlined in Figure 5.3a(i–iv), we obtain the current–voltage measurements for multiple salt solutions and salt concentrations. First, we examine the conductance in the case of different salt concentrations in Figure 5.5b: 10 mM KCl (yellow), 1 M KCl (blue), and 3 M KCl (green) at pH 8.7. We clearly observe a phenomenon where the 0D pore demonstrates an ionic conductance largely independent of the salt concentration, all three I–V of 10 mM, 1 and 3 M KCl correspond to $G \sim 0.71$ nS, 0.69 nS and 0.75 nS, respectively, extracted as slopes of the linear fits to the I–V curves in the voltage ranges ± 100 mV.

I–V characteristics acquired for other salt solutions such as 1 M LiCl (orange) and 1 M MgCl₂ (pink) from an applied voltage range of ± 200 mV are presented in Figure 5.5(c). Given that these salt solutions have a significant difference in bulk conductivity (precisely, 1 M LiCl = 9.5 S/m, 1 M MgCl₂ = 12.3 S/m, 10 mM KCl = 0.14 S/m, 1 M KCl = 10.8 S/m and 3 M KCl = 29.28 S/m), it is noteworthy that we observe a small change in pore

conductance value in these salt solutions through the zero-D pore in the ± 200 mV range, compared to the difference in respective bulk values. In contrast to the typical linear behavior of nm-sized pores, these zero-D pores also exhibit somewhat non-linear current-voltage curves. These non-linearities are more evident at higher voltages, as shown in the inset of Figure 5.5(c), which are I-V curves obtained from an array of sub-nm zero-D pores produced in the MoS₂ membrane by FIB irradiation and measured over a range of ± 800 mV.¹⁹⁰ These arrays contained on average $\sim 300 - 1200$ small pores of diameters smaller than ~ 1 nm (out of which $\sim 30 - 240$ pores on average were larger than 0.6 nm – the hydrated K⁺ ion diameter) and these samples exhibited G in a wide range ~ 0.5 nS to 50 nS in 1M KCl (these G values are for the dose used for “Array 3”). While the particular sample “Array 3” in Figure 5(c) is found to be less conducting than Pore 4, the mean conductance of all such measured samples, FIB irradiated at the same dose, was larger than G of Pore 4, with a mean conductance value of ~ 20 nS.¹⁹⁰ Additional, slight non-linearity is also observed in case of multiple pore devices, for example Pore 7, in Section 5.10 Figure 5.7 (e) for 1M KCl. We also plot in Section 5.10 Figure 5.6, a bar graph of calculated conductance ranges by fitting a line to *I-V* curves over several voltage ranges, such as ± 30 mV, ± 50 mV, ± 100 mV, ± 200 mV from zero-D pores measured in this work (Pores 2, 3, 4) in section 5.10 Figure 5.6. We note that there is a difference of ± 0.01 to 0.086 nS across different voltage range for a given zero-D pore, reflecting the degree of non-linearity. About 42% of the zero-D pores fabricated, yielded a conductance of 0.7 nS- 0.9 nS across various cation-based chloride salt solutions from 0.1 M to 3 M with a slight variation in conductance (± 0.1 nS). While the other devices showed hysteretic *I-V*, the current was immeasurably small and/or pores could not be wet.

5.7 Calculation of pore conductivities based on measured conductance and pore sizes

We can estimate pore conductivities based on measured conductance G and effective pore diameters from TEM images prior to I - V measurements, d_{TEM} , and those obtained from pore models, d_{Model} , assuming a known pore thickness, L , discussed below. Using a continuum model applicable for bulk behavior in nm-size and larger diameter solid-state pores, conductance G can be well-described for solid-state pores²⁹:

$$G = \sigma \left(\frac{4L}{\pi d^2} + \frac{1}{d} \right)^{-1} \quad (\text{Eq. 2})$$

where σ is conductance of the solution that depends on the molarity, d is effective pore diameter (assuming circular pores) and L is the effective pore thickness; d and L correspond to the effective dimensions of the ionic conducting cylindrical channel. As d and L approach zero, ions are confined in spaces of dimensions comparable to ionic radii, and the ion concentrations, mobilities and hydration are theoretically different from bulk^{192,24,40} Perez *et al.*¹⁸⁸ recently proposed an analytical expression similar to Eq. 2, based on inputs from molecular dynamics simulations, for small MoS₂ pores, but with a modified multiplication pre-factor σ in Eq. 2, to reflect the reduced K⁺ and Cl⁻ ion concentrations and mobilities compared to bulk (See the Equation in Section 5.10). In other words, for small pores, the authors proposed that one can consider that a small pore has a modified conductivity compared to bulk, and Eq. 2 can be modified by replacing σ with another function of diameter, $\sigma_{\text{pore}}(d) \neq \sigma_{\text{bulk}}$. For an effective MoS₂ pore diameter around 1 nm, the ion mobility was computed to be about 60% of bulk mobility and ion concentration to be about 30% of bulk concentration.¹⁸⁸

In Equation 2, the total resistance $R = 1/G = R_{pore} + R_{access}$, where $R_{pore} = (\frac{4L}{\sigma \pi d^2})$ is the resistance of the pore, which is modeled as a cylinder. The second term, $R_{access} = (\frac{1}{\sigma d})$ is the so-called “access” resistance, arising from the solution in the top and bottom hemispheres on the two sides of the membrane.^{58,4} In our case, the effective pore diameter, d , and the effective pore length, L , are comparable (both ~ 1 nm). For L in our calculations and for error estimation, we use here a range of values for L previously used, from $L = 0.7$ nm^{42,190} (the geometric thickness of the MoS₂ membrane) up to $L = 1.6$ nm estimated from previous MoS₂ pore conductance measurements on larger diameter pores.¹¹⁴ For the effective diameter estimates here, we use, $A_{TEM} \sim 0.22$ nm² to 0.59 nm², and $A_{Model} \sim 0.34$ nm² to 1.0 nm², yielding d_{TEM} from ~ 0.53 nm to ~ 0.87 nm, and d_{Model} from 0.65 to 1.12 nm. The pores could be thicker if there is contamination and have larger diameters if they expanded over time.

From measured conductances, G_{meas} , we can estimate the equivalent pore conductivities that would yield these conductances, a perspective proposed by Perez *et al.* to view sub-5 nm diameter MoS₂ pores,¹⁸⁸ as

$$\sigma_{pore} = G_{meas} \left(\frac{4L}{\pi d^2} + \frac{1}{d} \right), \quad (Eq. 3)$$

,where G_{meas} is the measured conductance, d is the diameter, and L is the pore thickness. Using measured conductance from zero-D pores, a range of pore diameters from AC-STEM images, from corresponding pore models and L values from 0.7 nm - 1.6 nm^{43, 114}, we calculated σ_{pore} , plotted for various salt solutions and concentrations in Figure 5.5(d).²⁹,

^{58,3} Therefore, error bars in Figure 5.5(d) reflect uncertainties in d from our analysis. Errors are plotted using the ranges of d_{TEM} and d_{MODEL} for d , and the range from 0.6 nm to 1.6 nm for L .

For comparison, also plotted in red symbols are the corresponding bulk conductivities for each solution. Our results at 1 M KCl display $\sigma_{\text{pore}}/\sigma_{\text{bulk}} = 25\% - 65\%$ (for 0.53 nm - 0.87 nm diameter pores) which also somewhat agrees with the trend from molecular dynamics simulations for sub-5 nm MoS₂ pores where they reported 8% - 40% (for 0.7 nm - 1.25 nm diameter pores).¹⁸⁸

The conductance values observed are a bit smaller than 1 nS and similar across different concentrations and cations (K⁺, Li⁺, Mg⁺⁺). Furthermore, I-V characteristics are non-linear, although non-linearities are mostly pronounced for higher voltages (Figure 5.5(c)). While hydrophobicity can lead to such observations as discussed above, another contributing factor in small pores is the spatial confinement and interactions experienced by the salt ions when the pore is of the similar size to the size of the hydrated salt ions. This has also been shown in other MD simulations where dehydration of the first hydration layer, orientation of water dipoles inside and outside the pore dictate the type of non-linearities observed in these small measurable currents.¹⁶⁴ Further, Richards *et al.*¹⁵⁷ showed that ion transport is hindered when pore size is comparable to dimensions of hydrated ion molecules and that partial dehydration is the main factor for energy barriers.^{157,156} Ion selectivity of pores is another aspect that has been experimentally investigated, such as in cation-selective sub-nm graphene pores¹⁴⁰ but the available body of reproduced experimental work is limited.¹⁹²

5.8 Saturation of Conductance vs Molarity

We observe a saturation in conductance across 3 M to 0.01 M KCl and other salt solutions. For larger, nanometer size solid-state pores, this saturation in KCl solution was previously observed to occur for molarities below ~ 0.1 M.^{41,205} This molarity corresponds to Debye length, $\lambda_D \approx 1$ nm for 0.1 M KCl, equivalent to about four water molecule diameters, and $\lambda \approx 3$ nm for 10 mM KCl. We see that for a 0D pore ($d < 1$ nm) the saturation of G with decreasing molarity, M , occurs at higher molarities than for one order of magnitude larger nm-size pores. This is likely because the characteristic pore size d is now comparable to λ_D even at relatively higher molarities such as 1–3 M KCl, where $\lambda_D \approx 0.1$ –0.3 nm, explaining why we observe similar conductance for 3 M and 10 mM KCl.

At low molarity < 0.1 M KCl, we observe in Figure 5.5(d) that conductance is similar or larger than expected from the corresponding bulk value and assuming an idealized inert transport channel governed by *Eq. 2*.¹⁷⁸ This is because Equation 2 does not take directly into account that pores have charged surfaces (although this is effectively taken into account in *Eq. 3* by assuming some equivalent pore conductivity, σ_{pore}). For “large” pores, the pore’s surface charge effect on G can be negligible given that surface charges are screened within Debye’s length $\lambda_D \approx 0.3$ nm in 1 M KCl. It was previously established that as the system size decreases approximately below micron and nm-scales, surface charge effects on G can be noticeable on ionic transport at molarities below ~ 0.1 M, and transport can even become fully governed by surface charges in nanofluidic channels in very “small” systems and/or very “low” molarities.¹⁷⁸ The lower the molarity, the larger the size of the channel for which surface charge effects on G are noticeable.

In nanofluidic channels, as molarity M decreases, conductance transitions from a regime where $G \sim M$ to the regime where G saturates as a function of M at low molarities.¹⁷⁸ This dependence was established experimentally in silicon nitride (see for example SI in Ref. 64)²⁰⁵ and 2D pores, with negative surface charge densities of the order $\sim -0.01 \text{ C/m}^2$ to -0.1 C/m^2 reported⁴¹ for MoS_2 pores with diameters $d > 2 \text{ nm}$ by fitting G vs. M and dependent on pH. This “low-molarity transport behavior”, where the definition of what is “low” depends on the system size, is explained by electrostatic effects of the channel’s surface charge on the fluid. The smaller the system, the higher the molarity at which this saturation occurs: a charged pore surface attracts oppositely charged counterions from solution while repelling co-ions. This results in a charged layer forming close to the pore walls, called the double layer, and this layer screens the immobile surface-charge. To maintain charge neutrality the number of mobile counterions in a channel can exceed the bulk ion concentration and dominate transport.¹⁷⁸

Low conductance presents a challenge for higher bandwidth measurements, requiring capacitance minimization to reduce noise and current contributions from capacitor charging. Compared to zero-D MoS_2 pores supported on Si chips (Figure 5.1), pores fabricated on low-capacitance glass chips^{12,13} exhibited a lower noise but significantly higher polymer contamination (see section 5.10 Figures 5.8 and 5.9). Future studies will benefit by using low-capacitance platforms combined with low-noise transimpedance amplifiers^{28, 53,54, 170} to get insight into the short timescale behavior of both ion channels and zero-D solid state pores, such as to resolve short current events and probe the mechanisms of the channel on/off dynamics.⁵³

5.9 Additional Experimental Methods

CVD Growth: Monolayer MoS₂ flakes were grown using CVD processes reported in previous works.¹⁹³ Solutions of 0.2% sodium cholate growth promoter and 18×10^{-3} m ammonium heptamolybdate were spun onto piranha-cleaned Si substrates coated with 300 (150) nm of SiO₂, which were then loaded into the center of a 1 in. tube furnace (Thermo Scientific Lindberg/Blue M). For the MoS₂ growth, samples were heated under N₂ gas flow (700 sccm) at a rate of 70 °C min⁻¹ and held at 750 °C for 15 min. Approximately 100 mg of sulfur precursor placed 22 cm from the substrates was kept at 180 °C during the growth procedures. Samples were rapidly cooled to room temperature by opening the furnace.

Device Fabrication: MoS₂ crystals were transferred from Si/SiO₂ substrates with a focused ion beam (FIB) hole (~ 150 – 200 nm in diameter) using a wet etch technique. Crystals were first coated with C4 PMMA while aqueous 1 M KOH solution was used to etch away the underlying substrate. After being washed in deionized (DI) H₂O, crystals were scooped onto TEM grids and dried for 30 min. Polymer liftoff and sample cleaning were performed using acetone and rapid thermal annealing in Ar : H₂ gas at 300 °C, respectively. While tears and other failures modes of membranes and pores are possible, we have optimized our procedure to have continuous triangular flakes of MoS₂, that are sealed to the supporting chip by annealing. When there are tears, the measured current is significantly larger; for example, for pores larger than 1 nm in diameter, the current is in the tens of nA's and for larger tears significantly more. We had a few samples that clearly broke as evidenced by a sudden surge of current, followed by confirmation in microscopy. The small magnitude of current is an indicator of two possible outcomes: either the conducting pore

is small or that the membrane and/or pore are not fully wetting to allow maximum current flow based on pore size.

Pore Fabrication and Imaging: Sub-nm MoS₂ pores were fabricated and imaged using a Cs-corrected JEOL ARM 200CF STEM operating at 80 kV. The spherical aberration coefficient was generally Cs ~ 100 nm. Pores were drilled by switching the instrument with a 22 pA probe current to selected area (1×1 nm) exposure and monitoring the radiolysis process. After approximately 10 seconds, the instrument was switched back to full scan (13 × 13 nm). Images were obtained using a HAADF detector with a collection angle of 54–220 mrad and 10 cm camera length. Only one image was acquired after pore drilling to minimize beam-induced knock-on damage.

We note that TEM images provide structural information *only* for the initial, as-fabricated pores in vacuum, prior to any I-V measurements. This presents a limitation here as well as previous nanopore studies where it was experimentally challenging to locate and image the pores after ionic measurements. Previous similar individual pore studies have not measured the pore diameter directly.^{72, 43} It is possible and likely that once the pores are taken out of vacuum and immersed in solution their structure can change and these changes can include pore clogging as well as pore etching over time in salt solution². Moreover, these changes could be amplified by the applied electric field to enlarge the pores.⁴² Here, we limit the applied voltage to 0.1 V and we also calibrate our conductance values using results from larger 2D pores^{114,189,190} as expected upper bounds for our sub-nm pores (~ 1 nS to 10 nS). Conductance larger than 1 nS may strongly indicate that the

pores have expanded beyond 1 nm in diameter over the course of handling and measurements.

There can be several complications in device fabrication. While we did not probe the extent of debris, we observe that annealing is critical to seal the membrane and make it not leaky or lift off in ionic solution. We go by the amount of measured ionic current as an indicator of the degree of holes or current paths. We did not observe membranes lifting off, but we observed pore expansions and increase in ionic current if higher voltages are applied.

Pore Diameter Determination: The geometric models (Table 5.1 and pore schematic in figures) were carefully created based on the missing atoms observed in TEM images and the 3D view such as in Figure 5.2f. These models do not consider the electron cloud space or the orbital distance which can perhaps be accounted for through Molecular Dynamics (not employed here). Additionally, we assume that the pore edges follow a perfect lattice from which the missing atoms are simply cut out. In the real TEM images however, we see that there can be lattice distortions and bunching of Mo atoms, such that the distances between atoms along the edge can vary and be slightly shorter or longer than in the pristine lattice. Furthermore, in the real pores there is a consistent uncertainty in the number of S atoms specially along the pore edges due the weaker intensity of S atoms produced in contrast to heavier Mo atoms. Therefore, we use both the pore areas obtained through TEM images (d_{TEM}) (see Figure 5.5) and geometric models (d_{Model}).

Definition of effective pore diameters used in this study: For the purpose of careful analysis we define two pore diameters, d_{TEM} and d_{Model} , both calculated as diameters of equivalent circles with the same area as the pore, where the pore area is estimated in two different ways. For $d_{TEM} = \sqrt{4A_{TEM}/\pi}$, we estimate the pore area, A_{TEM} , directly from the AC-TEM zoomed in image of the pore and the scale bar is obtained experimentally in the TEM. This image analysis is done using functions and filter in software ImageJ (See Image Processing SI S1). For $d_{Model} = \sqrt{4A_{Model}/\pi}$, we use the area calculated from the geometric model of the pore and the scale bar is obtained theoretically from the atomic distances in the 2D MoS₂ lattice. An example analysis and calculation of d_{TEM} for Pores 2,3,4, are given in Figure SI S1. The differences in values of d_{TEM} and d_{Model} primarily come from the deviation of the pore edges from the perfect lattice, for example if a pore has atoms that are bunched up on the edges, such as in Figure 5.1f.

Ionic Measurements: EPC-10 HEKA amplifier setup⁵⁶ with Ag/AgCl electrodes was used to perform ionic measurements on our devices. 1 M KCl and other salt solutions (with 10 mM EDTA and 1 mM Tris; measured solution conductivity = 11.18 S/m for 1 M KCl, pH 8.7) solution was prepared using DI water, and the conductivity and pH were measured with Accumet XL-20 pH conductivity meter. Similar measurements were also conducted for glass chips^{12,13} but on the Chimera amplifier setup with higher-bandwidth (1-MHz).²⁰⁶ Prior to ionic measurements, the device was annealed at 300 °C in an Ar : H₂ environment for 90 minutes. The device was then immersed in a 50% water-ethanol solution typically for 15 to 30 minutes, which we empirically found to help wetting and formation of ionic channels through the pores. Some samples were immersed for longer time from 3-5 hours

to 12 hours. The device in ethanol was intermittently bubbled in the solution with the glass pipette to ensure no air bubbles are left trapped in the device. Voltage (V) was applied across the pore while measuring the ionic current (I). Voltage bias was kept below ± 0.1 V for most pores in this work. A custom-built LabView Software is used to run experiment on Heka amplifier, I-V sweeps and time-trace features of this program was utilized.⁵⁶ Majority of the I-V measurement involved a sweep rate of 5 mV per second, 10 mV per second was used for faster acquisition. All I-V sweeps were offset to start at zero and were averaged in case of multiple I-V sweeps. “Pristine membranes” (membranes without holes) are control devices and not the same devices used to drill pores. It was challenging for us to measure in salt solution and then use the same membrane again to drill the pore and remeasure in solution. This is because the membrane gets dirty from the salt solution and there are additional possible failure modes such as membrane breaking. Therefore, we rely on control samples (membranes without drilling) to establish the baseline current, and on samples with drilling to establish the current through the pore. Because these are not the same samples, this presents a limitation of the present study.

Image processing for TEM pore area and diameter determination:

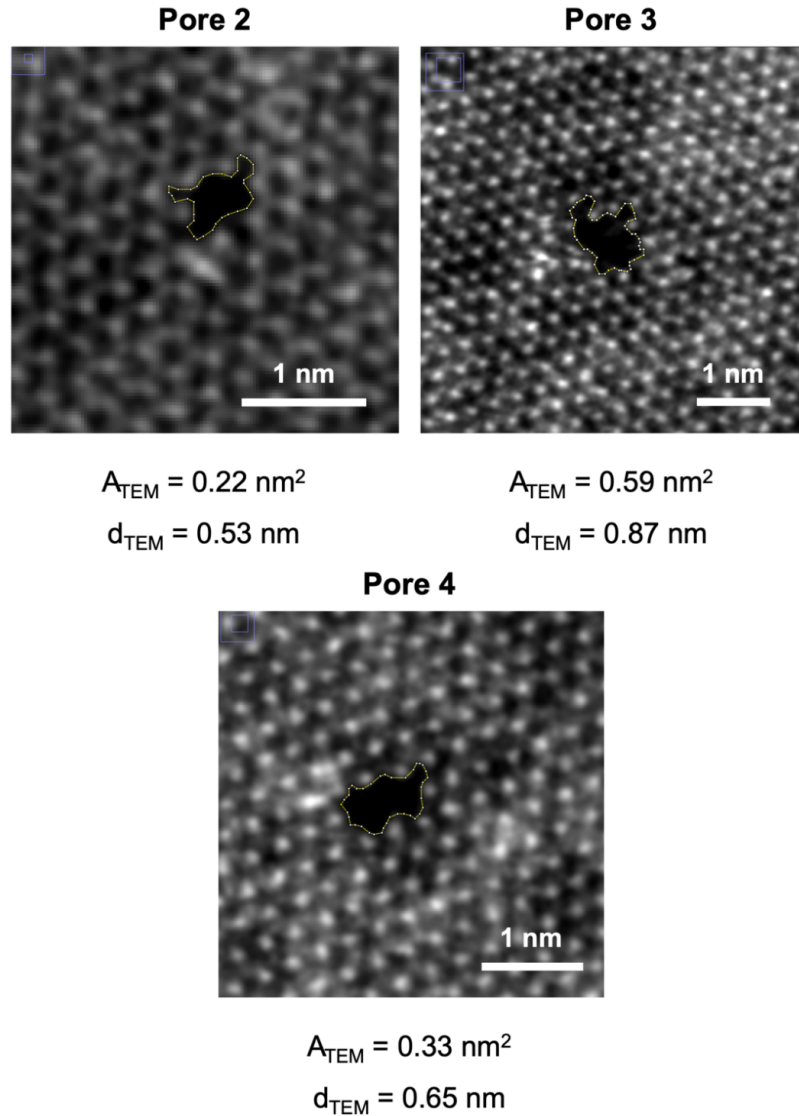


Figure 5.6. Image processing for TEM pore area and diameter determination.

To calculate experimental pore diameters (d_{TEM}) from AC-STEM, atomic resolution images were first exposed to background subtraction and Gaussian blur filtering to reduce noise. The area of the pore (A_{TEM}) was then calculated by performing a thresholding function that differentiates the pore (zero contrast) from the pore edge (nonzero contrast), as outlined in yellow for Pores 2, 3, and 4 above. The diameter is then calculated using $d_{TEM} = \sqrt{4A_{TEM}/\pi}$. The entire process was performed in ImageJ software.

Conductance of zero-D pores:

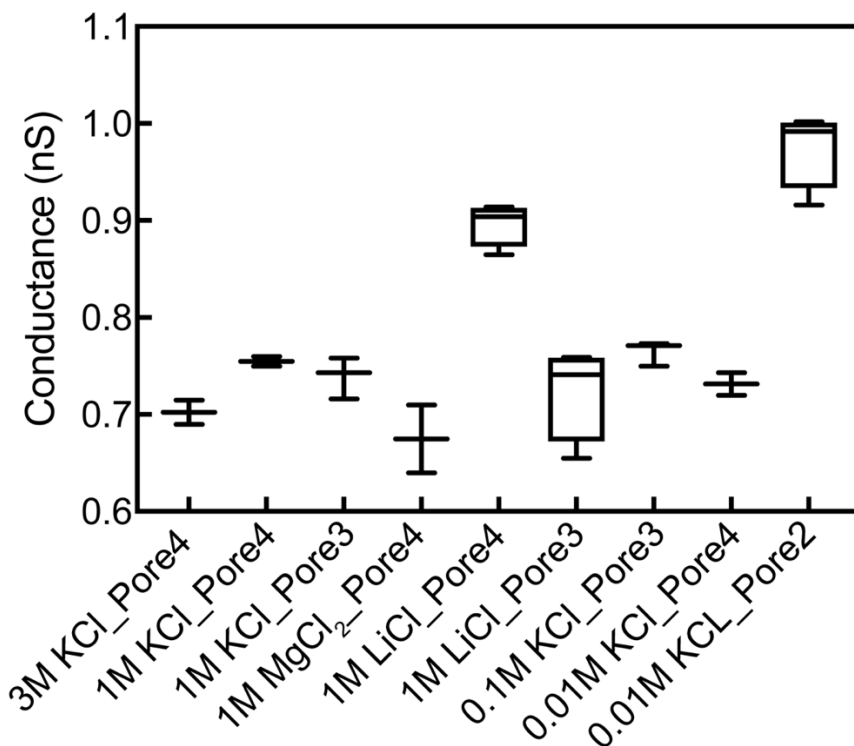


Figure 5.7. Conductance of zero-D pores

Zero-D pores showing an average conductance of 0.79 nS across various cation-based chloride salt solutions with a standard deviation of ~ 0.1 nS in conductance. Each data bar includes conductance from an individual zero-D device for a given salt solution with a variation in the range of ± 0.01 to 0.086 nS arising from the slope of the fitted line obtained at various voltage ranges such as ± 30 mV, ± 50 mV, ± 100 mV, ± 200 mV (as applicable). The line inside the bar indicates the median of the conductance for a given salt solution, error bar shows the 75 % and 25 % percentile.

Samples containing multiple sub-nm MoS₂ pores drilled with AC-TEM:

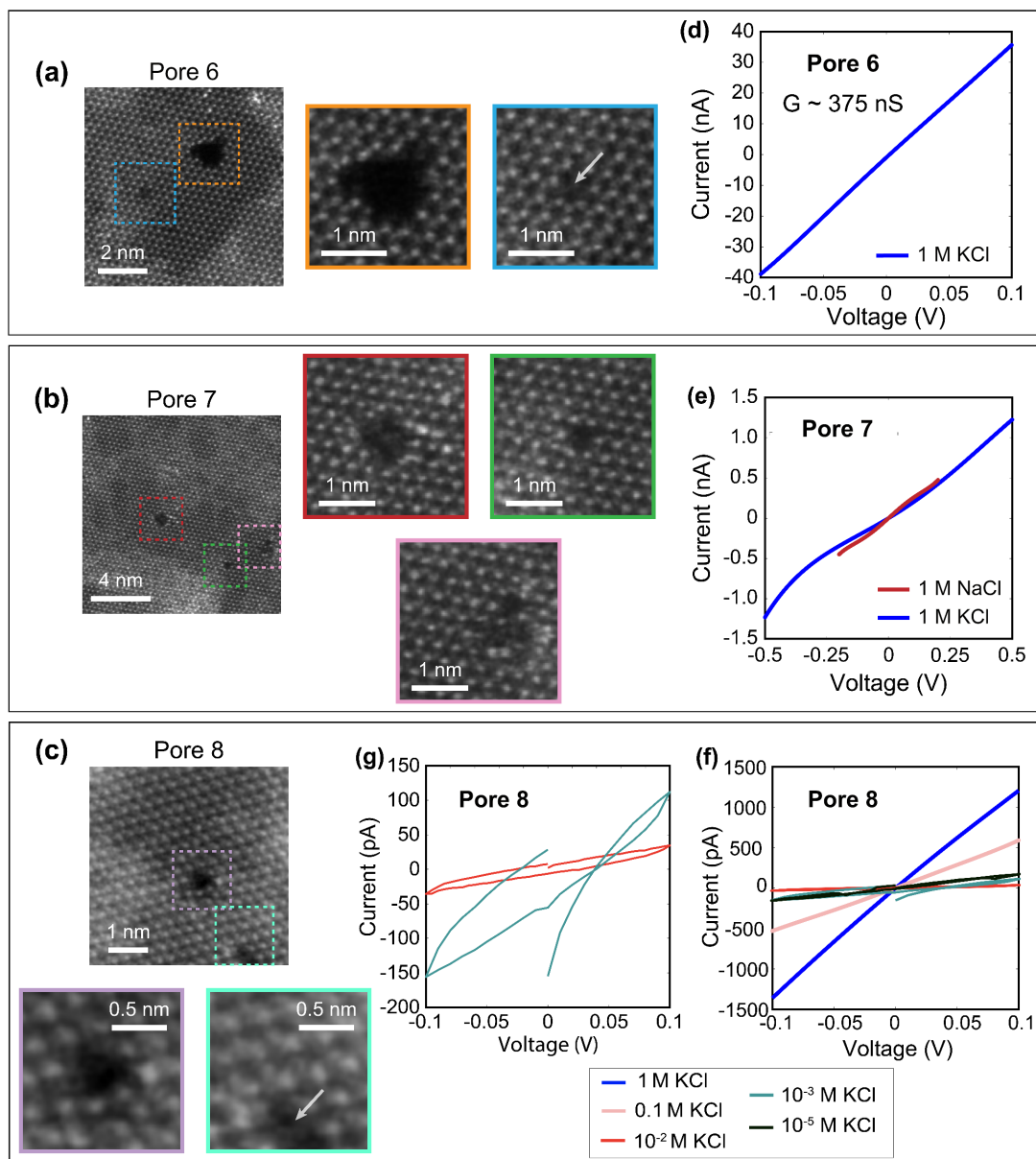


Figure 5.8. Samples containing multiple sub-nm MoS₂ pores drilled with AC-TEM

AC-STEM images monolayer MoS₂ samples containing multiple pores. (a) The conductance of Pore 6 (orange, $d_{\text{TEM}} = 1.2$ nm; blue, $d_{\text{TEM}} = 0.55$ nm) was observed to increase up to ~ 375 nS with successive I - V measurements, suggestive of pore enlargement. (b) Pore 7 is composed of 3 individual zero-D pores (red, $d_{\text{TEM}} = 0.92$ nm; green, $d_{\text{TEM}} = 0.52$ nm; pink, $d_{\text{TEM}} = 1.0$ nm) that cumulatively contributed to a conductance of 2.20 nS in 1 M KCl and 2.23 nS for 1 M NaCl. (c) Pore 8 had two individual zero-D pores (purple, $d_{\text{TEM}} = 0.53$ nm; green, estimated $d_{\text{TEM}} \sim 0.60$ nm) which gave a total conductance of 12.8 nS for 1 M KCl, 5.56 nS for 0.1 M KCl, and 1.65 nS for 10^{-5} M KCl. The I - V curves for 10^{-2} M KCl and 10^{-3} M KCl show hysteresis-like behavior (as shown in panel (g) – State 2) with $G \sim 0.3$ nS and $G \sim 1.09$ nS respectively. As discussed previously, I - V sweeps with

hysteresis exhibit a loop-like hysteresis (no crossover) with the current value for a given voltage differing significantly (~ 80 pA), or the maximum current is close to background signal (as low as ± 10 pA).

Current-voltage and noise characteristics of sub-nm MoS₂ pores on a low-capacitance glass chip:

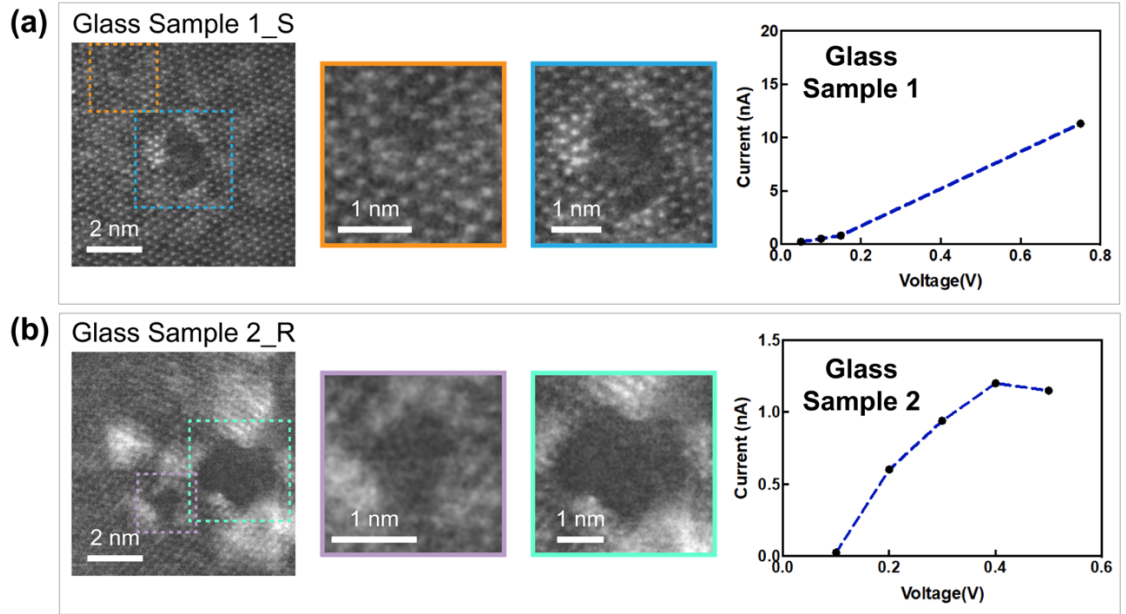


Figure 5.9. Current-voltage and noise characteristics of sub-nm MoS₂ pores on a low-capacitance glass chip

AC-STEM images of multiple sub-nm pores in monolayer MoS₂ transferred on a low-capacitance glass chips.^{12,13} Both samples were measured in 1 M KCl. (a) The ionic current of Glass chip Sample 1 was found to steadily and irreversibly increase with voltage, resulting in a high conductance ($G \sim 15$ nS), likely caused by enlargement of pores. (b) Glass chip Sample 2 was also found to be unstable with $G \sim 3$ nS. Compared to the continuous I-V measurements shown in the main text and other supplementary figures, the ionic currents here were obtained by acquiring current-time traces at discrete voltages.

Because of the low current level in sub-nm pores and the need for better signal-to-noise, we integrated the 2D materials on low-noise all-glass chips^{12,28} and measured with our higher-bandwidth (1-MHz) Chimera amplifier setup³. TEM images and conductance values for two devices are shown in Figure 5.8, with corresponding noise properties given in Figure 5.9. While glass chip devices displayed a reduced noise compared to Si-based

chips (see Figure 5.8(d) in the main text), they were found to be especially delicate and prone to breakage, *i.e.*, either the suspended region or the pore collapsed resulting in high conductances, and more work is needed.

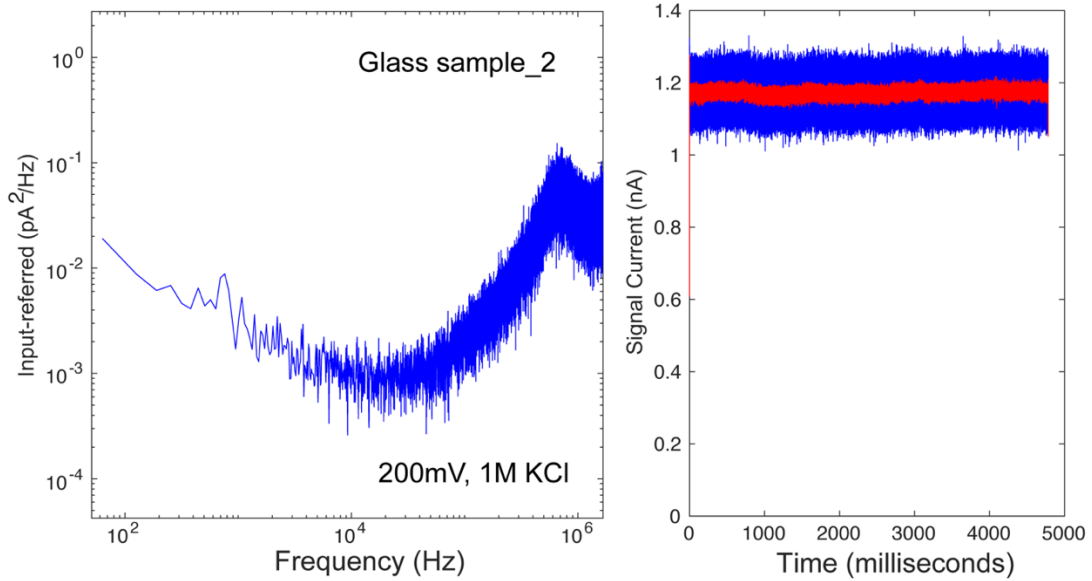


Figure 5.10. Power Spectral Density of a glass chip

The (left) power spectrum density and (right) current-time trace for Glass chip Sample 2. The pore was conducting with ionic current $I \sim 1.2$ nA at a bias voltage of 200 mV in 1 M KCl. The glass chips provide reduced capacitance which inevitably reduces the noise across the entire frequency range by more than a factor of 2.²⁸

Molecular dynamics simulation equation for sub-5 nm-diameter MoS₂ pore conductance in 1 M KCl:

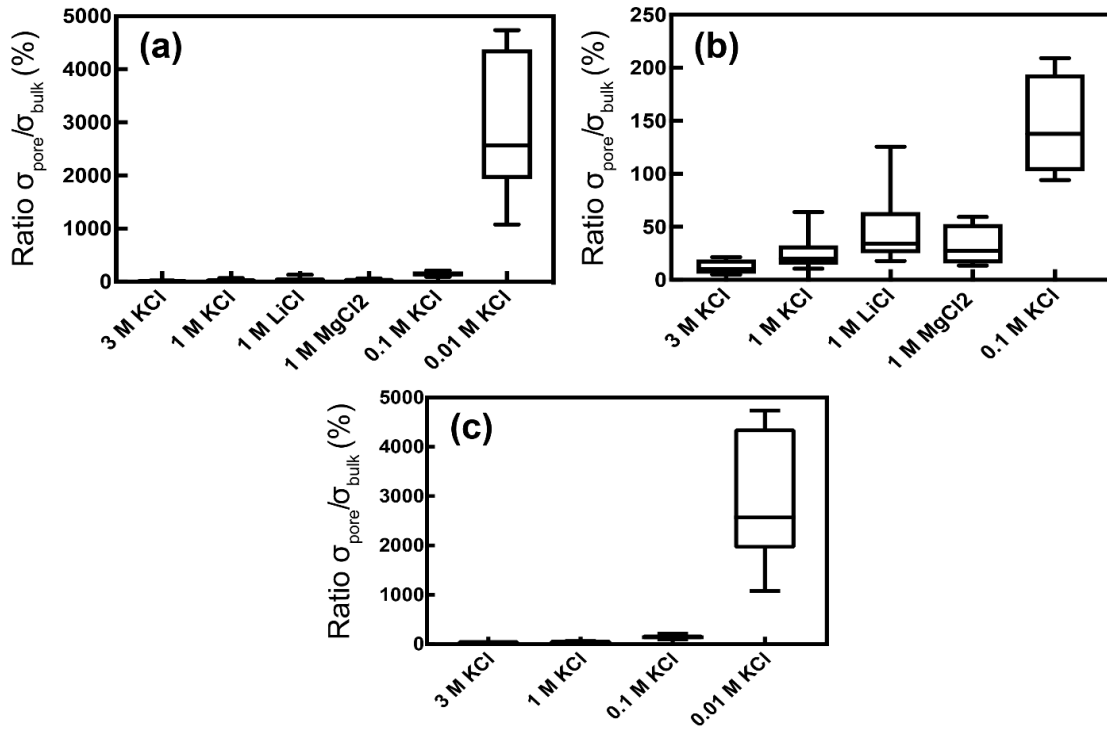


Figure 5.11. Molecular dynamics simulation equation for sub-5 nm-diameter MoS₂ pore conductance in 1 M KCl

(a) Pore to bulk conductivity ratios ($\sigma_{\text{pore}}/\sigma_{\text{bulk}}$) for different salt solutions and concentrations. (b) Magnification of the 0-250% range of panel (a) for five solution conditions (excluding 0.01 M KCl). (c) $\sigma_{\text{pore}}/\sigma_{\text{bulk}}$ for different concentrations of KCl solution. As described below, $\sigma_{\text{pore}}/\sigma_{\text{bulk}}$ was studied theoretically as a function of effective pore diameter by Perez *et al.* in MD studies⁴. Figure 5.5(d) of the main text contains the pore conductivities obtained using Eq. 3 used to produce the plots above.

The equation for sub-5 nm-diameter MoS₂ pore conductance in 1 M KCl reported by Perez *et al.*¹⁸⁸ to account for reduced ion concentrations and mobilities is given by:

$$G_0 = \sigma_{\text{bulk}} \left(\frac{1}{2} \sum_{i=1}^2 \exp\left(\frac{-4\phi^i}{\pi d^2}\right) \frac{d}{\delta^i + \varepsilon^i d} \right) \left[\frac{4t}{\pi d^2} + \frac{1}{d} \right]^{-1}$$

Where, $\delta^{K^+} = 0.38 \text{ nm}$, $\delta^{Cl^-} = 0.41 \text{ nm}$, $\epsilon^{K^+} = 1.03$, $\epsilon^{Cl^-} = 0.97$, $\phi^{K^+} = 0.832 \text{ nm}^2$, $\phi^{Cl^-} = 0.793 \text{ nm}^2$.

Our findings at 1 M KCl generally agree with the trend from molecular dynamics simulations of MoS₂ pores that calculated reduced ion mobilities and concentrations in the regime of pore sizes comparable to ionic radii.¹⁴⁸ Our smallest pores show more conductance of $\sim 0.7 \text{ nS}$ however the uncertainty in ‘L’ (membrane thickness) and range of diameter ‘d’ result in pore conductivities $\sim 25 - 65 \%$ of the bulk conductivity at 1 M KCl (obtained by fitting to Equation 3 of main manuscript). This is about two times larger than $\sim 8 \%$ - 40% from molecular dynamics¹⁴⁸, for effective pore diameters $\sim 0.53 \text{ nm}$ to 0.92 nm . Our range $\frac{\sigma_{pore}}{\sigma_{bulk}} = 25\% - 65\%$ would correspond to theoretical pore diameters $\sim 1 \text{ nm}$ to 1.8 nm in the MD model.¹⁴⁸ These discrepancies are not surprising, given the expected sharp change of $\sigma_{pore}/\sigma_{bulk}(\%)$ in this diameter range, about 5% change per 0.1 nm diameter change¹⁴⁸ and given our possible experimental errors in determining the pore diameter at the time of ionic measurements, among the possible sources of errors. We remind that experimental diameters correspond to pores in vacuum prior to ionic measurements.

5.10 Conclusion and Future Directions

With the help of the state-of-art transmission electron microscopy and advancement of 2D material devices, we report an elaborate device fabrication of a single zigzag-armchair zero-D pores which have definite pore edges and known atomic composition of pore edges. In this regime of sub-nm pores, we observe the conductance of zero-D pore is largely independent of bulk conductivity and dependent on the applied bias to drive ions through

the pores. We observe a quenched ionic conductance (~ 0.8 nS) compared to nm-scale pores in case of pores with the diameters similar to the size of hydrated salt ions, and the conductance saturation vs. molarity in a wide ion concentration range. This conductance is close to values recently reported in other solid-state atomic-scale systems where ion transport was confined to ~ 1 nm in one or more dimensions, such as in single 0.8 nm and 1.5 nm diameter, 10-nm-long carbon nanotubes.^{192,252,221}

Blockade of ion passage by small pores and dehydration of solvated ions were hypothesized as mechanisms to explain experimentally observed suppressed ionic current at low voltages and non-linear I-V curves as voltage is increased.^{72,43} We are now able to fabricate Zero-D pores that mimic the bio pores, with good reproducibility and similar ionic conductance ($\sim 0.6 - 1$ nS) to that of proteins that occur naturally.^{170,53} Another important aspect of these biological pores is their transport mechanisms and selectivity for specific cations or anions. This feature is yet to be studied in our zero-D, future experiments can investigate conductance at various pH and attempt to modify the surface charge of these zero-D pores. We were not able to image the nanopores after the ionic conductance measurements. Future studies can also attempt AC-TEM imaging of the pores after the ionic measurements and examine the extent to which these measurements result in some geometry changes of the pore.

Several limitations existed in our study. TEM images correspond to pores before ionic measurements, and we were not able to image the pores after the ionic measurements. Also, because the membrane is contaminated after being in a salt solution, the baseline ionic current was established from pristine membrane samples (with no intentional pores) that

are not the same samples used for pore TEM drilling, although all samples came from the nominally identical batch of membranes (from the same CVD growth) and the same fabrication procedures.

Pretreatment with ethanol here is seen to enhance the pore hydrophilicity and enable measurements of small but measurable currents through the pore. Studies have proven that the methanol or ethanol/water solvent mixture change the dielectric constant of the solution which could alter the surface charge on the pore in a favorable way to allow ions to translocate.¹⁷ This wetting technique aided by an alcohol is being used by several experimental studies already on 2D nanopores and nanochannels.^{34,39,43, 114,130} So far, our experimental investigation leads to the conclusion that wetting the pore is possible through a polar solvent such as ethanol which is important for translocating ions through the entirety of the zigzag-armchair pore. Future studies may design pore edges to further control ion translocation through the pores, maybe also guided by molecular dynamics simulation studies addressing pore stability and transport.

6 Gas flow through atomic-scale apertures

This section has been represented from the publication titled, “Gas flow through atomic-scale apertures” by Jothi Priyanka Thiruraman, Sidra Abbas Dar, Paul Masih Das, Nasim Hassani, Mehdi Neek-Amal, Ashok Keerthi, Marija Drndić, Boya Radha. *ACS Nano* 2020 14 (9), 11831-11845

6.1 Introduction

Gas flows are often analyzed with the theoretical descriptions formulated over a century ago and constantly challenged by the emerging architectures of narrow channels, slits, and apertures. Here, we report atomic-scale defects in two-dimensional (2D) materials as apertures for gas flows at the ultimate quasi-0D atomic limit. We establish that pristine monolayer tungsten disulfide (WS_2) membranes act as atomically thin barriers to gas transport. Atomic vacancies from missing tungsten (W) sites are made in freestanding (WS_2) monolayers by focused ion beam irradiation and characterized using aberration-corrected transmission electron microscopy. WS_2 monolayers with atomic apertures are mechanically sturdy and showed fast helium flow. We propose a simple yet robust method for confirming the formation of atomic apertures over large areas using gas flows, an essential step for pursuing their prospective applications in various domains including molecular separation, single quantum emitters, sensing and monitoring of gases at ultralow concentrations.

6.2 Background

Understanding confined gas flows in angstrom-scale tight spaces not only plays a major role in the design of gas extraction techniques but also for gas separation and production¹⁴⁴. In extremely narrow pores, the mean free path of a gas is much larger than that of the dimensions of the pore itself, which leads to gas dynamics dominated by molecular collisions with walls of the pore rather than the intermolecular collisions. This is known as the free molecular regime, and the gas flux through such pores was comprehensively described using the Knudsen equation, which has since been modified and adapted to explain the flows through various confined systems. From a theory standpoint, a pore or an aperture is a simple model system, through which gas transmission is proportional to the impingement of gas molecules i.e., likelihood of a gas molecule encountering a pore, and the activation barrier if any to cross the pore. In the cases where the membrane surface can adsorb gases, the flow is a combination of direct transmission through the pore and surface diffusion along the membrane¹⁸¹. Despite the emergence of many nanoscale gas flow conduits such as nanopores^{27,93,219,210,232}, nanotubes^{47,59,61}, nanochannels^{84,168}, nanolaminates^{89, 106}, etc., ultimately narrow quasi-0D apertures with atomic-scale dimensions in both the transmembrane and lateral directions, which challenge the applicability of Knudsen equation for gas flows have been limited^{93,210,85,232}. Although one-atom vacancies have been ideal candidates for theoretical simulations and modelling of gas flows^{18,78}, they have not been studied extensively in experiments^{266,232}. Here we investigate an inert gas, i.e., helium flow through pristine impermeable membranes as well as atomic defect vacancies in freestanding monolayer tungsten disulfide (WS_2) membranes, to validate the Knudsen description in the ultimate atomic aperture limit.

6.3 Fabrication of Devices with Atomic Apertures

Several studies in the past have explored various sources for atomic defect creation in 2D materials; among those, the popular techniques are oxygen plasma^{71,92}, thermal annealing¹¹, ion and electron beam irradiation^{156,190}, acid etching^{71, 193}, and ultraviolet-induced oxidation etching¹⁰⁶. In particular, ion irradiation offers a precise method of creating atomic vacancies with a controlled localization of defect sites at comparatively high densities ($>10^{11}$ cm⁻²). Recently, we have illustrated how to create highly controlled single-atom defects by focused ion beam (FIB) irradiation on a monolayer transition metal dichalcogenide (TMD) flake¹¹³. In particular, TMDs provide better imaging contrast in aberration-corrected scanning transmission electron microscopy (AC-STEM) imaging and appear less prone to contamination, enabling easier characterization of the defects. We compared the effects of FIB irradiation on various suspended monolayer TMDs and established that defects with areas down to 8 Å² (single transition metal vacancy) can be produced in WS₂ with a specific low irradiation dose (increasing dose produces larger vacancies in the membrane). Therefore, we choose monolayer WS₂ as an optimal base support for hosting single-atom defects. Apart from being mechanically stable with a Young's modulus of 270 GPa and a thickness of ~0.7 nm²², our detailed investigation of the controlled ion irradiation mechanism minimizes the possibility of undesired damage or tears. The FIB irradiation mechanism used here allows for exclusively hosting single atomic apertures on a freestanding monolayer WS₂ membrane, enabling a high density of uniform defects in the range of $9 \times 10 \pm 3.5 \times 10$ cm⁻² (see sections 6.6). These defect densities are comparable to that achieved in graphene membranes.

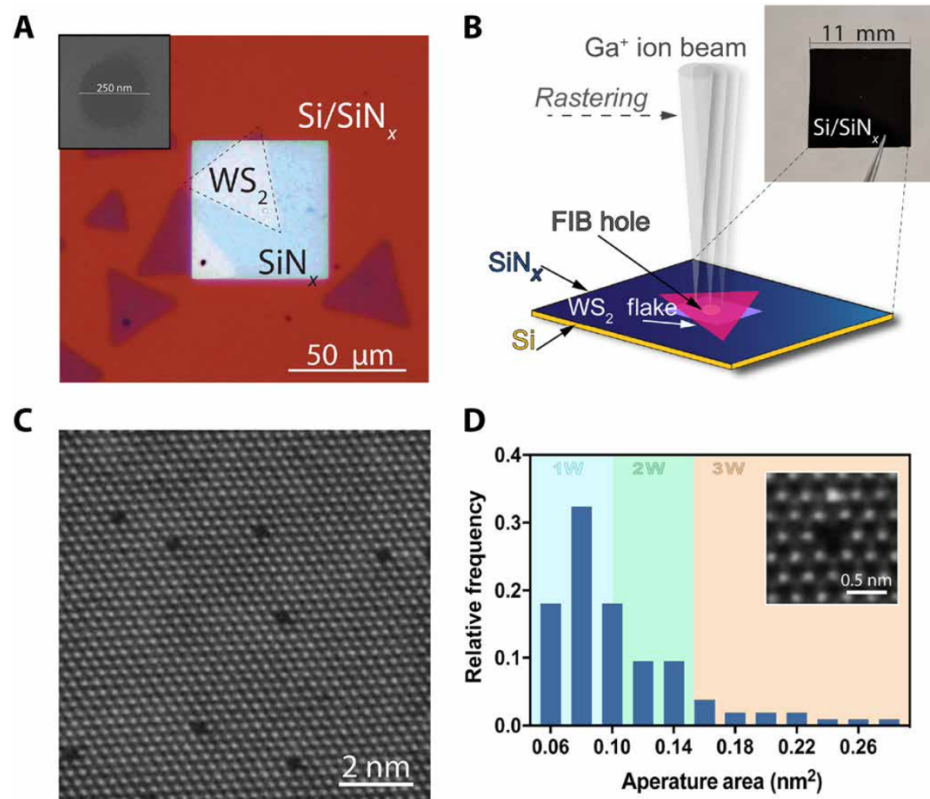


Figure 6.1. Atomic apertures fabricated using an FIB scanning technique.

(A) Optical microscope of a monolayer WS₂ flake suspended in the center of a silicon nitride (SiN_x) membrane (~50-nm thickness, 50 μm by 50 μm) using position-control transfer technique. The inset shows a scanning electron microscopy image of a hole of 250 nm in diameter drilled in the center of the SiN_x membrane. (B) Schematics of the irradiation technique on the suspended WS₂ flake, and the inset shows a photograph of a SiN_x/Si chip (11 mm by 11 mm). (C) Aberration-corrected high-angle annular dark-field (AC-HAADF) image of irradiated monolayer WS₂ flake at a dose of $\sim 5.1 \times 10^{13}$ ions/cm². Bright spots indicate W atoms. (D) Histogram of apertures produced with the irradiated dose used in (C). Light shading of blue, green, and orange indicate the size ranges of 1W, 2W, and 3W atomic apertures in the graph, respectively. Inset: A high-magnification AC-HAADF STEM image of one such aperture.

The WS₂ membranes incorporating atomic vacancies are supported on silicon chips (SiN/Si) with a size of 11 mm by 11 mm (Fig. 6.1A and fig. 6.4). In the center of each chip, one or more sub-micrometer holes were drilled in a freestanding silicon nitride (SiN_x) membrane (Fig. 6.1B). A monolayer WS₂ flake was suspended on sub-micrometer holes

present on these silicon chips (see fig. 6.4). The suspended flake was irradiated with a 30-kV gallium-sourced FIB under specific pre-calibrated irradiation dose conditions to produce single atomic vacancies (illustration is shown in Fig. 6.1B). We exposed samples to an ion irradiation dose of 5.1×10^{13} ion/cm² and obtained a defect density of $0.08 \pm 0.03\%$, with an average defect area of 0.12 nm² and a median defect area of 0.09 nm². Figure 6.1C is a representative image of atomic-scale defects produced through this method. We observe single atomic apertures where 1W atom vacancies can be seen, as included in Fig. 6.1D. It is often challenging to locate S atoms in AC-STEM images because of their weaker contrast compared to heavier W atoms. The creation of atomic defects possibly leads to reconstruction of immediate surrounding sulfurs in the monolayer lattice; hence, we see a variety of shapes of the apertures such as triangular, truncated triangular, to pseudo-spherical (see table 6.1 and fig. 6.5 in Section 6.6). On the basis of analysis of several atomic-resolution images, we estimate the total defect sites resulting from missing W atoms to be few hundreds to few thousands per one device depending on the supported membrane area.

6.4 Experimental Gas Measurements in Atomic Apertures Devices

The relatively large number of atomic apertures (up to ~2000) in our samples enables gas flows detectable by conventional mass spectrometers, such as helium leak detector. Our membranes are mechanically robust and sustained the pressure differences of up to ~1 bar. For gas flow measurements, the experimental setup consists of mounting the silicon chips with O-rings to separate two vacuum chambers, one held at variable pressure P and the other in high vacuum connected to a mass spectrometer as depicted in the inset of Fig. 6.2A (also see fig. 6.6). The samples are well sealed such that atomic apertures in the WS₂

membrane act as the only connecting paths between the two chambers where gas molecules can flow. As control samples, three replicas were done for each of the pristine silicon nitride membrane with and without holes and nonirradiated WS₂ membrane suspended over the silicon nitride hole. The control samples used to establish baseline flow are a different set of membranes than those used for gas transport; however, they all come from the same fabrication procedures and chemical vapor deposition (CVD) growth. A bare hole without WS₂ layer exhibits large gas flow, as expected, and has been used as a standard leak for validation of the experimental setup (Fig. 6.2). A freestanding pristine WS₂ monolayer covering nine holes each with diameters of ~250 nm, without any irradiated defects, exhibited negligible helium flow below our detection limit ($\sim 10^{-18}$ mol s⁻¹mbar⁻¹). It is remarkable that the WS₂ monolayer grown by CVD methods (see fig. 6.5) has such low intrinsic defect density that it is practically impermeable over a suspended area of a few square micrometers. Let us recall the ultralow permeability, ranging from 10⁻²³ mol s⁻¹mbar⁻¹ to only few gas molecules per hour^{128,182}, of intrinsic defects in 2D materials with high crystal quality such as mechanically exfoliated graphene, studied extensively with specialized device architectures and atomic force microscopy measurements done over several days. Apart from the high crystal quality of our WS₂ monolayer, the impermeability emphasizes the excellent sealing of the WS₂ layer on the SiN_x membrane in our devices, which is achieved by repeated annealing of the samples in H₂/Ar atmosphere at 350°C, both right after the WS₂ monolayer transfer and also before the gas flow measurements (see section 6.6).

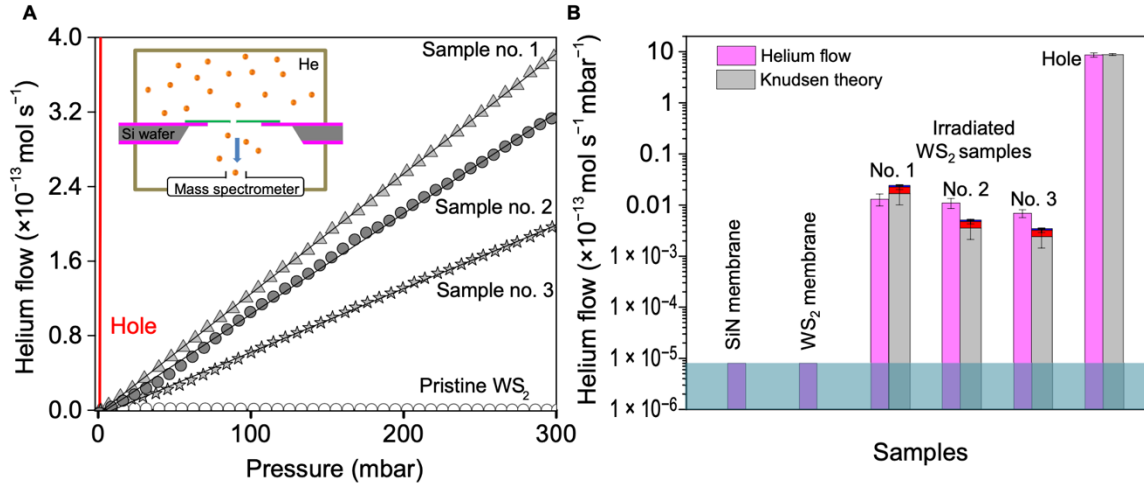


Figure 6.2. Gas flow through atomic apertures.

Helium gas permeation measured through atomic apertures in WS_2 made with same irradiation dose (5.1×10^{13} ions/cm²) but with different WS_2 areas leading to difference in the number of defects in a given sample. The proportion of the 1W, 2W, and 3W vacancies in each sample is 69:22:9%, sample no. 1, $N \sim 2070 \pm 830$; sample no. 2, $N \sim 440 \pm 170$; sample no. 3, $N \sim 300 \pm 120$. Pristine WS_2 membranes without any irradiation and large bare hole not covered with WS_2 (shown in red color) are shown alongside as controls. Solid lines running through symbols indicate best fit to the data. Inset shows a schematic of our experimental setup. (B) Comparison of normalized permeance per unit pressure of irradiated samples and controls, with the Knudsen estimates. The colors within the gray bars representing Knudsen estimates arise from the flow contributions due to 2W (red) and 3W (dark blue) vacancies. Horizontal light blue color bar indicates the detection limit. Error bars on the helium flow of samples are from the SD of flow values recorded over a series of helium flow measurements (measured three times) on the same sample repeated after annealing three times. For the Knudsen theory estimates, the error bars arise from the error values associated with the number of defects and with the total area of the apertures A in each sample.

6.4.1 Understanding Apertures “Sizes”

Next, we did helium (He) gas flow measurements on FIB-irradiated samples containing atomic vacancy defects in suspended WS membranes. Three typical irradiated samples along with controls are shown in Fig. 6.2A, in which sample no. 1 has WS_2 suspended on nine holes each with a diameter of ~ 200 nm. From our fabrication method, mainly three types of defects are possible such as 1W ($\sim 69\%$), 2W ($\sim 22\%$), and 3W ($\sim 9\%$) defects,

respectively. Here, the pore configuration is focused on W atoms since experimentally, the AC-STEM contrast from S atoms is weak, and hence, their locations are not identified with certainty. Unlike the geometric area given in Fig. 6.1D, to get the effective area (accessible pore area for He atom), the van der Waals (vdW) diameter of each atom on the aperture edge is subtracted (see section S2)²¹⁰. The total estimated tungsten defects are given as $N = N_1 + N_2 + N_3$, where N_1 , N_2 , and N_3 are estimated numbers of 1W, 2W, and 3W vacancies, respectively, from AC-STEM image analysis. In our samples, $N \sim 2070 \pm 830$ for sample no. 1; the sample no. 2 was WS₂ on a single hole with a diameter of 250 nm to yield total defects $N \sim 440 \pm 170$; the sample no. 3 was WS₂ on a 200-nm-diameter hole to give estimated defects, $N \sim 300 \pm 120$. Helium flow through atomic apertures increases linearly with increasing pressure and also with increasing number of defects in a sample (Fig. 6.2A). The gas flux is not exactly linearly correlated with the increase in N . The additional sources of error include the variation in the substrate hole area leading to an overall WS₂ suspended membrane area variation and errors in the ion irradiation dose, in total amounting to about ~40% error. At the experimental working pressure P ranges from few to 200 mbar, the mean free path of helium is $>0.5 \mu\text{m}$, and the Knudsen number for these atomic apertures in our WS₂ monolayer is $>10^3$. Here, the defects are not circular and have a well-defined atomic structure (see inset in Figs. 6.1D and 6.3), meaning that a diameter (typically used for larger circular pores) is not an optimal measure of size. We quote their geometric area, i.e., mean area $\langle A \rangle$, and the characteristic sizes in table S1. As an example, the 1W (+6S) defect has a pore with characteristic size, $\sim 3.15 \text{ \AA}$, and an area of 0.08 nm^2 , whereas the 3W (+6S) defect has a pore size of $\sim 5.25 \text{ \AA}$ and an area of 0.216 nm^2 . To represent the size of the He, we use the kinetic diameter ($\sim 2.6 \text{ \AA}$), which is a

semiclassical notion; however, for monoatomic spherical molecules like He, this is quite close to the quantum-mechanical size of the electron cloud around the nuclei¹⁸⁸. As the aperture size is much smaller than the mean free path, the mass flow of the gas Q (moles per second) through the aperture is simply the impingement rate upon the area of the pore (see section 6.6, Figure 6.7), as described by Knudsen^{68, 140}.

$$Q = PA(1/2\pi MRT)^{1/2} \quad (1)$$

where P is the inlet pressure, A is the total area of the conducting apertures, M is the atomic mass of the gas being transported ($M = 4 \text{ g mol}^{-1}$ for helium), $R = 8.314 \text{ J mol}^{-1} \text{ K}^{-1}$ is the gas constant, and T is the temperature ($T = 295 \text{ K}$ in our experimental setup). In our case, A is the sum of all individual atomic aperture areas in the WS_2 membrane, which is, on average, $N_1 \times A_1 + N_2 \times A_2 + N_3 \times A_3$ (in our samples, N can be varied from 300 to 2000 for an individual sample by increasing the membrane area; A_1 , A_2 , and A_3 are the accessible aperture areas for 1W, 2W, and 3W vacancies, i.e., ~ 0.08 , ~ 0.13 , and $\sim 0.23 \text{ nm}^2$, respectively, given in table 6.1. In the case of control devices, i.e., large bare holes, A is the sum of individual hole areas (with diameters in the range of ~ 200 to $\sim 300 \text{ nm}$). Taking into consideration the proportion of the various defects observed in AC-STEM images, we calculated the Knudsen estimates from all the vacancies such that 3W vacancies contribute to $\sim 9\%$ of the flux, whereas $\sim 91\%$ of the flux is contributed by 1W (+6S) and 2W vacancies together (Fig. 6.2B). If the pores are much narrower than the size of the molecule, then there can be a finite energy barrier, which is expressed as an exponential term in the Eq. 1, $\exp(-E/RT)$, where E is the energy barrier that substantially reduces the transmission coefficient of the gas even for small E ^{210, 140}.

The 2D membranes with atomic apertures show measurable helium flux $\sim 10^{-16}$ to 10^{-15} mol $\text{s}^{-1} \text{mbar}^{-1}$, over two to three orders higher than the detection limit and significantly lower than the leakage rate for sub-micrometer holes (Fig. 6.2B). This corresponds to a flow of about $\sim 10^7$ to 10^8 He molecules per second per millibar pressure difference across the membrane. Theoretical simulations with such small pores in graphene have estimated a pass through frequency of 10 He molecules per second per defect (close to our flow values per millibar for a sample with ~ 2000 defects; Fig. 6.2), which can be likely ascribed to a low diffusion barrier for He resulting from its noninteracting nature^{18, 210}. As a check for the reproducibility of devices with atomic apertures, we would like to point out that in a given batch of irradiated samples, about 40 to 50% samples show the measurable flow commensurate with the number of defects estimated by the irradiation dose¹¹³. Other devices either did not conduct gas or showed much higher gas flow. From the He flow, we back-calculated the number of defects contributing to the flow using Eq. 1, and N matches close to the defect numbers from AC-STEM image analysis for the sample numbers. 1 to 3. For high leaking samples, substituting experimental Q in Eq. 1 gave large contributing defect area A, which does not correlate with the defect density statistics attained from AC-STEM, hinting that these samples might have tears or cracks in the membrane. Examination of these samples by scanning electron microscopy (SEM) on large areas indeed indicates that they are damaged samples (see tears in suspended WS₂; fig. 6.7).

The measured He flow values are within an order of magnitude of the values predicted by the Knudsen estimates, despite the uncertainties in our defect densities and the distribution of the type of defects. Equation 1 is based on the kinetic theory and has been applied to

describe the flows through apertures using effusion mechanism in both theoretical²⁶⁶ and experimental literature^{89, 106}. To more precisely validate the agreement to Eq. 1 and/or evaluate its limitations in our experiments, we would need to further decrease our experimental sources of error, including the calibration of all defect areas, which is a challenging experimental task. To verify whether there is any energy barrier, we measured gas flows by varying the temperature between $\sim 25^\circ$ to $\sim 100^\circ\text{C}$, by using a heating tape wound around the chamber, interfaced with a temperature controller. We did not see noticeable variation in the gas flow with temperature, hinting an absence of an energy barrier (an exponential dependence is expected if an energy barrier is present). As per Eq. 1, a $T^{-1/2}$ dependence would lead to variation of flux by $<10\%$ within the temperature range tested, and this is beyond our experimental measurement error.

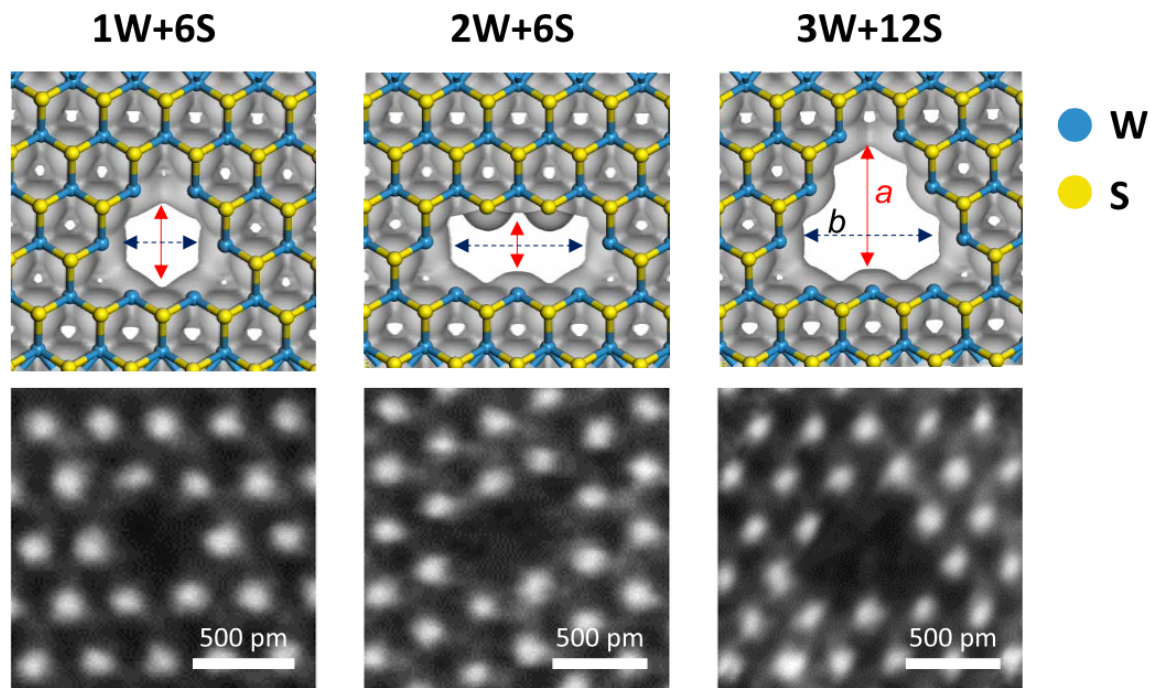


Figure 6.3. Atomic apertures and electron density isosurfaces.

Typical aperture sizes with the irradiation dose ($\sim 5.1 \times 10^{13}$ ions/cm²) are shown. The top panel shows the density functional theory (DFT) results for electron density isosurfaces of atomic apertures in a WS₂ membrane (isovalue of $0.2 \text{ e}/\text{\AA}^3$). The S and W atoms are shown in yellow and blue, respectively. The blue and red arrows inside the images are the accessible dimensions in width *a* and length *b* across the pores (1W+6S, $a \approx b \sim 3.2 \text{ \AA}$; 2W+6S, $a \sim 2.1 \text{ \AA}$, $b \sim 6.2 \text{ \AA}$; 3W+12S, $a \sim 5.8 \text{ \AA}$, $b \sim 6.2 \text{ \AA}$). The accessible aperture areas for helium molecules are ~ 0.08 , ~ 0.13 , $\sim 0.23 \text{ nm}^2$, respectively. The bottom row includes the AC-STEM images of the defect, while the top row illustrates the observed atomic configuration. From the electron density isosurface (EDI) of defects shown in Fig. 6.3 (and fig. 6.5) using first-principles density functional theory (DFT) calculations, accessible pore areas are obtained (table 6.1). The accessible pore areas from EDI closely match with those estimated using vdW radii (section 6.6). The surface transport contributions can be negligible as He does not adsorb sufficiently on the WS₂ basal plane, similar to that observed on graphene (typical adsorption layer thickness, ~ 4 to 6 \AA).²⁰⁸

Ideal atomic apertures with only 1W missing and with no missing sulfurs on the pore edge would likely, theoretically, be nonconducting. On the other hand, 1W defects with six sulfur vacancies with an accessible pore diameter of $\sim 3.2 \text{ \AA}$, which is larger than the kinetic diameter of helium (2.6 \AA), would be amenable to gas flows. As shown in Fig. 6.1D, the minimum area of the defects obtained from AC-STEM imaging was about 0.06 to 0.1 nm^2 ,

which corresponds to the defects with 1W and 6S missing ($\sim 0.08 \text{ nm}^2$), whereas the 1W defects with no sulfurs missing would be of significantly lower area ($\sim 0.002 \text{ nm}^2$). As the characteristic pore size decreases, the electron-overlap between He and membrane significantly increases, thereby increasing the energy barriers for the flow. However, the theoretical calculation of energy barriers might not necessarily capture all the favorable electronic interactions in real systems as there can be rearrangements in the vacancies. These discrepancies between the computed energy barriers and the experimental flows have been noted before by Wang et al⁹³. Specifically, our results do not imply a significant energy barrier compared to theoretical predictions^{209,93,140, 210}, and we also note that different levels of DFT calculations (and supercell size, or equivalently, the ratio between the pore area and the simulated defect area in membrane) can give different energy barriers; thus, a separate systematic DFT study is required for carefully probing the energy barriers. We stored our samples with atomic vacancy defects under ambient conditions. When we tested the samples after a few weeks, it was observed that they tend to get clogged with time, leading to reduced/ no He flow. As is well known, all surfaces are likely to be covered by hydrocarbons, which might cause the clogging²³² of atomic apertures in our case. However, upon reannealing at 350°C , He flow was regained to the previously observed value within a factor of 2. Storage of samples in activated charcoal helped extend the life span of the atomic apertures to be open for few months. Annealing with a combination of storage in charcoal has enabled us to keep the atomic apertures open for about a year. The atomic vacancy defects, once created, are quite stable and show similar helium flow with repeated annealing, indicating that the atomic apertures do not expand or propagate rapidly. Those samples that have been irradiated but did not conduct gas remained nonconductive

even after repetitive annealing. We speculate that these samples could have contained a majority of the dominant 1W defect type with one “W” atom missing but with partial or all S atoms at that site, thereby increasing the energy barrier and leading to no He flux. While the ion irradiation dose is optimized for single-atom (W) defect pores, the removal of sulfur atoms from ion irradiation and the subsequent AC-STEM imaging to precisely know the composition of sulfur vacancies at a defect site have remained a challenge. However, in the extreme limit, when there were large holes, tears, or cracks in the membrane, the flow was much higher, and the membranes themselves were not stable. In addition, we performed ion flow measurements in KCl solution on our atomic apertures as a cross-check. Those samples that showed inconsistent and unexpectedly high gas flows showed high ionic conductance (~ 400 nS in 1 M KCl; see fig. 6.8), again indicating the presence of tears (visible in SEM; see fig. 6.7). The samples that showed gas flows commensurate with the Knudsen equation exhibited only a small ionic conductance, < 1 nS in 0.1 M KCl for total membrane area ~ 0.4 to 0.6 mm², as shown in fig. S7. This is expected as the atomic apertures with sizes < 6 Å exclude ions¹⁵⁶, but the presence of tears in the membranes leads to bulk ionic flow (see fig. 6.7). These observations further emphasize that the sealing of WS₂ monolayers to the SiN_x membranes is leak proof, leaving no gaps, and hence, only irradiated defects contribute to the observed gas flow.

6.5 Additional Experimental Methods

CVD growth of monolayer WS₂ flakes:

Monolayer WS₂ flakes were grown using CVD processes similar to previously reported methods. Solutions of 2% sodium cholate growth promoter and 15×10^{-3} M ammonium

heptamolybdate (metatungstate) were spun onto piranha-cleaned silicon (Si) substrates coated with 150 nm of SiO₂, which were then loaded into the center of a tube furnace (Thermo Fisher Scientific Lindberg/Blue M). For WS₂, samples were heated in argon atmosphere [100 standard cubic centimeters per minute (sccm)] at a rate of 65°C min⁻¹ and held at 800°C for 10 min, during which time 15 sccm of H₂ was also added. Approximately 100 mg of sulfur precursor placed 22 cm from the substrates was kept at 180°C during the growth procedures. Both samples were rapidly cooled to room temperature by cracking open the furnace.

Position-controlled transfer of WS₂ flakes:

With WS₂ flakes grown on Si/SiO₂ wafer pieces, we cut smaller pieces with areas about 3 × 3 mm² that contain good WS₂ flakes. Using a wet transfer technique, the TMD flake side of the SiO₂ pieces is coated with poly (methyl methacrylate) (PMMA) (MicroChem C4, 4000 rpm for 60 s). The PMMA-coated substrates are left to dry at ambient temperature for a few minutes before being floated onto the KOH etchant (8 g per 100 ml of water). Depending on the thickness of the SiO₂ wafer, the time for etching away the SiO₂ layer varies. Last, we observe the PMMA + TMD flake floating on the KOH etchant. These PMMA + TMD flakes are then rinsed three times in clean water baths before being used to transfer them onto a SiN_x/Si chip with a hole (diameter range, 200 to 300 nm) drilled by FIB. Position transfer is practiced when the flake size and their number density are high, so that in this case, it is possible to place one PMMA + TMD flake onto the SiN_x FIB hole. This step of placing the PMMA + TMD flake over the SiN_x FIB hole is somewhat challenging since the coverage of the FIB hole depends on the number of the as-grown

flakes. However, because in a given batch of CVD growth, the number of grown flakes is large, the transfer is completed within several transfer trials. In addition to this manual transfer, we have also used custom-built manipulators, with needles and tweezers to move the flake on the substrate to increase device yield. These manipulations came at a cost, since there was now a higher risk of device failure caused by the usage of additional tools, which can sometimes break the membrane. In this work, all devices were fabricated by manually “fishing” (moving) the PMMA + TMD flake onto the SiN_x FIB hole. After we transfer the flake and optically verify the coverage, the sample is then dried in ambient temperature for 30 min. Furthermore, the sample is placed into hot acetone (90°C) to remove the supporting PMMA.

Gallium

Ion

Irradiation:

Monolayer TMD flakes were irradiated with a Ga -sourced ion beam FEI Strata Dual-Beam instrument. The acceleration voltage of the ion beam was set to 30 kV and incident normal to the surface. The beam spot size was observed to be 100 nm for a flash second at 10-pA current. To produce atomic defects, an area of 250 nm by 250 nm was irradiated with the dwell time (16 μs) and current (10 pA). Pixel resolution (1024 × 884) was kept constant. The exposure was carried out in an imaging mode, which followed a raster pattern where the beam sequentially exposed each pixel in a row. The instrument, FEI FIB Strata DB 235, has an option to “grab frame,” which takes a single scan at a set resolution; this option was used for all the scans. The dose was varied by changing the number of scans. Suspended and substrate-supported samples were exposed to FIB irradiation while sitting on holey carbon TEM grids and Si/SiO substrates, respectively.

AC-STEM imaging:

AC-STEM images of WS₂ samples were acquired using a Cs-corrected JEOL ARM 200CF STEM operating at 80 kV. Images were obtained using a high-angle annular dark-field (HAADF) detector with a collection angle of 54 to 220 mrad and 10-cm camera length. Probe current (22 pA), focusing time (<2 s), and electron dose ($\approx 6.0 \times 10^6 e^- \text{ nm}^{-2}$) were kept low to minimize beam-induced knock-on damage

First-principle calculations for Helium transport through atomic apertures:

To shed light on the energy barriers of the He atom crossing through the defected WS₂, the density functional theory (DFT) was performed with the Generalized Gradient Approximations (GGA)¹⁴⁶ form with exchange-correlation potential parametrization of Perdew–Burke–Ernzerhof (PBE)¹⁵⁴. The calculations were carried out by the Quantum-ESPRESSO (QE) package⁴⁹ and have been performed based on the plane-wave basis sets and ultrasoft nonlocal pseudopotentials²⁰³. To take the vdW contributions into account in the total energy, the Tkatchenko–Scheffler (vdW-TS)¹⁹⁶ method was used. The cut-off of kinetic energy in the plane-wave expansion and the convergence threshold for the self-consistent field (SCF) calculations were chosen as 280.0 eV and 10^{-6} eV/atom, respectively. Calculations were done at zero kelvin for a rectangular supercell shape with size $15.953 \times 16.579 \text{ \AA}^2$ for all considered defects consisting of 29(60), 29(54), 28(58), 28(54), 27(54), and 27(48) atoms of W (S) for 1W, 1W (+6S), 2W (+2S), 2W (+6S), 3W (+6S), and 3W (+12S) with a vacuum layer of 30 Å between periodic images in the vertical direction. The total energy of the He/defected WS₂ structures was calculated by placing a

He atom at distance z above the center of the pore. For a given structure, the total interaction energy was calculated by using equation $E(z)=E_t(z)-E_{\text{ref}}$ where $E_t(z)$ is the total energy of the system (He+ defected WS_2) and E_{ref} is the energy of the system when He atom is far from WS_2 , i.e. $z \gg 1\text{nm}$. This calculation was repeated for different z values in steps of 0.25 \AA . The corresponding results (interaction energy and energy barriers) are shown in Figure S5 and Table S1 for six different vacancies. We also calculated the electron density isosurface (EDI) using the using the above aforementioned functionals and energy cut-off and etc. For the EDI image, the isovalue set to be 0.2 e/\AA^3 . From the interaction energy profile versus distance from WS_2 plane, we can determine the adsorption thickness (typically about ~ 4 to 6 \AA).

Molecular Dynamics Simulations:

In order to find the probability density of He atoms along the z -direction, we conducted molecular dynamics simulations (MDS). The simulations were done using LAMMPS (Large-scale Atomic/Molecular Massively Parallel Simulator). The simulation box has a dimension of $3 \times 3 \times 3 \text{ nm}^3$, where the WS_2 layer is located at the middle of the z -axis. 500 He atoms were added to the system. Reflective boundary conditions were applied in the z -direction of the simulation box (normal to the WS_2 plane) and periodic boundary conditions were applied in two other directions (x and y). For a given defect, each MDS was run in the NVT ensemble for a period of 1ns with a time step of 1fs. The temperature was kept constant at 300 K using a Nosé-Hoover thermostat. To make the model simple and because of mechanical stiffness of WS_2 , we fixed WS_2 atoms. The interatomic interactions between He and WS_2 were modeled by the well-known Lennard-Jones (LJ) potential. Using

Lorentz-Berthelot combining rules, the parameters for the LJ potentials are chosen as $\epsilon_{W-He} = \sqrt{6} \text{ meV}$, $\epsilon_{S-He} = \sqrt{8.5} \text{ meV}$ and $\sigma_{W-He} = 3.3 \text{ \AA}$, $\sigma_{S-He} = 3.2 \text{ \AA}$. The parameters for W and S can be found in reference⁵⁰, with further details about the MDS method in reference¹⁸¹.

Characterization of Pristine WS₂:

The quality of as-grown monolayer WS₂ flakes was extensively characterized using electron and optical microscopy. Selected area electron diffraction (SAED) of suspended flakes confirmed the monocrystallinity and 2H phase of the pristine material (see Supplementary Figure S2). Atomic-resolution images were used to quantify intrinsic defect densities, which can result from imperfections and dopants during the CVD growth and/or transfer process. Multiple (> 50) AC-HAADF STEM images of monolayer WS₂ flakes transferred onto holey carbon TEM grids were sampled over to obtain an intrinsic transition metal defect density of 0.013%. During imaging, electron knock-on and radiolysis damage was minimized with a low electron acceleration voltage (80 kV) and beam current (20 pA). No discernible defect creation during STEM imaging was observed. Due to their strong optoelectronic absorption and direct visible-range band gap, monolayer TMDs can also be characterized through photoluminescence (PL) spectroscopy. Obtained PL spectra for monolayer flakes indicate spectral weight percentages that are consistent with previously reported values for high-quality WS₂³⁰.

Characterization of Pristine and Irradiated WS₂:

Monolayer WS₂ membranes were exposed to energetic 30 keV Ga⁺ ions in a focused ion beam (FIB) as outlined in Supplementary Figure S1. The 30 keV energy of impinging Ga⁺

ions is above the displacement threshold of W atoms ($\sim 20\text{-}25$ eV), resulting in atomic defects. Afterwards, defects in the monolayer WS_2 flakes were characterized again using aberration-corrected STEM (AC-STEM) imaging. Quantitative statistics for average defect size and density were obtained by averaging over multiple STEM images. For an irradiation dose of 5.07×10^{13} ions/cm², an average defect density of 7.9×10^{-2} % ($\pm 2.2 \times 10^{-2}$ %) and size of 1.2×10^{-1} nm² ($\pm 5.5 \times 10^{-2}$ nm²) are observed. Since AC-STEM images also contain mass contrast information, the atomic configurations of various defects were analysed. Based on the contouring bright metal atoms in the image, their relative frequencies for each defect site were assessed from several TEM images for the histogram in Figure 1d. However, the accessible pore areas for transport of He atoms is expected to be much lower than pure geometric area (see below, Effective pore size calculations). Additionally, the uncertainty with TEM imaging in finding the S atoms on the defect edge would largely influence the effective area. While no changes in the Raman spectra of irradiated membranes were seen under a 532 nm excitation, photoluminescence spectroscopy revealed an increase in defect-induced midgap states (X^D).

Effective pore size calculations:

The accessible effective area of the aperture for a gas molecule (in our case, He gas with kinetic diameter ~ 0.26 nm) is calculated based on the van der Waals radii of the terminal atoms on the WS_2 defect edges. For example, in 1W+6S site, the center-to-center distance between opposite W sites on the pore, $D_{\text{W-W}} = 0.63$ nm. The van der waals diameter of W atom, $d_{\text{vdw}} = 0.42$ nm. The effective pore size between W atoms excluding the collision cross section is calculated using the formula²⁰⁹ (4)

$$D_{\text{vdw}} = D_{\text{W-W}} - (d_{\text{vdw}})/\sqrt{2},$$

which gives D_{vdw} for $(1W+6S) = 0.33$ nm. We have also simulated electron density isosurfaces using density functional theory and calculated edge-to-edge distance between two adjacent W atoms of the aperture. Both values are almost equal and indicate that the effective area is lower than the geometric area and that the He transport is in the steric regime.

Annealing before Gas Measurements:

All the devices including controls are annealed at 350 °C for four hours in 10% H₂ / 90% Ar atmosphere. Gas measurements are performed soon after the annealing of devices. Annealing helps in unclogging of devices from atmospheric hydrocarbons and other adsorbing gases. However, this annealing step has not increased the gas flux by further widening the atomic apertures or damaging the WS₂ membranes in control samples.

Gas Flow Measurements:

Helium (He) gas permeation was measured using a mass spectrometer (helium-leak detector, Leybold phoenix L300i). The SiN_x/Si wafer with monolayer WS₂ membrane was clamped between O-rings (Kalrez) to separate two chambers (Figure S5). At first, both the chambers were evacuated using a bypass loop connected to a vacuum pump. Then, He gas was released into one of the chambers with controlled pressure P, and detected from the other chamber connected to the mass spectrometer as it flows through membrane with atomic defects. It was found that the gas flux detected by the mass spectrometer increased linearly with He gas pressure (main Figure 2). Since the diameter of the pores in the membrane are much smaller than the mean free path of He atoms (~140 nm at room temperature), the flux (Q_K) through these angstrompores can be described by equation (1).

For temperature variation experiments, we used a heating tape (Hemiheating AB) wound around the two chambers. A PID temperature controller (HTC-5500) interfaced with the tape, controlled the temperature with an accuracy of ± 2 °C. At each temperature, we waited ~5 min for stabilization before measuring the gas flow.

Ionic current measurements:

Ionic current measurements and experimental details are performed with parameters as in reference²⁴. Briefly, Ag/AgCl electrodes and a patch-clamped amplifier are used to monitor ionic current as voltage is applied across the irradiated WS₂ suspended membranes. The data in this figure correspond to 0.1 M KCl and 1 M KCl solutions with a buffer (10 mM EDTA and 1 mM Tris). The pH was 8.7. Irradiated membranes were first annealed at 300 °C in an Ar-H₂ (10% H₂ in argon) for 90 minutes, then they were immersed in 50% water-ethanol for 30 minutes or longer to aid in wetting of membranes in KCl solutions. Wetting of sub-nm pores is a well-acknowledged problem in nanopore measurements, and therefore some pores may not contribute to ionic conductance. Maximum applied voltage was ± 0.1 V to minimize the possibility of membrane dielectric breakdown and pore enlargement during repeated measurements.

We observed several faulty devices with tears in our fabrication process (Figure S6). These devices result in excessive flow (in both ionic current measurements and gas flow) and therefore are included as failed/leaky devices. Another signature of these leaky devices, after annealing, they have showed much increased flux compared to their initial flux.

Gas flow through apertures – analysis:

Equation (1) is derived from the kinetic theory, and described by Knudsen as a solution for gas flow through infinitely thin apertures³⁷. For apertures with diameters far less than the mean free path λ , the probability of intermolecular collisions near the vicinity of the aperture goes down drastically, and the free molecular transport can be described by effusion. There are several models (*e.g.*, BKT model, dual region model) for rarefied gas flows with Knudsen numbers $0.1 \leq Kn \leq 10$ taking the slip, adsorption of the molecules to the walls, drag *etc.*, into account. Previous studies on carbon nanotubes, cylindrical, and slit-like pores with finite length, showed enhanced flow compared to Knudsen estimates, which was attributed to specular reflection of gas molecules off the atomically smooth graphite walls or pore surfaces^{217,218}. In graphene slit-pores, ballistic flow of He was observed due to specular reflections, while MoS₂ slit-pores showed diffusive reflections⁸⁴. However, here our atomic-scale apertures are within essentially infinitesimally thin membranes and these can be approximated as orifices, hence effusion-based mechanism seems the most suitable to describe the flow^{27,93, 181}. The effusion mechanism depends on the impingement of gas molecule and can be quantified as $Q = v \Delta n/4$, where $v = \sqrt{8RT/\pi M}$ is the mean velocity of the molecule, Δn is the gas number density. Combining with ideal gas law,

$$Q = P A \sqrt{1/2\pi MRT} \quad (\text{eq. 1})$$

As the gas traverses through the aperture, the main hindrance to the flow is the probability of the gas hitting the aperture at a critical angle so as to be able to pass through the pore. As per Sun et al. article¹⁸¹, the critical angle of incidence, $\theta = \cos^{-1}(R_m/R_p)$, where radius of the helium molecule $R_m = 1.3 \text{ \AA}$ and radius of the pore $R_p \sim 1.6 \text{ \AA}$ to 3.1 \AA in our case.

Therefore, θ will be in the range of 35° to 65° for 1W to 3W defect pores. However, from our experiments, we observe that the He permeation/flux is within the expected estimates of equation (1) which indicates that the steric hindrance is likely not significantly reducing the flux. The steric hindrance can lead to a reduction factor of “ R_p/R_m ” (< 1) from ideal flux¹⁸¹ (4). This factor “ R_p/R_m ” will be >1 for 1W+6S pores and ~ 0.8 for 2W defects, which have pore sizes of $\sim 3.1 \text{ \AA}$ and $\sim 2 \text{ \AA}$ respectively. For 2W pores, there can be slight reduction of the flow, however, as the number of such pores are relatively small ($\sim 22\%$), the reduction of flow if any is not captured well in our measurements.

Let us note that although it is the area of the aperture that is in the equation (1), the shape of the defect is also known to influence the resulting Knudsen flux as shown by the unified model for slit-like pores with finite length²¹⁷. For our aperture case, we neglect the variations if any, due to the shape of the defect, as the dimensions of the aperture are quite close to the He kinetic diameter, and hence the corners of the aperture remain inaccessible. New models need to be developed in this new experimental regime to explain the shape and end effects and/or the phase transitions of the fluid while passing through such thin membranes²¹⁸.

For flux estimates, we have considered their area by approximating the pore as circular (1W defect) or rectangular shape (2W defects) or truncated triangular shape (3W defect). The accessible pore sizes and their effective areas are summarized in Figure S4 and Table S1.

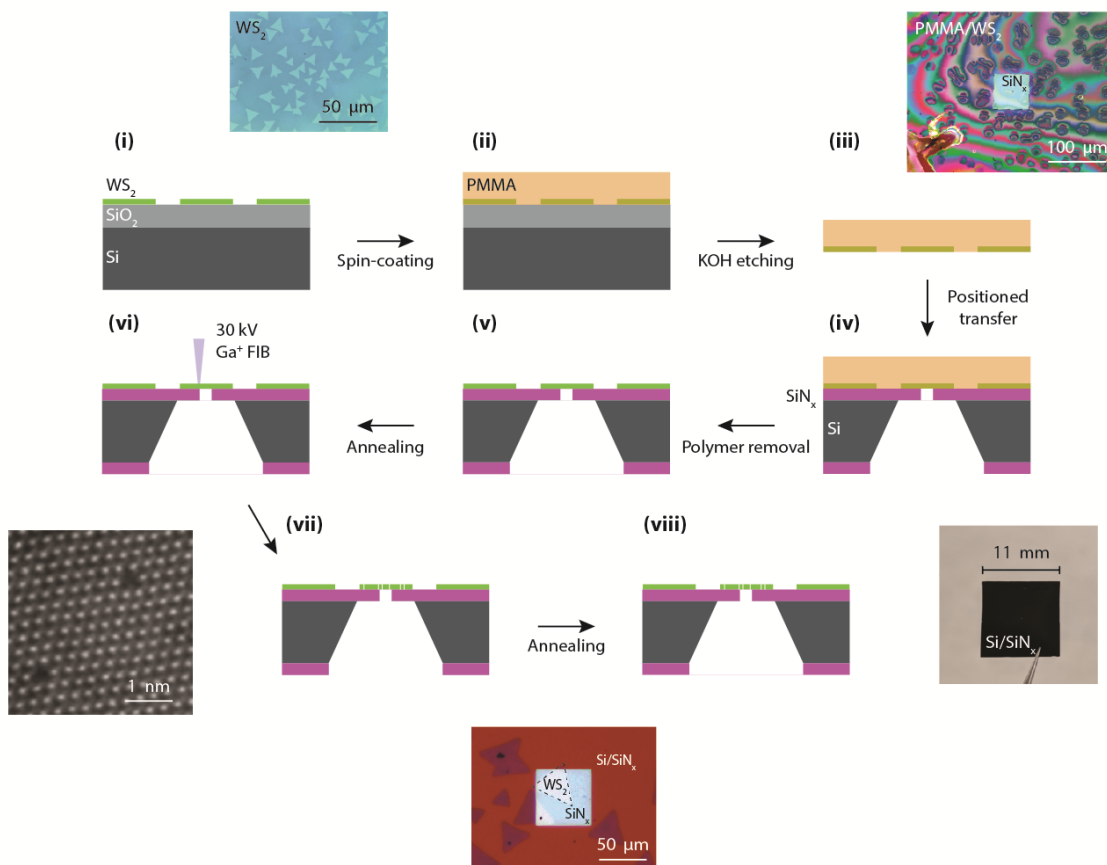


Figure 6.4. Schematic of fabrication process for WS_2 single atom aperture devices

(i) CVD-grown monolayer WS_2 flakes on Si/SiO_2 substrates are (ii) spin-coated with PMMA and (iii) etched in KOH solution. (iv) The PMMA/ WS_2 stack is then positioned on top of a 200-300 nm diameter hole in a Si/SiN_x substrate. (v) The PMMA is subsequently removed in acetone and annealed in Ar/H_2 . (vi-vii) Single atom defects in the WS_2 membrane are formed using Ga^+ FIB irradiation (Supplementary Section 1.3). (viii) Samples are annealed again prior to gas transport measurements (Supplementary Section S3). Top insets, left to right - Optical images of CVD-grown WS_2 material and a PMMA/ WS_2 stack after positioning onto a sub-micron hole. Bottom insets, left to right - Atomic resolution STEM image of single atom apertures in monolayer WS_2 , optical image of final FIB-irradiated WS_2 (outlined in black) on a SiN_x membrane, and optical image of the square, 11-mm-large, Si/SiN_x substrate.

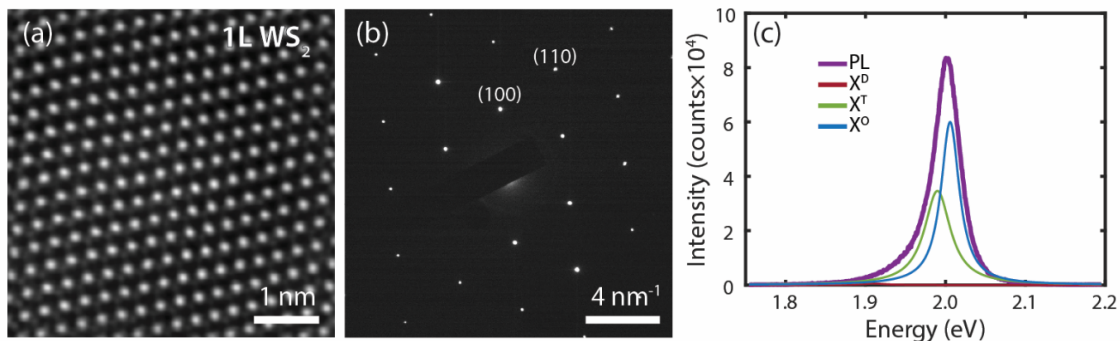


Figure 6.5. Characterization of CVD-grown pristine WS₂ flakes.

(a) Aberration-corrected STEM image of as-grown monolayer WS₂ flakes on a holey carbon TEM grid. W and S₂ atomic sites appear as bright and dim atoms, respectively, in a trigonal prismatic (2H) coordination due to the mass-contrast behaviour of high-angle annular dark-field (HAADF) imaging. Multiple atomic-resolution STEM images were sampled over to obtain quantitative defect statistics (see also Supplementary Figure S3). (b) SAED pattern of suspended monolayer WS₂. The presence of a single set of six-fold symmetric (100) and (110) diffraction spots indicate monocrystalline 2H-phase WS₂. (c) PL spectrum of a pristine flake on a 150 nm SiO₂/Si wafer taken at room temperature with a laser excitation wavelength of 532 nm (*i.e.*, green). Spectra were fit to the defect (X^D), charged trion (X^T), and neutral exciton (X^O) peaks at 1.88, 1.96, and 2.02 eV, respectively³⁰. Pristine WS₂ was found to have X^D, X^T, and X^O spectral weight percentages of 0.6%, 44, and 55%, respectively.

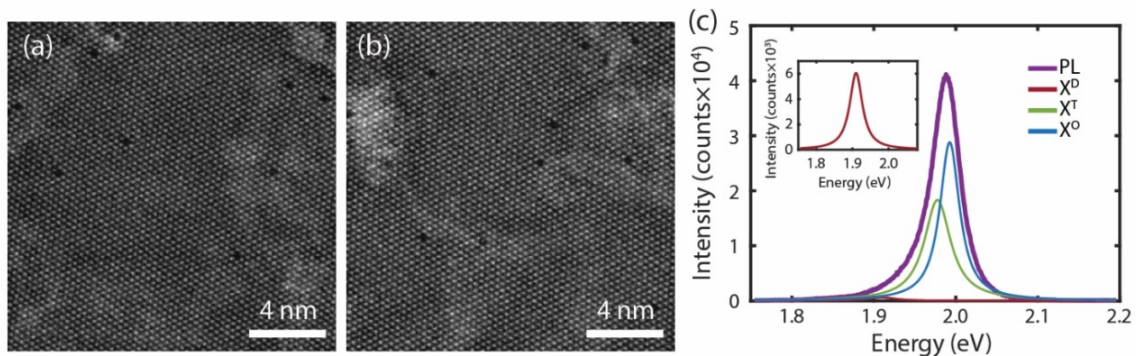


Figure 6.6. Characterization of FIB-irradiated WS₂ flakes.

(a,b) Aberration-corrected HAADF STEM images of monolayer WS₂ flakes after exposure to 5.1×10^{13} ions/cm² of 30 keV Ga⁺ focused ion beam irradiation. Single defects appear as the absence of contrast at transition metal lattice sites. Multiple atomic-resolution STEM images were sampled over to obtain quantitative defect statistics (see also Supplementary Figure S2). (c) PL spectrum of a monolayer WS₂ flake suspended on a holey carbon film

after exposure to 5.07×10^{13} ions/cm² of FIB irradiation. The 1.6% spectral weight percentage of the defect peak (X^D) to 1.6% suggests that FIB irradiation causes a slight increase in the PL midgap states localized at transition metal defect sites.

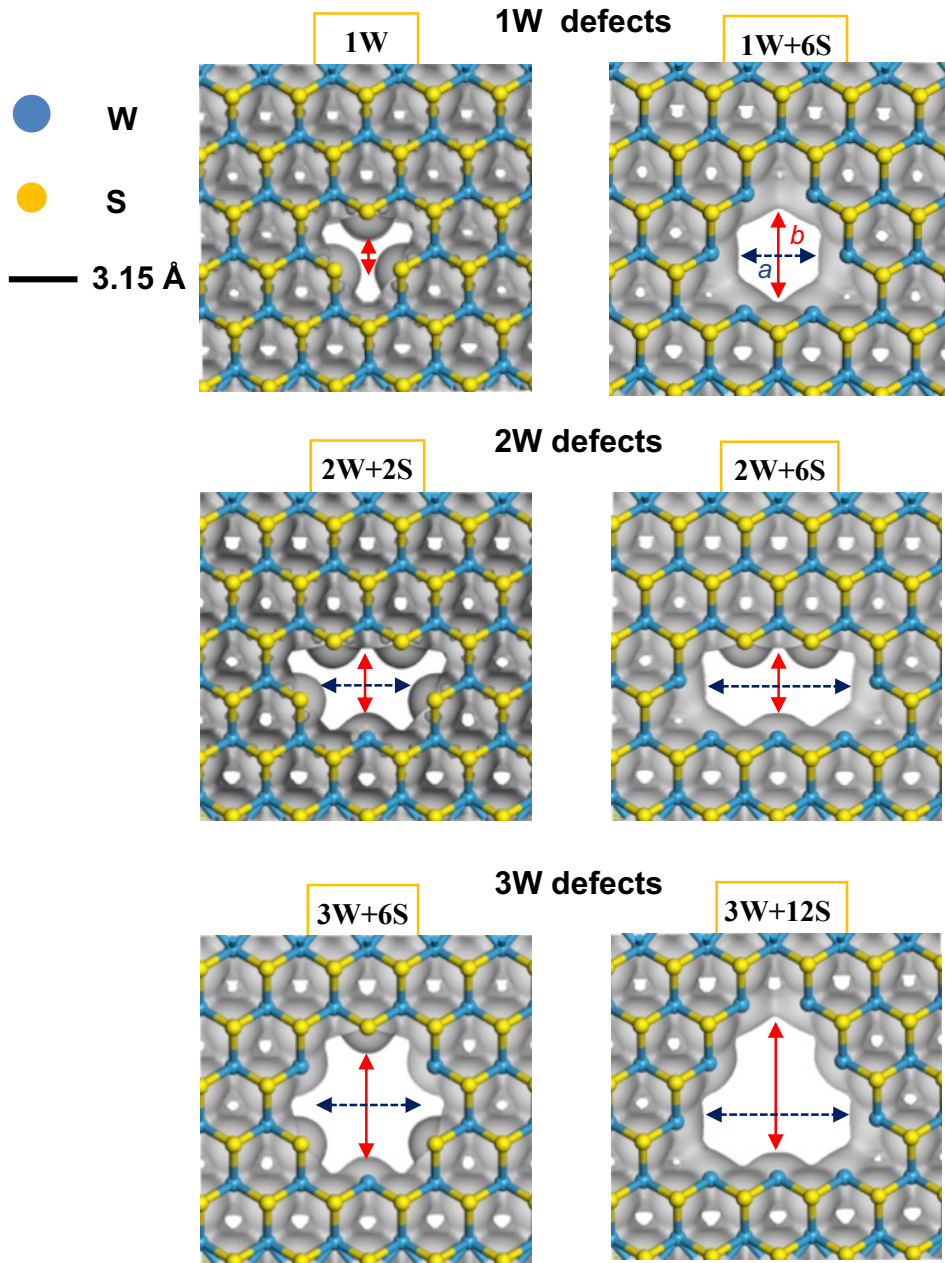


Figure 6.7. Atomic apertures.

Typical apertures created on WS₂ monolayer upon the irradiation dose ($\sim 5.1 \times 10^{13}$ ions/cm²) with FIB are shown here with simulated isosurfaces. The aperture sizes were calculated using DFT based on accessible area after the electron density contours from isosurfaces (a and b indicate the width and length of the defect respectively as depicted on images). Effective areas of the defect sites, one tungsten defect sites (1W with area, AI^*

and 1W+6S with area, $A1$), two tungsten defect sites (2W+2S with area, $A2^*$ and 2W+6S with area, $A2$), and three tungsten defect sites (3W+6S with area, $A3^*$ and 3W+12S with area, $A3$) were approximated based on their close match with regular shapes and values were presented in Table S1. Single W vacancy with no sulfur vacancies is likely non-conducting due to its extremely small accessible pore size (~ 1 Å) compared to Helium size (2.6 Å).

Defect type	Width of the pore (a , nm)	Height of the pore (b , nm)	Area (nm ²), approximated shape
1W	0.105	0.105	0.009 ($A1^*$, circle)
1W+6S	0.315	0.315	0.079 ($A1$, circle)
2W+2S	0.36	0.21	0.075 ($A2^*$, rectangle)
2W+6S	0.62	0.21	0.129 ($A2$, rectangle)
3W+6S	0.525	0.525	0.216 ($A3^*$, circle)
3W+12S	0.62	0.58	0.23 ($A3$, truncated triangle)

Table 6.1. Effective areas of atomic-scale apertures in WS₂ monolayer membrane for transport of He

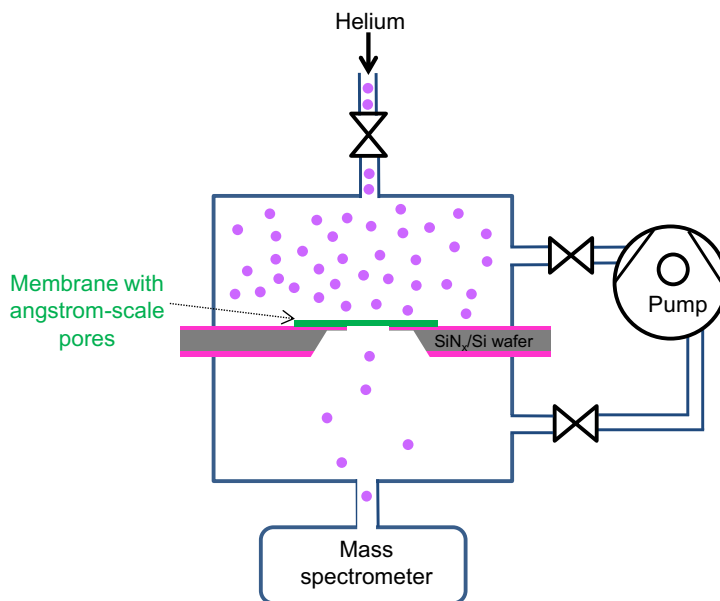


Figure 6.8. Helium flow measurement

Schematic representation of gas permeation measurement setup using mass spectrometer (Leybold phoenix L300i). In this setup, the only pathway between the top and bottom chambers is through the one-atom defects in WS₂ membranes, i.e., atomic apertures.

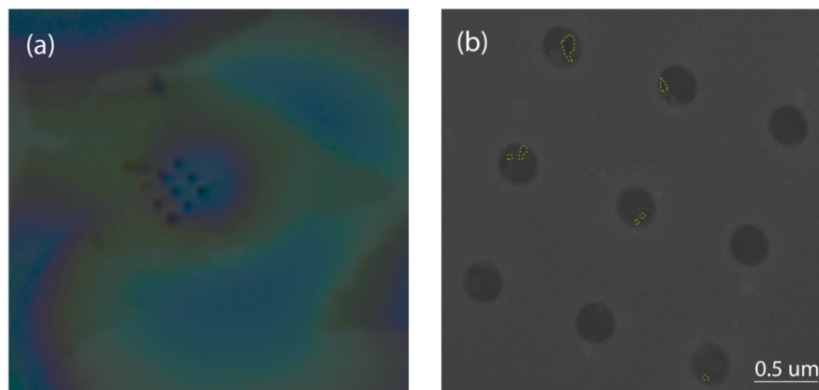


Figure 6.9. Tears in SEM analysis

(a) Optical image of the device after WS_2 transfer with PMMA. The image shows nine large pre-drilled holes in the centre of the chip, onto which the WS_2 monolayers are deposited. (b) Scanning Electron Microscope image of sub-micron tears within the WS_2 monolayer membranes, indicated by dashed yellow markers in five out of the nine holes.

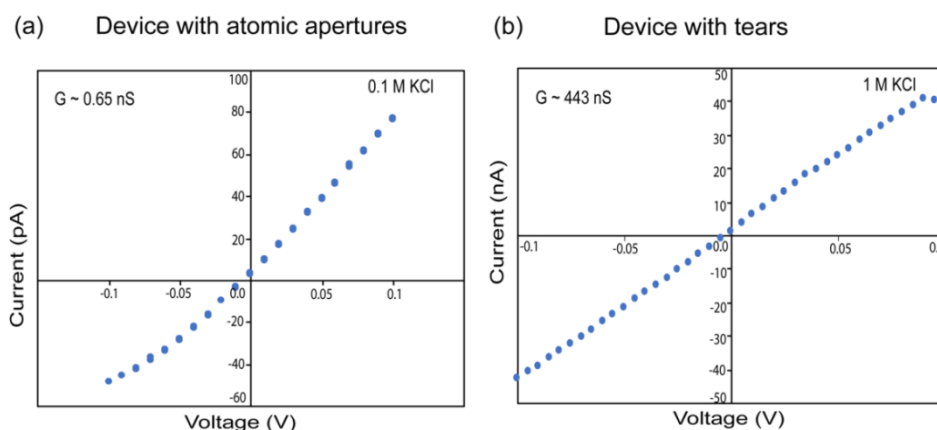


Figure 6.10. Current-voltage (I-V) analysis

(a) I-V of device showing negligible ionic currents (< 100 pA) up to ± 0.1 V applied voltage (conductance ~ 0.65 nS), in 0.1 M KCl. This device had nine FIB-drilled holes (with diameters in the range of 250 to 300 nm) onto which the 2D membrane was suspended. The atomic apertures were created with Ga ion irradiation dose = 5.1×10^{13} ions/cm². The defects with size of about < 0.6 nm are not expected to conduct ions based on MD simulations, and the observed small conductance could be due to one or two pores of the size < 1 nm. One single pore of the size, ~ 1 nm in a TMD membrane showed a conductance of ~ 1 nS in 1 M KCl¹⁹⁰, which can further indicate upper limit on pore sizes in this sample. (b) Device showing high conductance ~ 443 nS in 1 M KCl indicative of membrane tears.

6.6 Discussion on Gas Permeance in literature and Conclusion

Let us analyze the gas flow in nano- and angstrom-scale pores from the literature, in comparison to our atomic vacancy defects presented here. It has been shown in the literature that when the pores are less than the size of the gas molecule passing through⁹³, activated transport is observed and highly sensitive energy barriers play a major role in the transport, and the barrier is usually estimated using combined theoretical and experimental efforts. In this work, since the atomic vacancy apertures are only slightly larger than the gas molecule (i.e., less than twice the size of helium molecule, 2.6 Å), the flow is governed by simple effusion. In general, effusive flow is seen as detrimental and the cause of reduction for selectivity between gases in size exclusion. Because of this, an accurate comparison of the observed permeability and value estimated from the Knudsen description for the known size of the aperture is often overlooked. Such a comparison made for nanometer-sized holes showed the validity of the Knudsen description in graphene pores down to ~ 7 nm in size, where a N_2 permeance of $\sim 0.05 \text{ mol m}^{-2}\text{s}^{-1}\text{Pa}^{-1}$ was observed⁸⁹. Angstrom-size defects (size, ~ 0.38 to ~ 0.43 nm) made by ozone-induced etching in a CVD-grown graphene layer were shown to have a H_2 permeance of about $10^{-7} \text{ mol m}^{-2}\text{s}^{-1}\text{Pa}^{-1}$ ²⁷, which is only one order higher than the permeability of graphene membrane, $10^{-8} \text{ mol m}^{-2}\text{s}^{-1}\text{Pa}^{-1}$ hosting the defects¹⁰⁶. However, the observed gas flow values for atomic defects are still much lower than that estimated from the Knudsen description for given defect densities, which might be due to the overestimation of the conducting apertures. In our WS_2 atomic aperture samples, the He gas flow obtained matches the Knudsen estimates within a factor of 2 to 3, and the gas flow normalized by the total area of defects translates to ~ 0.05 to $0.1 \text{ mol m}^{-2}\text{s}^{-1}\text{Pa}^{-1}$. From theoretical studies on graphene pores with sizes 3.6 to 4.8 Å, for

defect densities up to $\sim 10^{14}$ cm⁻², large permeance of ~ 0.1 mol m⁻²s⁻¹Pa⁻¹ has been predicted^{19,210}, which closely matches with our experimental values. These permeance values are higher than those typically observed in silica⁷⁰, zeolite, and metal-organic framework membranes, graphene oxide membranes¹⁶⁸, which are in the range of $\sim 10^{-6}$ to 10^{-7} mol m⁻²s⁻¹Pa⁻¹. Large permeance values are obtained through our WS₂ apertures, even when normalized with the area of the membrane, i.e., $\sim 10^{-4}$ to 10^{-5} mol s⁻¹mbar⁻¹, which indicates that most of the atomic apertures are in the predicted size range and hence conductive to gases.

In conclusion, we demonstrate the fast He transport through quasi-0D atomic-scale apertures ($\sim W$ sites). To our knowledge, this is the first experimental observation on He gas transport in such angstrom-scale pores in WS₂/TMD monolayers where we attempt to evaluate the applicability of the Knudsen equation down to the ultimate limit. Our results indicate the necessity of future theoretical models to explore the role of sensitive variation of the energy barriers of various gas molecules and their critical dependence on the size of the aperture at this atomic limit, especially taking the electron density isosurfaces of atoms to account for the enhanced flux. In addition, this work provides a new method for corroborating atomic pore formation and their density over large areas via a simple bulk measurement technique of measuring gas flow through them. This is analogous to using nanoholes (few hundred nanometers in size) as standard leak elements for calibration.⁷⁰ So far, the only way to inspect and confirm the atomic pore formation in the case of atomic vacancy defects is by AC-STEM, which is limited to relatively small areas. Conventional ionic transport measurements through nanopores are mediated by Hille's equation¹⁵⁶, which yields a linear relationship between conductance and total aperture area. However,

for pores that are smaller in dimensions than many common salts, ionic conductance measurements do not yield a predictable or a measurable signal, leading to the breakdown of Hille's model for atomic aperture limit¹⁹³. With our study, we would like to highlight that once the pore creation is confirmed and calibrated by AC-STEM locally, gas flow measurements can act as a standard to test for the presence of these pores and their density over large areas. Let us also note that the stability of pore/aperture configuration of these atomic scale defects needs further investigation^{156,215} as the pores could change over time, which can be attempted in future experiments by imaging the pores over time. More advanced methods including dynamic scanning tunneling microscopy need to be devised to locate S atoms¹⁴⁶ and also any other atoms such as possible contaminants (C, O, and N) to be certain of pore compositions and sizes. Future work may involve efficient gas separation investigations using a scaled-up version of such membranes.

BIBLIOGRAPHY

- (1) Adams, D. P.; Vasile, M. J. Accurate Focused Ion Beam Sculpting of Silicon Using a Variable Pixel Dwell Time Approach. *Journal of Vacuum Science & Technology B: Microelectronics and Nanometer Structures Processing, Measurement, and Phenomena* **2006**, 24 (2), 836–844.
- (2) Ahlgren, E. H.; Kotakoski, J.; Krasheninnikov, A. V. Atomistic Simulations of the Implantation of Low-Energy Boron and Nitrogen Ions into Graphene. *Physical Review B* **2011**, 83, 115424.
- (3) Albrecht, T.; Gibb, T.; Nuttall, P. Ion Transport in Nanopores. In *Engineered Nanopores for Bioanalytical Applications*; Elsevier, 2013; pp 1–30.
- (4) Albrecht, T.; Gibb, T.; Nuttall, P. *Ion Transport in Nanopores*, First Edit.; Elsevier Inc., 2013.
- (5) Algara-Siller, G.; Kurasch, S.; Sedighi, M.; Lehtinen, O.; Kaiser, U. The Pristine Atomic Structure of MoS₂ Monolayer Protected from Electron Radiation Damage by Graphene. *Applied Physics Letters* **2013**, 103 (20).
- (6) Aliofkhaezrai, Mahmood, Ali, Nasar, Milne, William, Ozkan, Cengiz, Mitura, Stanislaw, G. *Graphene Science Handbook: Fabrication Methods*; 2016.
- (7) Amiri, H.; Shepard, K. L.; Nuckolls, C.; Hernández Sánchez, R. Single-Walled Carbon Nanotubes: Mimics of Biological Ion Channels. *Nano Lett.* **2017**, 17 (2), 1204–1211.
- (8) Antonelou, A.; Syrokostas, G.; Sygellou, L.; Leftheriotis, G.; Dracopoulos, V.; Yannopoulos, S. N. Facile, Substrate-Scale Growth of Mono- and Few-Layer Homogeneous MoS₂ Films on Mo Foils with Enhanced Catalytic Activity as Counter Electrodes in DSSCs. *Nanotechnology* **2016**, 27 (4), 045404.
- (9) Aryal, P.; Sansom, M. S. P.; Tucker, S. J. Hydrophobic Gating in Ion Channels. *Journal of Molecular Biology* **2015**, 427 (1), 121–130.
- (10) Bai, H.; Ma, J.; Wang, F.; Yuan, Y.; Li, W.; Mi, W.; Han, Y.; Li, Y.; Tang, D.; Zhao, W.; Li, B.; Zhang, K. A Controllable Synthesis of Uniform MoS₂ Monolayers on Annealed Molybdenum Foils. *Materials Letters* **2017**, 204, 35–38.
- (11) Bai, Z.; Zhang, L.; Li, H.; Liu, L. Nanopore Creation in Graphene by Ion Beam Irradiation: Geometry, Quality, and Efficiency. *ACS Appl. Mater. Interfaces* **2016**, 8 (37), 24803–24809.
- (12) Balan, A.; Chien, C.-C.; Engelke, R.; Drndić, M. Suspended Solid-State Membranes on Glass Chips with Sub 1-PF Capacitance for Biomolecule Sensing Applications. *Sci Rep* **2016**, 5 (1), 17775.
- (13) Balan, A.; Drndic, M. ULTRALOW CAPACITANCEGLASS SUPPORTED DIELECTRIC MEMBRANES FORMACROMOLECULAR ANALYSIS. US2017/0254796A1, September 7, 2017.
- (14) Bangert, U.; Pierce, W.; Kepaptsoglou, D. M.; Ramasse, Q.; Zan, R.; Gass, M. H.; Berg, J. A. Van den; Boothroyd, C. B.; Amani, J.; Hofsass, H. Ion Implantation of Graphene—Toward IC Compatible Technologies. *Nano Lett.* **2013**, 13 (10), 4902–4907.
- (15) Berkdemir, A.; Gutierrez, H. R.; Botello-Mendez, A. R.; Perea-Lopez, N.; Elias, A. L.; Chia, C.-I.; Wang, B.; Crespi, V. H.; Lopez-Urias, F.; Charlier, J.-C.; Terrones, H.; Terrones, M. Identification of Individual and Few Layers of WS₂ Using Raman Spectroscopy. *Scientific Reports* **2013**, 3, 1755.
- (16) Bertolazzi, S.; Brivio, J.; Kis, A. Stretching and Breaking of Ultrathin MoS₂. *ACS Nano* **2011**, 5 (12), 9703–9709.
- (17) Besteman, K.; Zevenbergen, M. A. G.; Lemay, S. G. Charge Inversion by Multivalent Ions: Dependence on Dielectric Constant and Surface-Charge Density. *Physical Review E - Statistical, Nonlinear, and Soft Matter Physics* **2005**, 72 (6), 1–9.
- (18) Blankenburg, S.; Bieri, M.; Fasel, R.; Müllen, K.; Pignedoli, C. A.; Passerone, D. Porous Graphene as an Atmospheric Nanofilter. *Small* **2010**, 6 (20), 2266–2271.
- (19) Bocquet, L. Nanofluidics Coming of Age. *Nat. Mater.* **2020**, 19 (3), 254–256.
- (20) Bocquet, L.; Charlaix, E. Nanofluidics, from Bulk to Interfaces. *Chem. Soc. Rev.* **2010**, 39 (3), 1073–1095.
- (21) Branton, D.; Deamer, D. W.; Marziali, A.; Bayley, H.; Benner, S. A.; Butler, T.; Di Ventra, M.; Garaj, S.; Hibbs, A.; Huang, X.; Jovanovich, S. B.; Krstic, P. S.; Lindsay, S.; Ling, X. S.;

- Mastrangelo, C. H.; Meller, A.; Oliver, J. S.; Pershin, Y. V.; Ramsey, J. M.; Riehn, R.; Soni, G. V.; Tabard-Cossa, V.; Wanunu, M.; Wiggin, M.; Schloss, J. A. The Potential and Challenges of Nanopore Sequencing. *Nat Biotech* **2008**, *26* (10), 1146–1153.
- (22) Bunch, J. S.; Verbridge, S. S.; Alden, J. S.; van der Zande, A. M.; Parpia, J. M.; Craighead, H. G.; McEuen, P. L. Impermeable Atomic Membranes from Graphene Sheets. *Nano Lett.* **2008**, *8* (8), 2458–2462.
- (23) Caglar, M.; Silkina, I.; Brown, B. T.; Thorneywork, A. L.; Burton, O. J.; Babenko, V.; Gilbert, S. M.; Zettl, A.; Hofmann, S.; Keyser, U. F. Tunable Anion-Selective Transport through Monolayer Graphene and Hexagonal Boron Nitride. *ACS Nano* **2020**, acsnano.9b08168.
- (24) Carozo, V.; Wang, Y.; Fujisawa, K.; Carvalho, B. R.; McCreary, A.; Feng, S.; Lin, Z.; Zhou, C.; Perea-López, N.; Elías, A. L.; Kabius, B.; Crespi, V. H.; Terrones, M. Optical Identification of Sulfur Vacancies: Bound Excitons at the Edges of Monolayer Tungsten Disulfide. *Science Advances* **2017**, *3* (4), e1602813.
- (25) Carvalho, B. R.; Wang, Y.; Mignuzzi, S.; Roy, D.; Terrones, M.; Fantini, C.; Crespi, V. H.; Malard, L. M.; Pimenta, M. A. Intervalley Scattering by Acoustic Phonons in Two-Dimensional MoS₂ Revealed by Double-Resonance Raman Spectroscopy. *Nature Communications* **2017**, *8*, 14670.
- (26) Castellanos-Gomez, A.; Poot, M.; Amor-Amorós, A.; Steele, G. A.; van der Zant, H. S. J.; Agraït, N.; Rubio-Bollinger, G. Mechanical Properties of Freely Suspended Atomically Thin Dielectric Layers of Mica. *Nano Research* **2012**, *5* (8), 550–557.
- (27) Celebi, K.; Buchheim, J.; Wyss, R. M.; Droudian, A.; Gasser, P.; Shorubalko, I.; Kye, J.-I.; Lee, C.; Park, H. G. Ultimate Permeation Across Atomically Thin Porous Graphene. *Science* **2014**, *344* (6181), 289–292.
- (28) Chien, C.-C.; Shekar, S.; Niedzwiecki, D. J.; Shepard, K. L.; Drndić, M. Single-Stranded DNA Translocation Recordings through Solid-State Nanopores on Glass Chips at 10 MHz Measurement Bandwidth. *ACS Nano* **2019**, *13* (9), 10545–10554.
- (29) Chou, Y.-C.; Masih Das, P.; Monos, D. S.; Drndić, M. Lifetime and Stability of Silicon Nitride Nanopores and Nanopore Arrays for Ionic Measurements. *ACS Nano* **2020**, a-n.
- (30) Chow, P. K.; Jacobs-Gedrim, R. B.; Gao, J.; Lu, T. M.; Yu, B.; Terrones, H.; Koratkar, N. Defect-Induced Photoluminescence in Monolayer Semiconducting Transition Metal Dichalcogenides. *ACS Nano* **2015**, *9* (2), 1520–1527.
- (31) Cohen-Tanugi, D.; Grossman, J. C. Water Desalination across Nanoporous Graphene. *Nano Letters* **2012**, *12* (7), 3602–3608.
- (32) Cohen-Tanugi, D.; McGovern, R. K.; Dave, S. H.; Lienhard, J. H.; Grossman, J. C. Quantifying the Potential of Ultra-Permeable Membranes for Water Desalination. *Energy {&} Environmental Science* **2014**, *7* (3), 1134.
- (33) Danda, G.; Drndić, M. Science Direct Two-Dimensional Nanopores and Nanoporous Membranes for Ion and Molecule Transport. **2019**, 124–133.
- (34) Danda, G.; Masih Das, P.; Chou, Y.-C.; Mlack, J. T.; Parkin, W. M.; Naylor, C. H.; Fujisawa, K.; Zhang, T.; Fulton, L. B.; Terrones, M.; Johnson, A. T. C.; Drndić, M. Monolayer WS₂ Nanopores for DNA Translocation with Light-Adjustable Sizes. *ACS Nano* **2017**, *11* (2), 1937–1945.
- (35) Danda, G.; Masih Das, P.; Drndić, M. Laser-Induced Fabrication of Nanoporous Monolayer WS₂ Membranes. *2D Materials* **2018**, *5* (3), 035011.
- (36) Dang, K. Q.; Spearot, D. E. Effect of Point and Grain Boundary Defects on the Mechanical Behavior of Monolayer MoS₂ under Tension via Atomistic Simulations. *Journal of Applied Physics* **2014**, *116* (1).
- (37) Draushuk, L. W.; Strano, M. S. Mechanisms of Gas Permeation through Single Layer Graphene Membranes. *Langmuir* **2012**, *28* (48), 16671–16678.
- (38) Elibol, K.; Susi, T.; Brien, M. O.; Bayer, B. C.; Pennycook, T. J.; Mcevoy, N.; Duesberg, G. S.; Meyer, C. Molybdenum Disulfide Grown by Chemical Vapor Deposition †. **2017**, 1591–1598.
- (39) Esfandiari, A.; Radha, B.; Wang, F. C.; Yang, Q.; Hu, S.; Garaj, S.; Nair, R. R.; Geim, A. K.; Gopinadhan, K. Size Effect in Ion Transport through Angstrom-Scale Slits. *Science* **2017**, *358* (6362), 511–513.

- (40) Exarhos, A. L.; Hopper, D. A.; Patel, R. N.; Doherty, M. W.; Bassett, L. C. Hexagonal Boron Nitride at Room Temperature. *Nature Communications* **2019**, *10*, 222.
- (41) Feng, J.; Graf, M.; Liu, K.; Ovchinnikov, D.; Dumcenco, D.; Heiranian, M.; Nandigana, V.; Aluru, N. R.; Kis, A.; Radenovic, A. Single-Layer MoS₂ Nanopores as Nanopower Generators. *Nature* **2016**, *536*, 197–200.
- (42) Feng, J.; Liu, K.; Graf, M.; Lihter, M.; Bulushev, R. D.; Dumcenco, D.; Alexander, D. T. L.; Krasnozhan, D.; Vuletic, T.; Kis, A.; Radenovic, A. Electrochemical Reaction in Single Layer MoS₂: Nanopores Opened Atom by Atom. *Nano Letters* **2015**, *15* (5), 3431–3438.
- (43) Feng, J.; Liu, K.; Graf, M.; Dumcenco, D.; Kis, A.; Di Ventra, M.; Radenovic, A. Observation of Ionic Coulomb Blockade in Nanopores. *Nature Mater* **2016**, *15* (8), 850–855.
- (44) Fischbein, M. D.; Drndić, M. Electron Beam Nanosculpting of Suspended Graphene Sheets. *Appl. Phys. Lett.* **2008**, *93* (11), 113107.
- (45) Gadsby, D. C. Ion Channels versus Ion Pumps: The Principal Difference, in Principle. *Nat Rev Mol Cell Biol* **2009**, *10* (5), 344–352.
- (46) Garaj, S.; Hubbard, W.; Reina, A.; Kong, J.; Branton, D.; Golovchenko, J. A. Graphene as a Subnanometre Trans-Electrode Membrane. *Nature* **2010**, *467* (7312), 190–193.
- (47) Ge, L.; Du, A.; Hou, M.; Rudolph, V.; Zhu, Z. Enhanced Hydrogen Separation by Vertically-Aligned Carbon Nanotube Membranes with Zeolite Imidazolate Frameworks as a Selective Layer. *RSC Adv.* **2012**, *2* (31), 11793.
- (48) Ghorbani-Asl, M.; Kretschmer, S.; Spearot, D. E.; Krasheninnikov, A. V. Two-Dimensional MoS₂ under Ion Irradiation: From Controlled Defect Production to Electronic Structure Engineering. *2D Materials* **2017**, *4* (2), 025078.
- (49) Giannozzi, P.; Baroni, S.; Bonini, N.; Calandra, M.; Car, R.; Cavazzoni, C.; Ceresoli, D.; Chiarotti, G. L.; Cococcioni, M.; Dabo, I.; Dal Corso, A.; de Gironcoli, S.; Fabris, S.; Fratesi, G.; Gebauer, R.; Gerstmann, U.; Gougoussis, C.; Kokalj, A.; Lazzeri, M.; Martin-Samos, L.; Marzari, N.; Mauri, F.; Mazzarello, R.; Paolini, S.; Pasquarello, A.; Paulatto, L.; Sbraccia, C.; Scandolo, S.; Sclauzero, G.; Seitsonen, A. P.; Smogunov, A.; Umari, P.; Wentzcovitch, R. M. QUANTUM ESPRESSO: A Modular and Open-Source Software Project for Quantum Simulations of Materials. *J. Phys.: Condens. Matter* **2009**, *21* (39), 395502.
- (50) Goldbart, O.; Cohen, S. R.; Kaplan-Ashiri, I.; Glazyrina, P.; Wagner, H. D.; Enyashin, A.; Tenne, R. Diameter-Dependent Wetting of Tungsten Disulfide Nanotubes. *Proc Natl Acad Sci USA* **2016**, *113* (48), 13624–13629.
- (51) Gopinadhan, K.; Hu, S.; Esfandiar, A.; Lozada-Hidalgo, M.; Wang, F. C.; Yang, Q.; Tyurnina, A. V.; Keerthi, A.; Radha, B.; Geim, A. K. Complete Steric Exclusion of Ions and Proton Transport through Confined Monolayer Water. *Science* **2019**, *363* (6423), 145–148.
- (52) Graf, M.; Lihter, M.; Thakur, M.; Georgiou, V.; Topolancik, J.; Ilic, B. R.; Liu, K.; Feng, J.; Astier, Y.; Radenovic, A. Fabrication and Practical Applications of Molybdenum Disulfide Nanopores. *Nat Protoc* **2019**, *14* (4), 1130–1168.
- (53) Hartel, A. J. W.; Ong, P.; Schroeder, I.; Giese, M. H.; Shekar, S.; Clarke, O. B.; Zalk, R.; Marks, A. R.; Hendrickson, W. A.; Shepard, K. L. Single-Channel Recordings of RyR1 at Microsecond Resolution in CMOS-Suspended Membranes. *Proc Natl Acad Sci USA* **2018**, *115* (8), E1789–E1798.
- (54) Hartel, A. J. W.; Shekar, S.; Ong, P.; Schroeder, I.; Thiel, G.; Shepard, K. L. High Bandwidth Approaches in Nanopore and Ion Channel Recordings - A Tutorial Review. *Analytica Chimica Acta* **2019**, *1061*, 13–27.
- (55) He, Z.; Zhao, R.; Chen, X.; Chen, H.; Zhu, Y.; Su, H.; Huang, S.; Xue, J.; Dai, J.; Cheng, S.; Liu, M.; Wang, X.; Chen, Y. Defect Engineering in Single-Layer MoS₂ Using Heavy Ion Irradiation. *ACS Applied Materials and Interfaces* **2018**, *10*, 42524–42533.
- (56) Healy, K.; Ray, V.; Willis, L. J.; Peterman, N.; Bartel, J.; Drndić, M. Fabrication and Characterization of Nanopores with Insulated Transverse Nanoelectrodes for DNA Sensing in Salt Solution. *Electrophoresis* **2012**, *33* (23), 3488–3496.
- (57) Heiranian, M.; Farimani, A. B.; Aluru, N. R. Water Desalination with a Single-Layer MoS₂ Nanopore. *Nature Communications* **2015**, *6*, 1–6.
- (58) Hille, B. Pharmacological Modifications of the Sodium Channels of Frog Nerve. *The Journal of General Physiology* **1968**, *51* (2), 199–219.

- (59) Hinds, B. J. Aligned Multiwalled Carbon Nanotube Membranes. *Science* **2004**, *303* (5654), 62–65.
- (60) Hirunpinyopas, W.; Prestat, E.; Worrall, S. D.; Haigh, S. J.; Dryfe, R. A. W.; Bissett, M. A. Desalination and Nanofiltration through Functionalized Laminar MoS₂ Membranes. *ACS Nano* **2017**, *11* (11), 11082–11090.
- (61) Holt, J. K. Fast Mass Transport Through Sub-2-Nanometer Carbon Nanotubes. *Science* **2006**, *312* (5776), 1034–1037.
- (62) Hong, J.; Hu, Z.; Probert, M.; Li, K.; Lv, D.; Yang, X.; Gu, L.; Mao, N.; Feng, Q.; Xie, L.; Zhang, J.; Wu, D.; Zhang, Z.; Jin, C.; Ji, W.; Zhang, X.; Yuan, J.; Zhang, Z. Exploring Atomic Defects in Molybdenum Disulphide Monolayers. *Nature Communications* **2015**, *6*, 6293.
- (63) Hong, S.; Constans, C.; Surmani Martins, M. V.; Seow, Y. C.; Guevara Carrió, J. A.; Garaj, S. Scalable Graphene-Based Membranes for Ionic Sieving with Ultrahigh Charge Selectivity. *Nano Lett.* **2017**, *17* (2), 728–732.
- (64) Hoover, W. G. Canonical Dynamics: Equilibrium Phase-Space Distributions. *Physical Review A* **1985**, *31* (3), 1695–1697.
- (65) Hopman, W. C. L.; Ay, F.; Hu, W.; Gadgil, V. J.; Kuipers, L.; Pollnau, M.; de Ridder, R. M. Focused Ion Beam Scan Routine, Dwell Time and Dose Optimizations for Submicrometre Period Planar Photonic Crystal Components and Stamps in Silicon. *Nanotechnology* **2007**, *18*, 195305.
- (66) Huang, P. Y.; Ruiz-Vargas, C. S.; van der Zande, A. M.; Whitney, W. S.; Levendorf, M. P.; Kevek, J. W.; Garg, S.; Alden, J. S.; Hustedt, C. J.; Zhu, Y.; Park, J.; McEuen, P. L.; Muller, D. A. Grains and Grain Boundaries in Single-Layer Graphene Atomic Patchwork Quilts. *Nature* **2011**, *469* (7330), 389–392.
- (67) Huang, S.; Liang, L.; Ling, X.; Poretzky, A. A.; Geohegan, D. B.; Sumpter, B. G.; Kong, J.; Meunier, V.; Dresselhaus, M. S. Low-Frequency Interlayer Raman Modes to Probe Interface of Twisted Bilayer MoS₂. *Nano Letters* **2016**, *16* (2), 1435–1444.
- (68) Huang, S.; Dakhchoune, M.; Luo, W.; Oveisi, E.; He, G.; Rezaei, M.; Zhao, J.; Alexander, D. T. L.; Züttel, A.; Strano, M. S.; Agrawal, K. V. Single-Layer Graphene Membranes by Crack-Free Transfer for Gas Mixture Separation. *Nat Commun* **2018**, *9* (1), 2632.
- (69) Huey, B. D.; Langford, R. M. Low-Dose Focused Ion Beam Nanofabrication and Characterization by Atomic Force Microscopy. *Nanotechnology* **2003**, *14* (3), 409–412.
- (70) Ierardi, V.; Becker, U.; Pantazis, S.; Firpo, G.; Valbusa, U.; Jousten, K. Nano-Holes as Standard Leak Elements. *Measurement* **2014**, *58*, 335–341.
- (71) Jadwiszczak, J.; O'Callaghan, C.; Zhou, Y.; Fox, D. S.; Weitz, E.; Keane, D.; Cullen, C. P.; O'Reilly, I.; Downing, C.; Shmeliov, A.; Maguire, P.; Gough, J. J.; McGuinness, C.; Ferreira, M. S.; Bradley, A. L.; Boland, J. J.; Duesberg, G. S.; Nicolosi, V.; Zhang, H. Oxide-Mediated Recovery of Field-Effect Mobility in Plasma-Treated MoS₂. *Sci. Adv.* **2018**, *4* (3), eaao5031.
- (72) Jain, T.; Rasera, B. C.; Guerrero, R. J. S.; Boutilier, M. S. H.; O'Hern, S. C.; Idrobo, J.-C.; Karnik, R. Heterogeneous Sub-Continuum Ionic Transport in Statistically Isolated Graphene Nanopores. *Nature Nanotech* **2015**, *10* (12), 1053–1057.
- (73) Jaramillo, T. F.; Jorgensen, K. P.; Bonde, J.; Nielsen, J. H.; Horch, S.; Chorkendorff, I. Identification of Active Edge Sites for Electrochemical H₂ Evolution from MoS₂ Nanocatalysts. *Science* **2007**, *317* (5834), 100–102.
- (74) Jariwala, D.; Sangwan, V. K.; Lauhon, L. J.; Marks, T. J.; Hersam, M. C. Emerging Device Applications for Semiconducting Two-Dimensional Transition Metal Dichalcogenides. *ACS Nano* **2014**, *8* (2), 1102–1120.
- (75) Jensen, M. O.; Borhani, D. W.; Lindorff-Larsen, K.; Maragakis, P.; Jogini, V.; Eastwood, M. P.; Dror, R. O.; Shaw, D. E. Principles of Conduction and Hydrophobic Gating in K⁺ Channels. *Proceedings of the National Academy of Sciences* **2010**, *107* (13), 5833–5838.
- (76) Jeon, J.; Jang, S. K.; Jeon, S. M.; Yoo, G.; Jang, Y. H.; Park, J. H.; Lee, S. Layer-Controlled CVD Growth of Large-Area Two-Dimensional MoS₂ Films. *Nanoscale* **2015**, *7* (5), 1688–1695.
- (77) Jia, Y.; Wan, H.; Chen, L.; Zhou, H.; Chen, J. Facile Synthesis of Three Dimensional MoS₂ Porous Film with High Electrochemical Performance. *Materials Letters* **2017**, *195*, 147–150.

- (78) Jiang, D.; Cooper, V. R.; Dai, S. Porous Graphene as the Ultimate Membrane for Gas Separation. *Nano Lett.* **2009**, 9 (12), 4019–4024.
- (79) Jiang, J.-W. Parametrization of Stillinger–Weber Potential Based on Valence Force Field Model: Application to Single-Layer MoS₂ and Black Phosphorus. *Nanotechnology* **2015**, 26 (31), 315706.
- (80) Jiang, Y.; Chen, Z.; Han, Y.; Deb, P.; Gao, H.; Xie, S.; Purohit, P.; Mark, W.; Park, J.; Gruner, S. M.; Elser, V.; Muller, D. A. Electron Ptychography of 2D Materials to Deep Sub-Ångström Resolution. *Nature* **2018**, 559, 343–349.
- (81) Jorgensen, W. L.; Chandrasekhar, J.; Madura, J. D.; Impey, R. W.; Klein, M. L. Comparison of Simple Potential Functions for Simulating Liquid Water. *The Journal of Chemical Physics* **1983**, 79 (2), 926–935.
- (82) Joshi, R. K.; Carbone, P.; Wang, F. C.; Kravets, V. G.; Su, Y.; Grigorieva, I. V.; Wu, H. A.; Geim, A. K.; Nair, R. R. Precise and Ultrafast Molecular Sieving through Graphene Oxide Membranes. *Science (New York, N.Y.)* **2014**, 343 (6172), 752–754.
- (83) Ke, J.-A.; Garaj, S.; Gradecak, S. Nanopores in 2D MoS₂: Defect-Mediated Formation and Density Modulation. *ACS Applied Materials & Interfaces* **2019**, 11, 26228–26234.
- (84) Keerthi, A.; Geim, A. K.; Janardanan, A.; Rooney, A. P.; Esfandiari, A.; Hu, S.; Dar, S. A.; Grigorieva, I. V.; Haigh, S. J.; Wang, F. C.; Radha, B. Ballistic Molecular Transport through Two-Dimensional Channels. *Nature* **2018**, 558 (7710), 420–424.
- (85) Khan, M. H.; Moradi, M.; Dakhchoune, M.; Rezaei, M.; Huang, S.; Zhao, J.; Agrawal, K. V. Hydrogen Sieving from Intrinsic Defects of Benzene-Derived Single-Layer Graphene. *Carbon* **2019**, 153, 458–466.
- (86) Kidambi, P. R.; Nguyen, G. D.; Zhang, S.; Chen, Q.; Kong, J.; Warner, J. Facile Fabrication of Large-Area Atomically Thin Membranes by Direct Synthesis of Graphene with Nanoscale Porosity. **2018**, 1804977, 1–10.
- (87) Kim, D.-K.; Duan, C.; Chen, Y.-F.; Majumdar, A. Power Generation from Concentration Gradient by Reverse Electrodialysis in Ion-Selective Nanochannels. *Microfluid Nanofluid* **2010**, 9 (6), 1215–1224.
- (88) Kim, E. S.; Kim, S.; Lee, Y. S.; Lee, S. Y.; Lee, S.; Choi, W.; Peelaers, H.; Van De Walle, C. G.; Hwang, W. S.; Kosel, T.; Jena, D. Multilayer Transition-Metal Dichalcogenide Channel Thin-Film Transistors. *Technical Digest - International Electron Devices Meeting, IEDM* **2012**, 108–111.
- (89) Kim, H. W.; Yoon, H. W.; Yoon, S.-M.; Yoo, B. M.; Ahn, B. K.; Cho, Y. H.; Shin, H. J.; Yang, H.; Paik, U.; Kwon, S.; Choi, J.-Y.; Park, H. B. Selective Gas Transport Through Few-Layered Graphene and Graphene Oxide Membranes. *Science* **2013**, 342 (6154), 91–95.
- (90) Kim, K.; Artyukhov, V. I.; Regan, W.; Liu, Y.; Crommie, M. F.; Yakobson, B. I.; Zettl, A. Ripping Graphene: Preferred Directions. *Nano Letters* **2012**, 12 (1), 293–297.
- (91) Kim, S.; Konar, A.; Hwang, W.-S.; Lee, J. H.; Lee, J.; Yang, J.; Jung, C.; Kim, H.; Yoo, J.-B.; Choi, J.-Y.; Jin, Y. W.; Lee, S. Y.; Jena, D.; Choi, W.; Kim, K. High-Mobility and Low-Power Thin-Film Transistors Based on Multilayer MoS₂ Crystals. *Nature Communications* **2012**, 3, 1011.
- (92) Koch, C. DETERMINATION OF CORE STRUCTURE PERIODICITY AND POINT DEFECT By, 2002.
- (93) Koenig, S. P.; Wang, L.; Pellegrino, J.; Bunch, J. S. Selective Molecular Sieving through Porous Graphene. *Nature Nanotech* **2012**, 7 (11), 728–732.
- (94) Komsa, H. P.; Kurasch, S.; Lehtinen, O.; Kaiser, U.; Krasheninnikov, A. V. From Point to Extended Defects in Two-Dimensional MoS₂: Evolution of Atomic Structure under Electron Irradiation. *Physical Review B - Condensed Matter and Materials Physics* **2013**, 88 (3), 1–8.
- (95) Komsa, H.-P.; Kotakoski, J.; Kurasch, S.; Lehtinen, O.; Kaiser, U.; Krasheninnikov, A. V. Two-Dimensional Transition Metal Dichalcogenides under Electron Irradiation: Defect Production and Doping. *Phys. Rev. Lett.* **2012**, 109, 035503.
- (96) Kowalczyk, S. W.; Grosberg, A. Y.; Rabin, Y.; Dekker, C. Modeling the Conductance and DNA Blockade of Solid-State Nanopores. *Nanotechnology* **2011**, 22 (31), 315101.
- (97) Krems, M.; Di Ventra, M. Ionic Coulomb Blockade in Nanopores. *J. Phys.: Condens. Matter* **2013**, 25 (6), 065101.

- (98) Krems, M.; Pershin, Y. V.; Di Ventra, M. Ionic Memcapacitive Effects in Nanopores. *Nano Lett.* **2010**, *10* (7), 2674–2678.
- (99) Kretschmer, S.; Maslov, M.; Ghaderzadeh, S.; Ghorbani-Asl, M.; Hlawacek, G.; Krasheninnikov, A. V. Supported Two-Dimensional Materials under Ion Irradiation: The Substrate Governs Defect Production. *ACS Applied Materials & Interfaces* **2018**, *10* (36), 30827–30836.
- (100) Krishnamoorthy, K.; Veerasubramani, G. K.; Pazhamalai, P.; Kim, S. J. Designing Two Dimensional Nanoarchitected MoS₂ Sheets Grown on Mo Foil as a Binder Free Electrode for Supercapacitors. *Electrochimica Acta* **2016**, *190*, 305–312.
- (101) Krivanek, O. L.; Chisholm, M. F.; Nicolosi, V.; Pennycook, T. J.; Corbin, G. J.; Dellby, N.; Murfitt, M. F.; Own, C. S.; Szilagy, Z. S.; Oxley, M. P.; Pantelides, S. T.; Pennycook, S. J. Atom-by-Atom Structural and Chemical Analysis by Annular Dark-Field Electron Microscopy. *Nature* **2010**, *464* (7288), 571–574.
- (102) Kuan, A. T.; Lu, B.; Xie, P.; Szalay, T.; Golovchenko, J. A. Electrical Pulse Fabrication of Graphene Nanopores in Electrolyte Solution. *Applied Physics Letters* **2015**, *106* (20).
- (103) Kubena, R. L.; Ward, J. W. Current-Density Profiles for a Ga⁺ Ion Microprobe and Their Lithographic Implications. *Applied Physics Letters* **1987**, *51* (23), 1960–1962.
- (104) Larkin, J.; Henley, R.; Bell, D. C.; Cohen-Karni, T.; Rosenstein, J. K.; Wanunu, M. Slow DNA Transport through Nanopores in Hafnium Oxide Membranes. *ACS Nano* **2013**, *7* (11), 10121–10128.
- (105) Lehtinen, O.; Kotakoski, J.; Krasheninnikov, A. V.; Tolvanen, A.; Nordlund, K.; Keinonen, J. Effects of Ion Bombardment on a Two-Dimensional Target: Atomistic Simulations of Graphene Irradiation. *Phys. Rev. B* **2010**, *81*, 153401.
- (106) Li, H.; Song, Z.; Zhang, X.; Huang, Y.; Li, S.; Mao, Y.; Ploehn, H. J.; Bao, Y.; Yu, M. Ultrathin, Molecular-Sieving Graphene Oxide Membranes for Selective Hydrogen Separation. *Science* **2013**, *342* (6154), 95–98.
- (107) Li, H.; Xie, F.; Li, W.; Fahlman, B. D.; Chen, M.; Li, W. Preparation and Adsorption Capacity of Porous MoS₂ nanosheets. *RSC Advances* **2016**, *6* (107), 105222–105230.
- (108) Li, S.; Wang, S.; Tang, D. M.; Zhao, W.; Xu, H.; Chu, L.; Bando, Y.; Golberg, D.; Eda, G. Halide-Assisted Atmospheric Pressure Growth of Large WSe₂ and WS₂ Monolayer Crystals. *Applied Materials Today* **2015**, *1* (1), 60–66.
- (109) Liang, L.; Meunier, V. First-Principles Raman Spectra of MoS₂, WS₂ and Their Heterostructures. *Nanoscale* **2014**, *6* (10), 5394.
- (110) Liang, T.; Phillpot, S. R.; Sinnott, S. B. Parametrization of a Reactive Many-Body Potential for Mo-S Systems. *Physical Review B - Condensed Matter and Materials Physics* **2009**, *79* (24), 1–14.
- (111) Lin, Y.-C.; Zhang, W.; Huang, J.-K.; Liu, K.-K.; Lee, Y.-H.; Liang, C.-T.; Chu, C.-W.; Li, L.-J. Wafer-Scale MoS₂ Thin Layers Prepared by MoO₃ Sulfurization. *Nanoscale* **2012**, *4* (20), 6637.
- (112) Lin, Z.; Carvalho, B. R.; Kahn, E.; Lv, R.; Rao, R.; Terrones, H.; Pimenta, M. A.; Terrones, M. Defect Engineering of Two-Dimensional Transition Metal Dichalcogenides. *2D Materials* **2016**, *3* (2), 022002.
- (113) Liu, K.; Yan, Q.; Chen, M.; Fan, W.; Sun, Y.; Suh, J.; Fu, D.; Lee, S.; Zhou, J.; Tongay, S.; Ji, J.; Neaton, J. B.; Wu, J. Elastic Properties of Chemical-Vapor-Deposited Monolayer MoS₂, WS₂, and Their Bilayer Heterostructures. *Nano Lett.* **2014**, *14* (9), 5097–5103.
- (114) Liu, K.; Feng, J.; Kis, A.; Radenovic, A. Atomically Thin Molybdenum Disulfide Nanopores with High Sensitivity for DNA Translocation. *ACS Nano* **2014**, *8* (3), 2504–2511.
- (115) Liu, K.; Lihter, M.; Sarathy, A.; Caneva, S.; Qiu, H.; Deiana, D.; Tileli, V.; Alexander, D. T. L.; Hofmann, S.; Dumcenco, D.; Kis, A.; Leburton, J.-P.; Radenovic, A. Geometrical Effect in 2D Nanopores. *Nano Letters* **2017**, *17* (7), 4223–4230.
- (116) Liu, S.; Lu, B.; Zhao, Q.; Li, J.; Gao, T.; Chen, Y.; Zhang, Y.; Liu, Z.; Fan, Z.; Yang, F.; You, L.; Yu, D. Boron Nitride Nanopores: Highly Sensitive DNA Single-Molecule Detectors. *Advanced Materials* **2013**, *25* (33), 4549–4554.

- (117) Liu, X.; Ning, H.; Chen, J.; Cai, W.; Hu, S.; Tao, R.; Zeng, Y. High-Performance Back-Channel-Etched Thin-Film Transistors with Amorphous Si-Incorporated SnO₂ Active Layer. **2016**, *112106*, 1–6.
- (118) Liu, X.; Wood, J. D.; Chen, K. S.; Cho, E.; Hersam, M. C. In Situ Thermal Decomposition of Exfoliated Two-Dimensional Black Phosphorus. *Journal of Physical Chemistry Letters* **2015**, *6* (5), 773–778.
- (119) Maguire, P.; Fox, D. S.; Zhou, Y.; Wang, Q.; O'Brien, M.; Jadwiszczak, J.; Cullen, C. P.; McManus, J.; Bateman, S.; McEvoy, N.; Duesberg, G. S.; Zhang, H. Defect Sizing, Separation, and Substrate Effects in Ion-Irradiated Monolayer Two-Dimensional Materials. *Physical Review B* **2018**, *98*, 134109.
- (120) Mak, K. F.; He, K.; Lee, C.; Lee, G. H.; Hone, J.; Heinz, T. F.; Shan, J. Tightly Bound Trions in Monolayer MoS₂. *Nature Materials* **2012**, *12* (3), 207–211.
- (121) Mak, K. F.; Lee, C.; Hone, J.; Shan, J.; Heinz, T. F. Atomically Thin MoS₂: A New Direct-Gap Semiconductor. *Physical Review Letters* **2010**, *105* (13), 2–5.
- (122) Marcus, Y. Ionic Radii in Aqueous Solutions. *Chem. Rev.* **1988**, *88* (8), 1475–1498.
- (123) Marion, S.; Macha, M.; Davis, S. J.; Chernev, A.; Radenovic, A. Wetting of Nanopores Probed with Pressure. *arXiv:1911.05229* **2020**.
- (124) Masih Das, P.; Danda, G.; Cupo, A.; Parkin, W. M.; Liang, L.; Kharche, N.; Ling, X.; Huang, S.; Dresselhaus, M. S.; Meunier, V.; Drndić, M. Controlled Sculpture of Black Phosphorus Nanoribbons. *ACS Nano* **2016**, *10* (6), 5687–5695.
- (125) Masih Das, P.; Drndić, M. *In Situ* 2D MoS₂ Field-Effect Transistors with an Electron Beam Gate. *ACS Nano* **2020**, *14* (6), 7389–7397.
- (126) Masih Das, P.; Thiruraman, J. P.; Chou, Y.-C.; Danda, G.; Drndić, M. Centimeter-Scale Nanoporous 2D Membranes and Ion Transport: Porous MoS₂ Monolayers in a Few-Layer Matrix. *Nano Letters* **2019**, *19*, 392–399.
- (127) Masih Das, P.; Thiruraman, J. P.; Zhao, M.; Mandyam, S.; Johnson, A. T. C.; Drndić, M. Atomic-Scale Patterning in Two-Dimensional van Der Waals Superlattices. *Nanotechnology* **2019**.
- (128) Mehio, N.; Dai, S.; Jiang, D. Quantum Mechanical Basis for Kinetic Diameters of Small Gaseous Molecules. *J. Phys. Chem. A* **2014**, *118* (6), 1150–1154.
- (129) Melngailis, J. Focused Ion Beam Technology and Applications. *Journal of Vacuum Science & Technology B: Microelectronics Processing and Phenomena* **1987**, *5* (2), 469–495.
- (130) Merchant, C. A.; Healy, K.; Wanunu, M.; Ray, V.; Peterman, N.; Bartel, J.; Fischbein, M. D.; Venta, K.; Luo, Z.; Johnson, A. T. C.; Drndić, M. DNA Translocation through Graphene Nanopores. *Nano Lett.* **2010**, *10* (8), 2915–2921.
- (131) Mignuzzi, S.; Pollard, A. J.; Bonini, N.; Brennan, B.; Gilmore, I. S.; Pimenta, M. A.; Richards, D.; Roy, D. Effect of Disorder on Raman Scattering of Single-Layer MoS₂. *Phys. Rev. B* **2015**, *91*, 195411.
- (132) Mlack, J. T.; Masih Das, P.; Danda, G.; Chou, Y. C.; Naylor, C. H.; Lin, Z.; López, N. P.; Zhang, T.; Terrones, M.; Charlie Johnson, A. T.; Drndić, M. Transfer of Monolayer TMD WS₂ and Raman Study of Substrate Effects. *Scientific Reports* **2017**, *7*, 43037.
- (133) Mojtabavi, M.; VahidMohammadi, A.; Liang, W.; Beidaghi, M.; Wanunu, M. Single-Molecule Sensing Using Nanopores in Two-Dimensional Transition Metal Carbide (MXene) Membranes. *ACS Nano* **2019**.
- (134) Morita, S.; Ochi, M.; Kugimiya, T. Amorphous Oxide Semiconductor Adopting Back-Channel-Etch Type Thin-Film Transistor. **2016**, No. 34, 52–58.
- (135) Mortazavi, B.; Ostadhossein, A.; Rabczuk, T.; Van Duin, A. C. T. Mechanical Response of All-MoS₂single-Layer Heterostructures: A ReaxFF Investigation. *Physical Chemistry Chemical Physics* **2016**, *18* (34), 23695–23701.
- (136) Naylor, C. H.; Kybert, N. J.; Schneier, C.; Xi, J.; Romero, G.; Saven, J. G.; Liu, R.; Charlie Johnson, A. T. Scalable Production of Molybdenum Disulfide Based Biosensors. *ACS Nano* **2016**, *10* (6), 6173–6179.
- (137) Nicolaï, A.; Sumpter, B. G.; Meunier, V. Tunable Water Desalination across Graphene Oxide Framework Membranes. *Physical Chemistry Chemical Physics* **2014**, *16* (18), 8646–8654.

- (138) Nosé, S. A Unified Formulation of the Constant Temperature Molecular Dynamics Methods. *The Journal of Chemical Physics* **1984**, *81* (1), 511–519.
- (139) Ochedowski, O.; Lehtinen, O.; Kaiser, U.; Turchanin, A.; Ban-d'Etat, B.; Lebius, H.; Karlušić, M.; Jakšić, M.; Schleberger, M. Nanostructuring Graphene by Dense Electronic Excitation. *Nanotechnology* **2015**, *26*, 465302.
- (140) O'Hern, S. C.; Boutilier, M. S. H.; Idrobo, J. C.; Song, Y.; Kong, J.; Laoui, T.; Atieh, M.; Karnik, R. Selective Ionic Transport through Tunable Subnanometer Pores in Single-Layer Graphene Membranes. *Nano Letters* **2014**, *14* (3), 1234–1241.
- (141) O'Hern, S. C.; Jang, D.; Bose, S.; Idrobo, J. C.; Song, Y.; Laoui, T.; Kong, J.; Karnik, R. Nanofiltration across Defect-Sealed Nanoporous Monolayer Graphene. *Nano Letters* **2015**, *15* (5), 3254–3260.
- (142) O'Hern, S. C.; Stewart, C. A.; Boutilier, M. S. H.; Idrobo, J. C.; Bhaviripudi, S.; Das, S. K.; Kong, J.; Laoui, T.; Atieh, M.; Karnik, R. Selective Molecular Transport through Intrinsic Defects in a Single Layer of CVD Graphene. *ACS Nano* **2012**, *6* (11), 10130–10138.
- (143) Pan, C. T.; Hinks, J. A.; Ramasse, Q. M.; Greaves, G.; Bangert, U.; Donnelly, S. E.; Haigh, S. J. In-Situ Observation and Atomic Resolution Imaging of the Ion Irradiation Induced Amorphisation of Graphene. *Scientific Reports* **2014**, *4*, 6334.
- (144) Park, H. B.; Kamcev, J.; Robeson, L. M.; Elimelech, M.; Freeman, B. D. Maximizing the Right Stuff: The Trade-off between Membrane Permeability and Selectivity. *Science* **2017**, *356* (6343), eaab0530.
- (145) Parkin, W. M.; Balan, A.; Liang, L.; Das, P. M.; Lamparski, M.; Naylor, C. H.; Rodríguez-Manzo, J. A.; Johnson, A. T. C.; Meunier, V.; Drndić, M. Raman Shifts in Electron-Irradiated Monolayer MoS₂. *ACS Nano* **2016**, *10* (4), 4134–4142.
- (146) Perdew, J. P.; Chevary, J. A.; Vosko, S. H.; Jackson, K. A.; Pederson, M. R.; Singh, D. J.; Fiolhais, C. Atoms, Molecules, Solids, and Surfaces: Applications of the Generalized Gradient Approximation for Exchange and Correlation. *Phys. Rev. B* **1992**, *46* (11), 6671–6687.
- (147) Perez, B.; Senet, P.; Meunier, V.; I, A. N. Computational Investigation of the Ionic Conductance through Molybdenum Disulfide (MoS₂) Nanopores. **2017**, *16*, 35–44.
- (148) Pérez, M. D. B.; Nicolai, A.; Delarue, P.; Meunier, V.; Drndić, M.; Senet, P. Improved Model of Ionic Transport in 2-D MoS₂ Membranes with Sub-5 Nm Pores. *Appl. Phys. Lett.* **2019**, *114* (2), 023107.
- (149) Plecis, A.; Schoch, R. B.; Renaud, P. Ionic Transport Phenomena in Nanofluidics: Experimental and Theoretical Study of the Exclusion-Enrichment Effect on a Chip. *Nano Lett.* **2005**, *5* (6), 1147–1155.
- (150) Plimpton, S. Fast Parallel Algorithms for Short-Range Molecular Dynamics. *Journal of Computational Physics*. 1995, pp 1–19.
- (151) Powell, M. R.; Cleary, L.; Davenport, M.; Shea, K. J.; Siwy, Z. S. Electric-Field-Induced Wetting and Dewetting in Single Hydrophobic Nanopores. *Nature Nanotech* **2011**, *6* (12), 798–802.
- (152) Prozorovska, L.; Kidambi, P. R. State-of-the-Art and Future Prospects for Atomically Thin Membranes from 2D Materials. *Adv. Mater.* **2018**, *30* (52), 1801179.
- (153) Quereda, J.; Agraït, N.; Quereda, J.; Agra, N. Single-Layer MoS₂ Roughness and Sliding Friction Quenching by Interaction with Atomically Flat Substrates. **2016**, *053111* (2014), 2–7.
- (154) Rao, D.; Lu, R.; Meng, Z.; Wang, Y.; Lu, Z.; Liu, Y.; Chen, X.; Kan, E.; Xiao, C.; Deng, K.; Wu, H. Electronic Properties and Hydrogen Storage Application of Designed Porous Nanotubes from a Polyphenylene Network. *International Journal of Hydrogen Energy* **2014**, *39* (33), 18966–18975.
- (155) Reyntjens, S.; Puers, R. A Review of Focused Ion Beam Applications in Microsystem Technology. *Journal of Micromechanics and Microengineering* **2001**, *11* (4), 287–300.
- (156) Richards, L. A.; Richards, B. S.; Corry, B.; Schäfer, A. I. Experimental Energy Barriers to Anions Transporting through Nanofiltration Membranes. *Environmental Science and Technology* **2013**, *47* (4), 1968–1976.

- (157) Richards, L. A.; Schäfer, A. I.; Richards, B. S.; Corry, B. The Importance of Dehydration in Determining Ion Transport in Narrow Pores. *Small* **2012**, *8* (11), 1701–1709.
- (158) Rodríguez-Manzo, J. A.; Puster, M.; Nicolaï, A.; Meunier, V.; Drndić, M. DNA Translocation in Nanometer Thick Silicon Nanopores. *ACS Nano* **2015**, *9* (6), 6555–6564.
- (159) Rollings, R. C.; Kuan, A. T.; Golovchenko, J. A. Ion Selectivity of Graphene Nanopores. *Nat Commun* **2016**, *7* (1), 11408.
- (160) Roth, R.; Gillespie, D.; Nonner, W.; Eisenberg, R. E. Bubbles, Gating, and Anesthetics in Ion Channels. *Biophysical Journal* **2008**, *94* (11), 4282–4298.
- (161) Roux, B. Ion Channels and Ion Selectivity. *Essays Biochem.* **2017**, *61* (2), 201–209.
- (162) Russel, W. B. *Colloidal Dispersions* /; Cambridge University Press.; Cambridge.;, 1989.
- (163) Rycckaert, J. P.; Ciccotti, G.; Berendsen, H. J. C. Numerical Integration of the Cartesian Equations of Motion of a System with Constraints: Molecular Dynamics of n-Alkanes. *Journal of Computational Physics* **1977**, *23* (3), 327–341.
- (164) Sahu, S.; Di Ventra, M.; Zwolak, M. Dehydration as a Universal Mechanism for Ion Selectivity in Graphene and Other Atomically Thin Pores. *Nano Letters*. 2017, pp 4719–4724.
- (165) Schindelin, J.; Arganda-Carreras, I.; Frise, E.; Kaynig, V.; Longair, M.; Pietzsch, T.; Preibisch, S.; Rueden, C.; Saalfeld, S.; Schmid, B.; Tinevez, J.; White, D. J.; Hartenstein, V.; Eliceiri, K.; Tomancak, P.; Cardona, A. Fiji: An Open-Source Platform for Biological-Image Analysis. *Nature Methods* **2012**, *9*, 676–682.
- (166) Schleberger, M.; Kotakoski, J. 2D Material Science: Defect Engineering by Particle Irradiation. *Materials* **2018**, *11* (10), 1885.
- (167) Schneider, G. F.; Kowalczyk, S. W.; Calado, V. E.; Pandraud, G.; Zandbergen, H. W.; Vandersypen, L. M. K.; Dekker, C. DNA Translocation through Graphene Nanopores. *Nano Letters* **2010**, *10* (8), 3163–3167.
- (168) Scorrano, G.; Bruno, G.; Di Trani, N.; Ferrari, M.; Pimpinelli, A.; Grattoni, A. Gas Flow at the Ultra-Nanoscale: Universal Predictive Model and Validation in Nanochannels of Ångstrom-Level Resolution. *ACS Appl. Mater. Interfaces* **2018**, *10* (38), 32233–32238.
- (169) Secchi, E.; Nigues, A.; Jubin, L.; Siria, A.; Bocquet, L. Scaling Behavior for Ionic Transport and Its Fluctuations in Individual Carbon Nanotubes. *Phys. Rev. Lett.* **2016**, *116* (15), 154501.
- (170) Shekar, S.; Chien, C.-C.; Hartel, A.; Ong, P.; Clarke, O. B.; Marks, A.; Drndić, M.; Shepard, K. L. Wavelet Denoising of High-Bandwidth Nanopore and Ion-Channel Signals. *Nano Lett.* **2019**, *19* (2), 1090–1097.
- (171) Shekar, S.; Niedzwiecki, D. J.; Chien, C. C.; Ong, P.; Fleischer, D. A.; Lin, J.; Rosenstein, J. K.; Drndić, M.; Shepard, K. L. Measurement of DNA Translocation Dynamics in a Solid-State Nanopore at 100 Ns Temporal Resolution. *Nano Letters* **2016**, *16* (7), 4483–4489.
- (172) Shotan, Z.; Jayakumar, H.; Considine, C. R.; Mackoit, M.; Fedder, H.; Wrachtrup, J.; Alkauskas, A.; Doherty, M. W.; Menon, V. M.; Meriles, C. A. Photoinduced Modification of Single-Photon Emitters in Hexagonal Boron Nitride. *ACS Photonics* **2016**, *3* (12), 2490–2496.
- (173) Siria, A.; Poncharal, P.; Bianco, A.-L.; Fulcrand, R.; Blase, X.; Purcell, S. T.; Bocquet, L. Giant Osmotic Energy Conversion Measured in a Single Transmembrane Boron Nitride Nanotube. *Nature* **2013**, *494* (7438), 455–458.
- (174) Sledzinska, M.; Graczykowski, B.; Placidi, M.; Reig, D. S.; Sachat, A. El; Reparaz, J. S.; Alzina, F.; Mortazavi, B.; Quey, R.; Colombo, L.; Roche, S.; Torres, C. M. S. Thermal Conductivity of MoS₂ Polycrystalline Nanomembranes. *2D Materials* **2016**, *3* (3), 035016.
- (175) Smeets, R. M. M.; Keyser, U. F.; Dekker, N. H.; Dekker, C. Noise in Solid-State Nanopores. *Proceedings of the National Academy of Sciences* **2008**, *105* (2), 417–421.
- (176) Smirnov, S. N.; Vlassiuk, I. V.; Lavrik, N. V. Voltage-Gated Hydrophobic Nanopores. *ACS Nano* **2011**, *5* (9), 7453–7461.
- (177) Splendiani, A.; Sun, L.; Zhang, Y.; Li, T.; Kim, J.; Chim, C. Y.; Galli, G.; Wang, F. Emerging Photoluminescence in Monolayer MoS₂. *Nano Letters* **2010**, *10* (4), 1271–1275.
- (178) Stein, D.; Kruithof, M.; Dekker, C. Surface-Charge-Governed Ion Transport in Nanofluidic Channels. *Phys. Rev. Lett.* **2004**, *93* (3), 035901.
- (179) Suk Joung, I.; Cheatham, T. E. Determination of Alkali and Halide Monovalent Ion Parameters for Use in Explicitly Solvated Biomolecular Simulations. **2008**, 9020–9041.

- (180) Suk, M. E.; Aluru, N. R. Ion Transport in Sub-5-Nm Graphene Nanopores. *The Journal of Chemical Physics* **2014**, *140* (8), 084707.
- (181) Sun, C.; Boutilier, M. S. H.; Au, H.; Poesio, P.; Bai, B.; Karnik, R.; Hadjiconstantinou, N. G. Mechanisms of Molecular Permeation through Nanoporous Graphene Membranes. *Langmuir* **2014**, *30* (2), 675–682.
- (182) Sun, P. Z.; Yang, Q.; Kuang, W. J.; Stebunov, Y. V.; Xiong, W. Q.; Yu, J.; Nair, R. R.; Katsnelson, M. I.; Yuan, S. J.; Grigorieva, I. V.; Lozada-Hidalgo, M.; Wang, F. C.; Geim, A. K. Limits on Gas Impermeability of Graphene. *Nature* **2020**, *579* (7798), 229–232.
- (183) Surwade, S. P.; Smirnov, S. N.; Vlasiouk, I. V.; Unocic, R. R.; Veith, G. M.; Dai, S.; Mahurin, S. M. Water Desalination Using Nanoporous Single-Layer Graphene. *Nature Nanotechnology* **2015**, *10* (5), 459–464.
- (184) Susi, T.; Hardcastle, T. P.; Hofsass, H.; Mittelberger, A.; Pennycook, T. J.; Mangler, C.; Drummond-Brydson, R.; Scott, A. J.; Meyer, J. C.; Kotakoski, J. Single-Atom Spectroscopy of Phosphorus Dopants Implanted into Graphene. *2D Materials* **2017**, *4* (2), 021013.
- (185) Swope, W. C.; Andersen, H. C.; Berens, P. H.; Wilson, K. R. A Computer Simulation Method for the Calculation of Equilibrium Constants for the Formation of Physical Clusters of Molecules: Application to Small Water Clusters. *The Journal of Chemical Physics* **1982**, *76* (1), 637–649.
- (186) Tabard-Cossa, V. Instrumentation for Low-Noise High-Bandwidth Nanopore Recording. *Engineered Nanopores for Bioanalytical Applications: A Volume in Micro and Nano Technologies* **2013**, 59–93.
- (187) Tai, G.; Zeng, T.; Yu, J.; Zhou, J.; You, Y.; Wang, X.; Wu, H.; Sun, X.; Hu, T.; Guo, W. Fast and Large-Area Growth of Uniform MoS₂ Monolayers on Molybdenum Foils. *Nanoscale* **2016**, *8* (4), 2234–2241.
- (188) Tao, Y.; Xue, Q.; Liu, Z.; Shan, M.; Ling, C.; Wu, T.; Li, X. Tunable Hydrogen Separation in Porous Graphene Membrane: First-Principle and Molecular Dynamic Simulation. *ACS Appl. Mater. Interfaces* **2014**, *6* (11), 8048–8058.
- (189) Thakur, M.; Macha, M.; Chernev, A.; Graf, M.; Lihter, M.; Deen, J.; Tripathi, M.; Kis, A.; Radenovic, A. Wafer-Scale Fabrication of Nanopore Devices for Single-Molecule DNA Biosensing Using MoS₂. *Small Methods* *n/a* (n/a), 2000072.
- (190) Thiruraman, J. P.; Fujisawa, K.; Danda, G.; Das, P. M.; Zhang, T.; Bolotsky, A.; Perea-López, N.; Nicolaï, A.; Senet, P.; Terrones, M.; Drndić, M. Angstrom-Size Defect Creation and Ionic Transport through Pores in Single-Layer MoS₂. *Nano Lett.* **2018**, *18* (3), 1651–1659.
- (191) Thiruraman, J. P.; Fujisawa, K.; Danda, G.; Das, P. M.; Zhang, T.; Bolotsky, A.; Perea-López, N.; Nicolaï, A.; Senet, P.; Terrones, M.; Drndić, M. Correction to Angstrom-Size Defect Creation and Ionic Transport through Pores in Single-Layer MoS₂. *Nano Lett.* **2019**, *19* (1), 627–627.
- (192) Thiruraman, J. P.; Masih Das, P.; Drndic, M. Ions and Water Dancing through Atom-Scale Holes: A Perspective toward “Size Zero”. *ACS Nano* **2020**, *14* (4).
- (193) Thiruraman, J. P.; Masih Das, P.; Drndic, M. Irradiation of Transition Metal Dichalcogenides Using a Focused Ion Beam: Controlled Single-Atom Defect Creation. *Adv. Func. Mats.* **2019**, *29* (52), 1904668.
- (194) Thiruraman, J. P.; Masih Das, P.; Drndić, M. Stochastic Ionic Transport in Single Atomic Zero-Dimensional Pores. *ACS Nano* **2020** *14* (9), 11831-11845.
- (195) Thiruraman J.P; Dar S. A; Masih Das P.; Hassani N.; Neek-Amal M.; Keerthi A.; Drndic M.; Boya R. *Sci Adv.* **2020** *6* (51), eabc7927.
- (196) Tkatchenko, A.; Scheffler, M. Accurate Molecular Van Der Waals Interactions from Ground-State Electron Density and Free-Atom Reference Data. *Phys. Rev. Lett.* **2009**, *102* (7), 073005.s
- (197) Tongay, S.; Suh, J.; Ataca, C.; Fan, W.; Luce, A.; Kang, J. S.; Liu, J.; Ko, C.; Raghunathanan, R.; Zhou, J.; Ogletree, F.; Li, J.; Grossman, J. C.; Wu, J. Defects Activated Photoluminescence in Two-Dimensional Semiconductors: Interplay between Bound, Charged, and Free Excitons. *Scientific reports* **2013**, *3*, 2657.

- (198) Tongraar, A.; Liedl, K. R.; Rode, B. M. Born–Oppenheimer Ab Initio QM/MM Dynamics Simulations of Na⁺ and K⁺ in Water: From Structure Making to Structure Breaking Effects. *J. Phys. Chem. A* **1998**, *102* (50), 10340–10347.
- (199) Tripathi, M.; Markevich, A.; Bottger, R.; Facsko, S.; Besley, E.; Kotakoski, J.; Susi, T. Implanting Germanium into Graphene. *ACS Nano* **2018**, *12* (5), 4641–4647.
- (200) Tripathi, M.; Mittelberger, A.; Mustonen, K.; Mangler, C.; Kotakoski, J.; Meyer, J. C.; Susi, T. Cleaning Graphene: Comparing Heat Treatments in Air and in Vacuum. *Physica Status Solidi - Rapid Research Letters* **2017**, *11* (8), 1700124.
- (201) Tsai, C.; Abild-Pedersen, F.; Nørskov, J. K. Tuning the MoS₂edge-Site Activity for Hydrogen Evolution via Support Interactions. *Nano Letters* **2014**, *14* (3), 1381–1387.
- (202) Tunuguntla, R. H.; Henley, R. Y.; Yao, Y.-C.; Pham, T. A.; Wanunu, M.; Noy, A. Enhanced Water Permeability and Tunable Ion Selectivity in Subnanometer Carbon Nanotube Porins. *Science* **2017**, *357* (6353), 792–796.
- (203) Vanderbilt, D. Soft Self-Consistent Pseudopotentials in a Generalized Eigenvalue Formalism. *Phys. Rev. B* **1990**, *41* (11), 7892–7895.
- (204) Varshney, V.; Patnaik, S. S.; Muratore, C.; Roy, A. K.; Voevodin, A. A.; Farmer, B. L. MD Simulations of Molybdenum Disulphide (MoS₂): Force-Field Parameterization and Thermal Transport Behavior. *Computational Materials Science* **2010**, *48* (1), 101–108.
- (205) Venta, K. E.; Zanjani, M. B.; Ye, X.; Danda, G.; Murray, C. B.; Lukes, J. R.; Drndić, M. Gold Nanorod Translocations and Charge Measurement through Solid-State Nanopores. *Nano Lett.* **2014**, *14* (9), 5358–5364.
- (206) Venta, K.; Shemer, G.; Puster, M.; Rodríguez-Manzo, J. A.; Balan, A.; Rosenstein, J. K.; Shepard, K.; Drndić, M. Differentiation of Short, Single-Stranded DNA Homopolymers in Solid-State Nanopores. *ACS Nano* **2013**, *7* (5), 4629–4636.
- (207) Verschueren, D. V.; Yang, W.; Dekker, C. Lithography-Based Fabrication of Nanopore Arrays in Freestanding SiN and Graphene Membranes. *Nanotechnology* **2018**, *29*, 145302.
- (208) de Vos, R. M. High-Selectivity, High-Flux Silica Membranes for Gas Separation. *Science* **1998**, *279* (5357), 1710–1711.
- (209) Wang, L.; Boutilier, M. S. H.; Kidambi, P. R.; Jang, D.; Hadjiconstantinou, N. G.; Karnik, R. Fundamental Transport Mechanisms, Fabrication and Potential Applications of Nanoporous Atomically Thin Membranes. *Nature Nanotech* **2017**, *12* (6), 509–522.
- (210) Wang, L.; Draushuk, L. W.; Cantley, L.; Koenig, S. P.; Liu, X.; Pellegrino, J.; Strano, M. S.; Scott Bunch, J. Molecular Valves for Controlling Gas Phase Transport Made from Discrete Ångström-Sized Pores in Graphene. *Nature Nanotech* **2015**, *10* (9), 785–790.
- (211) Wang, Q. H.; Kalantar-Zadeh, K.; Kis, A.; Coleman, J. N.; Strano, M. S. Electronics and Optoelectronics of Two-Dimensional Transition Metal Dichalcogenides. *Nature Nanotechnology* **2012**, *7* (11), 699–712.
- (212) Wang, S.; Li, H.; Sawada, H.; Allen, C. S.; Kirkland, A. I.; Grossman, J. C.; Warner, J. H. Atomic Structure and Formation Mechanism of Sub-Nanometer Pores in 2D Monolayer MoS₂. *Nanoscale* **2017**, *9* (19), 6417–6426.
- (213) Wanunu, M.; Dadosh, T.; Ray, V.; Jin, J.; McReynolds, L.; Drndić, M. Rapid Electronic Detection of Probe-Specific MicroRNAs Using Thin Nanopore Sensors. *Nature Nanotechnology* **2010**, *5* (11), 807–814.
- (214) Wei, G.; Quan, X.; Chen, S.; Yu, H. Superpermeable Atomic-Thin Graphene Membranes with High Selectivity. **2017**.
- (215) Wen, Y.; Ophus, C.; Allen, C. S.; Fang, S.; Chen, J.; Kaxiras, E.; Kirkland, A. I.; Warner, J. H. Simultaneous Identification of Low and High Atomic Number Atoms in Monolayer 2D Materials Using 4D Scanning Transmission Electron Microscopy. *Nano Lett.* **2019**, *19* (9), 6482–6491.
- (216) Wilson, J.; Aksimentiev, A. Water-Compression Gating of Nanopore Transport. *Phys. Rev. Lett.* **2018**, *120* (26), 268101.
- (217) Wu, K.; Chen, Z.; Li, X. Real Gas Transport through Nanopores of Varying Cross-Section Type and Shape in Shale Gas Reservoirs. *Chemical Engineering Journal* **2015**, *281*, 813–825.

- (218) Wu, T.; Zhang, D. Impact of Adsorption on Gas Transport in Nanopores. *Sci Rep* **2016**, *6* (1), 23629.
- (219) Yamada, Y.; Murota, K.; Fujita, R.; Kim, J.; Watanabe, A.; Nakamura, M.; Sato, S.; Hata, K.; Ercius, P.; Ciston, J.; Song, C. Y.; Kim, K.; Regan, W.; Gannett, W.; Zettl, A. Subnanometer Vacancy Defects Introduced on Graphene by Oxygen Gas. *J. Am. Chem. Soc.* **2014**, *136* (6), 2232–2235.
- (220) Yang, Y.; Fei, H.; Ruan, G.; Xiang, C.; Tour, J. M. Edge-Oriented MoS₂ Nanoporous Films as Flexible Electrodes for Hydrogen Evolution Reactions and Supercapacitor Devices. *Advanced Materials* **2014**, *26* (48), 8163–8168.
- (221) Yao, Y.-C.; Taqieddin, A.; Alibakhshi, M. A.; Wanunu, M.; Aluru, N. R.; Noy, A. Strong Electroosmotic Coupling Dominates Ion Conductance of 1.5 Nm Diameter Carbon Nanotube Porins. *ACS Nano* **2019**, *13* (11), 12851–12859.
- (222) Ye, G.; Gong, Y.; Lin, J.; Li, B.; He, Y.; Pantelides, S. T.; Zhou, W.; Vajtai, R.; Ajayan, P. M. Defects Engineered Monolayer MoS₂ for Improved Hydrogen Evolution Reaction. *Nano Letters* **2016**, *16* (2), 1097–1103.
- (223) Yin, K.; Huang, S.; Chen, X.; Wang, X.; Kong, J.; Chen, Y.; Xue, J. Generating Sub-Nanometer Pores in Single-Layer MoS₂ by Heavy-Ion Bombardment for Gas Separation: A Theoretical Perspective. *ACS Applied Materials and Interfaces* **2018**, *10* (34), 28909–28917.
- (224) Yoon, K.; Rahnamoun, A.; Swett, J. L.; Iberi, V.; Cullen, D. A.; Vlasiouk, I. V.; Belianinov, A.; Jesse, S.; Sang, X.; Ovchinnikova, O. S.; Rondinone, A. J.; Unocic, R. R.; Van Duin, A. C. T. Atomistic-Scale Simulations of Defect Formation in Graphene under Noble Gas Ion Irradiation. *ACS Nano* **2016**, *10* (9), 8376–8384.
- (225) Yoshimura, A.; Lamparski, M.; Kharche, N.; Meunier, V. First-Principles Simulation of Local Response in Transition Metal Dichalcogenides under Electron Irradiation. *Nanoscale* **2018**, *10*, 2388–2397.
- (226) Zan, R.; Ramasse, Q. M.; Jalil, R.; Georgiou, T.; Bangert, U.; Novoselov, K. S. Control of Radiation Damage in MoS₂ by Graphene Encapsulation. *ACS Nano* **2013**, *7* (11), 10167–10174.
- (227) Van Der Zande, A. M.; Kunstmann, J.; Chernikov, A.; Chenet, D. A.; You, Y.; Zhang, X.; Huang, P. Y.; Berkelbach, T. C.; Wang, L.; Zhang, F.; Hybertsen, M. S.; Muller, D. A.; Reichman, D. R.; Heinz, T. F.; Hone, J. C. Tailoring the Electronic Structure in Bilayer Molybdenum Disulfide via Interlayer Twist. *Nano Letters* **2014**, *14* (7), 3869–3875.
- (228) Zhang, J.; Lin, L.; Sun, L.; Huang, Y.; Koh, A. L.; Dang, W.; Yin, J.; Wang, M.; Tan, C.; Li, T.; Tan, Z.; Liu, Z.; Peng, H. Clean Transfer of Large Graphene Single Crystals for High-Intactness Suspended Membranes and Liquid Cells. *Advanced Materials* **2017**, *29* (26), 1–7.
- (229) Zhang, Y.; Meng, Z.; Shi, Q.; Gao, H.; Liu, Y.; Wang, Y.; Rao, D.; Deng, K.; Lu, R. Nanoporous MoS₂ monolayer as a Promising Membrane for Purifying Hydrogen and Enriching Methane. *Journal of Physics Condensed Matter* **2017**, *29* (37).
- (230) Zhang, Y.; Zeng, W.; Li, Y. The Hydrothermal Synthesis of 3D Hierarchical Porous MoS₂ microspheres Assembled by Nanosheets with Excellent Gas Sensing Properties. *Journal of Alloys and Compounds* **2018**, *749*, 355–362.
- (231) Zhang, Z. Y.; Deng, Y. S.; Tian, H. B.; Yan, H.; Cui, H. L.; Wang, D. Q. Noise Analysis of Monolayer Graphene Nanopores. *International Journal of Molecular Sciences* **2018**, *19* (9), 1–11.
- (232) Zhao, J.; He, G.; Huang, S.; Villalobos, L. F.; Dakhchoune, M.; Bassas, H.; Agrawal, K. V. Etching Gas-Sieving Nanopores in Single-Layer Graphene with an Angstrom Precision for High-Performance Gas Mixture Separation. *Science Advances* **2019**, *5*, eaav1851.
- (233) Zheng, B.; Ma, C.; Li, D.; Lan, J.; Zhang, Z.; Sun, X.; Zheng, W.; Yang, T.; Zhu, C.; Ouyang, G.; Xu, G.; Zhu, X.; Wang, X.; Pan, A. Band Alignment Engineering in Two-Dimensional Lateral Heterostructures. *Journal of the American Chemical Society* **2018**, *140* (36), 11193–11197.
- (234) Zhou, W.; Zou, X.; Najmaei, S.; Liu, Z.; Shi, Y.; Kong, J.; Lou, J. Intrinsic Structural Defects in Monolayer Molybdenum Disulfide. **2013**.

- (235) Zhou, Z.; Hu, Y.; Wang, H.; Xu, Z.; Wang, W.; Bai, X.; Shan, X.; Lu, X. DNA Translocation through Hydrophilic Nanopore in Hexagonal Boron Nitride. *Sci Rep* **2013**, 3 (1), 3287.
- (236) Zhou, Z.; Lin, Y.; Zhang, P.; Ashalley, E.; Shafa, M.; Li, H.; Wu, J.; Wang, Z. Hydrothermal Fabrication of Porous MoS₂ and Its Visible Light Photocatalytic Properties. *Materials Letters* **2014**, 131, 122–124.
- (237) Ziegler, J. F.; Ziegler, M. D.; Biersack, J. P. SRIM – The Stopping and Range of Ions in Matter. *Nuclear Instruments and Methods in Physics Research B* **2010**, 268, 1818–1823.
- (238) Zwolak, M.; Lagerqvist, J.; Di Ventra, M. Quantized Ionic Conductance in Nanopores. *Phys. Rev. Lett.* **2009**, 103 (12), 128102.
- (239) Zwolak, M.; Wilson, J.; Di Ventra, M. Dehydration and Ionic Conductance Quantization in Nanopores. *J. Phys.: Condens. Matter* **2010**, 22 (45), 454126.